

*Investigation on Thermoelectric and Magnetic properties
of Transition metal based Chalcogenides*

by

CHINNU V. DEVAN

10PP19A39027

A thesis submitted to the
Academy of Scientific & Innovative Research
for the award of the degree of
DOCTOR OF PHILOSOPHY
in
SCIENCE

Under the supervision of
Dr. Biswapriya Deb



**CSIR-National Institute for Interdisciplinary
Science and Technology (CSIR-NIIST),
Thiruvananthapuram – 695 019**



Academy of Scientific and Innovative Research
AcSIR Headquarters, CSIR-HRDC campus
Sector 19, Kamla Nehru Nagar,
Ghaziabad, U. P. – 201 002, India

February 2024

*Dedicated to
My Family...*




राष्ट्रीय अंतर्विषयी विज्ञान तथा प्रौद्योगिकी संस्थान
NATIONAL INSTITUTE FOR INTERDISCIPLINARY SCIENCE AND TECHNOLOGY

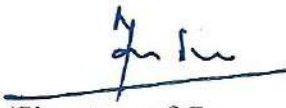
वैज्ञानिक तथा औद्योगिक अनुसंधान परिषद्
इन्डस्ट्रियल एस्टेट पी.ओ., पाप्पनकोड, तिरुवनंतपुरम, भारत - 695 019

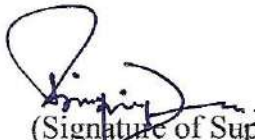
Council of Scientific & Industrial Research
Industrial Estate P.O., Pappanamcode, Thiruvananthapuram, India - 695 019

Certificate

This is to certify that the work incorporated in this Ph.D. thesis entitled, "Investigation on Thermoelectric and Magnetic properties of Transition metal-based Chalcogenides", submitted by Chinnu V.Devan to the Academy of Scientific and Innovative Research (AcSIR), in fulfillment of the requirements for the award of the Degree of DOCTOR OF PHILOSOPHY in SCIENCE, embodies original research work carried out by the student. We, further certify that this work has not been submitted to any other University or Institution in part or full for the award of any degree or diploma. Research material(s) obtained from another source(s) and used in this research work has/have been duly acknowledged in the thesis. Image(s), illustration(s), figure(s), table(s) etc., used in the thesis from other source(s), have also been duly cited and acknowledged.


(Signature of Student)
Chinnu V Devan

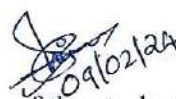

(Signature of Co-supervisor)
Dr. Manoj Raama Varma


(Signature of Supervisor)
Dr. Biswapriya Deb

Date: 09/02/2024

STATEMENTS OF ACADEMIC INTEGRITY

I Chinnu V. Devan., a Ph.D. student of the Academy of Scientific and Innovative Research (AcSIR) with Registration No. 10PP19A39027 hereby undertake that, the thesis entitled "Investigation on Thermoelectric and Magnetic properties of Transition metal based Chalcogenides" has been prepared by me and that the document reports original work carried out by me and is free of any plagiarism in compliance with the UGC Regulations on "Promotion of Academic Integrity and Prevention of Plagiarism in Higher Educational Institutions (2018)" and the CSIR Guidelines for "Ethics in Research and in Governance (2020)".



Signature of the student

Chinnu V. Devan

Date : 09/02/2024

Place : Thiruvananthapuram

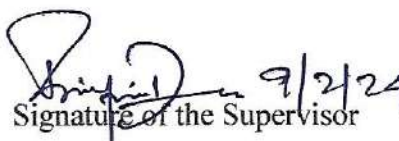
It is hereby certified that the work done by the student, under my/our supervision, is plagiarism free in accordance with the UGC Regulations on "*Promotion of Academic Integrity and Prevention of Plagiarism in Higher Educational Institutions (2018)*" and the CSIR Guidelines for "*Ethics in Research and in Governance (2020)*".


Signature of the Co-supervisor
9/2/2024

Dr. Manoj Raama Varma

Date: 09/02/2024

Place:Thiruvananthapuram


Signature of the Supervisor
9/2/24

Dr. Biswapriya Deb

Date: 09/02/2024

Place:Thiruvananthapuram

DECLARATION

I, Chinnu V. Devan, bearing AcSIR Registration No. 10PP19A39027 declare that my thesis entitled, "Investigation on Thermoelectric and Magnetic properties of Transition metal based Chalcogenides" is plagiarism free in accordance with the UGC Regulations on "*Promotion of Academic Integrity and Prevention of Plagiarism in Higher Educational Institutions (2018)*" and the CSIR Guidelines for "*Ethics in Research and in Governance (2020)*". I would be solely held responsible if any plagiarised content in my thesis is detected, which is violative of the UGC regulations 2018.


Chinnu V. Devan

Date : 09/02/2024

Place : Thiruvananthapuram

ACKNOWLEDGEMENTS

Ph.D. life was a challenging and rewarding experience. I consider myself very lucky to have been able to interact with many incredible scientists and friends, and I would like to take a moment to thank them for their role in this Ph.D. journey.

*It is with great pleasure that I extend my deepest sense of gratitude to my thesis supervisors, **Dr. Biswapriya Deb & Dr. Manoj Raama Varma**, for suggesting me the research problem. Their valuable support, encouragement, and guidance throughout the research period has led to the successful completion of this work. Throughout the Ph.D., we had great scientific and personal discussions. I thank them for introducing me to the world of material science and giving me the scientific freedom that helped me develop the confidence to move in this field.*

*I wish to thank **Dr. C. Anandharamakrishnan**, Director and **Dr. Ajay Ghosh** former Director of the CSIR-NIIST, for providing me with the necessary facilities for carrying out the work.*

*I sincerely thank my other DAC members **Dr. K.N. Narayanan Unni, Dr. K. P. Surendran, and Dr. Achu Chandran** for their support and insightful comments regarding my work and constructive criticism, which always helped me to constantly question myself and look at my work a different perspective. I extend my sincere thanks to **Dr. Jayamurthy P., Dr. V. Karunakaran, and Dr. C. H. Suresh**, present and former AcSIR coordinators at CSIR-NIIST, for their timely help and advice for the academic procedures of AcSIR. I want to thank **Prof. K.G.Suresh**, Indian Institute of Technology, Bombay, **Prof. Santhosh P.N**, Indian Institute of Technology, Madras and **Dr. Senoy Thomas**, Assistant Professor, CUSAT for their support during the research work.*

*I would also like to thank **Dr. S. Ananthakumar, Dr. U. S. Hareesh, Dr. T. P. D. Rajan, Dr. Satyajith Shukla, Dr. Savitri S. Dr. E. Bhoje Gowd, Dr. K. G. Nishanth, Dr. Subrata Das, Dr. K.V.Radhakrishnan, Dr.P.Sujatha Devi, Dr. C. Vijayakumar, Dr. Joshy Joseph, Dr. K.K. Maiti, Mr. Venkatesan and Mr. C. K. Chandrakanth** for their support and encouragement. I would like to thank **Dr. Saju Pillai and Mr. Peer Muhammad** for timely XPS measurements and valuable discussions. Also, I would like to thank **Ms. Anjali, and Mr. Harish Raj V.** for the XRD and SEM studies for the research work, and **Dr. Jerrin and Mr. Mohammad** for the TGA analysis. The support of **Mr. Robert Philip and Mr. Kiran Mohan** for TEM measurements is greatly acknowledged. The support of all the other scientists of NIIST is greatly acknowledged.*

*I would like to thank former technical assistant, Mr. S. Vishnu and Mr. Karthikey Singh for his technical support in PPMS measurements during my initial stages of research. Words are inadequate to express my gratitude to Mr. Anoop A. Nair and Dr. Revathy, they helped me a lot to carry out my work. The valuable advice and help provided by the senior research scholars of **Magnetism Group**, Dr. Revathy R, Dr. K. Aswathi, Dr. P. Neenu Lekshmi, Dr. B. Arun, Dr. V. R. Akshay, Dr. K. S. Dijith, and Dr. R. Aiswarya are acknowledged with gratitude. Their constant support and advice have helped me immensely throughout this research. I would especially like to thank my colleagues Ms. V. S. Aswathy, Mr. P. C. Shabeer Ali, Mr. Christan Sam, Mr. Rojerce Brown Job and Ms. Shamili C. Das. My group, the **Smart Materials & Devices Group**, including, Dr. Vijitha I., Dr. Shaiju S.S., Ranjana Venugopal, Nayan Dev Madhav, Amritha P., Nithin R.S., Dr. Swetha S., Vishnu Prasad C. V., Abhishek A. K., Siva Krishna P., Meritta James, Salil. P, Meenu, Arathy, Anjitha, Anju and Sandhesh helped to create a supportive and hardworking space for good science. I am deeply grateful to all the present and former students I've worked with within NIIST, that includes Mukesh, B. S. Athira, Abhilash, Harris, Anas, Shamini, Bhavya, Husan, Adarsh S., Sumith, Shafeeq, Suja, Haritha, Sophy, Malini, Thejas K.K, Ranjith P., Shisina, Meera, Dr. Thejus K.K., Dipa, Akhil M.G, Vibhu Dharshan, Naveen and Neethi. I am very much thankful to all the office, workshop and library staff at NIIST for their kind cooperation. I acknowledge the **University of Grant Commission (UGC)** and **Council of Scientific & Industrial Research (CSIR)** for providing fellowship to complete this work.*

The most important mentors who played a key role to focus of my research career are my teachers from school to college. I am very grateful to my friends Smitha, Josna, Athira, Remya, and Divya for their love and valuable support. I owe an unlimited debt of gratitude to my parents, especially my mother, Prasanna, my guide, and my mentor, for her unconditional love. Without her support and encouragement, I would not have reached this stage of my life. I am also indebted to all my family members for their encouragement, love, support, and understandability throughout these years, which has helped me in the successful and timely completion of this work. I thank my better half Akhil for his invisible support in balancing my research, career and life. Last but not least, I thank GOD, the Almighty, for blessings and for being so kind to me throughout my life

Chinnu V. Devan

CONTENTS

Acknowledgments	i
Contents	iii
List of Figures	vii
List of Tables	xiii
List of Abbreviations	xv
Preface	xvii
Introduction to Thermoelectrics and Magnetism	1-40
CHAPTER 1	
1.1. World Energy Scenario	1
1.2. Basic Concepts of Thermoelectricity	4
1.3. Optimization of thermoelectric parameters	5
1.3.1. Seebeck coefficient	6
1.3.2. Electrical conductivity	7
1.3.3 Thermal conductivity	8
1.4. Mechanisms and methods to enhance Figure of merit	9
1.5. Class of Inorganic thermoelectric materials	13

1.6.	Magnetic properties of Transition metal Chalcogenides	16
1.6.1.	General introduction to magnetism	17
1.6.2.	Classification of magnetic materials	18
1.6.3.	Glassy nature	20
1.6.4.	Griffith's like phase	21
1.7.	Magneto-transport properties	22
1.8.	Material manufacturing techniques	24
1.9.	Application of Transition metal-based chalcogenides.	26
	Outline of the thesis	29
	References	30
	CHAPTER 2	
	Experimental Methods	39-42
2.1	Materials	39
2.2	Sample fabrication	39
	CHAPTER 3	40-79
	Exotic Magnetic, Magneto-transport and Thermoelectric properties of BaVSe₃	
	Introduction	43
3.1.	Results and discussion	45
3.1.1.	Crystal structure and surface studies	45
3.1.2.	Magnetic properties	50
	3.1.2.1. Magnetic studies of BVS: BS	50
	3.1.2.2. Magnetic studies of BVS	58

3.1.3. Magneto-transport studies of BVS	61
3.1.4. Thermoelectric studies	64
3.2. Conclusion	67
References	68
CHAPTER 4	The Synthesis, Magnetic and Thermoelectric studies of
	CoMSe₂ (M = Ni, Fe)
	78 - 100
Introduction	78
4.1. Results and discussion	79
4.1.1. Structural and compositional analysis	79
4.1.2. Magnetic properties	83
4.1.2.1. Magnetic properties of CNS	83
4.1.2.2. Magnetic properties of CFS	87
4.1.3. Thermoelectric properties	89
4.2. Conclusion	94
References	95
CHAPTER 5	The Low-Temperature Thermoelectric Transport Behavior
	of AgSbTe₂
	101 -127
Introduction	101
5.1. Results and discussion	102
5.1.1. Structure and morphology	102

5.1.2. Thermoelectric studies	107	
5.2. Conclusion	118	
References	122	
CHAPTER 6	Summary and Outlook	128-129
Appendix	130	
Annexure	131	
Abstract	141	
Details of Publications and conference presentations	142	

LIST OF FIGURES

CHAPTER 1

Figure 1.1	Changes in the global energy mix, 2020-2040, IEA	2
Figure 1.2	Schematic representation of various sectors that contribute heat energy	3
Figure 1.3	The high ZT thermoelectric materials generated over the past two decades	4
Figure 1.4	Schematic diagram of (a) Seebeck effect, (b) Peltier effect	5
Figure 1.5	Optimization of various transport parameters with carrier density	8
Figure 1.6	Various mechanisms to enhance thermoelectric properties	10
Figure 1.7	(a) Schematic diagram of all scale hierarchical architectures for phonon scattering, (b) an analysis of variation of cumulative k_{lat} with phonon mean free path in PbTe, (c) Temperature dependence k_{lat} for all scale hierarchical architectures in SnSe	13
Figure 1.8	Class of thermoelectric materials	15
Figure 1.9	Schematic representation of spin alignment for different magnetic systems	19
Figure 1.10	Identifying various terms in the hysteresis loop of an FM material	20

Figure 1.11	Susceptibility versus temperature plot for AFM, FM and PM materials	21
Figure 1.12	The glassy nature of magnetic materials	22
Figure 1.13	$1/\chi$ versus T plot for (a) AFM, PM and FM materials (b) Griffith's like phase	24
Figure 1.14	Schematic diagram of (a) MR of GMR material, (b) BMR	25
Figure 1.15	Schematic diagram of various synthesis techniques (a) Bridgman method (single crystal growth), (b) aqueous solution method, (c) solvothermal route, (d) melting, (e) mechanical alloying, (f) chemical vapour deposition	26
Figure 1.16	Interconnection between thermal, electronic and magneto-transport	27
Figure 1.17	An overview of thermoelectric applications	28
Figure 1.15	An outline of spintronics	29
CHAPTER 2		
Figure 2.1	Schematic diagram for solid state route	39
Figure 2.2	Heat treatment of sample (a) BVS: BS (b) BVS	40
Figure 2.3	Heat treatment steps of samples CNS and CFS	41

CHAPTER 3

- Figure 3.1** (a) Rietveld refined XRD pattern of BVS: BS, (b) A graphical representation of the $BaVSe_3$ unit cell obtained from the refined XRD data, (c) Rietveld refined XRD pattern of BVS, (d)-(f) Unit cell of $BaVSe_3$ at different crystallographic direction from VESTA 46
- Figure 3.2** Deconvoluted high resolution XPS spectra of elements (a) Ba, (b) V, and (c) Se 47
- Figure 3.3** Scanning electron microscopy images of the pellet sample BVS:BS (a) on a $10\ \mu\text{m}$ scale, (b) associated needle-shaped crystals on the surface of the sample BVS:BS ($2\ \mu\text{m}$ scale), (c) EDS spectrum (d) elemental mapping of BVS: BS, (e)- (f) SEM images of BVS at different scales and (h) EDS spectrum of the sample BVS 48
- Figure 3.4** (a)-(d), Elemental mapping of the sample BVS at a micrometre scale, constituent elements Ba, V, Se were mapped 49
- Figure 3.5** (a)TEM image of the synthesized material BVS, (b) & (c) the HRTEM images with crystal planes and the corresponding d spacing were marked, (d) SAED pattern of the material 50
- Figure 3.6** (a) M-H loops at different temperatures, (b) zoomed-in portion of Figure 3(a), (c) M-T curves taken at the different magnetic field, (d) dM/dT versus T plot 51
- Figure 3.7** (a) C-W plot at different fields (b) C-W plot with linear fit in the PM region 54

Figure 3.8	(a) GP analysis, (b) M-H loop at 43 K, (c) M-H loop at 50 K, (d) Arrott plot	55
Figure 3.9	Frequency dependence of the (a) real component of AC-magnetic susceptibility, (b) relaxation time τ versus maximum spin-freezing temperature T_f fitted to the VF law (solid line) and power law (dashed line). Inset shows linear fitted $\ln(\tau)$ versus $\ln(t)$, where reduced temperature $t = (T_f - T_{SG})/T_{SG}$ and the solid line is the linear fit	57
Figure 3.10	(a) Temperature-dependent ZFC and FC magnetization of the sample at different fields, (b) dM/dT versus T plot at an applied field of 100 Oe, (c) Linear fit on the Curie-Weiss plot at 100 Oe, (d) M versus H at different temperatures	59
Figure 3.11	(a) Hysteresis loop at 50 K (b) GP analysis by the linear fit on the CW plot at different fields (c) $\ln(1/\chi)$ versus $\ln(T - T_C^R)$ at different fields (d) Arrott plot (M^2 versus H/M) at 41 K, 43 K, 44 K and 50 K	60
Figure 3.12	MR versus H at (a) 3 K, 5 K and 10 K, (b) 38 K, 40 K, 42 K and 50 K	61
Figure 3.13	Temperature-dependent (a) electrical conductivity, (b) Seebeck coefficient, (c) Power factor and (d) thermal conductivity of both BVS and BVS: BS	64
Figure 3.14	(a) Temperature dependence of Lorenz number, (b) electronic thermal conductivity, (c) lattice thermal conductivity and (d) thermoelectric figure of merit of the samples	66

CHAPTER 4

Figure 4.1	(a), (b) & (c), (d) XRD pattern and crystal structure of CNS & CFS respectively	80
Figure 4.2	(a)- (c) Higher resolution spectra of Co, Ni, Se of CNS and Co, Fe, Se of CFS	81
Figure 4.3	SEM images of (a) CNS and (b) CFS on a length scale of 10 μm (inset figures at 2 μm)	82
Figure 4.4	(a) HRTEM image of CNS, (b) Elemental mapping of CNS, (c) TEM-EDS spectra of the sample (d) SAED pattern of CNS	82
Figure 4.5	(a) SEM-EDAX and (b) elemental mapping of CFS	83
Figure 4.6	(a) M versus H at different temperatures, (b) M versus T at different fields, (c) Neel temperature from M-T plot at 500 Oe, and (d) CW plot in FC mode at 500 Oe	84
Figure 4.7	(a) M versus H plot at 7 K, 8 K and 9 K, (b) zoomed MH curve at 8 K, (c) & (d) linear fit on CW curve at 1000 Oe and 10000 Oe, (e) linear fit on $\ln(1/\chi)$ versus $\ln(T-T_C^R)$, and (f) Arrott's plot at 7 K	86
Figure 4.8	(a) M –H data at 500 K and 700 K, (b) M versus T at 500 Oe, (c) dM/dT versus T at 500 Oe, (d) linear fit on the CW plot at 500 Oe	88
Figure 4.9	Temperature-dependent (a) electrical conductivity, (b) Seebeck coefficient, (c) power factor, (d) thermal conductivity, (e) Lorenz number and (f) electronic thermal conductivity	90
Figure 4.10	Temperature-dependent (a) lattice thermal conductivity, (b) specific heat capacity, (c) & (d) linear fit on C/T versus T^2 plot, (e) ZT versus T for CNS and CFS	93

CHAPTER 5

Figure 5.1	(a). Powder X-ray diffraction pattern of the as-synthesized sample; (b) Crystal structure of AgSbTe ₂ from VESTA	102
Figure 5.2	XPS spectra of the as-synthesized sample (a) Survey spectrum (b)- (d) high-resolution spectra of Ag, Sb, and Te respectively	103
Figure 5.3	(a)-(d) SEM micrographs of the sample at different scale bars; (e)-(f) SEM-EDX of the sample	105
Figure 5.4	(a), (b), TEM images of AgSbTe ₂ , (c) SAED pattern of the material under study; (d)- (e) Observed nanostructures in AgSbTe ₂ , (f) HRTEM image of the sample confirms the Ag ₂ Te monoclinic phase, and (g) TEM-EDS elemental mapping of the material	106
Figure 5.5	(a)Temperature dependence of electrical conductivity; (b) VRH fit on electrical conductivity versus T data ; (c) Temperature dependence of Seebeck coefficient; (d) VRH fit on the S versus T data	108
Figure 5.6	(a) Magnetoresistance versus magnetic field plot; (b) Linear fit on $\ln \rho(H)/\rho(0)$ versus H^2 , Schematic representation of (c) VRH mechanism, (d) Electron filtering mechanism, and (e) PF versus T plot	111
Figure 5.7	(a) Calculated Lorenz number from S; (b) Variation of L with T; Variation of (c) electronic thermal conductivity with T; (d) total and lattice thermal conductivity with T	113
Figure 5.8	HRTEM images of the sample (a), amorphous, crystalline regions and dislocations; (b) IFFT of HRTEM images clearly shows the	114

lattice dislocations; (c) schematic representation of phonon scattering mechanisms; and (d) 1D ball and spring model for phonon-phonon interaction

- Figure 5.9** (a) Temperature - dependent heat capacity of the material (inset : C/T versus T^2 plot), (b) Schematic explanation for lattice softening, (c) Variation of ZT with temperature, (d) A comparison of ZT of the present material with previous reports 115
- Figure 5.10** (a) High temperature PF versus T; (b) Variation of calculated one - leg TE efficiency with ΔT 117

LIST OF TABLES

CHAPTER 3

Table 3.1	Comparison of H_C , M_S and M_R	52
Table 3.2	Experimentally obtained room temperature values of n , μ and m^* of the materials	65

CHAPTER 4

Table 4.1	Data obtained from CW linear fit	85
Table 4.2	All possible cationic combinations of the spin-only moment of CNS	85
Table 4.3	All possible cationic combinations of spin only moment of CFS	89
Table 4.4	Calculated n , μ , and m^* at room temperature for CNS and CFS	91
Table 4.5	Calculated Debye temperature and density of states at E_F of CNS and CFS	94

CHAPTER 5

Table 5.1	Elemental weight percentage of AgSbTe_2 calculated and obtained from SEM-EDX	105
Table 5.2	Obtained values of n , μ , and m^* from Hall effect measurement and Mott equation	110

LIST OF ABBREVIATIONS

Å	Angstrom
AFM	Antiferromagnetic
α	Seebeck coefficient
κ	Thermal conductivity
σ	Electrical conductivity
BE	Binding energy
CW	Curie-Weiss
DOS	Density of states
E_F	Fermi level
ETO	Electrical Transport Option
eV	Electron volt
FM	Ferromagnetic
GP	Griffith's like phase
h	Planck's constant
k_B	Boltzmann constant
ME	Mobility edge
MR	Magnetoresistance
PF	Power factor
PM	Paramagnetic
PPMS	Physical Property Measurement System
RT	Room temperature

SEM	Scanning Electron Microscopy
TE	Thermoelectrics
TEG	Thermoelectric generator
TEM	Transmission Electron Microscopy
TGA	Thermogravimetric Analysis
TTO	Thermal Transport Option
VSM	Vibrating Sample Magnetometer
VRH	Variable range hopping
XRD	X-ray Diffraction
XPS	X-ray Photoelectron Spectroscopy
ZT	Figure of merit

PREFACE

The global energy landscape faces a critical challenge—the looming energy crisis. With escalating demands and the finite nature of conventional energy sources, the need for sustainable and efficient energy conversion technologies has never been more pressing. In this context, thermoelectric materials emerge as promising candidates for addressing this crisis by providing a means to harness waste heat and convert it into useful electrical power. Thermoelectricity, a phenomenon that enables the direct conversion of temperature gradients into electrical voltage, holds great promise in mitigating energy scarcity and promoting sustainability.

Transition metal chalcogenides (TMCs) have garnered significant attention in the field of thermoelectrics and spintronics, owing to their unique electronic and magnetic properties. This class of compounds exhibits a rich array of features that make them promising candidates for advancing technology in both thermoelectric devices and spin-based electronics. By exploiting the coupling between charge and spin degree of freedom, TMCs hold potential in the development of spintronic components such as spin valves and magnetic tunnel junctions.

The core interest of this thesis is concerned with the synthesis of novel TMCs and the investigation of their low-temperature thermoelectric and magnetic properties. A thorough investigation is conducted on the originating mechanism that influences various properties in transition metal chalcogenides. The unusual magnetic properties like Griffith's like phase, glassy nature, the variation of thermoelectric and magnetic properties on the substitution at the transition metal site, and ultralow thermal conductivity due to the spontaneous nanostructures in these TMCs were explained. This thesis work outlines the design of a few transition metal ternary chalcogenides as well as cutting-edge methodologies for developing high-performance thermoelectric materials for power production and spintronics.

Chapter1

Introduction to Thermoelectrics and Magnetism

1.1. World Energy Scenario

The global energy scenario undergoing a profound transformation driven by a combination of environmental, technological and geopolitical factors [1]. Historically, the world's energy needs have largely been met by fossil fuels, including coal, oil, and natural gas. However, growing concerns about climate change, air pollution, and energy security have prompted a fundamental reevaluation of our energy sources and consumption patterns. The global energy demand is a dynamic and evolving concept, influenced by multiple factors, including technological advancements, policy decisions and societal preferences. Growing population, urbanization, industrialization and transportation are the core factors that play a major role in global energy consumption [2]. Addressing the critical issues associated with fossil fuels requires a transition to cleaner and more sustainable energy sources, such as renewable energy (solar, wind, hydro and geothermal) as well as energy efficiency measures.

The World Energy Outlook 2022 (WEO) [3] of the International Energy Agency (IEA) offers crucial analysis and perceptions on the effects of this significant and ongoing shock to energy systems around the world. With the Russia-Ukraine conflict in early 2022, the recovery in global energy consumption that had followed the pandemic-caused dip in 2020 came to an abrupt end, causing inflationary pressures to rise and economic development to decelerate. Governments are being forced to take immediate action in response to the global energy crisis brought on by Russia's invasion of Ukraine, as well as engage in a deeper discussion about how to promote energy security and reduce the risk of future disruptions [3]. In response to rising demand, high natural gas costs, and worries about energy security, many nations have recently experienced an increase in the usage of coal in the electrical industry; however, this is only likely to last a short time. Even in the STEPS (Stated Policies Scenario), unabated coal generation declines from 36% in 2021 to 26% in 2030 and 12% in 2050, demonstrating the rise of renewable energy, led by solar PV and wind. In the APS (Announced Pledges Scenario), promises are kept, including net zero emissions commitments in 83 nations and the European Union. While wind capacity will increase more than double to 210 GW in 2030 and reach 275 GW in 2050, solar PV capacity will increase from 151 gigawatts (GW) in 2021 to 370 GW in 2030 and over 600 GW in 2050 [4].

IEA estimates annual projections about potential energy demand using several different scenarios. Figure 1.1 shows an estimation of changes in the global energy based on the Stated Policies Scenario 2021 and it projects that the total energy demand will increase 21% by 2040 [4].

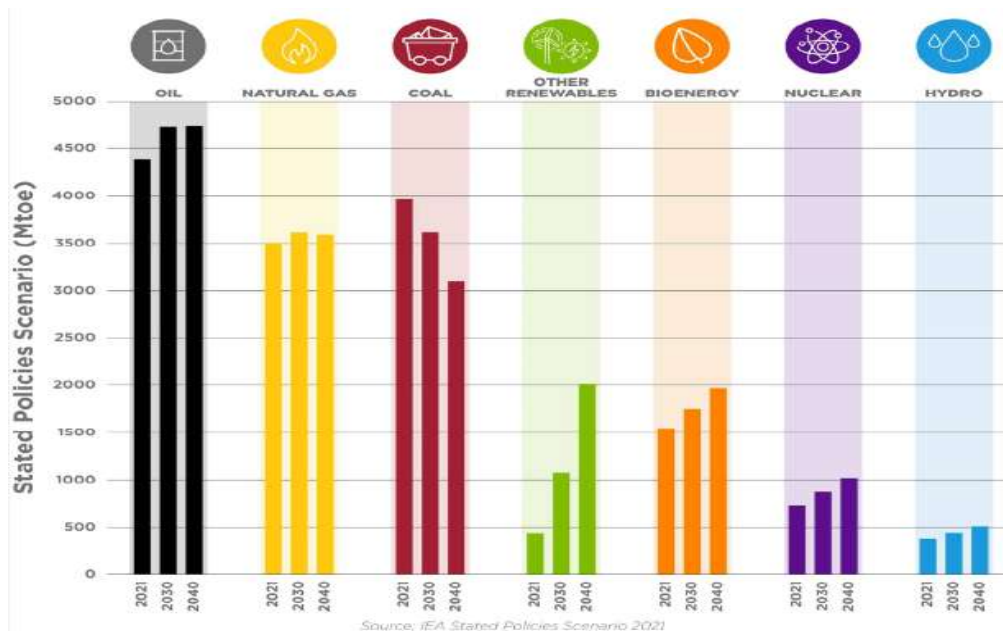


Figure 1.1. Changes in the global energy mix, 2020-2040, IEA (Adopted from Ref. [4])

The International Renewable Energy Agency (IRENA) released the World Energy Transitions Outlook 2023, which is mainly focused on the climate change arising around the globe. If global temperature rise can be kept to 1.5 °C over pre-industrial levels this century, as per the Paris Agreement's goals, depends on how well this decade's efforts to reduce greenhouse gas emissions perform. The World Energy Transitions Outlook's 1.5 °C scenario by IRENA proposes a strategy for reaching the 1.5 °C goal by 2050, highlighting electrification and efficiency as major transition drivers made possible by renewable energy, clean hydrogen, and sustainable biomass [5].

According to the world energy consumption statistics China, the United States and India are the biggest consumers of electricity [4]. India is the third largest energy-consuming country with noticeable progress in exploring renewable energy resources [6]. India bags 4th place in renewable energy installed capacity (1000 + GW) that includes wind power and solar power. The major contributions come from wind power (42.8 GW), solar Power: 67.07 GW, biomass/co-generation (10.2 GW), small hydropower (4.94 GW), waste-to-energy (0.55 GW) and large hydro (46.85 GW). India has set a 500 GW of renewable energy capacity as part of

a reduction in carbon emission by 1bn tones by 2030 and achieve a net zero carbon emission by 2070 [6].

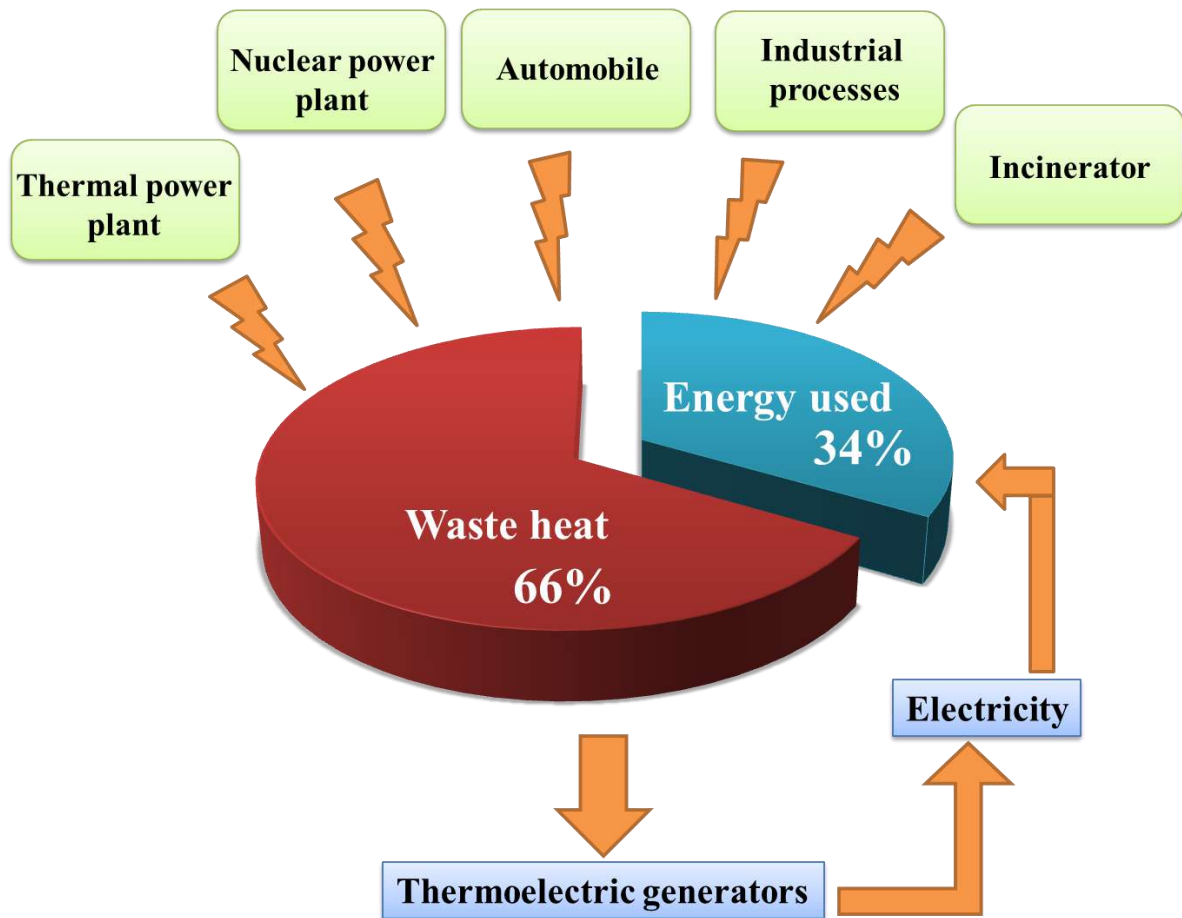


Figure 1.2. Schematic representation of production of heat energy from various sectors and the electricity generation from waste heat.

The need for sustainable energy resources is increasing day by day due to carbon emissions and other environmental effects caused by conventional energy resources [7]. A large proportion (60-70%) (Figure 1.2) of energy used worldwide is converted into unused heat energy and the recovery of this heat energy into useful electrical energy is considered as a potential candidate of sustainable energy resource [8]. Thermoelectric power generation has become one of the promising clean energy sources for future energy applications. Thermoelectric generators directly convert heat energy into electrical energy and also find applications in the field of heating and cooling [9]. Thermoelectric devices have special attention due to their reliability, compact size, silent operation, longevity, scalability, low operation cost, compatibility with renewable energy and environmental friendliness. The efficiency of the thermoelectric generators was limited to 5-8% and to get a higher efficiency

of ~30-33 % the material should possess the highest figure of merit (ZT) in the range of 3-4 [10]. The conventional inorganic thermoelectric materials have $ZT \sim 1$ and there is a serious search for new materials and methods that generate the highest efficiency [11]. In the past two decades, the field of thermoelectricity has advanced rapidly by introducing new concepts for the development of high-performance thermoelectric materials [12,13] (Figure 1.3).

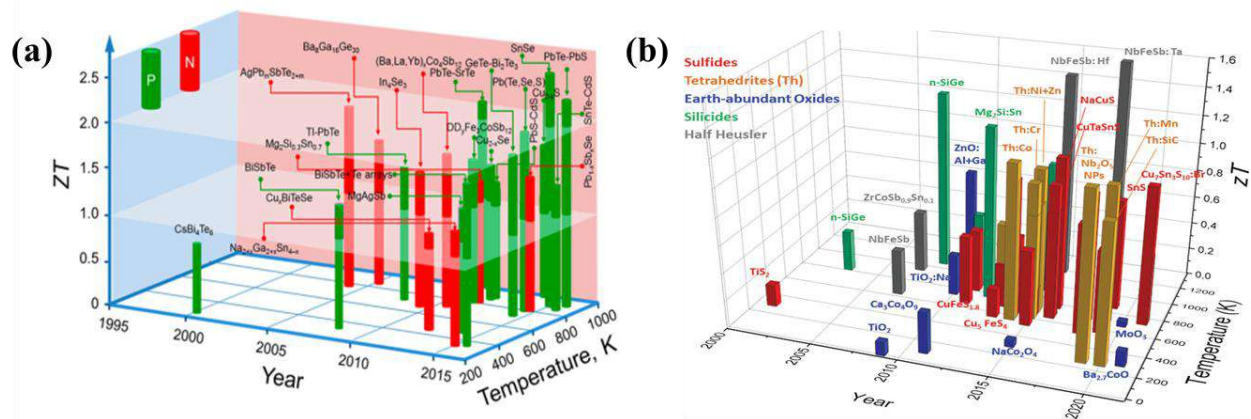


Figure 1.3. The high ZT thermoelectric materials generated over the past two decades {Ref. [10,14]}.

1.2. Basic Concepts of Thermoelectricity

The history of thermoelectricity started at the end of the XVIII century in connection with the research on the effect of electricity on animals by the Italian physician, physicist and biologist Luigi Aloisio Galvani [15]. In 1821 German physicists observed that a closed circuit made up of two dissimilar metals with the two junctions maintained at different temperatures resulted in a deflection on the compass needle kept near the circuit and later named it the Seebeck effect [16]. The reverse phenomenon of the Seebeck effect was discovered in 1834 by French physicist Jean Charles Athanase Peltier. In the Peltier effect, the applied current at the junctions of dissimilar metals results in the heating or cooling of the junction concerning the direction of current flow [16]. British mathematical physicist William Thomson found the third thermoelectric effect, which covers the release or absorption of heat due to the current flow in a homogeneous material under a temperature gradient [17]. Figure 1.4 depicts the working principle of Seebeck and Peltier effect [18].

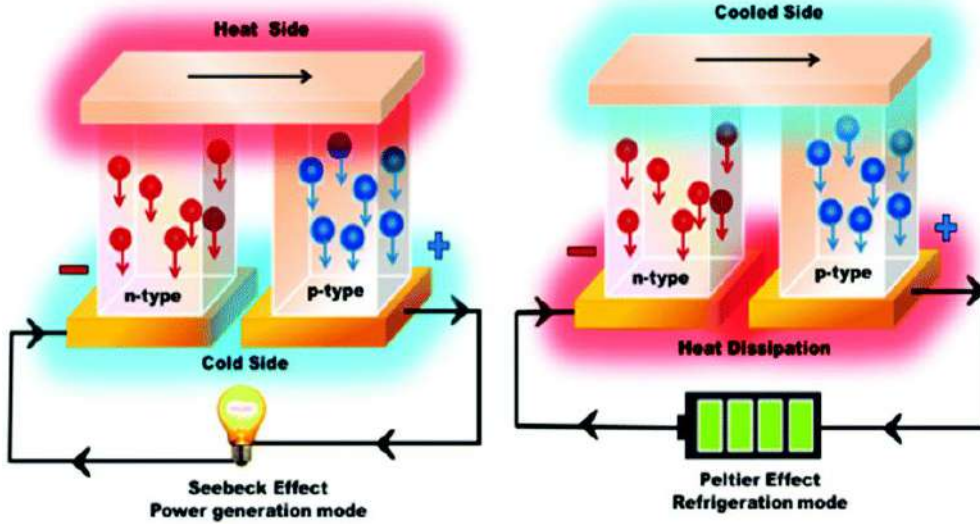


Figure 1.4. Schematic diagram of (a) Seebeck effect, (b) Peltier effect {Ref.[18]}

The thermoelectric modules are composed of electrically series and thermally parallel n-type and p-type semiconductor legs. The diffusion of charge carriers from the hot end to the cold end generates a thermal voltage in a thermoelectric device. The efficiency (η) of the thermoelectric module is the ratio of the applied power (P) of the heat flow to the heat absorbed (Q) from the hot side of the module and it is expressed as

$$\eta = \frac{P}{Q}$$

The maximum efficiency [19] of the thermoelectric device can be represented as

$$\eta = \eta_C \left(\frac{\sqrt{1+ZT}-1}{\sqrt{1+ZT} + \frac{T_C}{T_H}} \right)$$

Where $\eta_C = (T_H - T_C) / T_H$ is the Carnot efficiency, ZT , T_H and T_C are the figure of merit, hot and cold side temperatures respectively. The conversion efficiency of the thermoelectric module mainly depends on the ZT of the material.

1.3. Optimization of Thermoelectric parameters

The performance of a thermoelectric material is expressed by the dimensionless figure of merit (ZT) [20] and it mainly depends on three material properties electrical conductivity (σ), thermal conductivity (k) and Seebeck coefficient (α). It is expressed as

$$ZT = \frac{\alpha^2 \sigma T}{k}$$

Where T is the absolute temperature. Another parameter that quantifies the quality of the thermoelectric material is the power factor (PF) and it is the product of α^2 and σ . The optimization of various electronic and transport properties is required to get a high ZT value. In the area of thermoelectrics, there is an inevitable optimization of electronic and thermal transport parameters. To attain the maximum ZT the material should have a large Seebeck coefficient, high electrical conductivity and low thermal conductivity [21].

1.3.1. Seebeck coefficient

The magnitude of the thermoelectric effect is measured by the parameter Seebeck coefficient. It is also termed the thermopower and is expressed as the ratio of the voltage (dV) generated to the temperature gradient (dT)

$$\alpha = -\frac{dV}{dT}$$

The thermodynamic characteristics of the Seebeck coefficient are explained by considering the charge carriers within the material as a thermodynamic system. The change in Gibbs free energy (G) of the system is given by [22]

$$dG = -SdT + \mu dN$$

Where S is the entropy, μ is the chemical potential and N is the number of charge carriers. The temperature-dependent variation of chemical potential is connected to the entropy per charge carrier as

$$\frac{\partial \mu}{\partial T} = -\frac{\partial S}{\partial N} = -\theta$$

Where θ is the entropy per charge carriers. In the Seebeck effect, the thermoelectric material is maintained at different temperatures and it leads to the difference in chemical potential. The generated chemical potential can be related to the electrical potential (Φ) by

$$\Delta \Phi = \frac{\Delta \mu}{q} \text{ or } \frac{d\mu}{q}$$

Where q is the amount of charge per charge carrier and the Seebeck coefficient can be expressed in terms of both electrical potential and thermal potential

$$\alpha = -\frac{\partial \Phi}{\partial T} = \frac{-1}{q} \frac{\partial \mu}{\partial T} = \frac{\theta}{q}$$

The Seebeck coefficient can be positive (holes) or negative (electrons) depending on the nature of the carriers. The presence of both n-type and p-type carriers results in the cancellation of Seebeck voltage and that reduces the overall Seebeck coefficient. For metals or degenerate semiconductors, the Seebeck coefficient is given by the Mott equation [23]

$$\alpha = \frac{8\pi^2 k_B^2 T}{3eh^2} m^* \left(\frac{\pi}{3n}\right)^{2/3}$$

Where n is the carrier concentration and m* is the effective mass of the carrier. According to this relation low carrier concentration in semiconductors and insulators results in a high Seebeck coefficient and the effective mass of the carriers also enhances its value.

1.3.2. Electrical conductivity

The electrical conductivity of the material is related to the carrier concentration (n) and mobility (μ) through the relation

$$\sigma = ne\mu$$

The low carrier concentration results in low electrical conductivity (high α) and it is proposed that the material-optimized carrier concentration in the range of 10^{19} - 10^{21} per cm^3 (Figure 1.5) shows a high ZT value [23]. Heavily doped semiconductors are considered the promising thermoelectric candidate. The carrier concentration connects the transport parameters electrical conductivity, thermal conductivity and Seebeck coefficient, an optimized carrier concentration results in a high figure of merit. Another conflicting parameter is the effective mass (m*) of the charge carrier, the effective mass of the carriers will increase with a high DOS at the Fermi surface; it completely depends on the nature of bands. It is observed that a large effective mass enhances the Seebeck coefficient but results in lower electrical conductivity due to less contribution to mobility. Efficient thermoelectric materials can be found within a wide range of effective masses and mobilities [21].

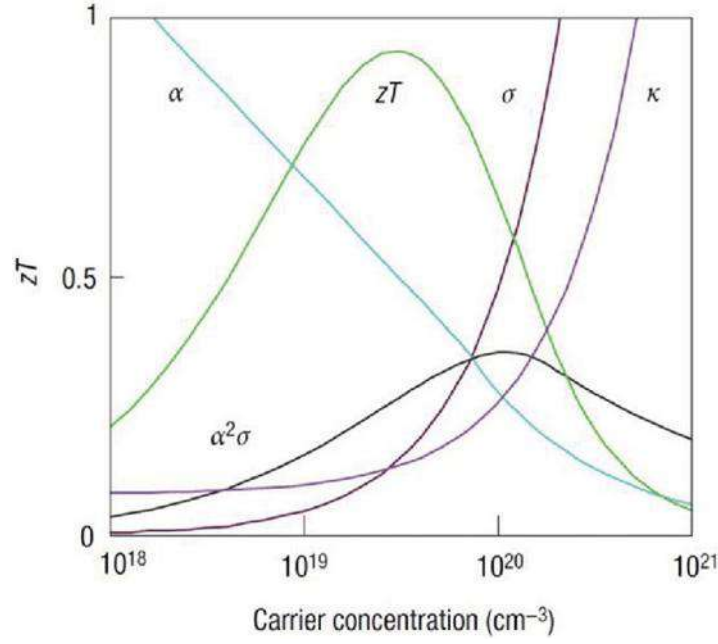


Figure 1.5. Optimization of various transport parameters with carrier density {Ref. [24]}

1.3.3. Thermal conductivity

The major transport parameter that controls the efficiency of the thermoelectric material is the thermal conductivity; the low thermal conductivity enhances the figure of merit of the material. The total thermal conductivity comes from both electron and phonon contribution as $k=k_e + k_l$, the electronic thermal conductivity is related to the electrical conductivity by Wiedemann-Franz law

$$k_e = L\sigma T$$

Where L is the Lorenz number, it has a value of $2.44 \times 10^{-8} \text{WK}^{-2}$ for metals and $1.48 \times 10^{-8} \text{WK}^{-2}$ for semiconductors. Decreasing electronic thermal conductivity will automatically reduce electrical conductivity. The Lorenz number can be deduced from the Seebeck coefficient by using the formula [25]

$$L = 1.5 + \exp\left[-\frac{|\alpha|}{116}\right]$$

Where L is in 10^{-8}WK^{-2} and α is in $\mu\text{V/K}$, k_e can be obtained by using this L value and thereby k_l . The only parameter that can be modified without affecting other electronic

parameters is lattice thermal conductivity. The lattice thermal conductivity can be expressed in terms of specific heat at constant volume (C_v), mean free path (l), acoustic velocity (V_s)

$$k_l = 1/3 C_v l v_s$$

At low temperatures (below 40K), the lattice thermal conductivity and C_v is a subject of Debye T^3 law, phonon scattering is not significant in this choice of temperature due to the low number of excited phonons and their extended wavelength. At elevated temperature, above Debye temperature, C_v reaches the classical value of $3R$, making k_l mainly depend on l which is contributed by phonon-phonon scattering. The complex structures, point defects, grain boundaries, nanostructures in bulk materials and lattice anharmonicity due to lone pair induce the phonon scattering and thereby reduce lattice thermal conductivity in thermoelectric materials to achieve the high figure of merit [26]. Latest studies reveal that the criteria for an ideal thermoelectric material are phonon-glass electron-crystal (PEGC) characteristics. The electron crystal part of the semiconductor provides high electrical conductivity; the phonon-glass nature blocks the phonons and thereby reduces the thermal conductivity [27].

1.4. Mechanisms and methods to enhance Figure of merit

The conflicting thermoelectric properties can be optimized through various mechanisms that include tuning the carrier concentration, enhancement of the effective mass (m^*), carrier mobility improvement by doping, reducing thermal conductivity and decoupling of electronic and thermal transport. The strong correlation between S , σ , and k with n can be tailored by controlled doping mechanisms. Instead of conventional doping functionally graded doping and temperature-dependent doping can certainly alter the carrier concentration at a required level and result in high ZT in the entire temperature range. In graded doping the materials with different carrier densities were stacked by spark plasma sintering or hot press method [28]. The temperature-dependent solubility of dopants in host material results in a carrier concentration gradient and can easily be controlled by varying the temperature. Bergum et al report that Ag, Cu and Pb are insoluble in PbTe at room temperature and are soluble at elevated temperatures and the temperature-dependent carrier concentration contributes to the enhanced thermoelectric properties [29]. Figure 1.6 (a)-(d) depicts the variation of thermoelectric parameters with various doping mechanisms [30].

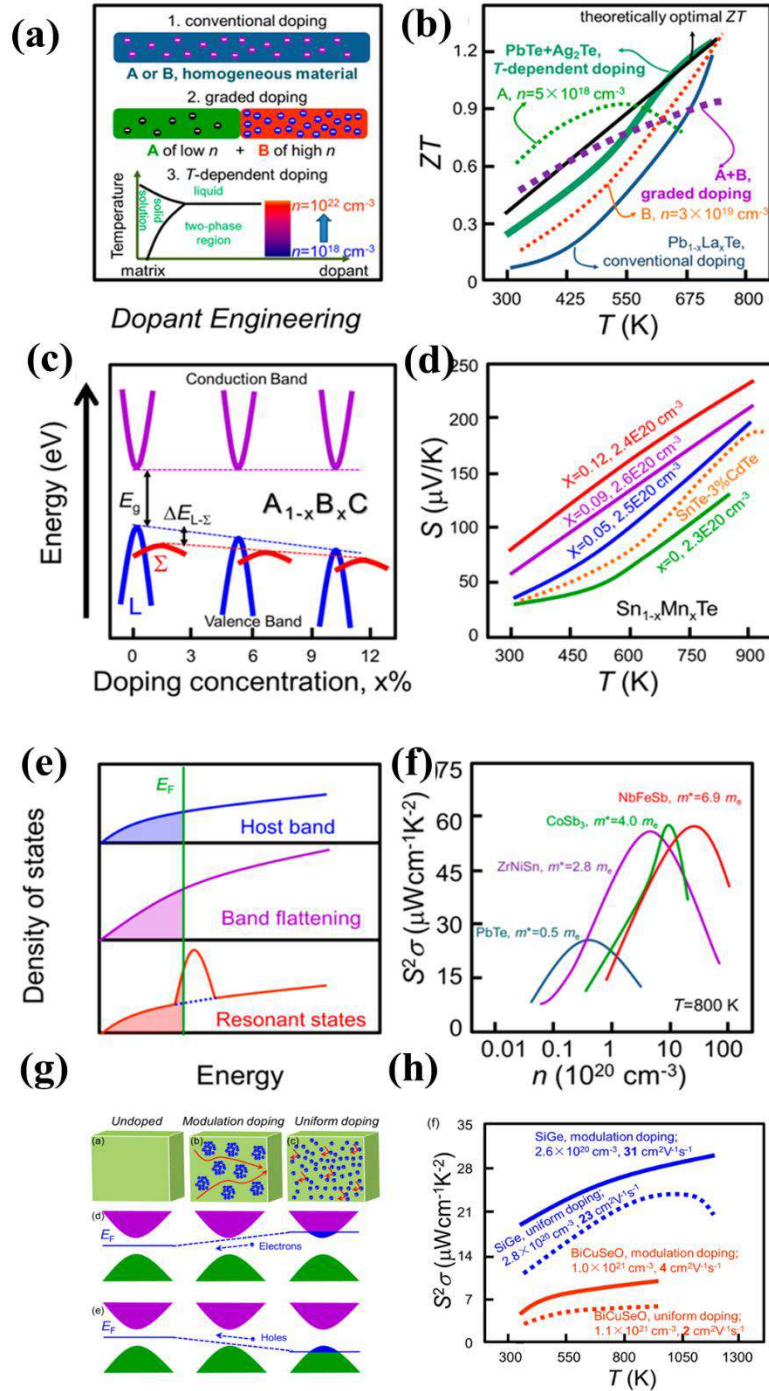


Figure 1.6. Various mechanisms to enhance thermoelectric properties [Ref. [14]]

The effective mass of the carrier has a major role in achieving the maximum ZT, the enhancement in the carrier effective mass can be attained by various methods that mainly comprise increasing the number of band extrema (N_V) and band effective mass (m_b^*). The number of band maxima is associated with the crystal structure symmetry, efficient thermoelectric materials like PbTe, SiGe, Mg_2Si and $CoSb_3$ possess $N_V > 1$. Band convergence is another widely acceptable technique that is used to increase the N_V on a higher level [31].

The band flattening and emergence of resonant levels through chemical doping are the two important strategies to achieve large band effective mass near the Fermi level (Figure 1.6 (e-g)). The dopants with highly localized orbitals can decrease the orbital overlap and the flattening of the band [32]. The resonant levels originated due to the coupling between the electrons of the dilute impurity with the valence or conduction band electrons of the host material and the excess density of states enhances the m_b^* and the Seebeck coefficient [33].

The high-efficiency TE materials are heavily doped semiconductors with carrier concentration in the range of 10^{19} - 10^{21} /cm³ and these results in the decrease of mobility due to the increased ionized impurity scattering. The 3D-modulation doping mechanism is presented to enhance the μ in TE materials. The modulation-doped samples are composites of undoped and heavily doped materials of lower carrier concentration (higher mobility) and higher carrier concentration (lower mobility) respectively. The Fermi level imbalance between the undoped and heavily doped materials results in the movement of charge carriers from the heavily doped region to the undoped region and that leads to mobility enhancement [34]. Figure 1.6h shows the mechanism of modulation doping on n and p-type material with examples of the materials SiGe and BiCuSeO.

The performance of the thermoelectric materials was widely enhanced through the reduction in total thermal conductivity by tuning the lattice thermal conductivity through various strategies. The lowering in k_l was achieved by phonon scattering at atomic scale defects, nanoscaled precipitates and mesoscaled grains of the materials. The imperfection in the host lattice in the atomic scale range was introduced by various doping methods such as single element, cross substitution and creation of lattice vacancies [35]. Cross-substituted compounds (replacing one or more elements with different oxidation states while maintaining the same overall valence) attained greater attention than single doping due to their larger solubility limit than that of the latter [36]. The atomic mass contrast between the guest and host atom can significantly reduce the lattice's thermal conductivity [37]. The presence of nanostructures plays a major role in thermoelectric materials due to their capability of promoting the scattering of phonons. The ex-situ and in-situ methods generate nanostructures in these materials[38,39]. The chemical/mechanical mixing of nanostructures on the host atom termed the ex-situ process and in the in-situ process, secondary precipitates emerge from the thermodynamically driven processes, which are act as the barriers for phonon transport. The mesoscale structuring was introduced for the scattering of long wavelength phonons. Row et.al reports that in SiGe, grains having a length scale less than 5 μ m

effectively scatter long wavelength phonons [40]. The combination of point defects, nanostructuring and mesoscale structuring results in all-scale hierarchical architectures that can achieve the strongest phonon scattering and lead-free chalcogenides such as SnTe, AgSbSe₂, GeTe, CoSb₃ and In₂O₃ comes under this category [27] (Figure 1.7).

Some compounds have low thermal conductivity due to the anharmonicity of the lattice vibrations and the lattice anharmonicity comes from the asymmetry in the vibrations of atoms about their mean positions.

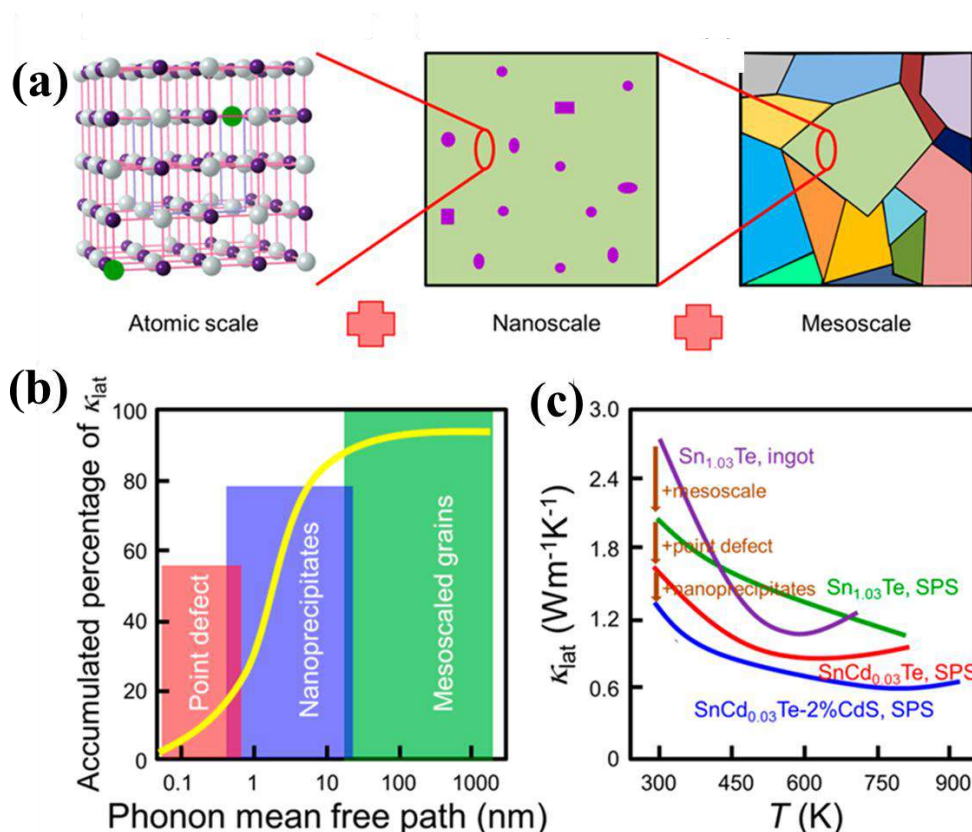


Figure 1.7. (a) Schematic diagram of all scale hierarchical architectures for phonon scattering, (b) an analysis of variation of cumulative k_{lat} with phonon mean free path in PbTe, (c) Temperature dependence k_{lat} for all scale hierarchical architectures in SnSe {Ref.[14]}

The asymmetry is generally exhibited by soft lattices or lattices that are not well packed and have some sort of asymmetric movement of atoms [41]. From previous reports, it was found that the presence of a lone pair of electrons can contribute to the lattice anharmonicity, rocksalt-based ABX₂ (A= Cu, Ag, Au, Na, K, Rb, Cs; B= Sb, Bi, As X = S, Se, Te) compounds normally comes under this category. The origin of the anharmonicity in these materials emerged from the s^2 lone pair of electrons of the group V elements. In AgSbTe₂; Sb has the valence electron configuration of $5s^25p^3$, the trivalent Sb forms polar covalent bonds

by sharing its p electrons with Te and the s^2 lone pair forms a separate band. The competition between the covalent bonding and lone pair repulsion results in crystal instability and thereby lattice anharmonicity [42].

1.5. Class of Inorganic Thermoelectric materials

A wide range of materials with diverse properties was reported in the area of thermoelectric applications. Numerous thermoelectric materials have been developed, which include metal oxides, skutterudites, clathrates, half-Heusler intermetallic compounds, zinc phases, inhomogeneous nanostructured materials, nanocomposites, chalcogenides and polymer-based thermoelectric materials (Figure 1.8).

Skutterudites are deeply studied compounds having efficient thermoelectric properties, having CoAs_3 -type structure with the cubic space group $\text{Im}\bar{3}$. The structure is made up of eight corner-shared AB_6 ($\text{A} = \text{Co, Rh, Ir}$; $\text{B} = \text{P, As, Sb}$) octahedra. It's a distorted version of the perovskite-type structure. The Figure 1.8a shows the structure of this system, it has framework of B atoms forming polyhedral cages, within which metal atoms are located. The arrangement of A and B atoms within the lattice gives unique electronic properties due to their geometry, scattering at A atoms lessen the lattice's thermal conductivity appreciably. The different sized ion in the voids leads to larger disorder and lesser thermal conductivity [43,44].

These are cage-like compounds where the cages are formed by the host atoms that include the so-called guest atoms, which are formed by the elements of groups 13 and 14 as host atoms and the cationic guests are group 1 or group 2 elements. **Clathrate 1** type has the general formula M_8T_{46} , with $\text{M} = \text{N, K, Ba}$; $\text{T} = \text{Al, Ga, In, Si, Ge, Sn}$ and Clathrates II, III have the general form $\text{M}_{24}\text{T}_{136}$ and $\text{M}_{30}\text{T}_{172}$ correspondingly with the similar M and T elements. Most of the Clathrates I have a narrow band gap semiconducting nature. $\text{Sr}_8\text{Ga}_{16}\text{Ge}_{30}$, $\text{Ba}_8\text{Ga}_{16}\text{Ge}_{30}$, $\text{Ba}_8\text{Ga}_{16}\text{Si}_{30}$, and $\text{Ba}_8\text{In}_{16}\text{Sn}_{30}$ were Clathrate I with an ideal number of 184 valence –electrons [45]. Both n-type and p-type Clathrates reported with ZT greater than 1 at high temperatures.

Heusler alloys are intermetallic compounds of the form X_2YZ , where X and Y and TMs, Z are from groups 13-15. These materials found applications in the fields of spintronics and thermoelectrics. Another class of thermoelectric materials are **half-Heusler** (HH) intermetallic compounds (general formula is XYZ, where X, Y are transition metals and Z is a main-group element), MNiSn ($\text{M} = \text{Ti, Hf, Zr}$) [46] is the widely studied compound. These materials have high melting points of 1100-1300° C and are chemically stable near 1000° C

[47]. For n-type $Zr_{0.5}Hf_{0.5}Ni_{0.8}Pd_{0.2}Sn_{0.99}Sb_{0.01}$ [48] reported with $ZT=0.7$ at 800K. It was observed that the thermal conductivity of the HH is reduced by increased atomic disorder at the transition-metal sites, which induces mass fluctuations and strain field effects [49].

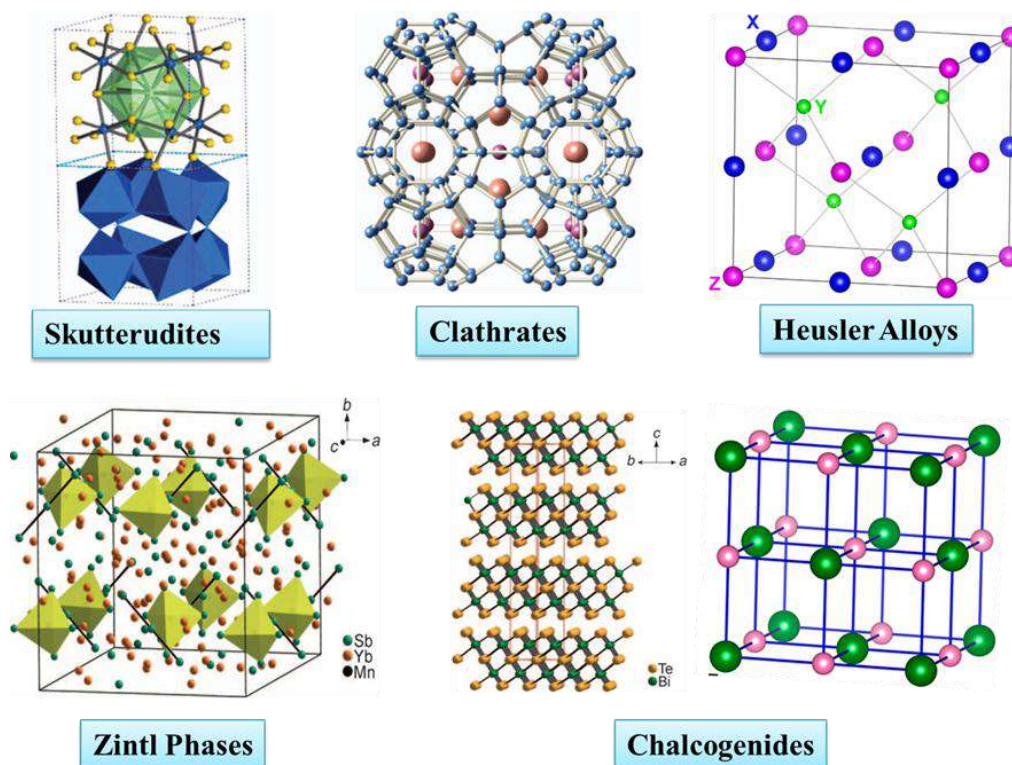


Figure 1.8. Class of thermoelectric materials

Metal oxide is another candidate for thermoelectric materials; they possess high thermal and chemical stability in air. Most oxides are poor conductors with low charge-carrier mobility. The well-known oxide thermoelectric material is $NaCo_2O_4$ [50] with thermopower of the order $150\mu V/K$ at a high-temperature range and the polycrystalline sample has $ZT\sim 0.8$ at 1000K and $ZT>1$ for single-crystal sample at 800K [51]. $Ca_3Co_4O_9$ [52], $(Bi, Pb)_2Sr_2Co_2O_8$ [53], $TiSr_2Co_2O_y$, $SrTiO_3$ [54], doped ZnO [55] are widely studied oxide thermoelectric materials.

Chalcogenides are promising thermoelectric materials, most of them show a semiconducting nature that is essential for the high figure of merit. Their versatility in combination with other elements and slight variation in electro negativity between sulfur, selenium and tellurium obtains semiconductors with energy gaps required for thermoelectric applications. These materials are air-stable have high melting points and can be applied for a wide range of

temperatures [56]. The majority of Chalcogenides are tellurium and recently selenium and sulfur-based materials have arisen due to their availability less toxicity and rich abundance in comparison with tellurium. PbTe, Bi₂Te₃, and SnTe are traditional thermoelectric materials. PbTe exhibits outstanding thermoelectric properties at high temperatures and has applications in NASA space missions. PbTe is a semiconductor with a band gap of 0.32eV [57], a highly symmetrical crystal structure that is contradictory to the postulate for an ideal thermoelectric material. It was reported that n-type PbTe holds a ZT value of ~1.4 between 700 K and 850 K [58]. SnTe crystallizing in a strongly distorted NaCl variant in two different modifications [59] has low thermal conductivity due to the combination of anharmonic and anisotropic bonding caused by the lone pair of Sn²⁺, as reflected in its heavily disordered SnSe₇ polyhedron. Nanostructuring in Bi₂Te₃ lowered the lattice thermal conductivity below $K_l = 0.5 \text{ Wm}^{-1}\text{K}^{-1}$ and maximised the zT. The Bi₂Te₃/Sb₂Te₃superlattices have $ZT_{\text{max}} = 2.4$, and Bi₂Te₃ nanowires also have $zT = 2$ at room temperature [60]. More recently, there has a significant research on the thermoelectric properties of SnSe materials due to their easiness in synthesis and stability for commercial applications [61]. The ternary chalcogenides with complex structures and interesting transport properties were reported in the past few years. There is serious research on designing such thermoelectric materials with large unit cells, low thermal conductivity and noticeable chemical properties. The hole-doped narrow band gap semiconductor CsBi₄Te₆ of this category has a ZT of 0.8 at 225 K [62].

Recently **transition metal based chalcogenides** having layers or without layered structure found special interest due to their special crystal structures and band characteristics originating from the electronic properties of the transition metals. Transition metal dichalcogenides have a general chemical formula MX₂, where M is the transition metal and X is the chalcogen. In these materials the atoms within the X-M-X sheets were bound by strong covalent bonds and the layers were connected through van der Waals forces and this van der Waals gap helps to intercalate organic or inorganic materials to tune their properties [63].

Thallium-based chalcogenides exhibit low thermal conductivity which includes TlAg₉Te₅ [62] with $ZT_{\text{max}} = 1.2$ at 700 K and Tl₂Ag₁₂Te_{7.4} with $ZT_{\text{max}} = 1.1$ at 520 K [27]. The double rattling phonon modes of Ag and Sb in AgBi₃S₅ contribute ultralow thermal conductivity of the order of $0.4 \text{ Wm}^{-1}\text{K}^{-1}$ at 800 K [64]. Another class of emerging thermoelectric materials is chalcocantimonates, the well-known thermoelectric materials AgSbTe₂ and AgSbSe₂ come under this category. The lone pair in heavy atoms contributes to anharmonicity and there is extremely low thermal conductivity and energy filtering, the large effective mass of charge

carriers due to the presence of localized states contributes to the high Seebeck coefficient in these materials [65]. Figure 1.8 shows the structure of various thermoelectric materials.

The transition metal-based **magnetic chalcogenides** have found applications in the field of spintronics. The materials having the general formula M_2AQ_4 (M- Transition metal; A-Si, Ge and Sn; Q-S, Se, Te) were reported with complex crystal structures and exotic magnetic properties. Compositional variation, doping or substitution at the TM site can vary the magnetic properties in a wide range. There is a recent study on the synthesis and magnetic properties in van der Waal (vdW) layered magnetic material [66], and the materials $FePS_3$, $MnPS_3$, $CrGeTe_3$ and $MnBi_2Te_4$ are a few examples of vdW materials. Korotaev et al. report that $CuCrS_2$ materials exhibit colossal magnetoresistance (CMR) and are considered a promising candidate for magnetic sensors and magnetic memory devices [67]. New magnetic chalcogenides were also investigated through theoretical studies, Rouf et al. investigated a new class of materials SrX_2S_4 ($X = Co, Fe, Mn$) with half-metallic ferromagnetism through DFT for spintronics application [68]. Recent studies reveal that a few magnetic ternary layered chalcogenides were also found with efficient thermoelectric properties. The class of magnetic chalcogenides $ACrX_2$, where $A = Ni, Cu, Ag$; $X = S, Se$ were considered as new layered thermoelectric materials. The new compounds $CuCrX_2$ and $AgCrX_2$ exhibit a maximum ZT of 2 at 300 K, and 1 at 873 K respectively [69]. Bhattacharya et Al. report that sandwich-like $(AgCrSe_2)_{0.5}(CuCrSe_2)_{0.5}$ exhibit ZT of 1.4 at 773 K [70]. Transition metal-based chalcogenides were the promising candidates for materials developed for thermoelectric and spintronics applications. There is also an emerging area of spin-based thermoelectric devices, the underlying effect is the spin Seebeck effect where the spin current in a ferromagnetic metal generates voltage perpendicular to the current direction [71].

1.6. Magnetic Properties of Transition metal Chalcogenides

1.6.1. General introduction to magnetism

Magnetism is an exciting phenomenon found in Nature and it plays an inevitable role in the present technology, especially in spintronics applications. The history of magnetism was associated with the loadstones (which are naturally magnetized pieces of magnetite $-Fe_3O_4$) that were found to attract iron. In 1820, the Danish physicist Hans Christian Oersted found the connection between electricity and magnetism and that resulted in a breakthrough in the area of magnetism. Later Pierre Curie and Pierre-Ernest Weiss formulated temperature-dependent magnetic properties [72]. The magnetic behavior of a compact material is

associated with the spins of the unpaired electrons; the associated magnetism of a single electron can be expressed in terms of Bohr magneton (μ_B)

$$\mu_B = \frac{e\hbar}{2m_e}$$

Where e is the charge of an electron, $\hbar=h/2\pi$, h is Planck's constant and m_e is the mass of the electron. When an external magnetic field (H_{app}) is applied to a material, the magnetic dipoles in the material align in a particular direction which is termed the magnetization direction resulting in a net magnetization (M). The magnetic induction (B), which is the total flux of magnetic field lines through a unit cross-sectional area of the material, is expressed as [72]

$$B = \mu_0 (M+H)$$

Where $\mu_0 = 4\pi \times 10^{-7}$ H/m is the permeability of free space and the other parameter that quantifies the magnetic response of a material is termed the magnetic susceptibility (χ) and it connects the magnetization (M) and the applied magnetic field (H_{app}) by the relation

$$\chi = \frac{M}{H_{app}}$$

1.6.2. Classification of magnetic materials

Materials were classified as diamagnetic (DM), paramagnetic (PM), ferromagnetic (FM), antiferromagnetic (AFM) and ferrimagnetic (FiM) based on the order of spin (Figure 1.9). The materials exhibit weak magnetism comes under the Diamagnetic and it arises from the orbital motion of the electron under the applied field. In DM the electrons are paired and they are repelled by the applied field. These materials have negative magnetic susceptibility and are independent of temperature, superconductors are perfect diamagnets and other examples are water, noble gases copper etc [73]. The paramagnetism is observed in materials having unpaired electrons, leading to the temporary alignment of their magnetic moment. The external magnetic field results in the alignment of a small fraction of spins in PM materials and that contributes to a small positive susceptibility.

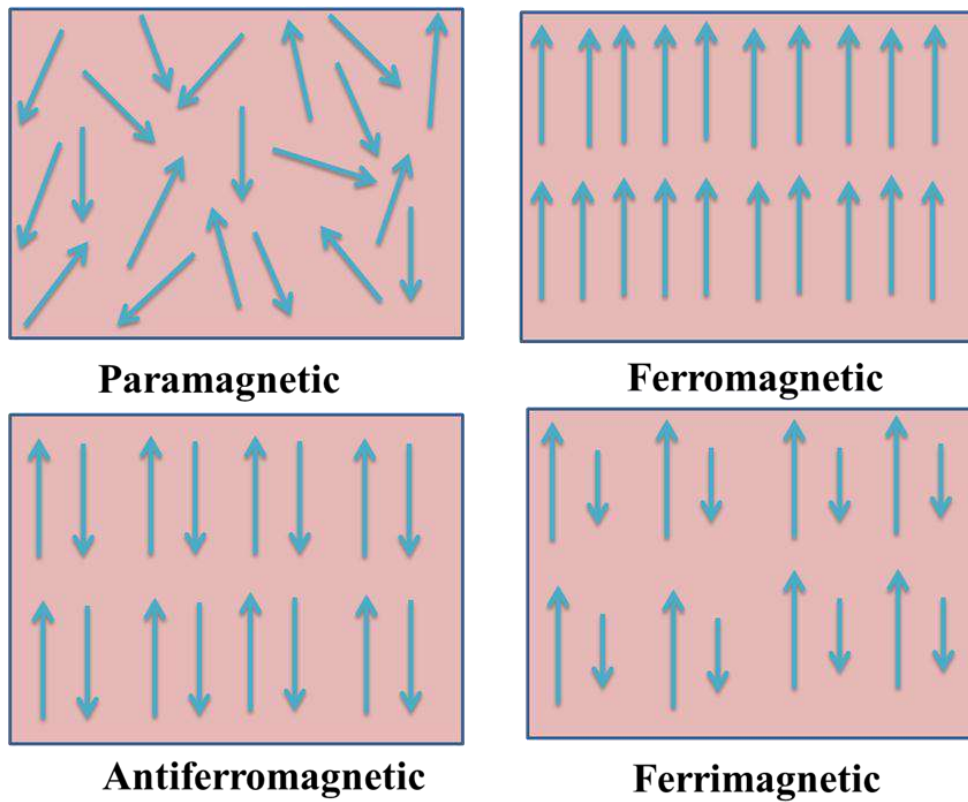


Figure 1.9. Schematic representation of spin alignment for different magnetic systems

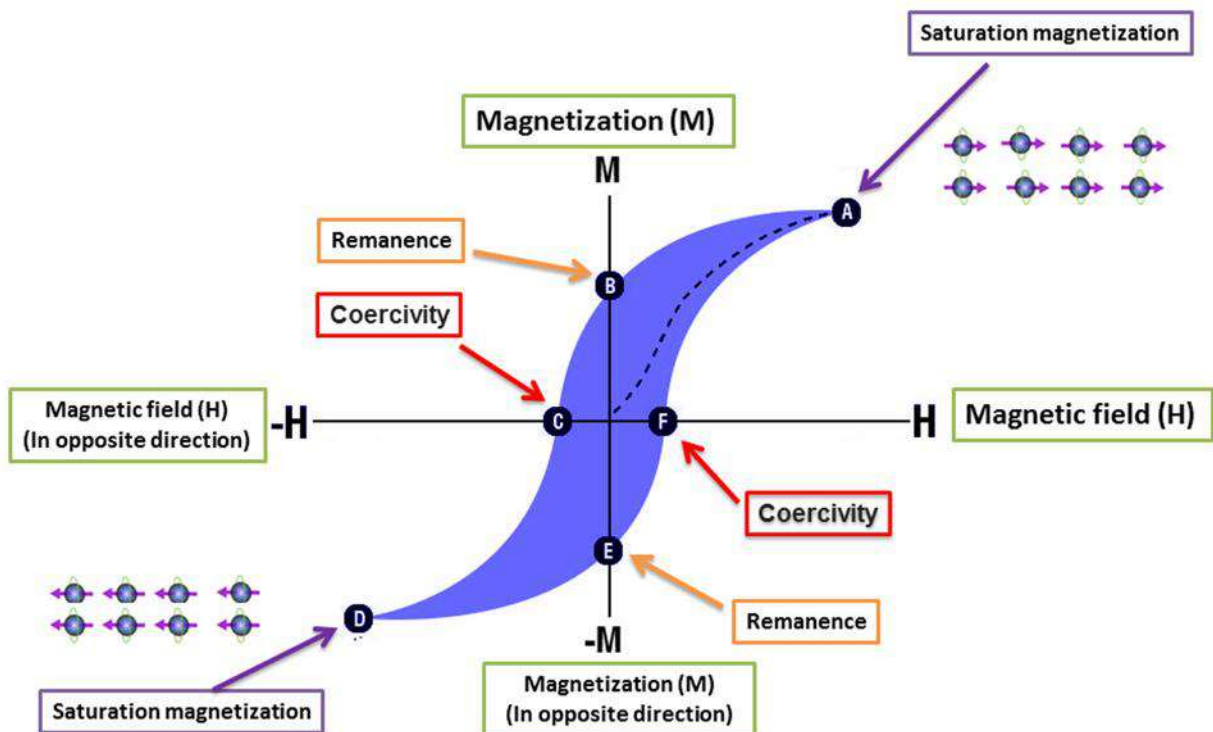


Figure 1.10. Identifying various terms in the hysteresis loop of an FM material, Ref. [74]

In FM materials, the strong interaction between the atomic moments results in the parallel arrangement of spins and that leads to spontaneous magnetization. To explain the strong interaction Weiss introduced the concept of molecular field and this internal magnetic field magnetizes the material to saturation. According to Weiss's theory, the FM materials are composed of small magnetic regions named as domains, the magnetic domains are aroused in this material due to mutual exchange interaction. The FM material has a transition temperature T_C , below this particular temperature material exhibits FM nature and above it is PM and also it has a non-linear field dependence of magnetization. The magnetic hysteresis loop shown in Figure 1.10 shows the saturation magnetization which is the point of saturation of magnetization at higher fields as M_s . The reduction in H_{app} to zero does not result in zero M , and some magnetic flux remains even at zero field is termed as remanent magnetization (M_R). The reverse field required to demagnetize the material is known as the coercivity (H_C).

In AFM materials, the spins are aligned antiparallel to each other and that results in net zero magnetization. This particular type of spin ordering is observed below a critical temperature known as Neel temperature (T_N). It has a linear field dependence on magnetization and has a small positive magnetic susceptibility. In FiM materials the spins are aligned antiparallel but there is a net magnetization due to the difference in magnitude of the magnetic moments of the associated spins. They have spontaneous magnetization below T_C in the absence of an applied field and act like an FM material [73]. The Curie-Weiss law is generally defined for the PM materials and other magnetic materials obey this law above their Curie or Neel temperature and are useful in calculating various constants. The expression for the Curie-Weiss law is given by

$$\chi = \frac{C}{T - \theta}$$

Where C is the Curie constant and θ is the Curie temperature and is positive for FM and negative for AFM [73].

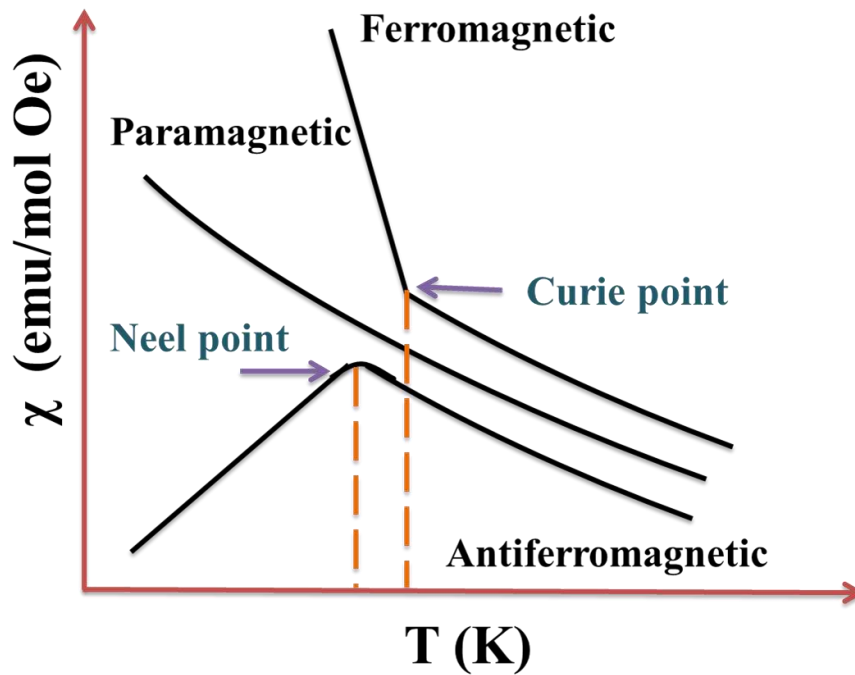


Figure 1.11. Susceptibility versus temperature plot for AFM, FM and PM materials

Figure 1.11 shows the magnetic susceptibility versus T plot for FM, AFM and PM materials. The transition from AFM to FM is denoted as T_N and FM to PM as T_C .

1.6.3. Glassy nature

In 1972 Candella and Mydosh [75] found the existence of a new kind of magnetic material having short-range ordered frustrated magnetic moments, which are termed spin glass (SG) materials. The interaction of the random distribution of magnetic spins results in a classical phase transition at a critical temperature and the phase transition into a new state of matter: a frozen glass of spins is defined as the spin glass. The magnetic frustration in these materials arises from the competing AFM and FM interaction and their behaviour is similar to glass. The glass materials are amorphous due to their short-range crystalline order and SG has a short-range magnetic order. The combination of randomness, frustration and competing interaction in magnetic material generates the frozen phase as the SG, this particular phase transition is associated with a temperature known as the freezing temperature (T_f). In SG the spins are individually oriented and if they form a cluster of frozen spins oriented in a particular direction below T_f is known as the cluster glass (CG). Figure 12 shows the pictorial representation of SG and CG, frequency-dependent AC susceptibility measurements were widely used to characterize the glassy nature. The magnetic disorder in these materials can be

intentionally introduced by various methods by alloying, doping or substitution at different sites and unintentionally by anti-site mixing, associated grains or boundaries [76].

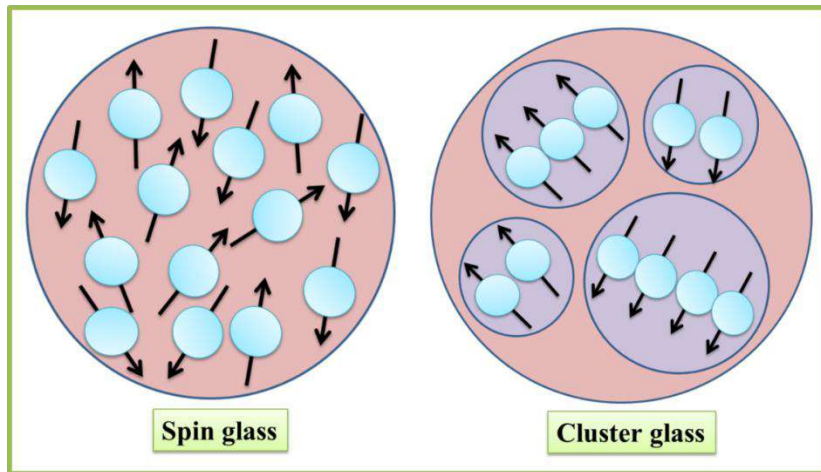


Figure 1.12. The glassy nature of magnetic materials

1.6.4. Griffiths-like phase

Figure 1.13a depicts the $1/\chi$ versus T plot for AFM, PM and FM materials, it was found that

magnetic materials exhibit a deviation from linear fit on the CW plot and that downturn in $1/\chi$ (Fig.1 13b) is associated with a different magnetic phase.

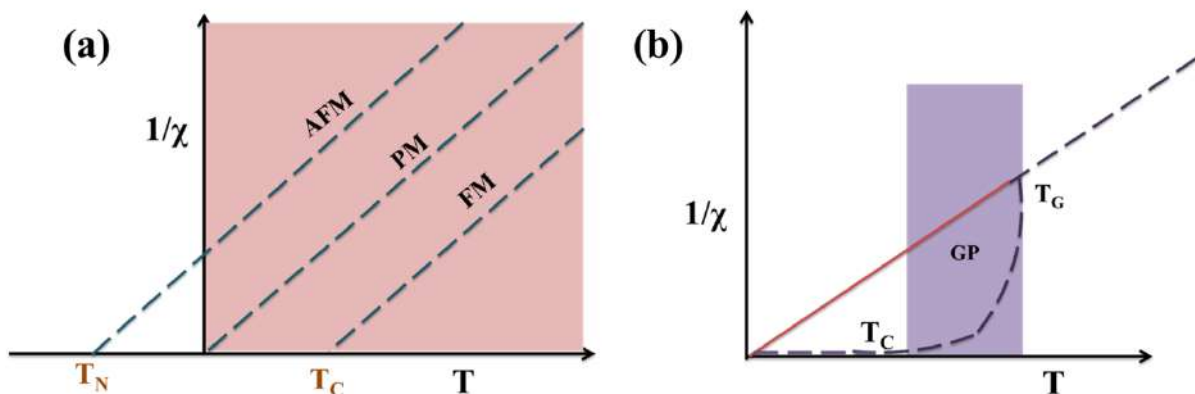


Figure 1.13. $1/\chi$ versus T plot for (a) AFM, PM and FM and (b) Griffith-like phase.

A new magnetic phase named Griffiths-like phase (GP) was introduced by Griffith in 1969 to discuss the quenched randomness on the magnetization of a dilute Ising FM and in this material, there is an arrangement of magnetic spins and nonmagnetic atoms or vacancies at

different sites of the lattice. The GP is defined as the presence of short-range ordering of FM clusters in the PM matrix in a particular range of temperature $T_C \leq T \leq T_G$, where T_G is the temperature at which the FM clusters tend to nucleate and T_C is the Curie temperature. This phase was initially reported in perovskite manganites and later in various systems like layered manganites, Fermi materials and spin glass systems [77]. The quenched magnetic disorder in these magnetic materials has multiple origins like phase separation, presence of nanometer or micrometre cluster, micro twinning and competing magnetic interactions [78]. In 1987 Bray elaborated the theory of GP phase and it defined in a range of temperature $T_C^R \leq T \leq T_G$, where T_C^R is compared to the Curie Weiss temperature. Therefore the GP phases are found in the PM region and are analyzed through a power law that is expressed in terms of susceptibility (χ), magnetic susceptibility exponent (λ) and temperature (T)

$$\frac{1}{\chi} = (T - T_C^R)^{1-\lambda}$$

Where λ has a value in the range, $0 \leq \lambda \leq 1$ and when its value is close to 1 confirms the GP phase and if it is close to 0 refers to the PM phase and decrease in λ with rise in field is one of its characteristics. Recently it was found that some intermetallic AFM compounds also exhibit the GP phase at low temperatures due to the local disorder in the crystal structure [79].

1.7. Magneto-transport properties

Magnetotransport properties of the materials were associated with the electronic transport characteristics under an applied magnetic field, the magnetoresistance and Hall effect are major measurements. Magnetoresistance (MR) refers to the variation of resistance of the material with an applied magnetic field H and is expressed as [80]

$$\frac{\Delta\rho}{\rho_0} = \frac{\rho(B) - \rho_0}{\rho_0} = \frac{R(B) - R_0}{R_0}$$

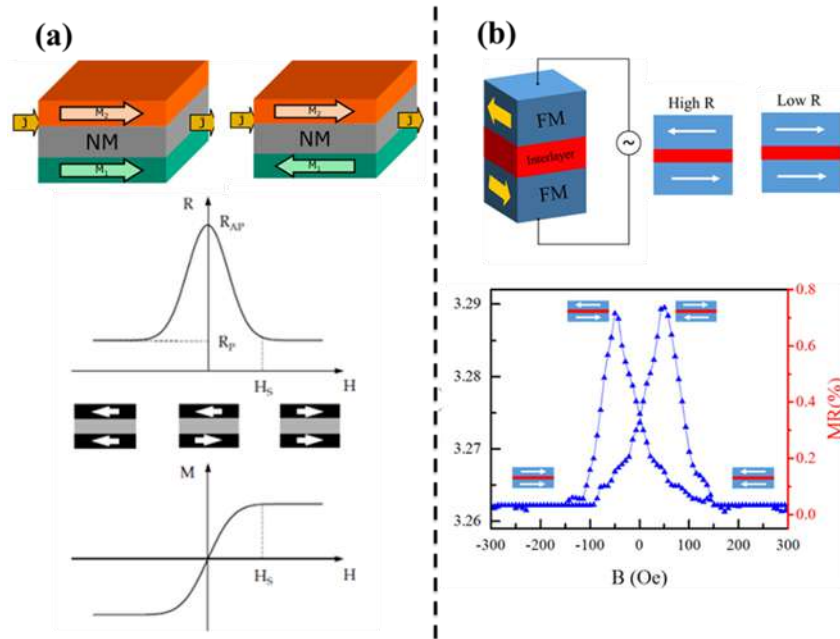


Figure 1.14. Schematic representation of (a) structure of GMR, (b) Butterfly magnetoresistance

The magnetoresistance is classified as ordinary magnetoresistance (OMR), anisotropic magnetoresistance (AMR), giant magnetoresistance (GMR), and colossal magnetoresistance (CMR). Ordinary magneto resistance was obtained in non-magnetic metals; in these materials, MR is very small at low fields and quite larger for high fields. The MR of the material is positive for both longitudinal and transverse magnetic fields, and it can vary about 5% in conventional materials, like metals (Cu, Al, Au, In, Na etc) [81]. The anisotropic magnetoresistance was observed in ferromagnetic alloys and compounds showing a variation of about 2%. The physical origin of the AMR is accompanying with the spin-orbit interaction, the resistivity changes by the relative angle between the direction of magnetization and current. The permalloy (NiFe) exhibits AMR and the material is useful as room temperature recording heads [82]. The giant magnetoresistance was observed in multilayered materials where the magnetic layers were separated by the nonmagnetic layers and these materials exhibit an MR of 50%. The GMR emerges from the relative orientation of the magnetic magnetization in the adjacent metal layers concerning the field and the thickness of the layers should be less than the mean free path of the electron [83]. The overall resistance depends on the spin-dependent scattering, the high resistance in GMR material comes from the AFM coupling of spins and when the applied magnetic field overcomes the AFM coupling results in the low resistance, it finds application in MR head sensor [81]. Spin valves are layered GMR devices of magnetic layers separated by the nonmagnetic spacers

(Figure 1.14a) and their electrical resistance varies with the spin orientation concerning the field. The low and high MR depends on the angle between the respective magnetization of the two magnetic layers and spin valve MR heads were already developed by IBM and HP. The spin valves exhibit butterfly magnetoresistance (BMR) and it is widely observed in van der Waal layered materials and also in strongly correlated electron systems. In BMR (Figure 1.14b), a butterfly cross curve is observed in the MR versus field data and has the same MR at both large positive and negative magnetic fields [84]. The colossal MR was first found in perovskite material $\text{La}_{1-x}\text{M}_x\text{MnO}_{3+\delta}$ ($\text{M} = \text{Ca}, \text{Sr}$), and exhibited a huge MR of $\sim 99.9\%$. The extraordinary hike in electrical conductivity with an applied field in some magnetic material is associated with the field-induced spin polarization and it reduces the spin scattering and there the electrical resistance [85]. Classical MR generally has quadratic dependence on the magnetic field at lower fields and it will saturate at higher fields. Recently a few nonmagnetic metals with open Fermi surfaces exhibit large linear and unsaturated MR, it is termed linear magnetoresistance (LMR). Parish and Littlewood have reported that the origin of LMR in inhomogeneous metals is due to the change in the current path generated by the macroscopic spatial variations in carrier mobility [86]. It is widely observed in self-doped silver chalcogenides, Bi_2Te_3 -based topological insulators, Heusler topological insulators and also in Zero band gap InSb [87].

1.8. Material manufacturing techniques

The transition metal chalcogenides can be produced through different routes that mainly depend on the area of applications. Recently bulk and thin film TMC structures were fabricated for spintronics and thermoelectric applications, it was found that TEG legs were fabricated from the bulk materials [88]. The main synthesis techniques are single crystal growth, physical/ chemical deposition method, powder synthesis by melting and mechanical alloying, and chemical synthesis routes incorporating solve/hydrothermal and aqueous solution methods [89]. Figure 1.15 shows the schematic diagram of various material manufacturing techniques.

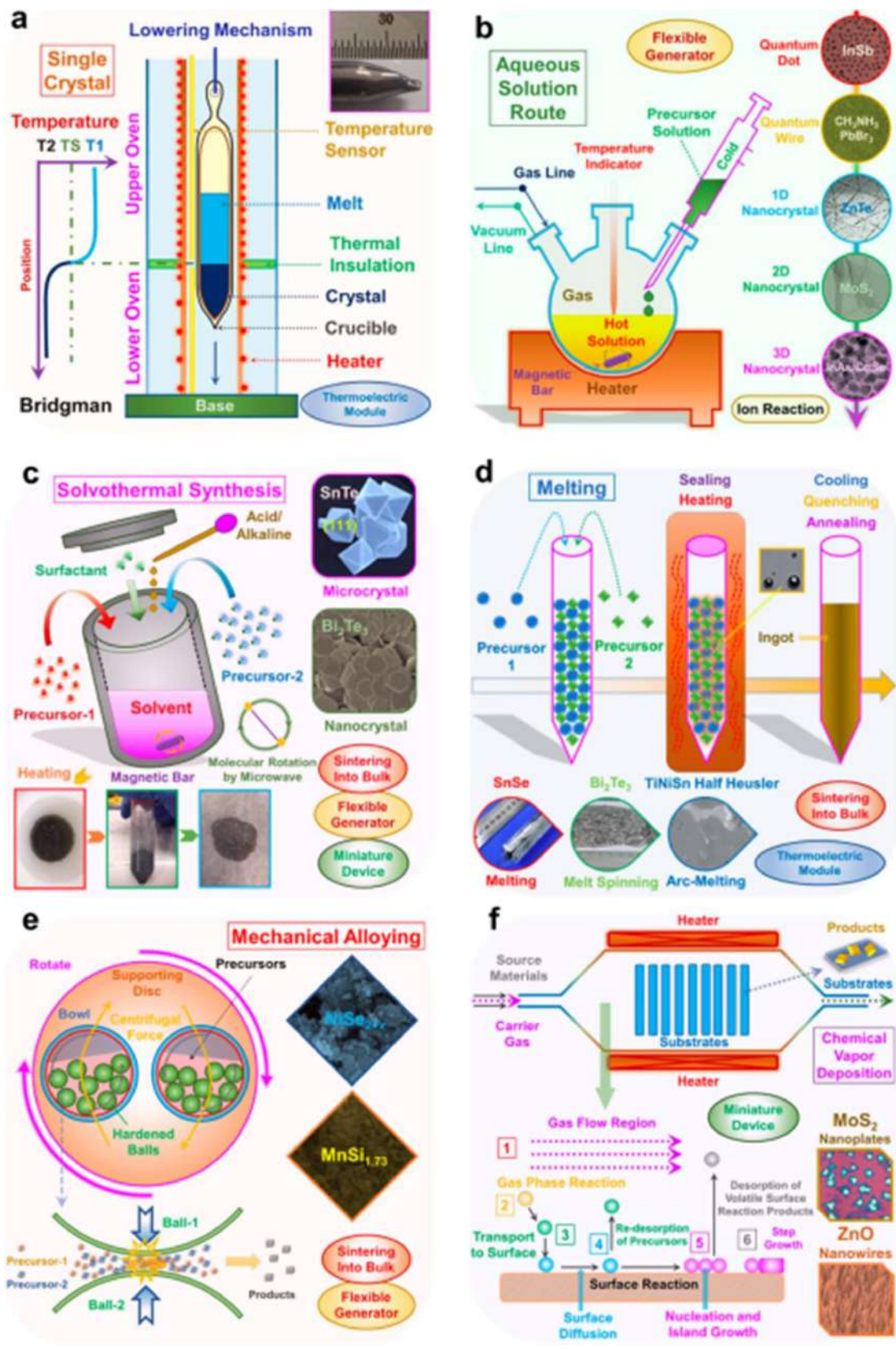


Figure 1.15. Schematic diagram of various synthesis techniques (a) Bridgman method (single crystal growth), (b) aqueous solution method, (c) solvothermal route, (d) melting, (e) mechanical alloying, (f) chemical vapour deposition {Ref.[89]}

1.9. Application of Transition metal-based chalcogenides.

The particle's electrons, phonons and magnons contribute to the transport properties under heat treatment and they are connected through various interactions. These particles are associated with different physical properties and Figure 1.16 shows the interconnection of the particles and corresponding effects. The magnetic transition metal-based chalcogenides can find applications equally in the field of thermoelectric power generation and spintronics. Along with the electronic properties, the thermal and mechanical stability promotes these materials as a promising candidate for thermoelectric applications.

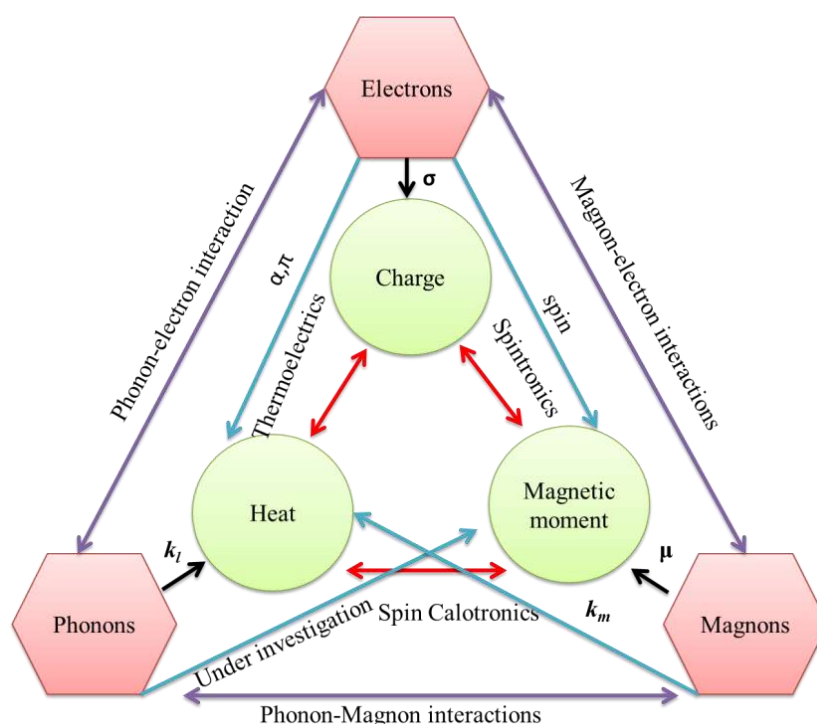


Figure 1.16. Interconnection between thermal, electronic and magnetotransport

The chalcogenides are promising candidates for high-temperature thermoelectric applications, especially in the area of industrial heat energy harvesting. It was found that a major part of heat energy is wasted in the low-grade temperature range and requires room-temperature TE materials. The main application includes thermoelectric power generation from body heat to power the health indicators; maintenance-free power regulation for the Internet of things (IoTs) and solid-state cooling strategies for thermal control of the optical communication modules in the 5G era [90]. The development of new low-temperature thermoelectric materials is essential today because most of the low-temperature thermoelectric generators and coolers are still working on conventional Bi_2Te_3 -based compounds. These materials can find application in the field of low-grade heat harvesting and

cooling purposes in microelectronics [91]. The various parts of the spacecraft system require low-temperature maintenance and efficient low-temperature TE materials can be applied for cooling applications [92]. The bridging of charge and spin leads to a new field of interest known as spintronics [93], transition metal chalcogenides have great interest in this field due to their diverse physical properties. The multifunctional materials like diluted magnetic semiconductors with ferromagnetism and semiconducting nature fulfil the criteria for spin-based electronics. The properties spin and charge of the electrons are utilized for storage and processing of data in spintronic applications. The spintronic devices include magnetic hard disks, magnetic sensors, MRAM and spin torque oscillators [94]; the figure shows the outline of spintronic devices in a nutshell.

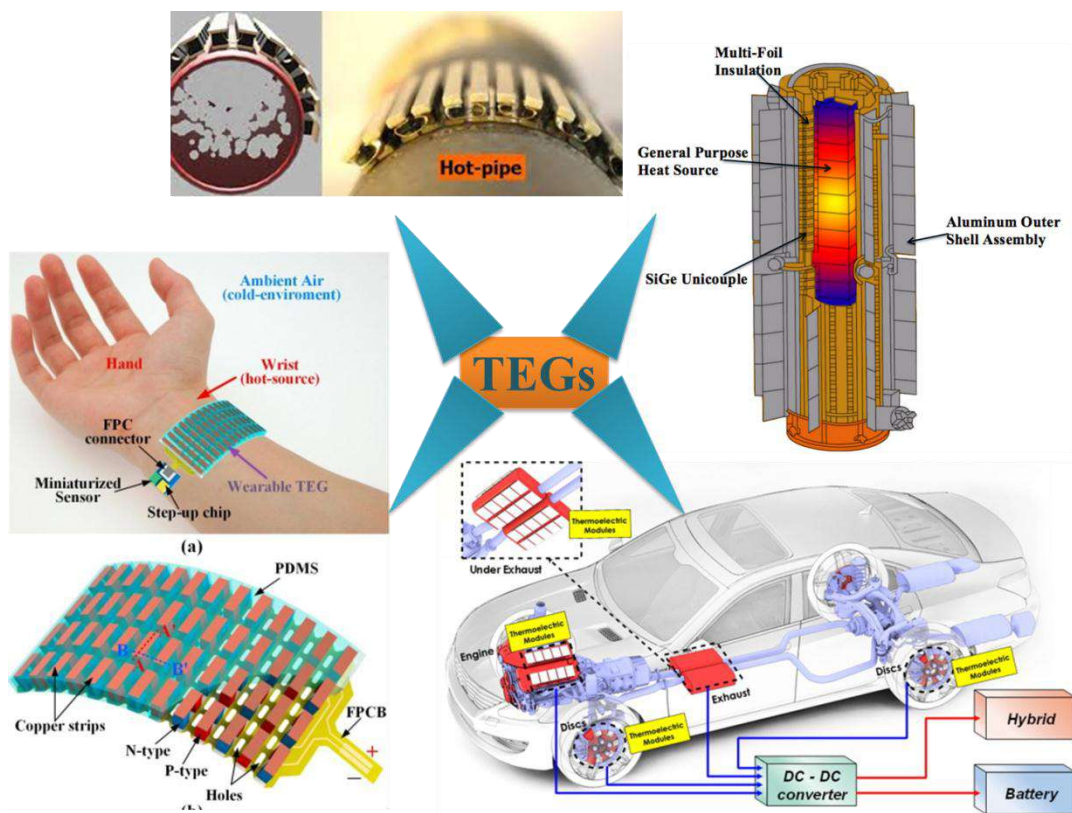


Figure 1.17. An overview of thermoelectric applications

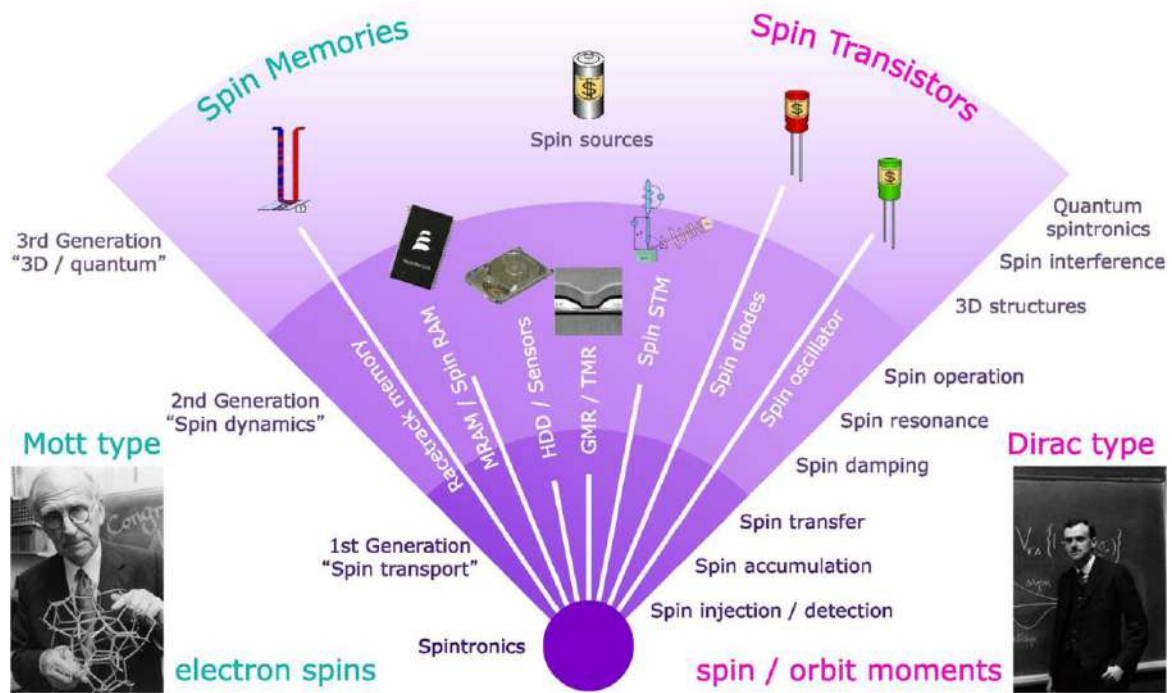


Figure 1.18. An outline of spintronics [Ref. [95]]

In 2008 Uchida et al. reported the spin Seebeck effect as a spin counterpart of the Seebeck effect (SSE); it is the generation of spin voltage in a ferromagnetic or ferromagnetic material as a result of an applied temperature gradient [96]. It opens up the application of FM chalcogenides also for SSE-based thermoelectric devices.

Outline of the thesis

In the current scenario, the magnetic and thermoelectric materials can be used to create multifunctional systems for spintronic and future energy applications. Our research focuses on the development of new transition metal-based ternary chalcogenides as well as the study of their electrical, magnetic, and thermoelectric properties. The thesis comprises three operational chapters subsequent to this introduction and summary of the thesis is as follows.

In **Chapter 1**, we discuss the theory, mechanisms and significance of the transition metal-based ternary chalcogenides as a thermoelectric and magnetic material. **Chapter 2** presents the experimental methods, In **Chapter 3**, discusses the Zintl phase BaVSe_3 through two different routes from constituent elements and using the advent of the new synthesis method with phase purity and less time consumption. A comparison study on the thermoelectric and magnetic properties of phases pure BaVSe_3 and impurity-assisted BaVSe_3 was done. The quasi-1D nature of this material leads to exotic magnetic properties like Griffiths-like phase, glassy nature and butterfly magnetoresistance. These materials can be candidates for low-temperature thermoelectric applications and spintronics. **Chapter 4** deals with the synthesis of pure transition metal-based selenides CoMSe_2 ($M = \text{Ni, Fe}$) and their low-temperature thermoelectric and magnetic properties. We have noticed that the replacement $\text{Ni} \rightarrow \text{Fe}$ enhances the thermoelectric properties and exhibits different magnetic characteristics. **Chapter 5** is focused on the synthesis of spontaneously nanostructured AgSbTe_2 as a promising candidate for future-generation thermoelectric materials. This chapter reveals the various mechanisms that contribute to the enrichment of the thermoelectric properties of this material. The highest Seebeck coefficient of $251.16 \mu\text{V}/\text{mK}^2$ along with the lowest thermal conductivity $\sim 0.20 \text{ W}/\text{mK}^2$ contributes to a maximum ZT of 1.10 at room temperature. Due to its satisfactory thermoelectric characteristics, this can be considered a potential candidate for future-generation thermoelectric applications. **Chapter 6** discusses the summary and outlook the thesis.

References

- [1] K. Hainsch, K. Löffler, T. Burandt, H. Auer, P. Crespo del Granado, P. Piscicella, S. Zwickl-Bernhard, Energy transition scenarios: What policies, societal attitudes, and technology developments will realize the EU Green Deal?, *Energy*. 239 (2022) 1–17.
- [2] L. Chandra Voumik, T. Sultana, Impact of urbanization, industrialization, electrification and renewable energy on the environment in BRICS: fresh evidence from novel CS-ARDL model, *Heliyon*. 8 (2022) 1–9.
- [3] International Energy Agency, International Energy Agency (IEA) World Energy Outlook 2022, 2022. <https://doi.org/https://www.iea.org/reports/world-energy-outlook-2022>.
- [4] International Energy Agency, Net Zero by 2050 A Roadmap for the Global Energy Sector, 2021. <https://doi.org/www.iea.org>.
- [5] International Renewable Energy Agency (IRENA), World energy transitions outlook 2022, 2022. <https://irena.org/Digital-Report/World-Energy-Transitions-Outlook-2022%0Ahttps://irena.org/publications/2021/March/World-Energy-Transitions-Outlook>.
- [6] <https://www.ireda.in>, (n.d.).
- [7] M.J.B. Kabeyi, O.A. Olanrewaju, Sustainable Energy Transition for Renewable and Low Carbon Grid Electricity Generation and Supply, *Front. Energy Res.* 9 (2022) 1–45. <https://doi.org/10.3389/fenrg.2021.743114>.
- [8] Fitriani, R. Ovik, B.D. Long, M.C. Barma, M. Riaz, M.F.M. Sabri, S.M. Said, R. Saidur, A review on nanostructures of high-temperature thermoelectric materials for waste heat recovery, *Renew. Sustain. Energy Rev.* 64 (2016) 635–659.
- [9] N. Jaziri, A. Boughamoura, J. Müller, B. Mezghani, F. Tounsi, M. Ismail, A comprehensive review of Thermoelectric Generators: Technologies and common applications, *Energy Reports*. 6 (2020) 264–287.
- [10] O. Caballero-Calero, J.R. Ares, M. Martín-González, Environmentally Friendly Thermoelectric Materials: High Performance from Inorganic Components with Low

- Toxicity and Abundance in the Earth, *Adv. Sustain. Syst.* 5 (2021) 1–19.
- [11] B. Ryu, J. Chung, M. Kumagai, T. Mato, Y. Ando, S. Gunji, A. Tanaka, D. Yana, M. Fujimoto, Y. Imai, Y. Katsura, S.D. Park, Best thermoelectric efficiency of ever-explored materials, *IScience*. 26 (2023) 106494.
- [12] L. Yang, Z.G. Chen, M.S. Dargusch, J. Zou, High-Performance Thermoelectric Materials: Progress and Their Applications, *Adv. Energy Mater.* 8 (2018) 1–28.
- [13] Q. Zhu, S. Wang, X. Wang, A. Suwardi, M.H. Chua, X.Y.D. Soo, J. Xu, Bottom-Up Engineering Strategies for High-Performance Thermoelectric Materials, *Nano-Micro Lett.* 13 (2021) 1–38.
- [14] G. Tan, L. Zhao, M.G. Kanatzidis, Rationally Designing High-Performance Bulk Thermoelectric Materials, *Chem.Rev.* 116 (2016) 12123–12149.
- [15] D. Beretta, N. Neophytou, J.M. Hodges, M.G. Kanatzidis, D. Narducci, M. Martin-Gonzalez, M. Beekman, B. Balke, G. Cerretti, W. Tremel, A. Zevalkink, A.I. Hofmann, C. Müller, B. Dörfling, M. Campoy-Quiles, M. Caironi, Thermoelectrics: From history, a window to the future, *Mater. Sci. Eng. R Reports*. 138 (2019).
- [16] TH.J. Seebeck, Magnetische polarisation der metalle und erze durch temperatur-differenz, 1895.
- [17] H.S. Lee, The Thomson effect and the ideal equation on thermoelectric coolers, *Energy*. 56 (2013) 61–69.
- [18] N. Bisht, P. More, P.K. Khanna, R. Abolhassani, Y.K. Mishra, M. Madsen, Progress of hybrid nanocomposite materials for thermoelectric applications, *Mater. Adv.* 2 (2021) 1927–1956.
- [19] B. Ryu, J. Chung, M. Kumagai, T. Mato, Y. Ando, S. Gunji, A. Tanaka, D. Yana, M. Fujimoto, Y. Imai, Y. Katsura, S.D. Park, Best thermoelectric efficiency of ever-explored materials, *IScience*. 26 (2023).
- [20] H.S. Kim, W. Liu, G. Chen, C.W. Chu, Z. Ren, Relationship between thermoelectric figure of merit and energy conversion efficiency, *Proc. Natl. Acad. Sci. U. S. A.* 112 (2015) 8205–8210.
- [21] Y. Sun, Y. Liu, R. Li, Y. Li, S. Bai, Strategies to Improve the Thermoelectric Figure of

- Merit in Thermoelectric Functional Materials, *Front. Chem.* 10 (2022) 1–22.
- [22] Chemical potential and Gibbs free energy, *MRS Bull.* 44 (2019) 520–523.
- [23] L. Kush, S. Srivastava, Y. Jaiswal, Y. Srivastava, Thermoelectric behaviour with high lattice thermal conductivity of Nickel Thermoelectric behaviour with high lattice thermal conductivity of, *Mater. Res. Express.* 7 (2020) 0–16.
- [24] X. Zhang, Heterostructures: new opportunities for functional materials, *Mater. Res. Lett.* 8 (2020) 49–59.
- [25] H.S. Kim, Z.M. Gibbs, Y. Tang, H. Wang, G.J. Snyder, Characterization of Lorenz number with Seebeck coefficient measurement, *APL Mater.* 3 (2015) 1–6.
- [26] J. Shuai, J. Mao, S. Song, Q. Zhu, J. Sun, Y. Wang, R. He, J. Zhou, G. Chen, D.J. Singh, Z. Ren, Tuning the carrier scattering mechanism to effectively improve the thermoelectric properties, *Energy Environ. Sci.* 10 (2017) 799–807.
- [27] X.C. Shen, Y. Xia, G.W. Wang, F. Zhou, V. Ozolins, Y. Wang, X. Lu, X.Y. Zhou, Phonon glass electron crystal behavior and thermoelectric performance in complex phosphides, *J. Mater. Chem. A.* 741603 (2017) 1–8.
- [28] W.T. Chiu, C.L. Chen, Y.Y. Chen, A strategy to optimize the thermoelectric performance in a spark plasma sintering process, *Sci. Rep.* 6 (2016) 1–9.
- [29] Y. Pei, A.F. May, G.J. Snyder, Self-tuning the carrier concentration of PbTe/Ag₂Te composites with excess Ag for high Thermoelectric performance, *Adv. Energy Mater.* 1 (2011) 291–296.
- [30] G. Tan, L.D. Zhao, M.G. Kanatzidis, Rationally Designing High-Performance Bulk Thermoelectric Materials, *Chem. Rev.* 116 (2016) 12123–12149.
- [31] Y. Pei, H. Wang, G.J. Snyder, Band engineering of thermoelectric materials, *Adv. Mater.* 24 (2012) 6125–6135.
- [32] S. Ohta, T. Nomura, H. Ohta, K. Koumoto, High-temperature carrier transport and thermoelectric properties of heavily La- Or Nb-doped SrTiO₃ single crystals, *J. Appl. Phys.* 97 (2005) 1–5.
- [33] J.P. Heremans, B. Wiendlocha, A.M. Chamoire, Resonant levels in bulk thermoelectric

- semiconductors, *Energy Environ. Sci.* 5 (2012) 5510–5530.
- [34] B. Yu, M. Zebarjadi, H. Wang, K. Lukas, H. Wang, D. Wang, C. Opeil, M. Dresselhaus, G. Chen, Z. Ren, Enhancement of thermoelectric properties by modulation-doping in silicon germanium alloy nanocomposites, *Nano Lett.* 12 (2012) 2077–2082.
- [35] E. Rugut, D. Joubert, G. Jones, Lattice dynamics and thermoelectric properties of YCuSe₂, *Interdiscip. Mater.* 21 (2023) 1–24.
- [36] X. Shi, J. Yang, S. Bai, J. Yang, H. Wang, M. Chi, J.R. Salvador, W. Zhang, L. Chen, W. Wong-Ng, On the design of high-efficiency thermoelectric clathrates through a systematic cross-substitution of framework elements, *Adv. Funct. Mater.* 20 (2010) 755–763.
- [37] G. Tan, W.G. Zeier, F. Shi, P. Wang, G.J. Snyder, V.P. Dravid, M.G. Kanatzidis, High Thermoelectric Performance SnTe-In₂Te₃ Solid Solutions Enabled by Resonant Levels and Strong Vacancy Phonon Scattering, *Chem. Mater.* 27 (2015) 7801–7811.
- [38] W. Xie, A. Weidenkaff, X. Tang, Q. Zhang, J. Poon, T.M. Tritt, Recent advances in nanostructured thermoelectric half-Heusler compounds, *Nanomaterials.* 2 (2012) 379–412.
- [39] J.F. Li, W.S. Liu, L.D. Zhao, M. Zhou, High-performance nanostructured thermoelectric materials, *NPG Asia Mater.* 2 (2010) 152–158.
- [40] D.M. Rowe, V.S. Shukla, N. Savvides, Phonon scattering at grain boundaries in heavily doped fine-grained silicon-germanium alloys, *Nature.* 290 (1981) 765–766.
- [41] W. Lai, Y. Wang, D.T. Morelli, X. Lu, From bonding asymmetry to anharmonic rattling in Cu₁₂Sb₄S₁₃ tetrahedrites: When lone-pair electrons are not so lonely, *Adv. Funct. Mater.* 25 (2015) 3648–3657.
- [42] B. Du, R. Zhang, K. Chen, A. Mahajan, M.J. Reece, The impact of lone-pair electrons on the lattice thermal conductivity of the thermoelectric compound CuSbS₂, *J. Mater. Chem. A.* 5 (2017) 3249–3259.
- [43] X. Shi, J. Yang, J.R. Salvador, M. Chi, J.Y. Cho, H. Wang, S. Bai, J. Yang, W. Zhang, L. Chen, Multiple-filled skutterudites: High thermoelectric figure of merit through

- separately optimizing electrical and thermal transports, *J. Am. Chem. Soc.* 133 (2011) 7837–7846.
- [44] G. Rogl, A. Grytsiv, E. Bauer, P. Rogl, M. Zehetbauer, Thermoelectric properties of novel skutterudites with didymium: $\text{DDy}(\text{Fe}_{1-x}\text{Co}_x)_4\text{Sb}_{12}$ and $\text{DDy}(\text{Fe}_{1-x}\text{Ni}_x)_4\text{Sb}_{12}$, *Intermetallics*. 18 (2010) 57–64.
- [45] N.P. Blake, S. Lattner, J.D. Bryan, G.D. Stucky, H. Metiu, Band structures and thermoelectric properties of the clathrates $\text{Ba}_8\text{Ga}_{16}\text{Ge}_{30}$, $\text{Sr}_8\text{Ga}_{16}\text{Ge}_{30}$, $\text{Ba}_8\text{Ga}_{16}\text{Si}_{30}$, and $\text{Ba}_8\text{In}_{16}\text{Sn}_{30}$, *J. Chem. Phys.* 115 (2001) 8060–8073.
- [46] A. Tavassoli, F. Failamani, A. Grytsiv, G. Rogl, P. Heinrich, H. Müller, E. Bauer, M. Zehetbauer, P. Rogl, On the Half-Heusler compounds $\text{Nb}_{1-x}\{\text{Ti,Zr,Hf}\}_x\text{FeSb}$: Phase relations, thermoelectric properties at low and high temperature, and mechanical properties, *Acta Mater.* 135 (2017) 263–276.
- [47] S. Ogut, K.M. Rabe, Band gap and stability in the ternary intermetallic compounds Ni_3M ($\text{M} = \text{Ti, Zr, Hf}$): A first-principles study, *Phys. Rev. B*. 51 (1995) 10443–10453.
- [48] J.P.A. Makongo, P. Paudel, D.K. Misra, P.F.P. Poudeu, Thermoelectric properties of $\text{Zr}_{0.5}\text{Hf}_{0.5}\text{Ni}_{0.8}\text{Pd}_{0.2}\text{Sn}_{0.99}\text{Sb}_{0.01}$ half-Heusler alloy with WO_3 inclusions, *Mater. Res. Soc. Symp. Proc.* 1267 (2010) 225–230.
- [49] L. J. Yang, G.P. Meisner and Chen, Strain field fluctuation effects on lattice thermal conductivity of ZrNiSn -based thermoelectric compounds, *Appl. Phys. Lett.* 1140 (2011) 5–8.
- [50] I. Terasaki, Transport properties and electronic states of the thermoelectric oxide NaCo_2O_4 , *Phys. B Condens. Matter*. 328 (2003) 63–67.
- [51] C. Matter, R. Communications, Large thermoelectric power in NaCo_2O_4 single crystals, *Phys. Rev. B*. 56 (1997) 685–687.
- [52] Z. Shi, T. Su, P. Zhang, Z. Lou, M. Qin, T. Gao, J. Xu, J. Zhu, F. Gao, Enhanced thermoelectric performance of $\text{Ca}_3\text{Co}_4\text{O}_9$ ceramics through grain orientation and interface modulation, *J. Mater. Chem. A*. 8 (2020) 19561–19572.
- [53] K. Yusupov, T. Inerbaev, M. Råsaender, D. Pankratova, I. Concina, A.J. Larsson, A. Vomiero, Improved thermoelectric performance of Bi-deficient BiCuSeO material

- doped with Nb, Y, and P, *IScience*. 24 (2021).
- [54] X.L. Shi, H. Wu, Q. Liu, W. Zhou, S. Lu, Z. Shao, M. Dargusch, Z.G. Chen, SrTiO₃-based thermoelectrics: Progress and challenges, *Nano Energy*. 78 (2020) 105195.
- [55] B. Zhou, L. Chen, C. Li, N. Qi, Z. Chen, X. Su, X.F. Tang, Significant Enhancement in the Thermoelectric Performance of Aluminum-Doped ZnO Tuned by Pore Structure, *ACS Appl. Mater. Interfaces*. 12 (2020) 51669–51678.
- [56] Y. Shi, C. Sturm, H. Kleinke, Chalcogenides as thermoelectric materials, *J. Solid State Chem*. 270 (2019) 273–279.
- [57] Y. Xiao, L.D. Zhao, Charge and phonon transport in PbTe-based thermoelectric materials, *Npj Quantum Mater*. 3 (2018).
- [58] J. Cui, M. Wang, X. Xu, Y. Chen, J. He, Understanding the effects of iodine doping on the thermoelectric performance of n-type PbTe ingot materials, *J. Appl. Phys*. 126 (2019) 1–6.
- [59] H. Pang, Y. Qiu, D. Wang, Y. Qin, R. Huang, Z. Yang, X. Zhang, L.D. Zhao, Realizing N-type SnTe Thermoelectrics with Competitive Performance through Suppressing Sn Vacancies, *J. Am. Chem. Soc*. 143 (2021) 8538–8542.
- [60] M. Winkler, X. Liu, U. Schürmann, J.D. König, L. Kienle, W. Bensch, H. Böttner, Current status in fabrication, structural and transport property characterization, and theoretical understanding of Bi₂Te₃ / Sb₂Te₃ superlattice systems, *Zeitschrift Fur Anorg. Und Allg. Chemie*. 638 (2012) 2441–2454.
- [61] M. Kumar, S. Rani, Y. Singh, K.S. Gour, V.N. Singh, Tin-selenide as a futuristic material: properties and applications, *RSC Adv*. 11 (2021) 6477–6503.
- [62] D.Y. Chung, T.P. Hogan, M. Rocci-Lane, P. Brazis, J.R. Ireland, C.R. Kannewurf, M. Bastea, C. Uher, M.G. Kanatzidis, A new thermoelectric material: CsBi₄Te₆, *J. Am. Chem. Soc*. 126 (2004) 6414–6428.
- [63] G.Z. and Y.-W. Zhang, Thermoelectric properties of two-dimensional transition metal dichalcogenides, *J.Mater.Chem.C*. 5 (2017) 7684–7698.
- [64] M.A. McGuire, T.K. Reynolds, F.J. DiSalvo, Exploring thallium compounds as thermoelectric materials: Seventeen new thallium chalcogenides, *Chem. Mater*. 17

- (2005) 2875–2884.
- [65] S. Zhan, T. Hong, B. Qin, Y. Zhu, X. Feng, L. Su, H. Shi, H. Liang, Q. Zhang, X. Gao, Z.H. Ge, L. Zheng, D. Wang, L.D. Zhao, Realizing high-ranged thermoelectric performance in PbSnS₂ crystals, *Nat. Commun.* 13 (2022) 1–9.
- [66] S. Yang, T. Zhang, C. Jiang, van der Waals Magnets: Material Family, Detection and Modulation of Magnetism, and Perspective in Spintronics, *Adv. Sci.* 8 (2021) 1–31.
- [67] V.S. Sulyaeva, I.Y. Filatova, Magnetic Properties of CuCr_{1-x}La_xS₂ Thermoelectric Materials, *Magnetochemistry.* 168 (2023) 1–1.
- [68] Q.M. Syed Awais Rouf , Hind Albalawi , Taharh Zelai , Othman Hakami , Nessrin A. Kattan , Samah Al-Qaisi , S. Bouzgarrou , Muhammad Younas , Khaild I. Hussein, Half-metallic ferromagnetism and thermoelectric effect in spinel chalcogenides SrX₂S₄ (X = Mn, Fe, Co) for spintronics and energy harvesting, *J.Phys.Chem.Solids.* 182 (2023) 1–4.
- [69] C. Han, Q. Sun, Z. Li, S.X. Dou, Thermoelectric Enhancement of Different Kinds of Metal Chalcogenides, *Adv. Energy Mater.* 6 (2016) 1–36.
- [70] S. Bhattacharya, A. Bohra, R. Basu, R. Bhatt, S. Ahmad, K.N. Meshram, A.K. Debnath, A. Singh, S.K. Sarkar, M. Navneethan, Y. Hayakawa, D.K. Aswal, S.K. Gupta, High thermoelectric performance of (AgCrSe₂)_{0.5}(CuCrSe₂)_{0.5} nano-composites having all-scale natural hierarchical architectures, *J. Mater. Chem. A.* 2 (2014) 17122–17129.
- [71] H. Adachi, K.I. Uchida, E. Saitoh, S. Maekawa, Theory of the spin Seebeck effect, *Reports Prog. Phys.* 76 (2013).
- [72] C.Kittel, *Introduction to Solid State Physics*, 2005.
- [73] N. A.Spaldin, *Fundamentals and Device Applications*, 2003.
- [74] S.M. Yakout, Spintronics: Future Technology for New Data Storage and Communication Devices, *J. Supercond. Nov. Magn.* 33 (2020) 2557–2580.
- [75] C.A.M. Mulder, A.J. Van Duynveldt, J.A. Mydosh, Frequency and field dependence of the ac susceptibility of the AuMn spin-glass, *Phy. Rev. B.* 25 (1982) 515–518.

- [76] S. Blundell, *Magnetism in Condensed Matter*, Oxford University Press, U.K, (2001) 251.
- [77] K. Ghosh, C. Mazumdar, R. Ranganathan, S. Mukherjee, Griffiths phase behaviour in a frustrated antiferromagnetic intermetallic compound, *Nat. Publ. Gr.* 5 (2015) 1–10.
- [78] C. He, M.A. Torija, J. Wu, J.W. Lynn, H. Zheng, J.F. Mitchell, C. Leighton, Non-Griffiths-like clustered phase above the Curie temperature of the doped perovskite cobaltite $\text{La}_{1-x}\text{Sr}_x\text{CoO}_3$, *Phys. Rev. B - Condens. Matter Mater. Phys.* 76 (2007) 1–5.
- [79] V. Kumar, A. Kumar, S. Singh, K. Kumar, M.K. Verma, V.S. Rai, G. Nirala, S. Upadhyay, N. Yadav, N.B. Singh, D. Tiwary, K.D. Mandal, The emergence of Griffiths phase in $\text{CaCu}_3\text{Ti}_{(4-x)}\text{Mn}_x\text{O}_{12}$ (CCTMO, $x = 1, 2$ and 3) geometrically frustrated antiferromagnetic complexes perovskite, *J. Mater. Sci. Mater. Electron.* 35 (2024) 1–11.
- [80] B. Kurniawan, F. Ruli, A. Imaduddin, R. Kamila, Transport Properties and Magnetoresistance of $\text{La}_{0.8}\text{Ca}_{0.13}\text{Ag}_{0.07}\text{MnO}_3$ Perovskite Manganite Synthesized by Sol-Gel Method, *IOP Conf. Ser. Mater. Sci. Eng.* 367 (2018) 0–6.
- [81] J. Nickel, Magnetoresistance Overview, in: Hewlett-Packard Co. 1995, 1995: p. 11.
- [82] Y.Q. Miao, J.J. Guo, Z.Y. Luo, M.Z. Zhong, B. Li, X.G. Wang, Y.Z. Nie, Q.L. Xia, G.H. Guo, Anisotropic Magnetoresistance Effect of Intercalated Ferromagnet FeTa_3S_6 , *Front. Phys.* 10 (2022) 1–7.
- [83] V.S. Sulyaeva, I.Y. Filatova, Magnetic Properties of $\text{CuCr}_{1-x}\text{La}_x\text{S}_2$ Thermoelectric Materials, *Magnetochemistry.* 168 (2023) 1–14.
- [84] M.Z. Iqbal, G. Hussain, S. Siddique, M.W. Iqbal, Enhanced magnetoresistance in graphene spin valve, *J. Magn. Magn. Mater.* 429 (2017) 330–333.
- [85] K. Uchida, S. Takahashi, K. Harii, J. Ieda, W. Koshibae, K. Ando, S. Maekawa, E. Saitoh, Observation of the spin Seebeck effect, *Nature.* 455 (2008) 778–781.
- [86] S. Roychowdhury, S. Ghara, S.N. Guin, A. Sundaresan, K. Biswas, Large linear magnetoresistance in topological crystalline insulator $\text{Pb}_{0.6}\text{Sn}_{0.4}\text{Te}$, *J. Solid State Chem.* 233 (2016) 199–204.

- [87] Z.H. Wang, L. Yang, X.J. Li, X.T. Zhao, H.L. Wang, Z.D. Zhang, X.P.A. Gao, Granularity controlled nonsaturating linear magnetoresistance in topological insulator Bi₂Te₃ films, *Nano Lett.* 14 (2014) 6510–6514.
- [88] M. d'Angelo, C. Galassi, N. Lecis, Thermoelectric Materials and Applications: A Review, *Energies.* 16 (2023) 1–50.
- [89] X.L. Shi, J. Zou, Z.G. Chen, Advanced thermoelectric design: From materials and structures to devices, *Chem. Rev.* 120 (2020) 7399–7515.
- [90] Z. Han, J.W. Li, F. Jiang, J. Xia, B.P. Zhang, J.F. Li, W. Liu, Room-temperature thermoelectric materials: Challenges and a new paradigm, *J. Mater.* 8 (2022) 427–436.
- [91] M. Jin, J. Liang, P. Qiu, H. Huang, Z. Yue, L. Zhou, R. Li, L. Chen, X. Shi, Investigation on Low-Temperature Thermoelectric Properties of Ag₂Se Polycrystal Fabricated by Using Zone-Melting Method, *J. Phys. Chem. Lett.* 12 (2021) 8246–8255.
- [92] V.K. Singh, S.S. Sisodia, A. Patel, T. Shah, P. Das, R.N. Patel, R.R. Bhavsar, Thermoelectric cooler (TEC) based thermal control system for space applications: Numerical study, *Appl. Therm. Eng.* 224 (2023) 2–7.
- [93] S.M. Yakout, Spintronics: Future Technology for New Data Storage and Communication Devices, *J. Supercond. Nov. Magn.* 33 (2020) 2557–2580.
- [94] A. Hirohata, K. Yamada, Y. Nakatani, L. Prejbeanu, B. Diény, P. Pirro, B. Hillebrands, Review on spintronics: Principles and device applications, 2020.
- [95] A. Hirohata, K. Yamada, Y. Nakatani, L. Prejbeanu, B. Diény, P. Pirro, B. Hillebrands, Review on spintronics: Principles and device applications, *J. Magn. Mater.* 509 (2020).
- [96] H. Search, C. Journals, A. Contact, M. Iopscience, I.P. Address, Longitudinal spin Seebeck effect : from fundamentals to applications, *J.Phys.:Condens.Matter.* 26 (2014) 15.

Chapter 2

Experimental Methods

2.1. Materials

Barium rods (99.99%), Vanadium pieces (99.7%), Cobalt pieces (99.8%), Nickel pieces (99.7%), Iron pieces (99.7%), Se granules (99.999%), Silver granules (99.99%), Antimony pieces (99.99%), and Tellurium pieces (99.99%) were purchased from Alfa Aesar.

2.2. Sample fabrication

Samples were fabricated by direct melting method; here we are using the high-purity constituent elements as the precursors. The raw materials were sealed in an evacuated quartz tube using the oxygen - LPG flame lamp. Finally, the quartz ampoules were kept for heat treatment in an air muffle furnace. The figure shows the schematic representation of sample preparation. The structural and magnetic characterization was done on the powder obtained by grinding the ingots. The melted ingots were cut into rectangular bars ($\sim 10 \times 2 \times 2 \text{ mm}^3$) for various transport studies.

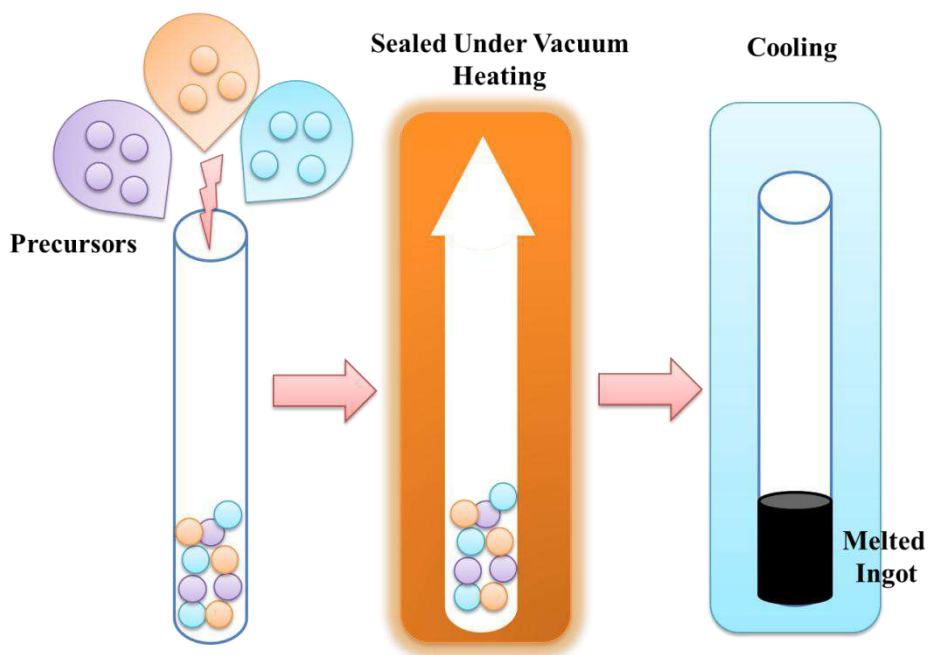


Figure 2.1. The schematic diagram for the solid-state route

In **chapter 1** Polycrystalline BaVSe_3 was synthesized via the solid-state reaction method (Figure 2.1), using the precursors Ba, V and Se in two routes.

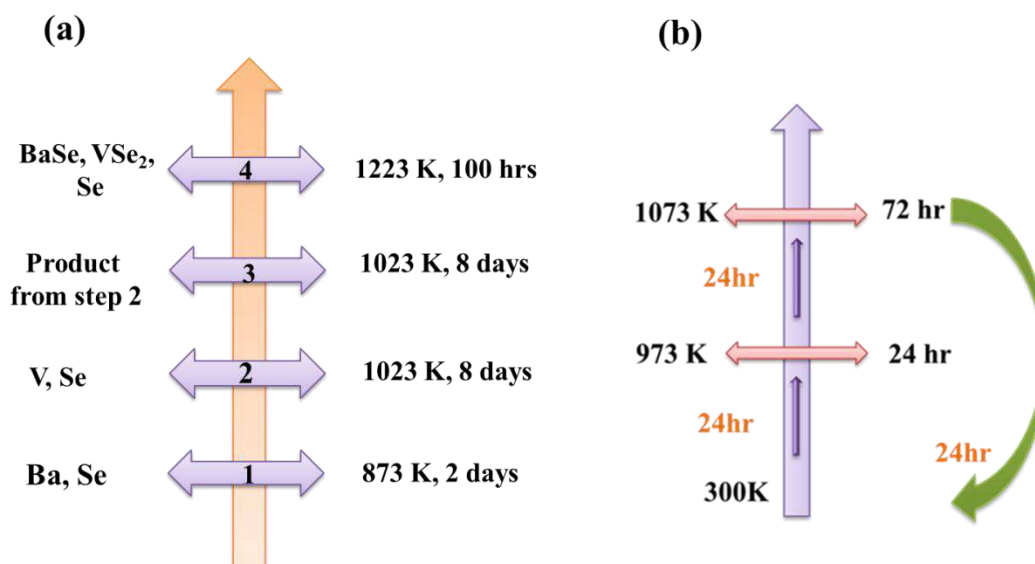


Figure 2.2. Heat treatment of sample (a) BVS: BS (b) BVS

Route 1: The synthesis was done in three steps (Figure 2.2 a), at first Ba and Se were weighed in 1:1 proportion under a nitrogen atmosphere in the Glove box with 1 ppm Oxygen level and moisture level, sealed under vacuum (10^{-4} Torr) in quartz tubes and annealed at 873 K for 2 days. In the second step, VSe₂ is prepared via the same solid-state route, with a heat treatment of the evacuated and sealed quartz tube at 1023 K for 8 days. The obtained pieces are ground and then subjected to recrystallization for an extended duration of 8 days at 1023 K. The synthesized material from the first step and VSe₂ are mixed with Se in the required stoichiometry in a glove box with ideal conditions and are sealed under vacuum in quartz tubes. The tubes are then heated at 1223 K for 100 hours. The obtained powder is crushed and pelletized for characterization by various techniques.

Route 2: High-purity precursor elements Ba, V, and Se were taken in the stoichiometric ratio under a nitrogen environment in the Glove box with more than 2 ppm oxygen and moisture level in quartz tubes. Following this, the sample tubes were deposited in a furnace after being sealed under a high vacuum (10^{-4} Torr). With a 24-hour ramp-up, the furnace temperature was maintained at 973 K for the next twenty-four hours. The temperature was raised to 1073 K in a 24-hour ramp immediately following the initial phase, annealed for three days, and then cooled to room temperature (Figure 2.2 b). For phase analysis, the molten samples were reduced to powder, subsequently pressed into rectangular pellets, and sintered at 973 K for 6 hours to facilitate diverse transport investigations. The pellets' specific gravity was determined to be 95% using the Archimedes method.

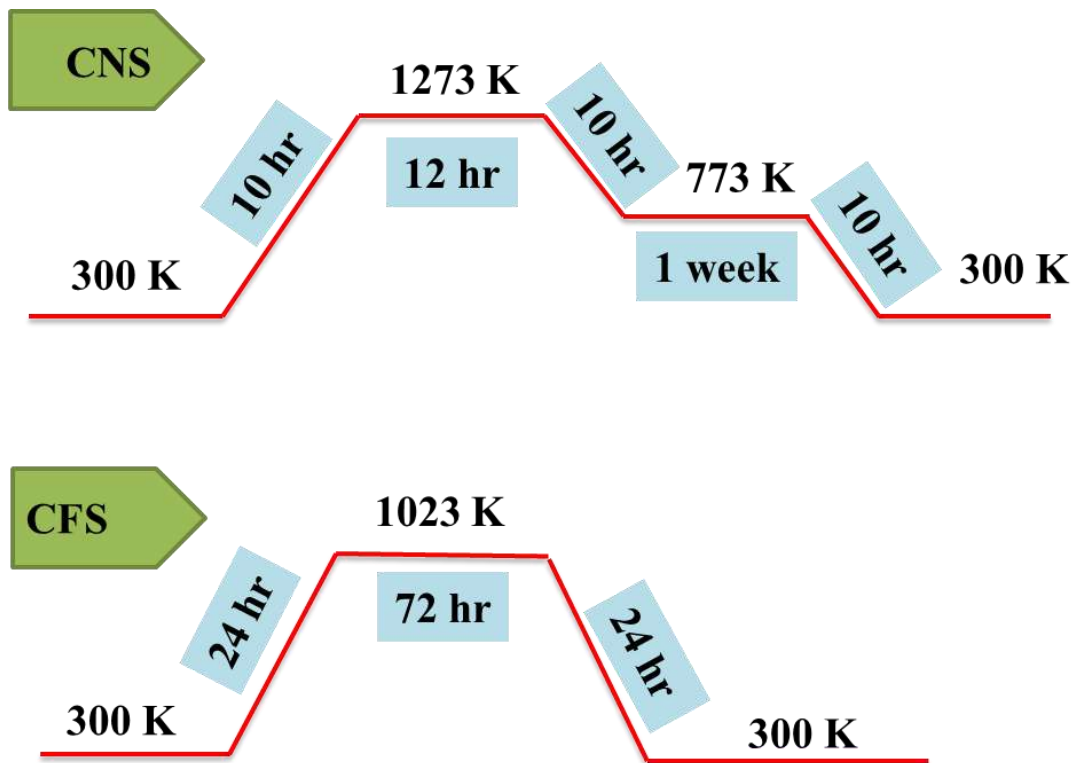


Figure 2.3. Heat treatment steps of samples CNS and CFS

In **chapter 3** Polycrystalline CoMSe_2 ($M = \text{Ni}, \text{Fe}$) was first time synthesized through the melting of the high purity constituent elements Ni, Co, Fe and Se of required stoichiometric ratio. These were transferred into quartz tubes, evacuated (10^{-4} torr) and sealed. The materials CoNiSe_2 (CNS) and CoFeSe_2 (CFS) were obtained through different heat treatment routes and Figure 2.3 summarizes the synthesis.

In **chapter 4** AgSbTe_2 compounds were synthesized from high-purity elements Ag, Sb and Te. The elements were weighed according to stoichiometry and loaded into the quartz tube under vacuum (10^{-5} mbar). The sealed ampoules were first heated at 1073 K for 10 hr and the obtained ingot was further heat treated at 773 K for 72 hr, then cooled to room temperature over 24 hr. The heat treatment resulted in high-density dark silvery-shaded metallic ingots. A part of the sample was ground for structure and morphology analysis; rectangular samples were cut and polished into a dimension of $10 \text{ mm} \times 3 \text{ mm} \times 2 \text{ mm}$ for various transport measurements.

The crystal structure, composition and morphology of synthesized samples was analysed through various techniques. The density of the pellets was measured using the Archimedes method, and the Vickers microhardness of the material was calculated using the Vickers Microhardness tester - Banbros. A detailed study on the magnetic properties of the present

compounds was carried out with the help of vibrating sample magnetometer (VSM). The low-temperature electrical and thermal transport measurements and heat capacity of the samples were done through the electrical transport option (ETO), thermal transport option (TTO) and heat capacity set-up of physical property measurement system (PPMS, Quantum Design). The detailed theory and working of characterization techniques was included in annexure.

Chapter 3

Exotic Magnetic, Magneto-transport and Thermoelectric properties of BaVSe_3

Zintl phases are a special class of complex structures with the general formula A-T-Q, where A is an alkali metal or an alkaline earth metal, T is TM, and Q is the main group element [1]. These intermetallic phases satisfy the Zintl-Klemm concept in which the electro-positive atoms act as electron donors and electro-negative atoms act as valence-electron acceptors. This donor-acceptor system leads to a valence-balanced condition [2]. The transition metal compounds exhibit a paramagnetic (PM) to ferromagnetic (FM) transition at particular temperatures, leading to some exciting phenomena like colossal magnetoresistance (CMR) [3] due to the critical FM fluctuations about T_C [4]. This property finds applications in device components like the magnetic reading head. CMR was initially observed in manganese-based oxides and recent reports suggest its presence in alloys and chalcogenides [5,6].

BaVSe_3 , having a hexagonal perovskite-like structure with the general formula BaVX_3 (with $X = \text{S, Se}$), satisfies the Zintl-Klemm concept [7]. Among the above-mentioned BaVX_3 compounds, BaVS_3 has been extensively studied [8]. BaVS_3 shows a metal-to-insulator transition at a temperature of 70 K, hexagonal to orthorhombic structural transition at 240 K and an antiferromagnetic (AFM) ordering below 30 K [7]. The selenium (Se) ions, being larger than the sulphur (S) ions, lead to orbital overlap in BaVSe_3 and generate a condition synonymous with one where BaVS_3 is under high pressure [9]. BaVSe_3 exhibits a structural transition from hexagonal to orthorhombic at a temperature of ~ 310 K [10,11].

Ternary chalcogenides with general formula BaMX_3 ($M=\text{Ti, V, Nb}$ or Ta and $X=\text{S}$ or Se) exhibit quasi-one-dimensional structure. At room temperature, BaVS_3 crystallizes in a CsNiCl_3 structure having space group $p63/mmc$ with a linear chain of vanadium atoms formed by the face sharing of VS_6 octahedra. In this structure, the unidimensionality arises from a short intrachain V-V (vanadium-vanadium) distance (2.805\AA) and a long interchain V-V separation (6.724\AA) [12]. The ideal quasi-one-dimensional nature is represented by vanadium ion chains that are slightly distorted, forming a zig-zag pattern along the crystallographic c-axis. BaVSe_3 also exhibits a metallic ferromagnetic nature and is considered to be an example of an itinerant electron magnet possessing a 1D structure [13]; hence its primary utility is in the field of spintronics [14]. Sugiyama *et al* reported that the V moments align ferromagnetically along the c-axis but they slightly canted towards the a-axis

by 28° and are coupled antiferromagnetically [15]. Recently, several studies have been conducted on the spin-glass behaviour and the long-range AFM ordering in dilute metallic alloys and layered transition metal chalcogenides [16–20]. Magnetic materials with glassy behaviour are characterized by randomness, competing interactions and geometrical frustrations, which leads to the freezing of magnetic moments below a temperature denoted as the freezing temperature (T_f) [20]. These metastable ground states are structurally similar to glassy states [21].

The materials exhibiting glassy behaviour are categorized into several classes based on the observed density of magnetic moments. Canonical spin-glass (SG) materials exhibit a small magnetic moment density and can be considered as single magnetic impurities being dispersed in a nonmagnetic host. These materials indicate a phase transition that is brought about due to the strong interaction and cooperative spin freezing present in them. These magnetic systems have some frozen-in structural disorder and no well-defined long-range order as observed in FM and AFM systems. These systems exhibit a freezing transition- with the order in which the spins are correlated to form clusters which are oriented in random directions [22]. Cluster glass (CG) materials exhibit large magnetic moment densities, resulting from the local magnetic moment and frustration between the neighbouring magnetic clusters [21]. This state can be distinguished from SG by the presence of clusters originating due to short-range magnetic ordering at temperatures near T_C [22]. When the density of magnetic moments of a material overcomes the glassy limit, it results in long-range magnetic order. Such magnetic materials exhibit a transition from the PM state to an ordered state at a transition temperature, before the glassy appearance at T_f . The PM, SG and CG states lack the long-range magnetic ordering [20,23,24].

Nowadays intense research and development (R&D) is underway to understand the Griffiths-like phases (GP) observed in different magnetic materials [25]. Griffith first observed GP in arbitrarily diluted Ising FM systems, the magnetization fails to be an analytical function of the magnetic field at temperatures between the Curie-Weiss temperature and the Griffiths temperature [26]. The reasons for the origin of GP vary from one material to another, some of which are phase separation, the presence of cluster sizes ranging from nanometers to micrometres and competing for intra-interlayer magnetic interactions [27]. In most of the materials, GP arises due to the result of the occurrence of short-range ordered FM clusters in the PM region [28]. In manganese oxide-based materials [29], quenched disorder plays an essential role in GP formation. In the case of 4f electron

alloys [30] the origin of GP is associated with characteristic disorder and competition between Ruderman-Kittel-Kasuya-Yosida (RKKY) interaction and the Kondo effect.

The current study presents the synthesis of BaVSe₃ through two synthesis routes (*chapter 2*), one from the previous report and the other through a time-reduced novel heat treatment process. A comparative analysis was conducted between these materials in their low-temperature magnetic properties, thermoelectric and magnetotransport. A detailed analysis of phase, morphology, composition, magnetic and thermoelectric characterizations (Annexure) were carried out.

3.1. Results and Discussions

3.1.1. Crystal structure and surface studies

The Rietveld refined XRD spectra of the synthesized samples from route 1 and route 2 are shown in Figure 2.2. The existence of the secondary phase of BaSe₃ is also evident in the XRD data of the first sample (BVS: BS) (Figure 3.1a). Hulliger et al. [31] reported the formation of BaSe₃ from their constituent elements at temperatures between 773 K and 973 K and existed as stable even after prolonged heat treatment. The presence of a secondary phase is common in solid-state synthesized materials from constituent elements [32]. The primary phase BaVSe₃, belongs to the hexagonal crystal system with a space group of $P6_3/mmc$ and the other phase, BaSe₃, belongs to the tetragonal system with a space group of $P4_2/m$. The goodness of fit factor of the refinement (χ^2) is obtained as 1.66. The lattice parameters of BaVSe₃ are $a = b = 6.9944 \text{ \AA}$, and $c = 5.8577 \text{ \AA}$. The α , β and γ angles are 90° , 90° , and 120° respectively. From the Rietveld refinement, the phase fraction obtained for the BaVSe₃ is 76.21% and for the secondary phase is 23.79%. A crystallographic information file (CIF) is created from the Rietveld refined XRD data using the software Crystal Maker (version 2.7.3). A graphical representation with the labelling of Ba, V and Se is given in Figure 3.1b, where the Barium, vanadium and selenium (Se) ions are labelled with purple, red and orange spheres respectively. From Figure 3.1c, the data indicated that the implementation of a novel thermal treatment procedure aided the production of pure phase BaVSe₃ (BVS), in contrast to the previously documented method [26], which resulted in the formation of BaVSe₃ with BaSe₃ impurities (BVS: BS).

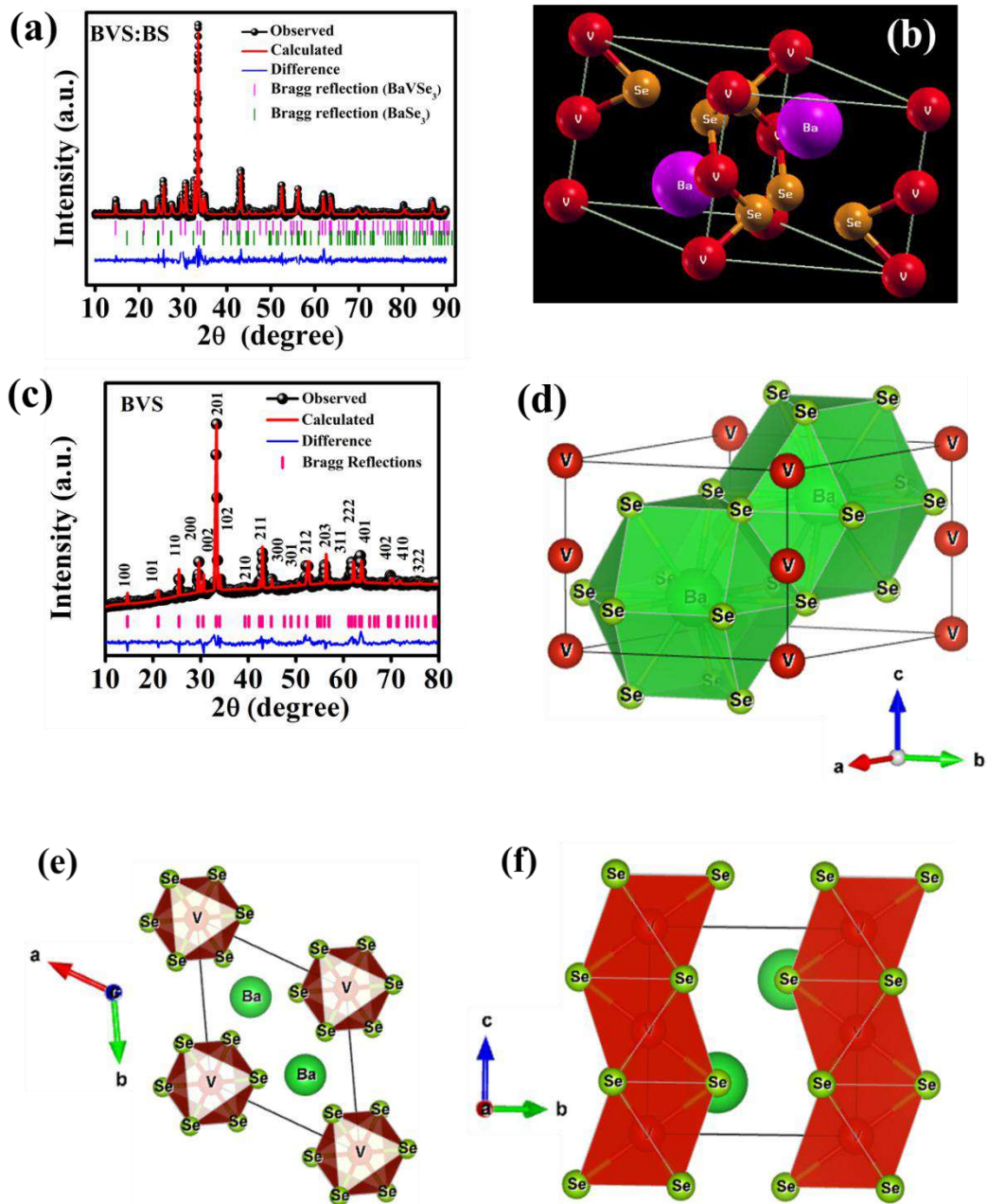


Figure 3.1. (a) Rietveld refined XRD pattern of BVS: BS, (b) A graphical representation of the $BaVSe_3$ unit cell obtained from the refined XRD data, (c) Rietveld refined XRD pattern of BVS, (d)-(f) Unit cell of $BaVSe_3$ at different crystallographic direction from VESTA

The crystal structure of hexagonal $BaVSe_3$ is depicted in Figure 3.1d. In this structure, the Ba atoms are surrounded by 12 Se atoms, while the V atoms form face-shared VSe_6 octahedra, as illustrated in Figure 3.1e. The material's one-dimensional nature arises from the presence of elongated chains of V atoms aligned along the crystallographic c-axis (as shown in Figure 2.2f). Each V atom is surrounded by face-sharing Se octahedra [33]. Typically, in $BaVSe_3$, the intra-chain V-V distance is 2.9310 Å and the inter-chain V-V distance is 6.999 Å ensuring the structural unidimensionality and weak van der Waal interactions [34].

X-ray photoelectron spectroscopy (XPS) studies of polycrystalline BaVSe₃ were carried out to observe the oxidation state and chemical composition of the sample BVS: BS. The binding energies are corrected with the reference energy of 284.60 eV (C 1s).

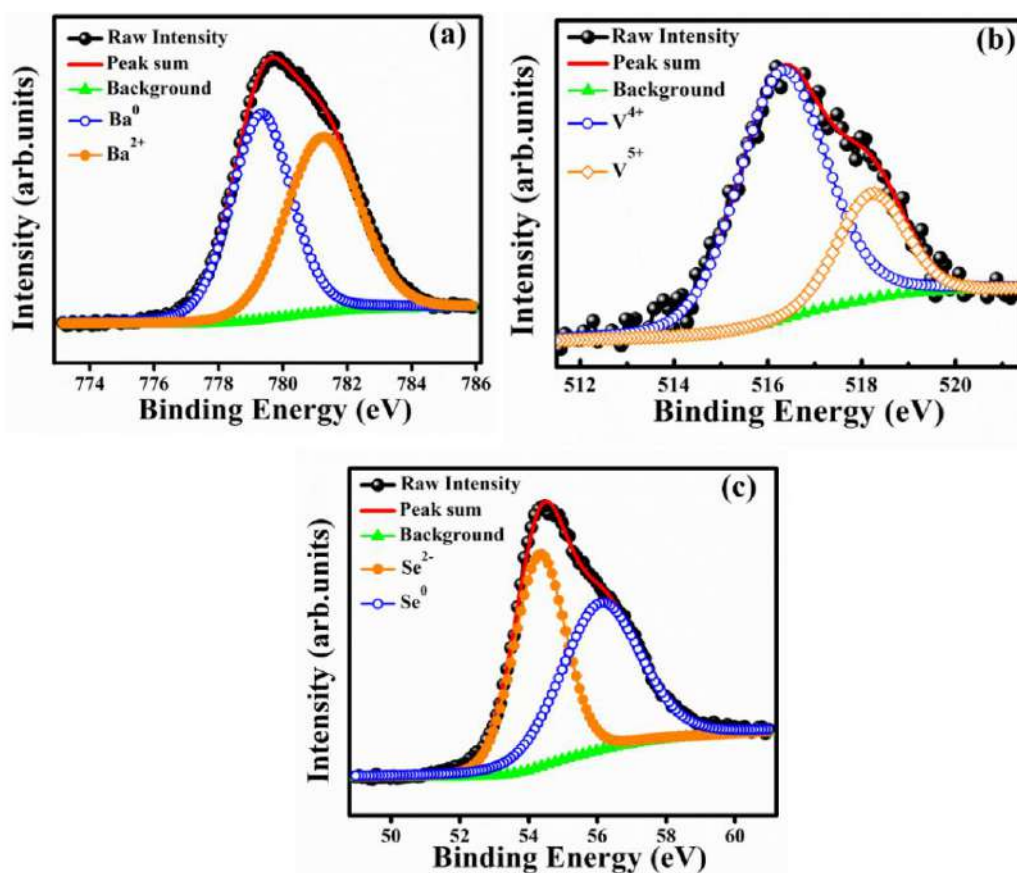


Figure 3.2. Deconvoluted high-resolution XPS spectra of elements (a) Ba, (b) V, (c) Se

Figure 3.2 a-c shows the peak-fitted high-resolution spectra of Ba, V, and Se, respectively. Figure 3.2a depicts the deconvolution of the Ba 3d_{5/2} peak, fitted with two curves at binding energies 781.27 eV and 779.35 eV, representing the Ba²⁺ and Ba⁰ states respectively [35]. In BaVSe₃, vanadium exists in the V⁴⁺ state (Figure 3.2b); however, the presence of V⁵⁺ may indicate surface oxidation [36] and the formation of V₂O₅ on the top 5 nm layer of BaVSe₃. However, the presence of V₂O₅ is not observed in XRD, indicating that the formation of V₂O₅ is negligible and does not influence the considered system's properties. Figure 3.2c shows the deconvoluted spectra of Se. It has a lower binding energy of 54.36 eV due to Se²⁻ [35] and a higher binding energy of 55.90 eV corresponding to the Se⁰ state [35]. Hulliger *et al* [37] reported that BaSe₃ has the ionic formulae of Ba⁺²Se⁰Se₂⁻¹, where Se⁰ corresponds to the formation of the secondary phase, BaSe₃ and is confirmed from Rietveld refinement of XRD spectra.

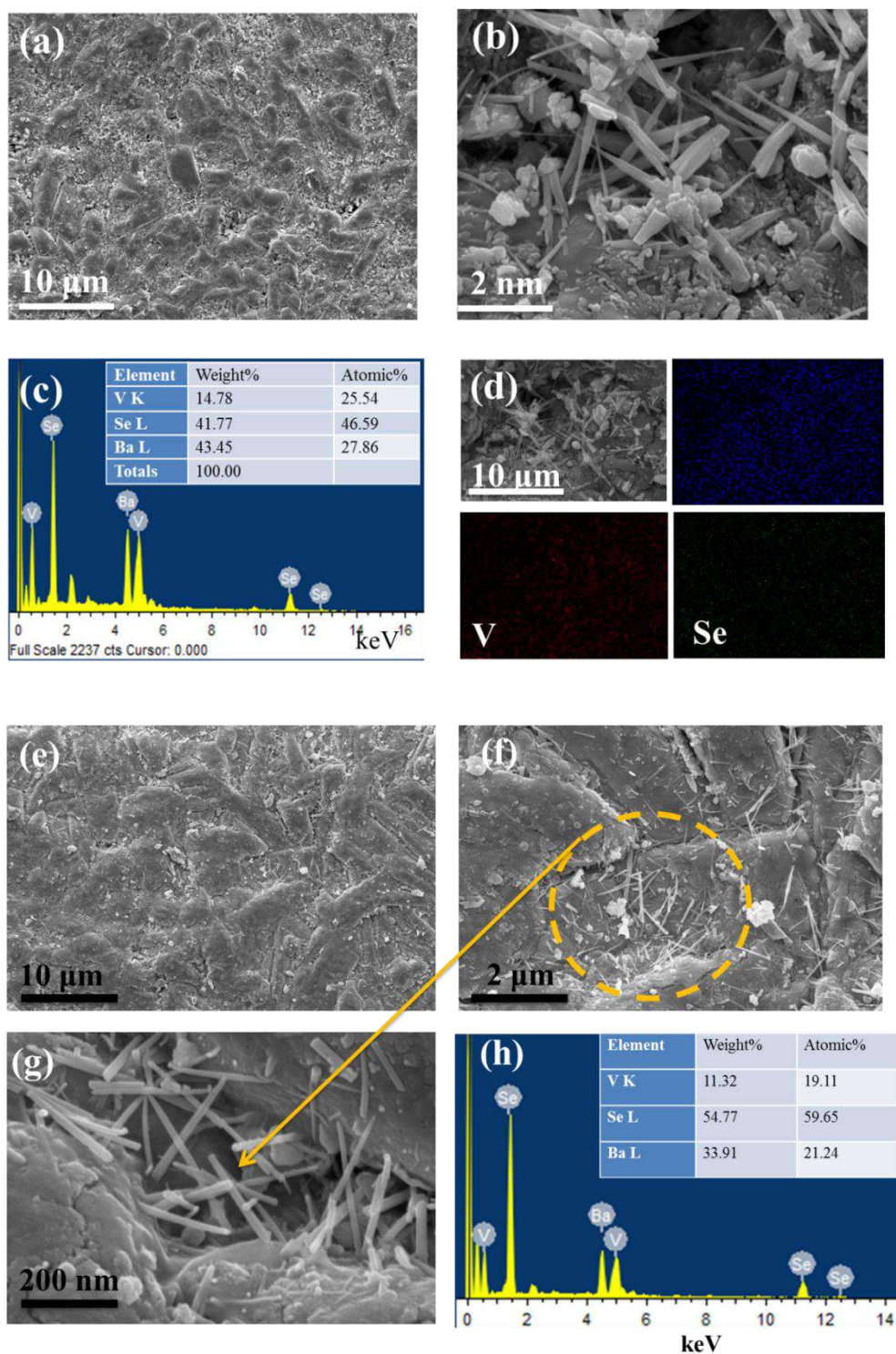


Figure 3.3. Scanning electron microscopy images of the pellet sample BVS: BS (a) on a 10 μm scale, (b) associated needle-shaped crystals on the surface of the sample BVS: BS (2 μm scale), (c) EDS spectrum (d) elemental mapping of BVS: BS, (e)- (f) SEM images of BVS at different scales and (h) EDS spectrum of the sample BVS

The SEM analysis revealed a highly compact and dense microstructure of the synthesized samples BVS: BS and BVS, as depicted in Figure 3.3. The compactness of the sample is

depicted in Figure 3.3a, and the presence of needle-shaped crystals between 100-200 nm in diameter is displayed in Figure 3.3b. Kelber et al. [11] were the first to report the synthesis and growth of needle-shaped crystals in BaVSe_3 . This growth is attributed to the structure of the Q1D material. Figure 3.3c displays the EDS spectrum, indicating the weight and atomic fraction of each element in the developed material BVS: BS and the homogeneity of the material is confirmed through elemental mapping (Figure 3.3d). The compact topography of the pellets and the presence of needle-shaped crystals in BVS at 10 μm , 2 μm and 200 nm is depicted in Figure 3.3 (e)-(g). From the EDS spectrum (Figure 3.3h), the local composition of the material aligns well with the expected stoichiometry. Figure 3.4 (a)-(d) displays the mapping of the constituent elements Ba, V, and Se. The distribution of all elements appeared homogeneous.

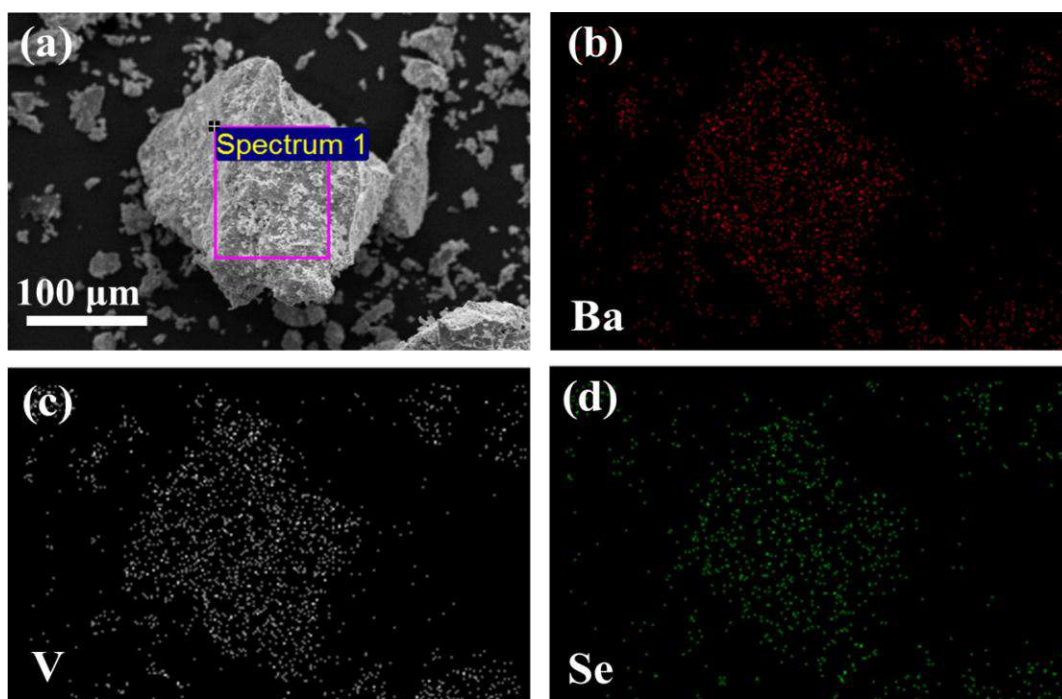


Figure 3.4. (a)-(d), Elemental mapping of the sample BVS at a micrometre scale, constituent elements Ba, V, Se were mapped

The transmission electron microscope studies incorporated to further inspect the nano/microstructure of the melted sample BVS. Figure 3.5a illustrates the coexistence of nanostructures and microstructures. The material's polycrystalline nature was verified using HRTEM analysis (Figure 3.5 (b) - (d)), and the identification of the planes was achieved by comparing them with the d spacing obtained from the XRD data.

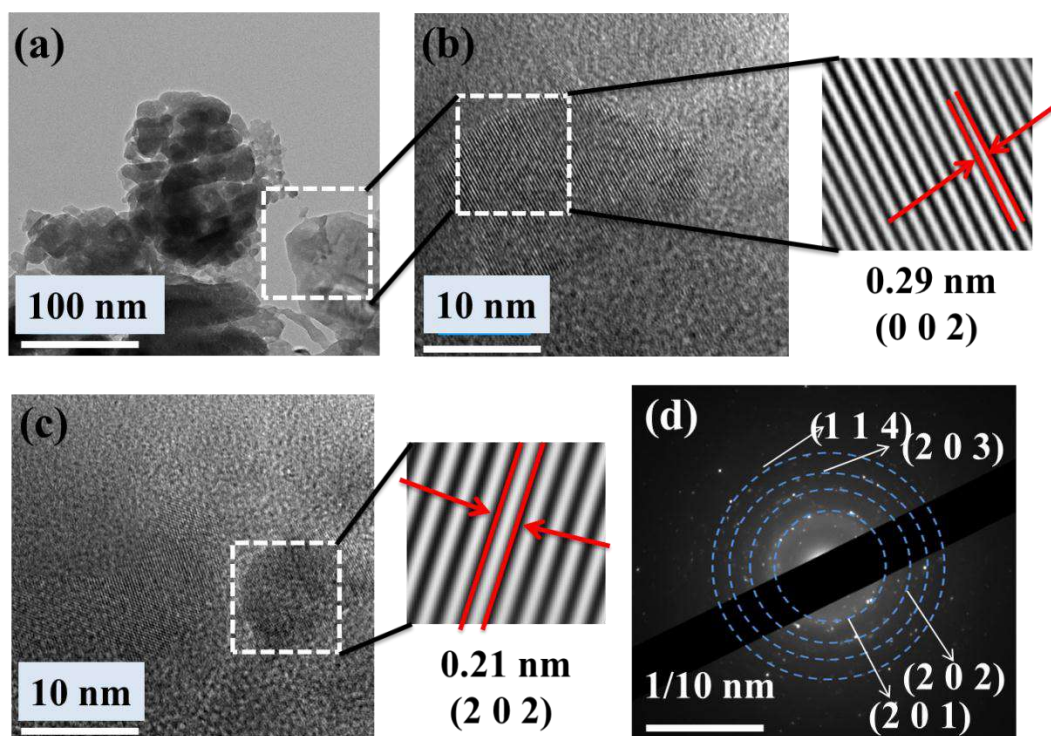


Figure 3.5. (a)TEM image of the synthesized material BVS, (b) & (c) the HRTEM images with crystal planes and the corresponding d spacing were marked, (d) SAED pattern of the material

The d-spacing of the planes in the sample was calculated with the help of GATAN microscopy suite software and the d-spacing of 0.29 nm and 0.21 nm was corresponding to the planes (0 0 2) and (2 0 2) respectively. The ring diffraction pattern in the selected area diffraction (SAED) was indexed to the corresponding crystal planes of hexagonal BVS. From SAED, it was observed that the present material has some randomly distributed single-crystalline zones along with the utmost polycrystalline nature.

3.1.2. Magnetic properties

3.1.2.1. Magnetic studies of BVS: BS

The magnetic hysteresis (M-H loops) was recorded at different temperatures in the applied field extending from -90 kOe to +90 kOe. Figure 2.7a shows the M-H loops taken at different temperatures such as 2 K, 10 K, 25 K, 43 K and 300 K. Up to 25 K, the MH loop shows FM nature, and the M (H) data at 43 K shows PM behaviour, which profoundly indicates the FM to PM transition at a critical temperature (*i.e.*, Curie temperature, T_C) in between 25 K and 43 K.

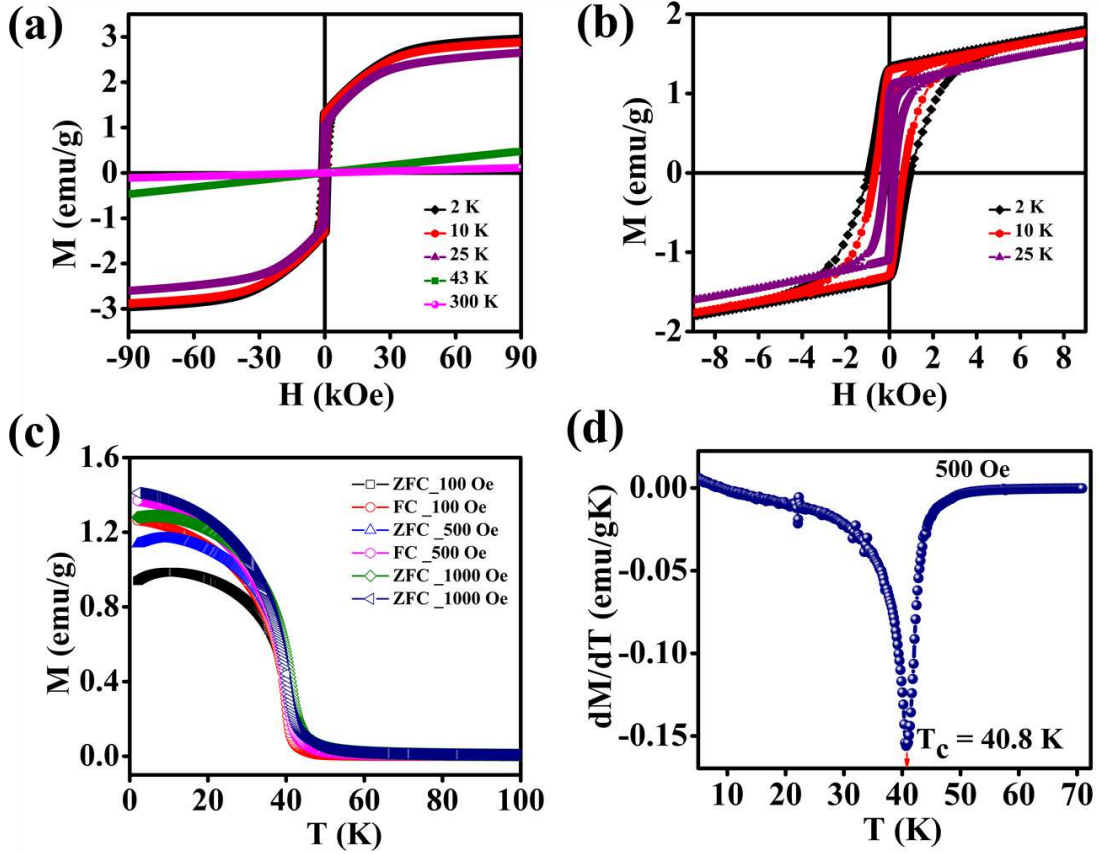


Figure 3.6. (a) M-H loops at different temperatures, (b) zoomed-in MH loops, (c) M-T curves taken at the different magnetic fields, (d) dM/dT versus T plot

However, the hysteresis loops below T_C exhibit an unsaturated magnetization even at a higher field of 90 kOe. Usually, this kind of unsaturated magnetization is due to the presence of AFM moments [38]. Also, an unsaturated M-H loop is one of the criteria for magnetic systems with glassy behaviour [39]. Figure 3.6a demonstrates the above-mentioned unsaturated nature of magnetization and is a profound indication of a frustrated ferromagnetic system [40]. In the magnified view of the hysteresis (shown in Figure 3.6b), a non-zero coercivity (H_C) and remanent magnetization (M_R) at temperatures 2 K, 10 K, and 25 K can be observed. Here, H_C and M_R are observed to decrease with the increase in temperature. Another parameter of interest is the anisotropy constant (K), as it depends strongly on temperature [41]. In Table 2.1, H_C , saturation magnetization (M_S) and M_R are presented. The reduction in coercivity can be a direct consequence of the reduction in effective magnetic anisotropy with the increase in temperature [42]. According to the Neel model of anisotropy, the magnetic energy barrier [43] is given in equation (1) as,

$$H_C = \frac{2K}{M_S} \quad (1)$$

The calculated values of K at different temperatures are given in Table 3.1. The anisotropy constant is observed to decrease with the increased temperature [43].

Table 3.1. Comparison of H_C , M_S and M_R

T (K)	H_C (kOe)	M_S (emu/g)	M_R (emu/g)	$K = \frac{M_S H_C}{2}$
2	1.00	2.80	1.32	1409.80
10	0.67	2.22	1.29	748.80
25	0.23	1.38	1.07	161.30

The temperature-dependent magnetization of the material is studied in the temperature range of 2 K–100 K at different field strengths. The zero-field cooled (ZFC) and field-cooled (FC) magnetization versus temperature (M-T) curves were taken at different field conditions. In ZFC, the material is cooled to 2 K in the absence of an external magnetic field, and subsequently warmed from 2 K to 300 K by applying the required field; the required data is collected during the warming process. In FC, M-T measurement was carried out in the presence of a constant field, when cooling the sample from 300 K to 2 K. Figure 3.6c shows the M-T curves of BVS under the influence of 100 Oe, 500 Oe and 1000 Oe fields, indicating that there is a split in ZFC and FC at low temperatures. This bifurcation in the M-T curves was not suppressed by applying strong magnetic fields; which is an indication of glassy behaviour [44]. The transition temperature, T_C is obtained from the minimum of the dM/dT versus T plot. Below T_C , the material exhibits FM ordering and a paramagnetic behaviour is observed above T_C . Figure 3.6d shows the dM/dT vs. T plot of BVS and the T_C obtained is 40.8 K. This is in good agreement with previous reports by Kelber *et al.* ($T_C = 41$ K) [45] and, Akrap *et al.* ($T_C = 43$ K) [9]. Some recent reports of 2D magnetic materials exhibit low T_C values (below 50 K) [46,47]. However, the Curie temperature of ferromagnetic materials depends on the size and shape effects of nanoparticles [48,49]. These results indicate that the presence of nonmagnetic $BaSe_3$ did not much affect the properties of $BaVSe_3$. Since, V is a first-row transition metal, orbital angular momentum does not contribute to the total magnetic moment, due to the orbital quenching [41]. Hence, the magnetic moment for these metals originates from electron spin-only magnetic moment and is given by

$$\mu_{eff} = g_s \sqrt{S(S+1)} \mu_B / \text{F.U.} \quad (2)$$

where S is the spin angular momentum quantum number and the Lande g factor, g_s has a value of 2. In BaVSe_3 , vanadium is the only element that contributes to magnetism. The spin-only magnetic moment for V^{4+} calculated from equation (2) is $1.73 \mu_B/\text{F.U.}$. The experimental effective magnetic moment is calculated from the C-W fit by using equation (4).

$$\mu_{eff} = 2.827\sqrt{\chi^T} \mu_B/\text{F.U.} \quad (3)$$

Here χ^T is the reciprocal of the slope of the linear fit, k_B is the Boltzmann constant and N_A is the Avogadro number. The paramagnetic μ_{eff} calculated from the C-W linear fit is $1.02 \mu_B/\text{F.U.}$ Yamasaki *et al.* reported the μ_{eff} of BaVSe_3 as $1.42 \mu_B/\text{F.U.}$ [13]. The reduction in the magnetic moment may have occurred due to the disorder induced by the secondary phase BaSe_3 . The C-W temperature (Θ) obtained is 17 K. The positive value of Θ confirms that the material is ferromagnetic below T_C .

In most of the substituted manganites, there is magnetic inhomogeneity at temperatures above T_C , and Griffith initially explained it for disordered magnetic systems [50–52]. It is defined for randomly diluted Ising ferromagnets and this phase appears as ferromagnetic clusters in a paramagnetic matrix above T_C [25]. This theory was first introduced to explain the CMR, magnetic susceptibility, and heat capacity in $\text{La}_{0.7}\text{Ca}_{0.3}\text{MnO}_3$ [53]. The downturn deviation from standard PM behaviour in the inverse susceptibility graph at lower applied fields is the hallmark of the presence of GP [54]. This is due to the short-range FM ordering in the PM region. However, on increasing the applied magnetic field the anomaly in the C-W plot gets softens and attains the classical C-W behaviour [55].

According to the concept of GP the presence of FM clusters with erratically distributed spins in the temperature region $T_C < T < T_G$, where T_C is the C-W temperature and T_G is the Griffiths temperature at which the deviation in χ^{-1} occurs. In the Griffiths phase, spontaneous magnetization is not visible in return of the lack of long-range FM order [56]. Further, Bray extended the concept of GP and at present, the GP is observed in the region $T_C^R < T < T_G$, where T_C^R is the critical temperature of the random FM at which the χ start to diverge [57]. So, GP is found in the area between entirely well-arranged states above T_C^R and the chaotic region below T_G . In general, T_C^R is considered as the C-W temperature, Θ . Hence, GP is defined as the region of the PM phase where the magnetic clusters are generated [58].

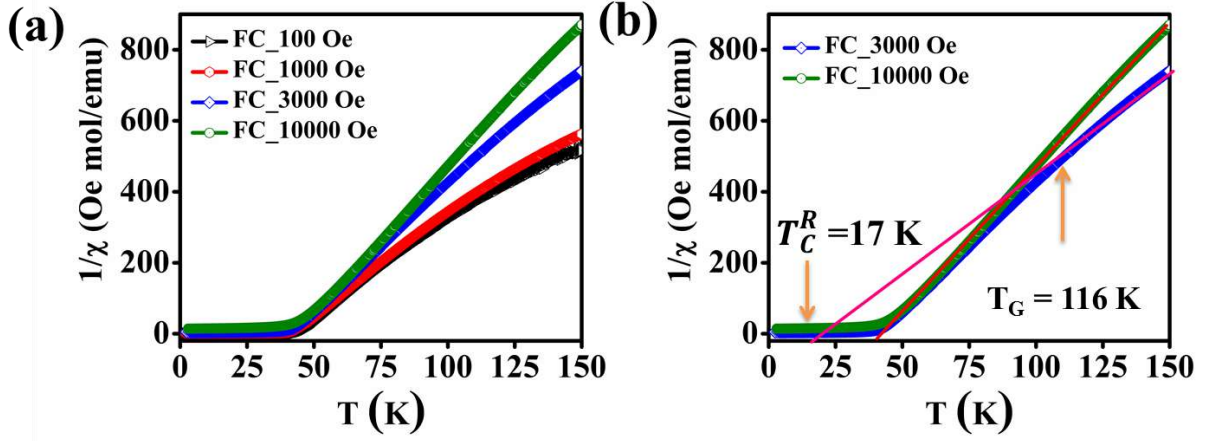


Figure 3.7. (a) C-W plot at different fields (b) C-W plot with linear fit in the PM region

Figure 3.7a shows the χ^{-1} versus T behaviour under the influence of various field strengths of 100 Oe, 1000 Oe, 3000 Oe and 10000 Oe. It can be seen that there is a visible downturn in the variation of χ^{-1} above the temperature T_C . The retention of this anomaly till field strength of 10000 Oe indicates that higher fields are required for its suppression. The linear fit of the C-W plot at fields 3000 Oe and 10000 Oe is depicted in Figure 3.7b. The fit exhibited a T_G value of 116 K and a Θ value of 17 K. The GP is observed in this temperature range. On increasing the field to 10000 Oe the linear fit overlaps with the PM region, confirming the disappearance of the FM cluster in the PM region. This is because the increase in field leads to the magnetization of the spins which are outside the clusters or the masking FM signal by the enhanced PM background [54].

The susceptibility of GP at low applied fields follows a power-law, that is formulated as in equation (3).

$$\frac{1}{\chi} = (T - T_C^R)^{1-\lambda} \quad (3)$$

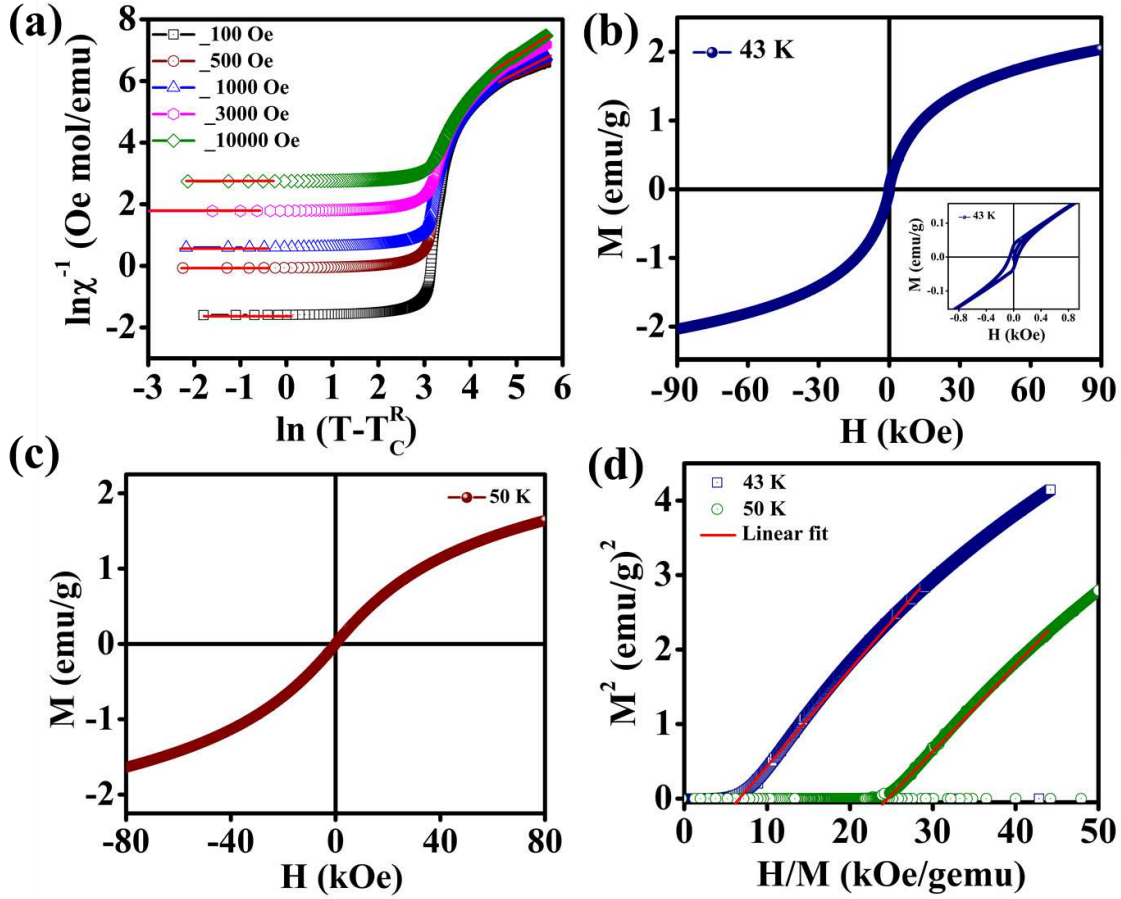


Figure 3.8. (a) GP analysis, (b) M-H loop at 43 K, (c) M-H loop at 50 K, (d) Arrott plot

Here λ is the magnetic susceptibility exponent with a value that lies between 0 and 1, and T_C^R is the random critical temperature. Based on the value of λ , the GP and PM phases can be distinguished. When $\lambda=1$, it corresponds to GP behavior and $\lambda = 0$ is indicative of the PM state. T_C^R is the random critical temperature at which the C-W law yields a λ value close to zero above T_G , and in the present case, the Θ can be considered as T_C^R [59]. In Figure 3.8a linear region of the graph $\ln(\chi^{-1})$ versus $\ln(T-T_C^R)$ is fitted with power law. The λ values for lower and higher fields are calculated from the slope of the fitted straight line in the GP region. The λ_{GP} value reduces from 0.99 to 0.94 when the applied field increases from 100 Oe to 10000 Oe. This is in good agreement with the required range. This confirms the presence of the GP phase in this Zintl phase compound and the high value of λ_{GP} indicates the prominence of GP. The linear fit in the paramagnetic region ($T > T_G$) at higher fields (10000 Oe) shows the reduction in λ_{PM} value to 0.12 and this is due to the decrease in size of the clusters in the PM region under large fields. On increasing the field, the exponent value gets reduced (this is a signature of GP behaviour), as higher fields are needed to remove the ferromagnetic clusters in the paramagnetic matrix. Here, the $M(H)$ measurements above T_C

also show FM-like behaviour with small loops as given in Figures 3.8b and c and its inset. This hysteresis above T_C and below T_G is due to the presence of FM or AFM clusters in the GP regime.

Another major analysis technique used to probe for the presence of the GP phase is the Arrott plot, in which the square of magnetization (M^2) is plotted as a function of H/M [60]. Figure 3.8d shows the Arrott plot at 43 K, which is well above T_C^R (17 K), and below T_G (116 K). The extrapolation of linear fit in the M^2 versus H/M plot exhibits a negative y-intercept. This indicates the absence of spontaneous magnetization (*i.e.* $M_S = 0$) above T_C . The absence of M_S in the GP regime is an indirect characteristic of the Griffiths-like phase in the BVS. Hence, the Arrott plot analysis further confirms the presence of GP in BVS.

The foremost measurement that indicates a glassy-like nature is the AC susceptibility measurement [61]. The AC susceptibility measurements are carried out by varying the temperature from 22 K to 44 K at frequencies of 177 Hz, 555 Hz and 777 Hz. Figure 3.9a depicts the real part of AC susceptibility (χ') vs. temperature at different frequencies. The temperature at which the peak point occurs in the χ' vs. T plot is the freezing temperature (T_f). χ' has a peak at T_f and it shifts towards the right when the frequency is increased. This frequency-dependent shift indicates the glassy nature of the material. The three models introduced to explain the T_f shift are the Arrhenius law, the Vogel-Fulcher (V-F) law and the critical scaling approach [62,63]. When the spin-glass material is cooled from a paramagnetic state, it results in a random configuration initially. The spins will locally optimize their respective orientations over longer length scales, which defines the time-growing correlation length, ξ [64]. Let's assume that τ_0 represents the spin relaxation time, E_a is the activation energy, T_{SG} represents the critical spin glass ordering temperature in which the frequency tends to zero, z is the dynamical critical exponent, ν represents the critical exponent of spin correlation length, $\xi = \left(\frac{T_f - T_{SG}}{T_{SG}}\right)^{-\nu}$ [65]. The relation between relaxation time τ with reduced temperature is given by $\tau = \frac{T_f - T_{SG}}{T_{SG}}$. The τ is associated with the frequency (f) at which the single-spin flip occurs and is given by $\tau = 1/2\pi f$. The relaxation time is obtained from the experiments and the other parameters are calculated by fitting the experimental data with the concerned model.

The first model is the Arrhenius law [66] as represented by equation (4).

$$\tau = \tau_0 \cdot e^{\frac{E_a}{k_B \cdot T_f}} \quad (4)$$

Similarly, the V-F law is defined by the relation represented in equation (5), and the critical scaling approach is given by the relation in equation (6) [67].

$$\tau = \tau_0 \cdot e^{\frac{E_a}{k_B(T_f - T_{SG})}} \quad (5)$$

$$\tau = \tau_0 \left[\frac{T_f}{T_{SG}} - 1 \right]^{z\nu} \quad (6)$$

For spin-glass nature to be evident in a system, the τ_0 must be in the range of 10^{-10} to 10^{-13} seconds and the value of $z\nu$ should be between 4 and 12 [67]. Another parameter of interest is the Mydosh parameter (g) that determines the relative temperature shift of T_f with frequency, that is given by the relation shown in equation (7).

$$g = \frac{\Delta T_f}{T_f \log(\Delta f)} \quad (7)$$

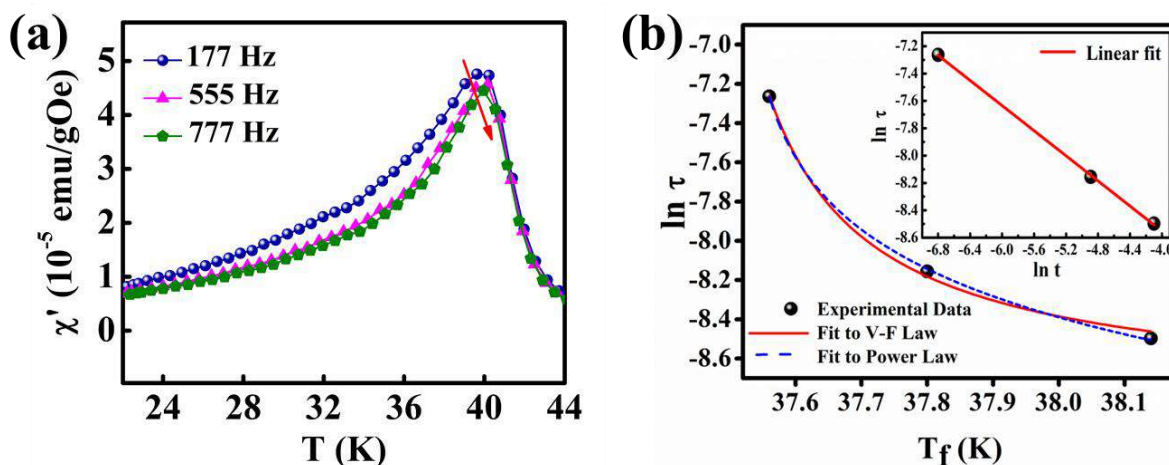


Figure 3.9. Frequency dependence of the (a) real component of AC-magnetic susceptibility, (b) relaxation time τ versus maximum spin-freezing temperature T_f fitted to the VF law (solid line) and power law (dashed line). Inset shows linear fitted $\ln(\tau)$ versus $\ln(t)$, where reduced temperature $t = (T_f - T_{SG})/T_{SG}$ and the solid line is the linear fit

The g value for spin glasses lies between 0.005 and 0.08 and for superparamagnetic materials this value is greater than 2 [68]. If the g value is in between the above two classes of materials, then the system exhibits a cluster glass nature. In the present case, the g value obtained is 0.1, which lies in the range of cluster glasses. The Arrhenius model is omitted because the fit does not converge with the experimental data. Therefore, the other two models are considered and are fitted to the experimental data. Figure 3.9b depicts the $\ln(\tau)$ versus T_f graph and the data are fitted using both the V-F model and the critical power law model. The

parameter values obtained from using the V-F model are $E_a/k_B = 0.243 \pm 0.011$, $T_0 = 37.401 \pm 0.001$ K and $\tau_0 = 1.522 \times 10^{-4}$ s. From the dynamical scaling analysis, T_{SG} and critical exponent $z\nu$ are obtained as 37.518 ± 0.012 K and 0.459 ± 0.008 respectively. From this analysis, the higher value of τ_0 and lower value of $z\nu$ confirm the slower spin-flipping mechanism and the existence of randomly oriented ferromagnetic clusters rather than atomic-level randomness [69].

3.1.2.2. Magnetic studies of BVS

The temperature-dependent magnetization measurements (Figure 3.10a) were conducted on the material BVS and it was observed that the material undergoes a transition from paramagnetic (PM) to ferromagnetic (FM) behaviour at a critical temperature $T_C \sim 41.2$ K (Figure 3.10b), which is consistent with prior findings[70,71]. At extremely low temperatures, a distinct cusp is detected in the ZFC curve of BVS also, which serves as an indication of the glassy behaviour of magnetic materials [71]. According to Zheng et al., the observable difference between the zero field cooling (ZFC) and field cooling (FC) curves is caused by the spin glass or cluster glass properties resulting from magnetic anisotropy or magnetic frustrations [72].

To gain a deeper comprehension of the magnetic properties of the recently produced BVS, we have examined the Curie Weiss plot (Figure 3.10c), which represents the reciprocal of magnetic susceptibility ($1/\chi$) versus T [73]. The calculated value of μ_{eff} is $1.73 \mu_B$, and the experimentally obtained values for θ and μ_{eff} were 17.6 K and $1.74 \mu_B$, respectively. The effective magnetic moment values closely correspond to the predicted value, and the positive indication of the Curie-Weiss temperature indicates the presence of ferromagnetic ordering in the material at low temperatures. The M vs H graph (Figure 3.10d), obtained by varying the applied magnetic field from -9 T to 9 T, at various temperatures both below and above T_C , provides more evidence supporting the transition from PM to FM behaviour.

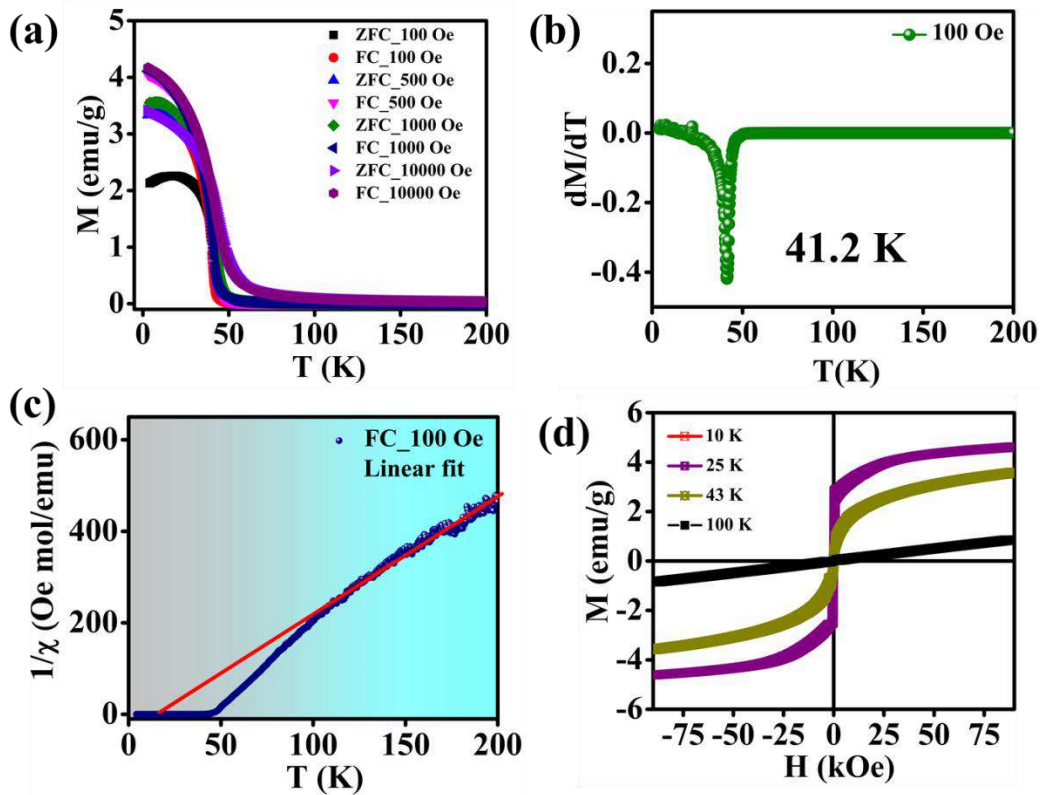


Figure 3.10. (a) Temperature-dependent ZFC and FC magnetization of the sample at different fields, (b) dM/dT versus T plot at an applied field of 100 Oe, (c) Linear fit on the Curie-Weiss plot at 100 Oe, (d) M versus H at different temperatures

Similar to BVS: BS, it was noted that this material exhibits a hysteresis loop even above the critical temperature T_C , as seen in Figure 3.11a. Additionally, the magnetization curve only becomes fully linear at high temperatures. The recent findings indicate that the presence of magnetic inhomogeneity in the PM region of specific systems might be referred to as the Griffiths phase (GP). BVS is classified as a quasi-one-dimensional van der Waals material [74], and the presence of magnetic interaction between the layers can cause this compound to exhibit inhomogeneity. The deviation observed in the $1/\chi$ vs T plot at low fields, as indicated by the Curie-Weiss fit [75] provides additional evidence supporting the existence of the GP phase. The decrease in $1/\chi$, as indicated by the deviation from a linear fit on the Curie-Weiss law (Figure 3.11b), suggests that the transition temperature (T_G) for this material is approximately 117 K. Furthermore, this material exhibits a GP phase within the temperature range of $17.6 \text{ K} < T < 117 \text{ K}$, which is distinct from both the PM and FM phases. We have previously documented that the material BVS, even with the presence of a secondary phase, also demonstrates the GP phase within a similar temperature range. This finding provides more

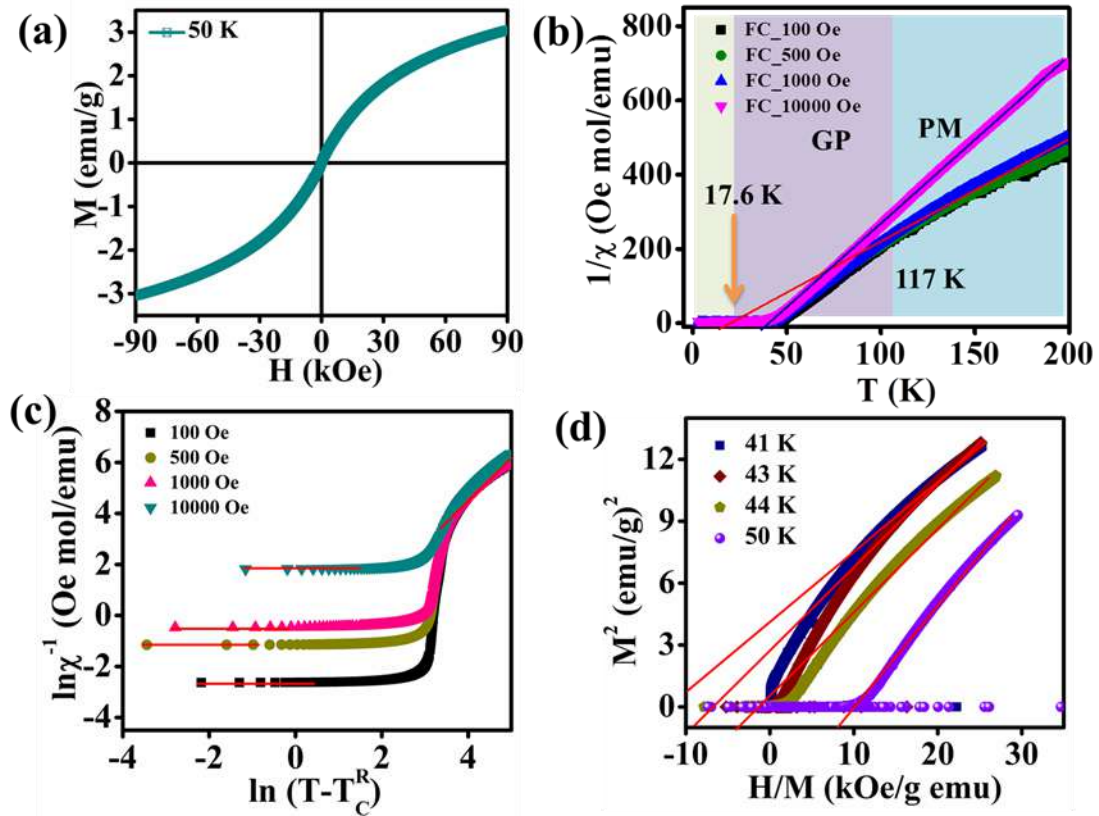


Figure 3.11. (a) Hysteresis loop at 50 K (b) GP analysis by the linear fit on the CW plot at different fields (c) $\ln(1/\chi)$ versus $\ln(T - T_C^R)$ at different fields (d) Arrott plot (M^2 versus H/M) at 41 K, 43 K, 44 K and 50 K

evidence that the GP phase is an inherent characteristic of BVS. It became apparent that when the field was increased to 10000 Oe, the decrease in $1/\chi$ could be attributed to the masking of FM clusters by the PM matrix or the saturation of the FM clusters at higher fields [76]. The power law at low temperatures is employed to analyze the Griffiths singularity, Figure 3.11c shows the plot of $\ln(T - T_C^R)$ versus $\ln\left(\frac{1}{\chi}\right)$ at different magnetic fields (100 Oe, 500 Oe, 1000 Oe, 10000 Oe). The gradient of the linearly fitted curve in the GP region yields a λ value of 0.99, while the linear fit in the PM region yields a λ value of 0.01. This confirms the GP behaviour of the synthesized material. Materials with GP do not exhibit any long-range magnetic ordering above T_C and do not display spontaneous magnetization. The Arrott plot (Figure 3.11d) has a positive y-intercept at a temperature (41 K) below T_C and a negative intercept on the M^2 axis at temperatures above T_C . This observation validates the absence of long-range order and the zero M_s [58]. The magnetic properties of these 1D spin chain materials are determined by the disparity in the strength of inter-chain exchange interaction and intra-chain coupling. The former is two to three orders of magnitude more than the latter

[77]. The unique magnetic properties seen in ABX_3 compounds can be attributed to the complex spin arrangements resulting from frustrated antiferromagnetic interactions and geometric magnetic frustration arising from the ordering of spin chains in the triangular lattice [78].

The magnetic and electrical characteristics of BVS mostly depend on the transition metal V. In octahedral coordination, the V 3d level splits into e_g and t_{2g} multiplets [79]. The t_{2g} energy levels are further split into a lower doublet ($d_{xy}, d_{x^2-y^2}$) and a higher singlet (d_z^2) as a result of the elongation of the VSe_6 octahedra along the crystallographic c axis. Within the V chains, the direct overlap of the closest d_z^2 orbitals results in the formation of a broad conduction band. The adjacent lower doublets indirectly overlap in the same direction, facilitated by the hybridization with intervening Se 3p orbitals. The doublets can divide at lower temperatures because of the orthorhombic distortion, which is referred to as the cooperative Jahn-Teller distortion [80]. The material exhibits structural disorder at low temperatures, which arises from the Jahn-Teller distortion. This disorder is responsible for the emergence of the GP phase and other unique magnetic properties [81].

3.1.3. Magneto-transport studies of BVS

The magnetotransport studies of BVS were conducted using an applied magnetic field of ± 9 T across a temperature range of 3 K to 300 K. In an FM material, overall resistivity is determined by the combination of a magnetic term and a nonmagnetic term. The nonmagnetic term is not dependent on the applied magnetic field strength.

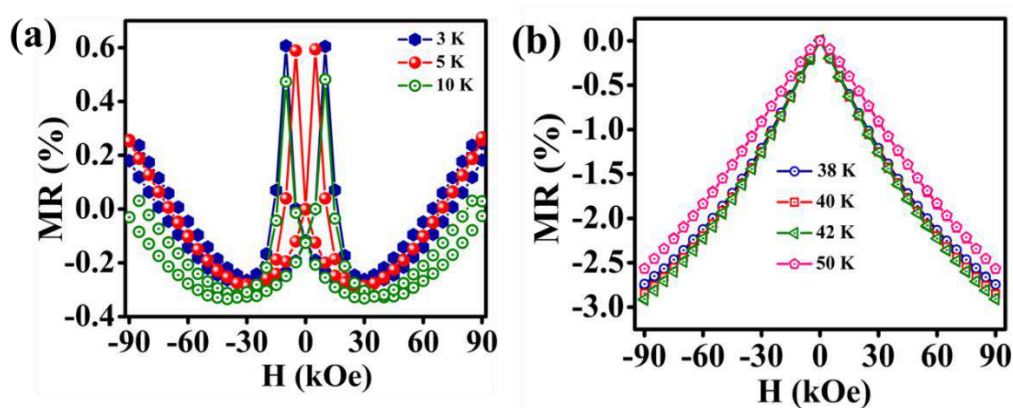


Figure 3.12. MR versus H at (a) 3 K, 5 K and 10 K, (b) 38 K, 40 K, 42 K and 50 K

The term "magnetic" is linked to three phenomena: spin-dependent anisotropy magnetoresistance (AMR), intrinsic domain wall resistance (DWR) and magnon magnetic

resistance (MMR) [78]. The magnetoresistance of a material is quantified by the equation $MR = [R(H) - R(0)]/R(0)$, where $R(H)$ and $R(0)$ represent the resistance of the material at a field H and at zero field respectively [82]. Figures 3.12a and b depict the MR of the synthesized sample at various temperatures. The material exhibits distinct magnetic behaviour when the temperature is increased. At extremely low temperatures, the material demonstrates a remarkable butterfly-shaped magnetoresistance (BMR) when measuring longitudinal resistance. It is worth noting that there have been no previous reports on the BMR in BVS. BMR is commonly encountered in materials exhibiting a hysteresis loop. In this case, the MR exhibits two equal upward resistance states, resulting in the formation of two crossing peaks at a magnetic field strength of 1 Tesla. Prior research indicates that the majority of FM materials exhibit a BMR on a scale of 0.1% [83]. In contrast, the current material demonstrates a BMR on the scale of 0.6% at 3 K, which subsequently decreases with increasing temperature.

The BMR is typically observed in materials having strong crystalline or magnetic anisotropy at low temperatures. However, the specific cause of BMR can differ between different materials. Several studies have examined the behaviour of the BMR in van der Waals materials. Ohta et al. revealed that the observed BMR in the van der Waals Fe_5GeTe_2 FM material is caused by the interaction between magnons and electrons, specifically due to magnetic fluctuations at the Fe(1) site at temperatures around 100 K [83]. The atypical MR observed in van der Waals CrI_3 layers is triggered by the presence of strong or weak electron scattering, leading to fluctuations in magnetization between neighbouring layers [84]. The presence of the BMR in the triangular lattice of AFM Ag_2CrO_2 is observable exclusively when a magnetic field is applied parallel to the c -axis that arises from the pronounced uniaxial anisotropy [85]. The presence of unpaired d^1 electrons in BVS contributes to a range of magnetic phenomena. Specifically, it results in an FM easy axis aligned with the direction of the V chain, which coincides with the crystallographic c -axis. Herak et al. conducted the initial investigation of the magnetic anisotropy in BVS and its corresponding uniaxial symmetry in the FM state [71]. BMR is widely observed in longitudinal resistance measurements and can be explained by Ohm's law. The longitudinal and transverse MR in a magnetic material is determined by the magnetization in the x (M_x) and y (M_y) directions. The current is applied along the x -axis and transverse voltage is measured along the y direction. The equation for the MR in amorphous or polycrystalline magnetic material could be expressed as,

$$R_{xx} = R_1 + A_1 M_x^2 \text{ (longitudinal)} \quad (1)$$

and

$$R_{xy} = R_1 M_z + A_1 M_x M_y \text{ (transverse)} \quad (2)$$

Where R_1 and A_1 are material parameters linked with the anomalous Hall effect and anisotropic MR respectively [86]. When certain magnetic materials are subjected to a strong positive magnetic field and a strong negative magnetic field, they exhibit two magnetizations that are opposing in direction: (M_{x0}, M_{y0}, M_{z0}) and $(-M_{x0}, -M_{y0}, -M_{z0})$. In longitudinal MR the quadratic term $M_x^2(H)$ (equation (1)) leads to two equal states of MR, the switching between $-M_{x0}$ and M_{x0} creates peaks and valleys, that result in BMR. The longitudinal MR studies revealed that as the temperature increases, the material undergoes a transformation from a spin valve-like BMR to a negative MR at 11 K. This change to negative MR is illustrated in Appendix (Figure A.2.1) and Figure 3.11b. The MR investigations conducted on individual crystals of BVS demonstrate a shift in the MR behaviour throughout the temperature range of 8 K to 15 K [9]. The resistivity in BaVS₃ is influenced by the changes in magnetic field, which are dependent on the alignment of E_g spins and their strong interaction with the A_{1g} electrons [9]. FM metals exhibit a negative MR at low temperatures due to electron-spin scattering. The applied magnetic field strengthens the effective field acting on the localized spins, which suppresses spin fluctuations and consequently reduces the material's resistivity [87]. At normal temperatures, the magnetism weakens and shows a positive MR due to the dominance of orbital effects [88]. Nie et al. found that as temperature increases, the magnetic polaron's spin-dependent scattering effect reduces, while the spatial fluctuations of the magnetic polarons rise, leading to positive MR [88]. The significant MR seen in these layered chalcogenides is a result of the inherent magnetic interaction between the E_g and A_{1g} electrons, as well as the crystallographic characteristics. The spin valve like MR [89] has potential applications in magnetic memory devices.

3.1.4. Thermoelectric studies

The efficiency of a TE material is determined by the dimensionless quantity, Figure of merit (ZT), $ZT = \alpha^2 \sigma T / (k_e + k_l)$ [90]. We investigated the thermoelectric properties of two samples: phase pure BVS and a previously reported BVS: BS (impurity phase) [91]. The purpose of our investigation was to gain a better understanding of the influence of impurities on thermoelectric capabilities. The temperature-dependent electrical conductivity of the material was measured between 8 K to 350 K temperature ranges as shown in Figure 3.13a.

The two materials exhibited entirely different electrical responses to the temperature variations. The electrical conductivity of BVS demonstrates the characteristics of a degenerate semiconductor while the material BVS: BS has normal semiconductor properties. The resistivity curve of the phase pure material closely resembles that of the BaVSe₃ single crystals described by Akarp et al. [9] and its order of magnitude was one-order less. We noted that the presence of impurity yielded 10-fold lower electrical conductivity in BVS: BS compared to BVS.

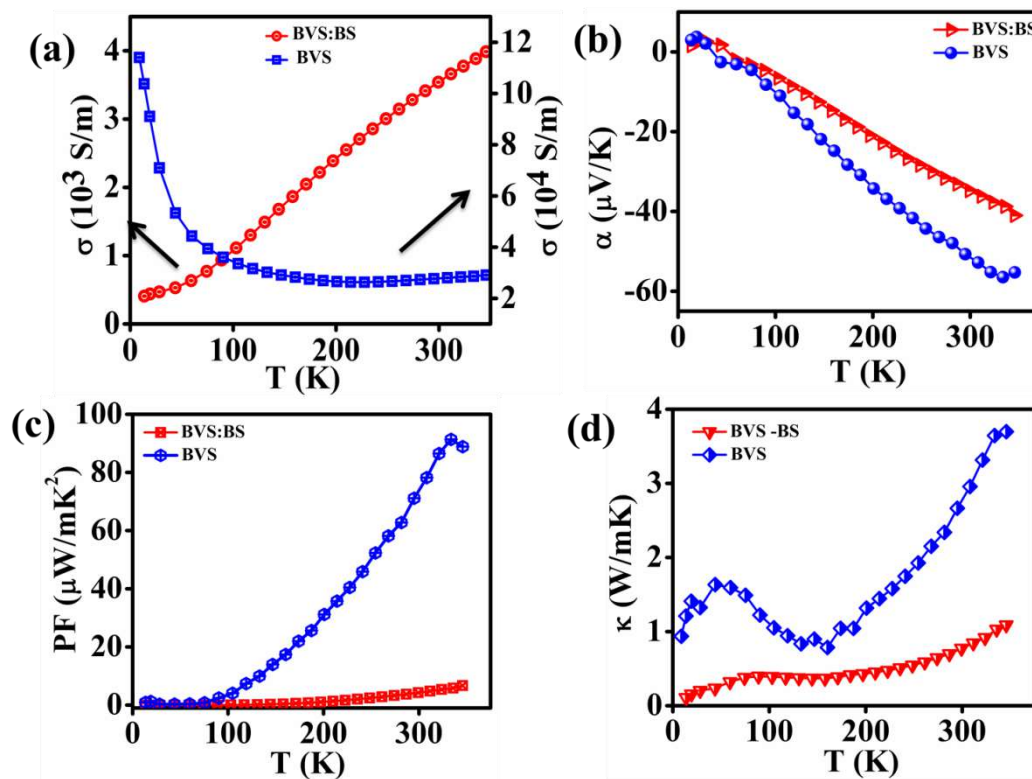


Figure 3.13. Temperature variation of (a) electrical conductivity, (b) Seebeck coefficient, (c) PF and (d) total thermal conductivity of both BVS and BVS: BS

The scattering of electrons at the interfaces and defects disrupt the pathway for electron conduction [92], which consequently leads to a decrease in electrical conductivity in BVS: BS [93]. Both materials have a negative Seebeck coefficient, indicating n-type conduction that increases with temperature (Figure 3.13b). The near room temperature Seebeck coefficient of BVS and BVS: BS was measured as -35 and -14 μ W/mK² respectively. A similar trend in α is observed for both materials resembling the single crystal behaviour. The low-temperature peak at 20 K can be attributed to the combined effects of phonon drag and magnon contribution [94]. The decrease of the Seebeck coefficient in semiconducting materials can be associated with the bipolar diffusion that occurs at higher temperatures [95].

In BVS the σ and α follow the general inverse trend and where as in BVS: BS, the presence of a secondary phase disturbs this trend. Table 3.2 shows the calculated values of carrier concentration mobility and effective mass of the samples at room temperature, the effective mass is calculated by using the Mott equation.

Table 3.2. Experimentally obtained room temperature values of n , μ and m^* of the materials

	n (/cm ³)	μ (cm ² /V.s)	m^* (m_0)
BVS	10^{18}	470	0.001
BVS: BS	10^{17}	55.3	0.0001

The Seebeck coefficient and the carrier concentration of metals and degenerate semiconductors could be linked by the Mott equation [96],

$$\alpha = \frac{8\pi^2 k_B^2 T}{3eh^2} m^* \left(\frac{\pi}{3n}\right)^{2/3} \quad (3)$$

Where n is the carrier concentration, k_B is the Boltzmann constant, e is the electronic charge, h is the Planck constant and m^* is the density of state effective mass. An increase in the energy dependence of either $\mu(E)$ or $n(E)$ can improve the Seebeck coefficient of a material. A higher value of $\mu(E)$ corresponds to a distinct electron scattering mechanism, while a higher value of $n(E)$ can be achieved by manipulating the density of states [97]. The Mott equation reveals that the effective mass of BVS at room temperature is larger than that of BVS: BS. This difference in effective mass is responsible for the increase in thermopower.

The power factor ($PF = \alpha^2 \sigma$) of the materials was determined from the measured σ and S values and plotted against temperature in Figure 3.13c. A peak PF of 92 $\mu\text{W}/\text{mK}^2$ at 335 K was obtained for BVS, surpassing the equivalent BVS: BS values by a significant margin (5.81 $\mu\text{W}/\text{mK}^2$). Figure 3.13d displays the total thermal conductivity vs temperature graph. The materials exhibit distinct thermal conductivity characteristics at extremely low temperatures. The total thermal conductivity is $k = k_e + k_l$, the electronic thermal conductivity can be determined by employing the Wiedemann-Franz law ($k_e = L\sigma T$, where L is the Lorenz number). In a degenerate semiconductor, the relationship between L and the Seebeck coefficient is given by the equation $L = 1.5 + (|\alpha|/116)$ [98], where L is in $10^{-8} \text{W}\Omega/\text{K}^2$ and S

is in $\mu\text{V}/\text{K}$. The temperature-dependent variations in L are shown in Figure 3.14a for both materials. The Lorenz number decreases as the temperature increases, and the BVS: BS material exhibits a greater L value due to bipolar diffusion in the semiconducting materials [99]. The thermal current in thermoelectric materials can be reduced by the phonon-mediated process, electron-electron scattering, and inelastic electron-phonon scattering [100]. Figure 3.14b depicts the computed electronic thermal conductivity, with the dominant contribution to thermal conductivity originating from the phonons (Figure 3.14c).

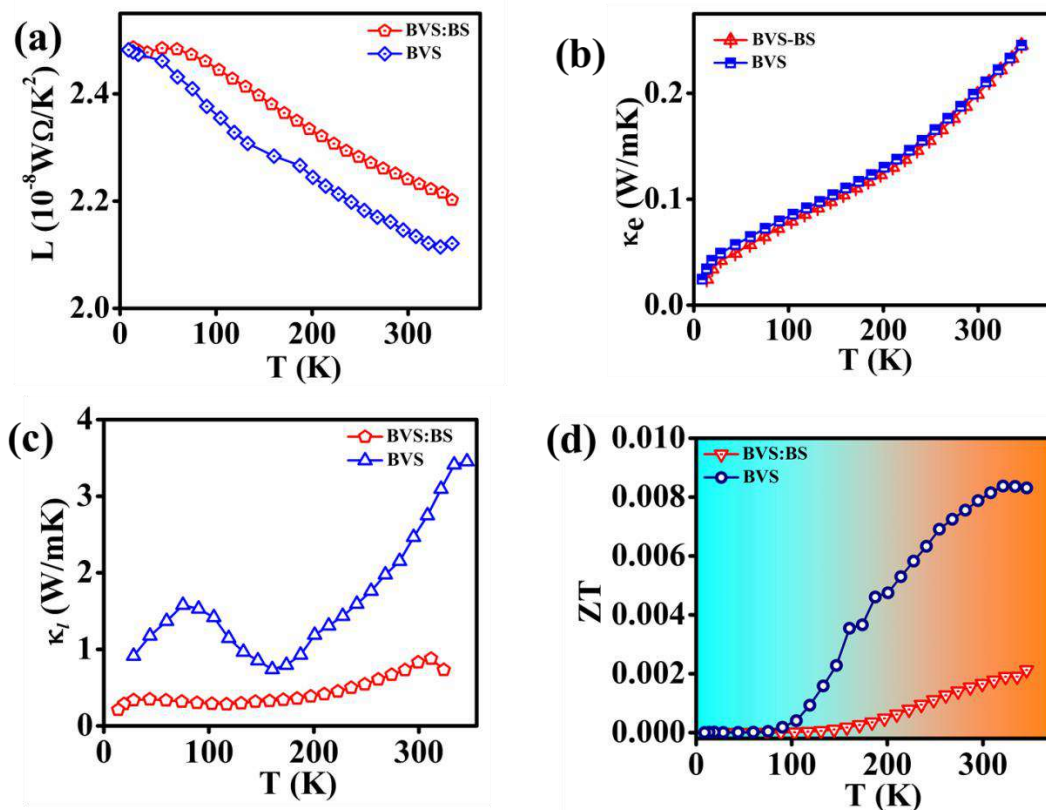


Figure 3.14. (a) Temperature dependence of Lorenz number, (b) electronic thermal conductivity, (c) lattice thermal conductivity and (d) thermoelectric figure of merit of the samples

At extremely low temperatures (< 80 K), BVS exhibited a T^3 dependence on thermal conductivity, which subsequently increases with temperature as a result of phonon generation. The T^3 dependence on k originates from the heat capacity of the phonons [101] and the dominant boundary scattering [102]. In general, the reduction in thermal conductivity of a material is associated with the impurities or imperfections in the crystal structure [103]. The presence of lattice defects and secondary phase in BVS: BS significantly reduces the overall thermal conductivity compared to BVS due to phonon scattering. The presence of a

chain-like structure in the layered TMCs increases the thermal conductivity [104] whereas the existence of an impurity phase may affect the Q1D characteristics of BVS. The thermoelectric figure of merit of the materials was determined based on the measured values of σ , k , and α . Figure 3.14d illustrates the changes in the thermoelectric figure of merit that increased with temperature for both materials. The phase pure BVS exhibits ZT values about four times higher than that of BVS: BS.

3.2. Conclusion

A novel solid-state method was used to synthesize quasi-one-dimensional and phase-pure BVS. The synthesized material displayed a hexagonal crystal structure with the $p63/mmc$ space group. The unidimensionality resulted from the V chains being arranged in a long chain formation along the crystallographic c -axis. The magnetic and thermoelectric properties of pure BVS and the previously described BVS: BS compound were studied to reveal the basic mechanism of a couples thermal and electrical transport. Based on the thorough examination of the magnetic data, it has been shown that this material undergoes a transition from a ferromagnetic to a paramagnetic state at a temperature of ~ 41 K. The observed PM magnetic moment of $1.74 \mu_B$ closely matches the calculated value of $1.73 \mu_B$. BVS exhibits unique magnetic characteristics such as a glassy behaviour, a Griffiths-like phase, and butterfly magnetoresistance at low temperatures, similar to BVS: BS, demonstrating that BVS possesses inherent magnetic properties that arise from its quasi-one-dimensional form and the robust interaction between the electrons in the E_g and A_{1g} energy levels. The glassy nature is probed and confirmed via AC magnetic susceptibility measurements. The thermoelectric investigations validated that electrons were the predominant charge carriers in both materials. However, the higher thermopower in the pure-phase BVS can be attributed to the higher effective mass of the carriers. Additionally, thermal transport is mostly governed by phonons. BVS demonstrated a maximum ZT value of 0.008, which is fourfold greater than that of BVS: BS. FM transition metal chalcogenides show great potential for use in thermoelectric power production and spintronics.

References

- [1] A. Balvanz, S. Baranets, S. Bobev, Synthesis, structural characterization, and electronic structure of the novel Zintl phase Ba_2ZnP_2 , *Acta Cryst.* 76 (2020) 869–873.
- [2] S.M. Kauzlarich, Special issue: Advances in zintl phases, *Materials (Basel)*. 12 (2019) 10–12.
- [3] Y. Tokura, Critical features of colossal magnetoresistive manganites, *Reports Prog. Phys.* 69 (2006) 797–851.
- [4] A.J. Millis, P.B. Littlewood, B.I. Shraiman, Double exchange alone does not explain the resistivity of $\text{La}_{1-x}\text{Sr}_x\text{MnO}_3$, *Phys. Rev. Lett.* 74 (1995) 5144–5147.
- [5] S. Jin, T.H. Tiefel, M. McCormack, R.A. Fastnacht, R. Ramesh, L.H. Chen, Thousandfold Change in Resistivity in Magnetoresistive La-Ca-Mn-O Films, *Science* (80-.). 264 (1994) 413–415.
- [6] A.P. Ramirez, R.J. Cava, J. Krajewski, Colossal magnetoresistance in Cr-based chalcogenide spinels, *Nature*. 386 (1997) 156–159.
- [7] N.J. Poulsen, Rietveld refinement and magnetic properties of polycrystalline $(\text{Ba},\text{K})\text{VSe}_3$ and $\text{BaV}(\text{S}, \text{Se})_3$, *Mater. Res. Bull.* 33 (1998) 313–322.
- [8] A.W. R.A. Gardner, M. Vlasse, Preparation, properties and crystal structure of barium vanadium sulfide, BaVS_3 , *Acta Crystallogr. Sect. B*. 25 (1969) 781–787.
- [9] A. Ana, Stevanovi, Vladan, Herak, Mirta, M. Miljak, N. Bariši, H. Berger, L. Forró, Transport and magnetic properties of BaVSe_3 , *Phy. Rev. B*. 78 (2008) 1–11.
- [10] D. Grieger, L. Boehnke, F. Lechermann, Electronic correlations in vanadium chalcogenides : Electronic correlations in vanadium chalcogenides : BaVSe_3 versus BaVS_3 , *J. Phys. D. Appl. Phys.* 22 (2010) 275601.
- [11] J. Kelber, A.H. Reis, A.T. Aldred, M.H. Mueller, O. Massenet, G. DePasquali, G. Stucky, Structural and magnetic properties of “one-dimensional” barium vanadium triselenide, *J. Solid State Chem.* 30 (1979) 357–364.
- [12] J. Gopalakrishnan, K.S. Nanjundaswamy, Transition metal chalcogenides exhibiting quasi-one-dimensional behaviour, *Bull. Mater. Sci.* 5 (1983) 287–306.

- [13] T. Yamasaki, S. Giri, H. Nakamura, M. Shiga, Magnetism of BaVSe₃, *J. Phys. Soc. Jpn.* 70 (2001) 1768–1771.
- [14] J. Dijkstra, C.F. van Bruggen, C. Haas, R.A.de.Groot, Electronic structure of the half-metallic ferromagnet KCrSe₂, *Phys. Rev. B.* 40 (1989) 7973–7976.
- [15] Sugiyama, Jun, Higemoto, Wataru, Andreica, Daniel, Forslund, O. Kenji, E. Nocerino, M. Månsson, Y. Sassa, R. Gupta, Khasanov, Rustem, Ohta, Hiroto, Nakamura, Hiroyuki, Pressure dependence of ferromagnetic phase boundary in BaVSe₃ studied with high-pressure μ +SR, *Phys. Rev. B.* 103 (2021) 1–10.
- [16] Z. Huang, B. Wolfgang, S. Mankovsky, P. Svitlana, H. Ebert, K.K. Reinhard, Anion substitution effects on structure and magnetism of the chromium chalcogenide Cr₅Te₈ — Part II: Cluster-glass and spin-glass behavior in trigonal Cr_(1+x)Q₂ with basic cells and trigonal Cr_(5+x)Q₈ with superstructures (Q = $\frac{1}{4}$ Te, Se), *J. Solid State Chem.* 179 (2006) 2067–2078.
- [17] F. Sun, Z. Guo, N. Liu, D. Wu, J. Lin, E. Cheng, T. Ying, S. Li, W. Yuan, Cs_{0.9}Ni_{3.1}Se₃: A Ni-Based Quasi-One-Dimensional Conductor with Spin-Glass Behavior, *Inorg. Chem.* 57 (2018) 3798–3804.
- [18] and C.P. H. Lei, E. S. Bozin, K. Wang, Antiferromagnetism in semiconducting KFe_{0.85}Ag_{1.15}Te₂ single crystals, *Phys. Rev. B.* 84 (2011) 3–6.
- [19] B. Wang, Z. Guo, F. Sun, J. Deng, J. Lin, D. Wu, W. Yuan, The transition between antiferromagnetic order and spin-glass state in layered chalcogenides KFeAgCh₂(Ch=Se,S), *J. Solid State Chem.* 272 (2019) 126–130.
- [20] J. A. Mydosh, *Spin Glasses: An Experimental Introduction*, 1993.
- [21] G. Benka, A. Bauer, P. Schmakat, S. Säubert, M. Seifert, P. Jorba, C. Pfleiderer, Interplay of itinerant magnetism and reentrant spin-glass behavior in Fe_xCr_{1-x}, *Cond-Mat.Str-El.* (2020) 1–14.
- [22] S. Mukherjee, R. Ranganathan, P. Anilkumar, P. Joy, Static and dynamic response of cluster glass, *Phy. Rev. B.* 54 (1996) 9267–9274.
- [23] W. Bronger, K. Klepp, P. Müller, The magnetic structure of TlFe₃Te₃, *J. Less-Common Met.* 106 (1985) 301–303.

- [24] P.R. Mandal, T.K. Nath, Evolution of Griffith phase in hole doped double perovskite $\text{La}_{2-x}\text{Sr}_x\text{CoMnO}_6$ ($x= 0.0, 0.5, \text{ and } 1.0$), *Mater. Res. Express.* 2 (2015) 66101.
- [25] P.R.M. and T.K. Nath, Evolution of Griffith phase in hole doped double perovskite $\text{La}_{2-x}\text{Sr}_x\text{CoMnO}_6$ ($x= 0.0, 0.5, \text{ and } 1.0$), *Mater. Res. Express.* 2 (2015) 66101.
- [26] R.B. Griffiths, Nonanalytic Behavior Above the Critical Point in a Random Ising Ferromagnet, *Phys. Rev. Lett.* 23 (1969) 563–890.
- [27] C. K. Ghosh, Mazumdar, and S.M. R. Ranganathan, Griffiths phase behaviour in a frustrated antiferromagnetic intermetallic compound, *Sci. Rep.* 5 (2015) 15801.
- [28] Y. Öner, A. Guler, Evidence of a Griffiths phase in a mixed compound of YFe_2 and YFe_3 Evidence of a Griffiths phase in a mixed compound of YFe_2 and YFe_3 , *J. Appl. Phys.* 141 (2013) 5–8.
- [29] and E.D. J. Burgy, M. Mayr, V. Martin-Mayor, A. Moreo, Colossal Effects in Transition Metal Oxides Caused by Intrinsic Inhomogeneities, *Phys. Rev. Lett.* 87 (2001) 277202.
- [30] A.H.C. Neto, G. Castilla, and B.A. Jones, Non-Fermi Liquid Be, *Phys. Rev. Lett.* 81 (1998) 3531–3534.
- [31] T.S. F. Hulliger, The Crystal Structures of BaSe_2 and BaSe_3 , *Z.Naturforschung-B.* 36b (1981) 14–15.
- [32] S.K. Bux, A. Zevalkink, O. Janka, D. Uhl, S. Kauzlarich, J.G. Snyder, J.P. Fleurial, Glass-like lattice thermal conductivity and high thermoelectric efficiency in $\text{Yb}_9\text{Mn}_4.2\text{Sb}_9$, *J. Mater. Chem. A.* 2 (2014) 215–220.
- [33] J. Kelber, A.H. Reis, A.T. Aldred, M.H. Mueller, O. Massenet, G. DePasquali, G. Stucky, Structural and magnetic properties of “one-dimensional” barium vanadium triselenide, *J. Solid State Chem.* 30 (1979) 357–364.
- [34] V. Ilakovac, M. Guarise, M. Grioni, T. Schmitt, K. Zhou, L. Braicovich, G. Ghiringhelli, V.N. Strocov, H. Berger, Opening of a Peierls gap in BaVS_3 probed by ν L3 edge resonant inelastic x-ray scattering, *J. Phys. Condens. Matter.* 25 (2013) 505602.
- [35] URL: https://srdata.nist.gov/xps/main_search_menu.aspx, (n.d.).

- [36] G. Silversmit, D. Depla, H. Poelman, G.B. Marin, R. De Gryse, An XPS study on the surface reduction of $V_2O_5(001)$ induced by Ar^+ ion bombardment, *Surf. Sci.* 600 (2006) 3512–3517.
- [37] F. Hulliger, T. Siegrist, The Crystal Structures of $BaSe_2$ and $BaSe_3$, *Cryst. Struct. BaSe₂ BaSe₃*. 36b (1981) 14–15.
- [38] M. Motin Seikh, V. Caignaert, O.I. Lebedev, B. Raveau, Cubic structure and canted antiferromagnetism of $CaMn_7O_{12}$ doped with trivalent cations (Fe, Al, Cr), *Solid State Commun.* 180 (2014) 52–55.
- [39] J. Kroder, J. Gooth, W. Schnelle, G.H. Fecher, C. Felser, Observation of spin glass behavior in chiral $Mn_{48}Fe_{34}Si_{18}$ with a β -Mn related structure Observation of spin glass behavior in chiral $Mn_{48}Fe_{34}Si_{18}$ with a β -Mn related structure, *AIP Adv.* 055327 (2019) 0–5.
- [40] V. Kumar, R. Kumar, K. Singh, S.K. Arora, I. V. Shvets, R. Kumar, Evidence for spin glass state of $NdCo_{1-x}Ni_xO_3$ ($x = 0.3-0.5$), *J. Appl. Phys.* 116 (2014) 1–6.
- [41] S. Blundell, *Magnetism in condensed matter*, 2001.
- [42] N. A. Spaldin, *Magnetic materials : fundamentals and applications.*, 2011.
- [43] S. Upadhyay, K. Parekh, B. Pandey, Influence of crystallite size on the magnetic properties of Fe_3O_4 nanoparticles, *J. Alloys Compd.* 678 (2016) 478–485.
- [44] H. Neuendorf, W. Gunßer, Transition from quasi-one-dimensional to spin-glass behaviour in insulating $FeMg_2BO_5$, *J. Magn. Magn. Mater.* 173 (1997) 117–125.
- [45] J. Kelber, A.H. Reis, A.T. Aldred, M.H. Müller, Structural and Magnetic Properties of “One-Dimensional” Barium Vanadium Triselenide, *J. Solid State Chem.* 30 (1979) 357–364.
- [46] Z. Zheng, K. Ren, Z. Huang, Z. Zhu, K. Wang, Z. Shen, J. Yu, Remarkably improved Curie temperature for two-dimensional CrI_3 by gas molecular adsorption: A DFT study, *Semicond. Sci. Technol.* 36 (2021) 1–9.
- [47] S. Wang, J. Yu, Magnetic Behaviors of 3d Transition Metal-Doped Silicane : a First-Principle Study, *J Supercon Nov Magn.* 31 (2018) 2789–2795.

- [48] L. fei CAO, D. XIE, M. xing GUO, H.S. Park, T. Fujita, Size and shape effects on Curie temperature of ferromagnetic nanoparticles, *Trans.of Nonferrous Met.Soc.China.* 17 (2007) 1451–1455.
- [49] R. Revathy, M.R. Varma, K.P. Surendran, *Effect of morphology and ageing on the magnetic properties of nickel nanowires*, Elsevier Ltd, 2019.
- [50] and V.I.C. Y. E. Samoshkina, M. V. Rautskii, E. A. Stepanova, D. S. Neznakhin, N. V. Andreev, Determination of the Existence Region of a Griffith-Like Phase in $\text{Pr}_{1-x}\text{Sr}_x\text{MnO}_3/\text{YSZ}$ Films, *J. Exp. Theor. Phys.* 125 (2017) 1090–1095.
- [51] G.G.L. A.N. Ulyanov, N.E. Pismenova, D.S. Yang, On the doubts related to the local structure, magnetization and Griffiths phase of self-doped $\text{La}_{1-x}\text{MnO}_{3+\delta}$ manganites, *J. Alloy. Compd.* 618 (2015) 607–608.
- [52] R.M. Eremina, I. V. Yatsyk, Y.M. Mukovskii, and A.L. H. A. Krug Von Nidda, Determination of the region of existence of ferromagnetic nanostructures in the paraphase of $\text{La}_{1-x}\text{Ba}_x\text{MnO}_3$ by the EPR method, *JETP Lett.* 85 (2007) 51–54.
- [53] M.B. Salamon, P. Lin, S.H. Chun, Colossal magnetoresistance is a Griffiths singularity, *Phys. Rev. Lett.* 88 (2002) 1972031–1972034.
- [54] E.D. A. Tozri, Structural and magnetotransport properties of (La, Pr)-Ba manganites, *J. Alloy. Compd.* 783 (2019) 718e728.
- [55] P. Tong, B. Kim, D. Kwon, T. Qian, S.I. Lee, S.W. Cheong, B.G. Kim, Griffiths phase and thermomagnetic irreversibility behavior in slightly electron-doped manganites $\text{Sm}_{1-x}\text{Ca}_x\text{MnO}_3$ ($0.80 \leq x \leq 0.92$), *Phy. Rev. B.* 77 (2008) 1–7.
- [56] S.O. Manjunatha, A. Rao, P. Poornesh, W.J. Lin, Y.K. Kuo, Magnetic inhomogeneity and Griffiths phase in Bi substituted $\text{La}_{0.65-x}\text{Bi}_x\text{Ca}_{0.35}\text{MnO}_3$ manganites, *Phys. B Condens. Matter.* 498 (2016) 82–91.
- [57] A.J. Bray, M.A. Moore, On the eigenvalue spectrum of the susceptibility matrix for random spin systems, *J. Phys. C Solid State Phys.* 15 (1982).
- [58] H.S. Nair, D. Swain, N. Hariharan, S. Adiga, C. Narayana, S. Elizabeth, Griffiths phase-like behavior and spin-phonon coupling in double perovskite $\text{Tb}_2\text{NiMnO}_6$, *J. Appl. Phys.* 110 (2011) 123919.

- [59] and A.K.N. M K. Majee, P. A. Bhoje, Griffiths phase in antiferromagnetic $\text{CuCr}_{0.95}\text{Ti}_{0.05}\text{O}_2$, *J. Magn. Magn. Mater.* 485 (2019) 112–117.
- [60] I.N. Bhatti, I.N. Bhatti, R.N. Mahato, M.A.H. Ahsan, Magnetic behavior, Griffiths phase and magneto-transport study in 3d based nano-crystalline double perovskite $\text{Pr}_2\text{CoMnO}_6$, *Phys. Lett. A.* 383 (2019) 2326–2332.
- [61] C.A.M. Mulder, A.J. Van Duynveldt, J.A. Mydosh, Frequency and field dependence of the ac susceptibility of the AuMn spin-glass, *Phy. Rev. B.* 25 (1982) 515–518.
- [62] G. Balaji, G. Wilde, J. Weissmüller, N.S. Gajbhiye, V.K. Sankaranarayanan, Spin-glass-like transition in interacting MnFe_2O_4 nanoparticles, in: *Phys. Stat. Sol(B)*, (2004) 1589–1592.
- [63] G.F. Goya, H.R. Rechenberg, V. Sagredo, Study of the spin-glass transition in $\text{FeCr}_{2x}\text{In}_{2-2x}\text{S}_4$ thiospinel, *J. Magn. Magn. Mater.* 226–230 (2001) 1298–1299.
- [64] E. Vincent, V. Dupuis, Spin glasses: Experimental signatures and salient outcomes, in: *Springer Ser. Mater. Sci.*, (2018) 31–56.
- [65] P. Bag, K. Somesh, R. Nath, A study of cluster spin-glass behaviour at the critical composition $\text{Mn}_{0.73}\text{Fe}_{0.27}\text{NiGe}$, *J. Magn. Magn. Mater.* 497 (2020) 165977.
- [66] J. Souletie, J.L. Tholence, Critical slowing down in spin glasses and other glasses: Fulcher versus power law, *Phy. Rev. B.* 32 (1985) 516–519.
- [67] P. Bag, P.R. Baral, R. Nath, Cluster spin-glass behavior and memory effect in $\text{Cr}_{0.5}\text{Fe}_{0.5}\text{Ga}$, *Phys. Rev. B.* 98 (2018) 1–10.
- [68] R. Yadav, S. Elizabeth, Magnetic frustration and dielectric relaxation in insulating $\text{Nd}_2\text{NiMnO}_6$ double perovskites, *J. Appl. Phys.* 117 (2015) 053902.
- [69] M. Viswanathan, P.S.A. Kumar, Observation of reentrant spin glass behavior in $\text{LaCo}_{0.5}\text{Ni}_{0.5}\text{O}_3$, *Phys. Rev. B - Condens. Matter Mater. Phys.* 80 (2009) 3–6.
- [70] N.J. Poulsen, Rietveld refinement and magnetic properties of polycrystalline $(\text{Ba},\text{K})\text{VSe}_3$ and $\text{BaV}(\text{S},\text{Se})_3$, *Mater. Res. Bull.* 33 (1998) 313–322.
- [71] M. Herak, M. Miljak, A. Akrap, L. Forró, H. Berger, Magnetic anisotropy of paramagnetic and ferromagnetically ordered state of single crystal BaVSe_3 , *J. Phys.*

- Soc. Japan. 77 (2008) 1–4.
- [72] N. Thi Dung, Y. Pham, D.S. Lam, N. Van Dang, A.G. Gamzatov, A.M. Aliev, D.H. Kim, S.C. Yu, T.D. Thanh, Critical behavior of polycrystalline $\text{Pr}_{0.7}\text{Ca}_{0.1}\text{Sr}_{0.2}\text{MnO}_3$ exhibiting the crossover of first and second order magnetic phase transitions, *J. Mater. Res. Technol.* 9 (2020) 12747–12755.
- [73] A. Tozri, E. Dhahri, Structural and magnetotransport properties of (La, Pr)-Ba manganites, *J. Alloy. Compd.* 783 (2019) 718–728.
- [74] C.P. Sujith, S. Joseph, T. Mathew, V. Mathew, Ab initio investigation of the structural and electronic properties of tantalum thallium chalcogenides TaTlX_3 (X = S, Se), *J. Solid. State. Chem.* 315 (2023) 3–7.
- [75] I. Noor, I. Noor, R. Nath, M.A.H. Ahsan, Magnetic behavior, Griffiths phase and magneto-transport study in 3d based nano-crystalline double perovskite $\text{Pr}_2\text{CoMnO}_6$, *Phys. Lett. A.* 383 (2019) 2326–2332.
- [76] R. Revathy, M.R. Varma, K.P. Surendran, Observation of Cluster Glass and Griffiths-like Phase in Fe_3O_4 Nanostructures, *Phys. Status Solidi.* 2000341 (2021) 1–12.
- [77] L. Duan, X. Wang, J. Zhang, J. Zhao, L. Cao, Synthesis, structure, and properties of $\text{Ba}_9\text{Co}_3\text{Se}_{15}$ with one-dimensional spin chains Synthesis, structure, and properties of $\text{Ba}_9\text{Co}_3\text{Se}_{15}$ with one-dimensional spin chains, *Chinese Phys. B.* 29 (2020) 1–6.
- [78] A.P. Mihai, J.P. Attané, A. Marty, P. Warin, Y. Samson, Electron-magnon diffusion and magnetization reversal detection in FePt thin films, *Phys. Rev. B - Condens. Matter Mater. Phys.* 77 (2008) 1–4.
- [79] A.M. and M.T. M. Nakamura, Sekiyama, A.H. Namatame, A. Fujimori, H. Yoshihara, T. Ohtani, Metal-semiconductor transition and Luttinger-liquid behavior in quasi-one-dimensional BaVS_3 studied by photoemission spectroscopy, *Phys. Rev. B.* 49 (1994) 16193–16201.
- [80] M.T. M. Nakamura, A. Sekiyama, H. Namatame, A. Fujimori, H. Yoshihara, T. Ohtani, A. Misu, Metal-semiconductor transition and Luttinger-liquid behavior in quasi-one-dimensional BaVS_3 studied by photoemission spectroscopy, *Phys. Rev. B.* 49 (1994).

- [81] P.R. Mandal, T.K. Nath, Evolution of Griffith phase in hole doped double perovskite, *Mater. Res. Express.* 2 (2015) 66101.
- [82] D.D. Sarma, E. V. Sampathkumaran, S. Ray, R. Nagarajan, S. Majumdar, A. Kumar, G. Nalini, T.N. Guru Row, Magnetoresistance in ordered and disordered double perovskite oxide, $\text{Sr}_2\text{FeMoO}_6$, *Solid State Commun.* 114 (2000) 465–468.
- [83] T. Ohta, M. Tokuda, S. Iwakiri, K. Sakai, B. Driesen, Y. Okada, K. Kobayashi, Y. Niimi, Butterfly-shaped magnetoresistance in van der Waals ferromagnet Fe_5GeTe_2 , *AIP Adv.* 11 (2021).
- [84] D.R. Klein, D. MacNeill, J.L. Lado, D. Soriano, E. Navarro-Moratalla, K. Watanabe, T. Taniguchi, S. Manni, P. Canfield, J. Fernández-Rossier, P. Jarillo-Herrero, Probing magnetism in 2D van der Waals crystalline insulators via electron tunneling, *Science* (80). 360 (2018) 1218–1222.
- [85] H. Taniguchi, M. Watanabe, M. Tokuda, S. Suzuki, E. Imada, T. Ibe, T. Arakawa, H. Yoshida, H. Ishizuka, K. Kobayashi, Y. Niimi, Butterfly-shaped magnetoresistance in triangular-lattice antiferromagnet Ag_2CrO_2 , *Sci. Rep.* 10 (2020) 1–7.
- [86] H.T. Wu, T. Min, Z.X. Guo, X.R. Wang, On universal butterfly and antisymmetric magnetoresistances, *Front. Phys.* 10 (2022) 1–10.
- [87] H. Yamada, S. Takada, Negative Magnetoresistance of Ferromagnetic Metals due to Spin Fluctuations, *Prog. Theor. Phys.* 48 (1972) 1828–1848.
- [88] T. Nie, W. Zhao, K.L. Wang, Engineering Magnetoresistance in $\text{Mn}_x\text{Ge}_{1-x}$ System for Magnetic Sensor Application, in: *Magn. Sensors - Dev. Trends Appl.*, 2017: pp. 65–87.
- [89] S. Singh, R. Rawat, S.E. Muthu, S.W. Dâsouza, E. Suard, A. Senyshyn, S. Banik, P. Rajput, S. Bhardwaj, A.M. Awasthi, R. Ranjan, S. Arumugam, D.L. Schlagel, T.A. Lograsso, A. Chakrabarti, S.R. Barman, Spin-valve-like magnetoresistance in Mn_2NiGa at room temperature, *Phys. Rev. Lett.* 109 (2012) 1–5.
- [90] H. Wang, H. Hu, N. Man, C. Xiong, Y. Xiao, X. Tan, G. Liu, J. Jiang, Band flattening and phonon-defect scattering in cubic SnSe-AgSbTe_2 alloy for thermoelectric enhancement, *Mater. Today Phys.* 16 (2021) 100298.

- [91] C. V. Devan, A.A. Nair, R. Revathy, B. Deb, M.R. Varma, Exotic magnetic properties in Zintl phase BaVSe₃: a theoretically supported experimental investigation, *New J. Chem.* 47 (2022) 97–108.
- [92] K. Bin Masood, U. Farooq, J. Singh, Evolution of the structural, dielectric and electrical transport properties of Bi₂Te₃ nano-sticks synthesized via polyol and solvothermal routes, *Phys. B Condens. Matter.* 588 (2020) 412183.
- [93] J.D. Musah, A.M. Ilyas, A. Novitskii, I. Serhiienko, K.O. Egbo, G. Saianand, V. Khovaylo, S. Kwofie, K.M. Yu, V.A.L. Roy, Effective decoupling of seebeck coefficient and the electrical conductivity through isovalent substitution of erbium in bismuth selenide thermoelectric material, *J. Alloys Compd.* 857 (2021).
- [94] L.F. Ana Akrap, Vladan Stevanović, Mirta Herak, Marko Miljak, Neven Barišić, Helmuth Berger, Transport and magnetic properties of BaVSe₃, *Phys. Rev. B - Condens. Matter Mater. Phys.* 78 (2008) 1–11.
- [95] P.G. Burke, B.M. Curtin, J.E. Bowers, A.C. Gossard, Minority carrier barrier heterojunctions for improved thermoelectric efficiency, *Nano Energy.* 12 (2015) 735–741.
- [96] S. Watanabe, M. Ohno, Y. Yamashita, T. Terashige, H. Okamoto, J. Takeya, Validity of the Mott formula and the origin of thermopower in π -conjugated semicrystalline polymers, *Phys. Rev. B.* 10 (2019) 1–7.
- [97] O. Ivanov, M. Yaprntsev, Variable-range hopping conductivity in Lu-doped Bi₂Te₃, *Solid State Sci.* 76 (2018) 111–117.
- [98] A. Das, A. Chauhan, V. Trivedi, M. Tiadi, R. Kumar, M. Battabyal, D.K. Satapathy, Effect of iodine doping on the electrical, thermal and mechanical properties of SnSe for thermoelectric applications, *Phys.Chem.Chem.Phys.* 23 (2021) 4230–4239.
- [99] Z. Luo, J. Tian, S. Huang, M. Srinivasan, J. Maassen, Y.P. Chen, X. Xu, Large Enhancement of Thermal Conductivity and Lorenz Number in Topological Insulator Thin Films, *ACS Nano.* 12 (2018) 1120–1127.
- [100] S.D. Sawtelle, M.A. Reed, Temperature-dependent thermal conductivity and suppressed Lorenz number in ultrathin gold nanowires, *Phys. Rev. B.* 99 (2019) 1–11.

- [101] M. Yao, C. Opeil, S. Wilson, M. Zebarjadi, Experimental determination of phonon thermal conductivity and Lorenz ratio of single-crystal bismuth telluride, *MRS Commun.* 7 (2017) 922–927.
- [102] Z. Tian, K. Esfarjani, J. Shiomi, A.S. Henry, G. Chen, On the importance of optical phonons to thermal conductivity in nanostructures, *Appl. Phys. Lett.* 99 (2011) 1–4.
- [103] D.T. Morelli, J.P. Heremans, G.A. Slack, Estimation of the isotope effect on the lattice thermal conductivity of group IV and group III-V semiconductors, *Phys. Rev. B - Condens. Matter Mater. Phys.* 66 (2002) 1953041–1953049.
- [104] J. Philip, P.D. Shima, B. Raj, Enhancement of thermal conductivity in magnetite based nanofluid due to chainlike structures, *Appl. Phys. Lett.* 91 (2007) 1–4.

Chapter 4

The synthesis, magnetic and thermoelectric studies of CoMSe_2 ($\text{M} = \text{Ni, Fe}$)

A deeper examination of novel materials for energy harvesting and spintronics is necessary to develop technologically advanced solutions that enhance energy efficiency and offer greater versatility, therefore contributing to the sustainability of electrical power. A multidisciplinary strategy might lead to more environmentally friendly and energy-efficient electronics [1]. The inherent magnetic and electronic properties classify the spintronics materials as magnetic metals, diluted magnetic semiconductors (DMS) and topological insulators (TI) and the integration of magnetism on semiconducting materials opens up potential applications [2]. Transition metal chalcogenides (TMCs) have some inherent physical properties that make them promising candidates for catalysis [3], energy storage applications like batteries and supercapacitors [4], 2D TMC semiconductors in electronics, thermoelectrics and spintronics [5,6]. TMCs exhibit noticeable magnetic, electronic and thermoelectric properties based on the combinations of transition metals and chalcogenides [7]. In transition metals, due to the crystalline field, the 3d orbitals will split into t_{2g} and e_g subbands which results in the low spin and high spin arrangement of electrons in these subbands resulting in various magnetic orderings and electronic properties [8]. The doping or the substitution at the TM site by magnetic ions can alter the magnetic and electronic properties of the material to a noticeable extent. TMCs were known for the existence of different frustrated magnetic states like spin glass (SG), cluster glass [9] and Griffiths-like phase (GP) [10]. The origin of GP varies from material to material [8,9], but the major reason is the spreading of short-range FM clusters in magnetically tangled PM matrix [11]. The GP phase existed in a temperature range $T_C < T < T_G$, where T_C is the Curie temperature and T_G is the Griffiths temperature (the temperature at which the deviation from Curie Weiss law begins). There are some recent reports on the existence of GP in antiferromagnetic (AFM) materials such as FeCl_2 [12], $\text{Ca}_3\text{CoMnO}_6$ [13], $\text{GdFe}_{0.17}\text{Sn}_2$ [14] and rare-earth-based manganites [15].

Chalcogenides have found major applications in thermoelectric power generation also [16,17]. Most of the traditional thermoelectric materials are tellurides due to the heaviest tellurium reduces the thermal conductivity and has the desired electrical conductivity better Seebeck coefficient [18,19]. The lower abundance and toxicity of tellurium searched for new materials having selenium or sulfur as chalcogen. The higher availability, low cost and low

toxicity of these materials are advantageous for thermoelectric applications [20] as the development of reliable and nonpolluting energy is our major concern. Reduction of fossil-based energy resources needs alternative methods for power generation [21] and thermoelectric power generation is a viable option with a wide range of advantages. Thermoelectric devices convert unusable heat energy to useful electrical energy [22]. The performance of TE is quantified ZT [23,24], the high ZT requires a large α , σ and low k . These transport characteristics depend on interconnected material properties and several parameters must be enhanced to maximize ZT. Ternary chalcogenides have been widely reported as promising thermoelectric materials [25–28] due to their lower thermal conductivity. The CoMSe_2 ($\text{M}=\text{Ni, Fe}$) is a bimetallic ternary chalcogenide and it finds application in electrochemical energy storage fields as an electrode material [29]. The previous reports on these selenides propose solvothermal and hydrothermal synthesis methods [29,30]. In the present investigation, the class of materials CoMSe_2 ($\text{M} = \text{Ni, Fe}$) was synthesized by direct melting method from the constituent elements with a newly adopted heat treatment. The effect of the magnetic and thermoelectric properties of the material on the substitution of Fe at the Ni site was investigated from cryogenic temperature to near room temperature.

Polycrystalline CoMSe_2 ($\text{M} = \text{Ni, Fe}$) was synthesized (chapter 2) through melting of the corresponding elements concerning the stoichiometry. The obtained ingots were subjected to various analyses that include structural, morphological, magnetic and transport properties.

4.1. Results and discussion

4.1.1. Structural and compositional investigation

The phase and purity of the synthesized samples were examined by powder XRD measurements and Figure 4.1a shows the Rietveld refinement of CNS with a goodness of fit = 2. All the diffraction peaks of the sample were indexed to the hexagonal structure (JCPDS no: 70-2851) [31] with space group $P63/mmc$ (194) and the obtained lattice parameters were $a = b = 3.63 \text{ \AA}$, $c = 5.33 \text{ \AA}$. Figure 4.1b shows the crystal structure of CNS in which Co and Ni occupy the octahedral site [29]. The phase of the sample CFS (Figure 4.1c) was identified as orthorhombic [JCPDS no: 01-088-2293, space group $pca21$] with lattice parameters $a = 5.38 \text{ \AA}$, $b = 5.39 \text{ \AA}$, $c = 5.37 \text{ \AA}$ and Rietveld refined with a goodness of fit ~ 2.1 . Figure 4.1d shows the obtained crystal structure of the material where the TMs occupy octahedral sites. No impurity phases were detected in both CNS and CFS.

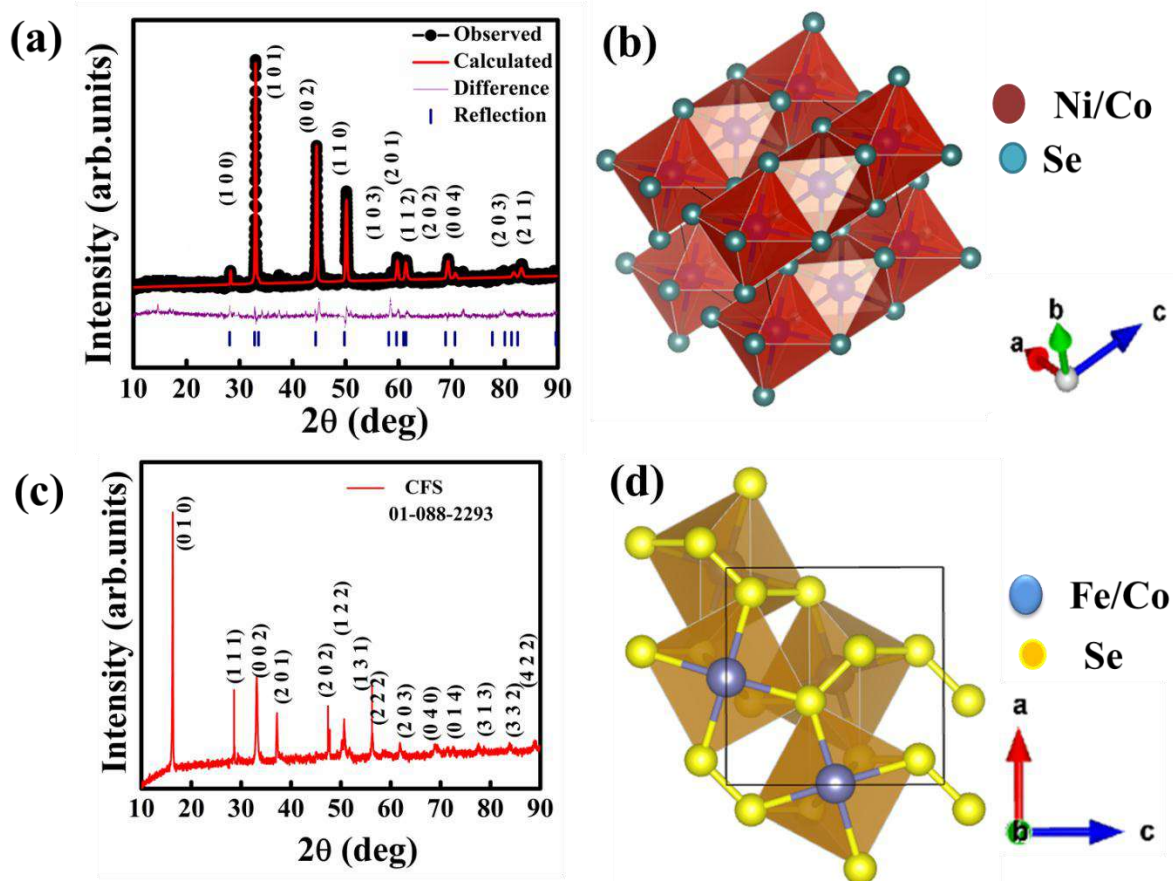


Figure 4.1. (a), (b) & (c), (d) XRD pattern and crystal structure of CNS & CFS respectively

The X-ray photoelectron spectrum (XPS) of CNS and CFS was carried out to reveal the surface composition and oxidation states of the constituent elements. Figure 4.2 (a)- (c), (d-f) shows the high-resolution spectra of the Co, Ni, Se of the sample CNS and Co, Fe, Se of CFS respectively. The binding energies were corrected by C1s with reference energy 284.8 eV. We have fitted Co 2p spectra in CNS with 3 curves, the peaks at 781.74 eV and 797.32 eV correspond to Co^{2+} [31], and the peak at 802.77 eV indicates the associated satellite peak. In the Ni 2p spectrum (Figure 4.2b) the peaks at 856.08 eV and 873.75 eV correspond to the Ni $2p_{3/2}$ and Ni $2p_{1/2}$ [32] respectively, which confirms the Ni^{2+} oxidation state. The peaks at 879.72 eV and 861 eV indicate the satellite peaks [32]. The high-resolution spectrum of Se 3d shows (Figure 4.2c) two peaks at 54.54 eV and 59.03 eV, which were assigned to the Se^{2-} of Se $3d_{5/2}$ and Se-O bonding due to surface oxidation respectively. For CFS, the Co^{2+} peaks were observed at 781 eV ($\text{Co}2p_{3/2}$) and 796.4 eV ($\text{Co}2p_{1/2}$), shake-up satellite peaks were also found at 786 eV and 802 eV (Figure 3.2d) near the main peaks [33].

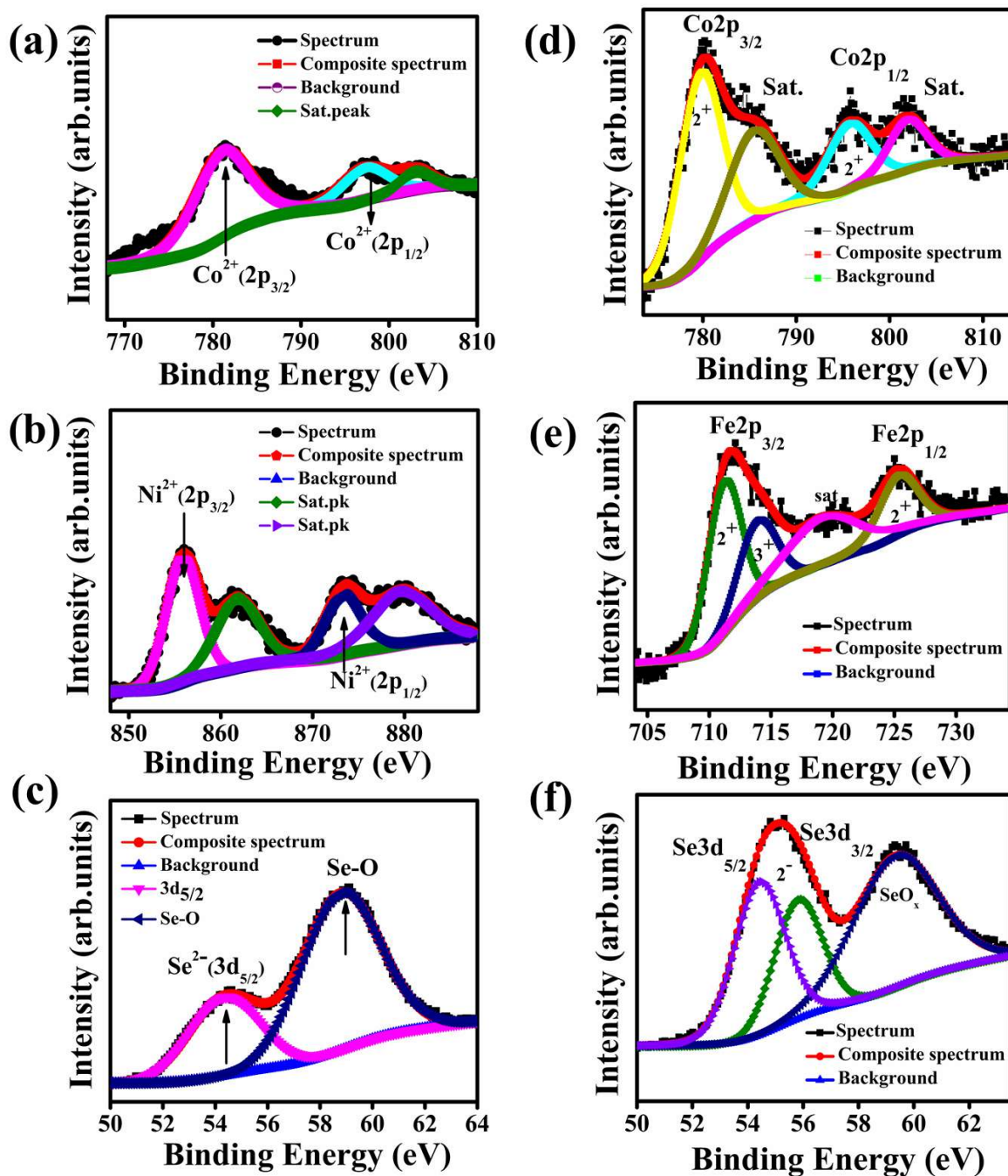


Figure 4.2. (a)-(c) Higher resolution spectra of Co, Ni, Se of CNS and (d)-(f) 6Co, Fe, Se of CFS

Figure 4.2e shows the deconvoluted spectra of Fe 2p and it is composed of three peaks. On comparing with the XPS standard data the binding energies 711.2 eV ($2p_{3/2}$) and 725.3 eV ($2p_{1/2}$) correspond to Fe^{2+} and 714.2 eV for Fe^{3+} ($2p_{1/2}$) [32]. In the case of CFS, the peaks at 54.4 eV and 55.8 eV corresponded to Se $3d_{5/2}$ and Se $3d_{3/2}$ respectively, the broad peak at 59.4 eV was associated with surface oxidation [34]. The XPS analysis demonstrates that the oxidation states of the constituent elements were consistent with the actual composition of the materials. The morphology, local composition and homogeneity of the materials were

examined through SEM, SEM-EDAX, HRTEM, and TEM-EDS. The surface morphology of the samples was analyzed using scanning electron microscopy (SEM). Figure 4.3a and b shows the SEM images of the pellets of CNS and CFS, respectively, at a length scale of 10 μm (inset figures at 2 μm). The compactness of the melted ingots was confirmed through SEM analysis.

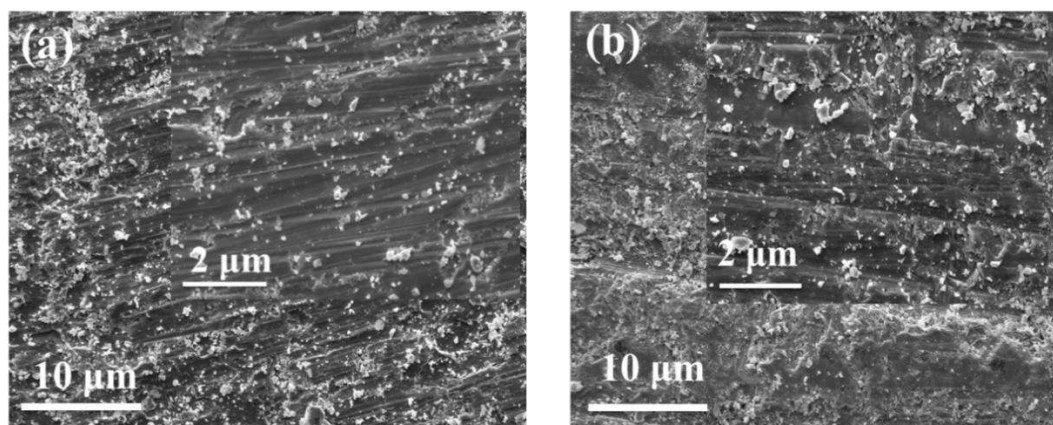


Figure 4.3. SEM images of (a) CNS and (b) CFS on a length scale of 10 μm (inset figures at 2 μm)

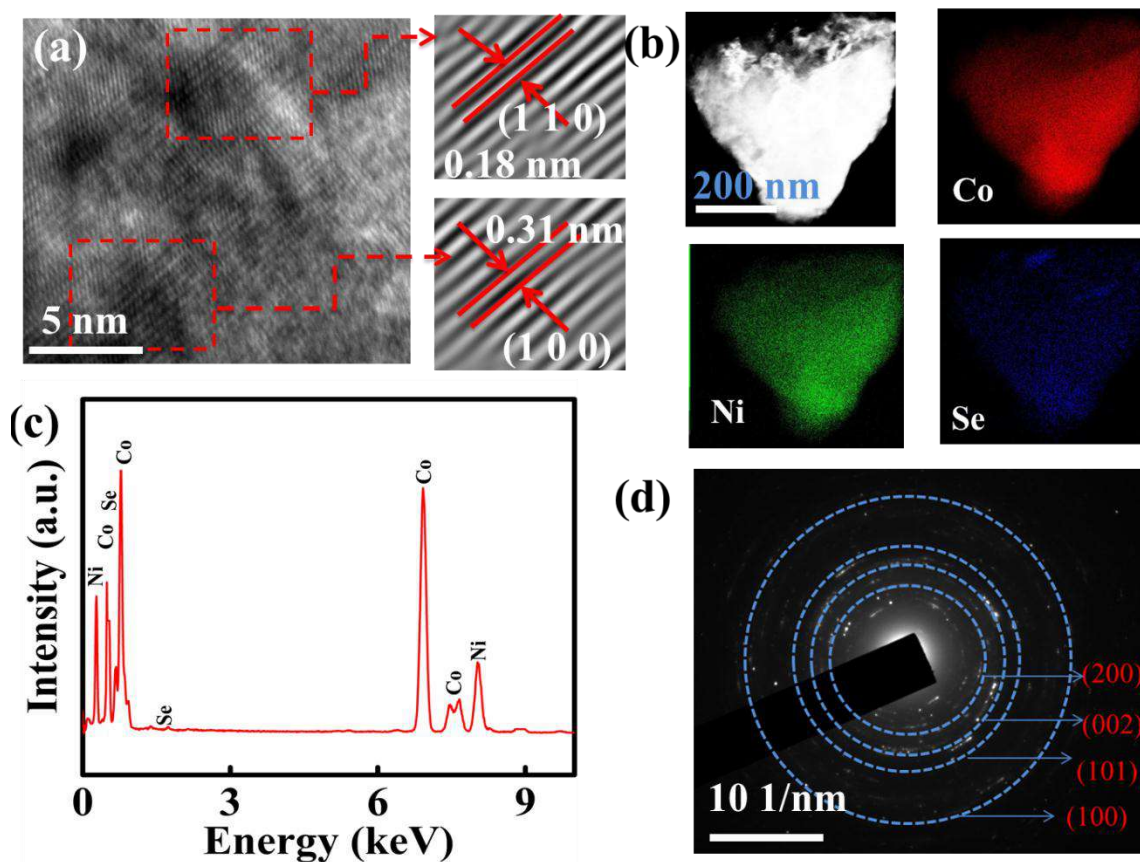


Figure 4.4. (a) HRTEM image of CNS, (b) Elemental mapping of CNS, (c) TEM-EDS spectra of the sample (d) SAED pattern of CNS

The crystalline nature of the sample CNS was further investigated through HRTEM (Figure 4.4a) by measuring the measured d spacing and the measured values were compared with the d spacing measured using XRD data. The planes (1 1 0) and (1 0 0) correspond to the XRD calculated d spacing 0.18 nm and 0.31 nm respectively were observed in SAD patterns. Figure 4.4b reveals the homogeneity of the sample on a nanometer scale through elemental mapping of constituent elements Co, Ni and Se, Figure 4.4c shows the associated EDS spectrum. The ring SAED pattern (Figure 4.4d) confirms the polycrystallinity of CNS and it is in agreement with the observations made using XRD.

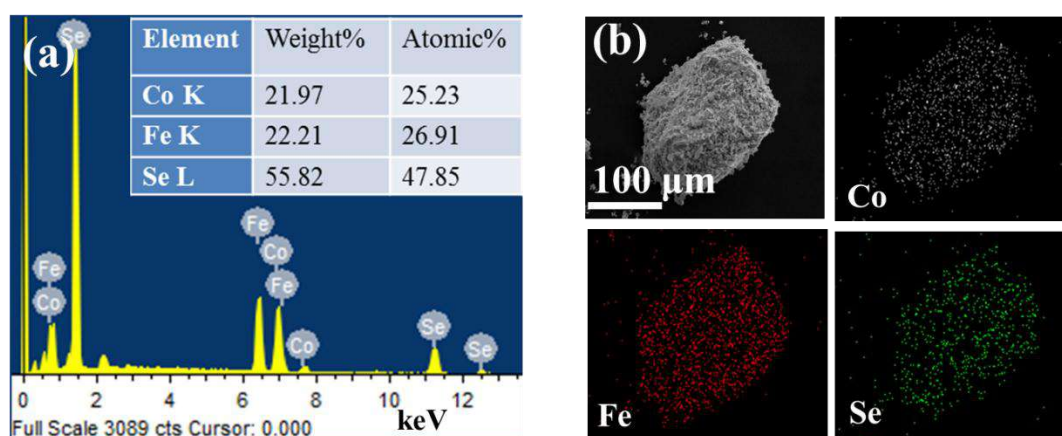


Figure 4.5. (a) SEM-EDAX and (b) elemental mapping of CFS

Figure 4.5a displays the SEM-EDAX spectrum of the sample CFS with the obtained weight and atomic percentage of the constituent elements. The surface elemental composition of the sample CFS was obtained and it matches with the actual composition. The homogeneity of the sample was established through elemental mapping on a micrometer scale (Figure 4.5b). This proves the correctness of the new synthesis route for CNS and CFS.

4.1.2. Magnetic Properties

4.1.2.1. Magnetic properties of CNS

Transition metal chalcogenides exhibit various magnetic properties and can be evaluated using different magnetic measurement techniques. Figure 4.6a indicates the magnetic hysteresis loop of the sample at different temperatures and low temperatures the material has narrow MH loops. The S-shaped unsaturated hysteresis loops were associated with the antiferromagnetic (AFM) with weak ferromagnetic (FM) [35] ordering and have a nearly paramagnetic nature at room temperature. To confirm AFM further, magnetization versus (M-T) temperature studies were carried out at various fields from 3 K to 150 K. M-T measurements were done in two modes, zero field cooling (ZFC) and field cooling (FC)

conditions at low temperatures. In ZFC the spin system is cooled to the low temperature at zero applied fields and measured the moment during the warming step. However, in FC, the measurements were taken in the same applied field during the cooling cycle. Figure 4.6b depicts the M-T plots at different fields 100 Oe, 500 Oe and 1000 Oe, a sharp peak at low temperature was observed. The characteristic cusp-like maximum at the low temperature corresponds to the AFM nature of the material along with the weak ferromagnetism (FM) [36]. In AFM materials the PM to AFM transition temperature is termed as Neel temperature (T_N) and it was obtained as 5.5 K for CNS in Figure 4.6c.

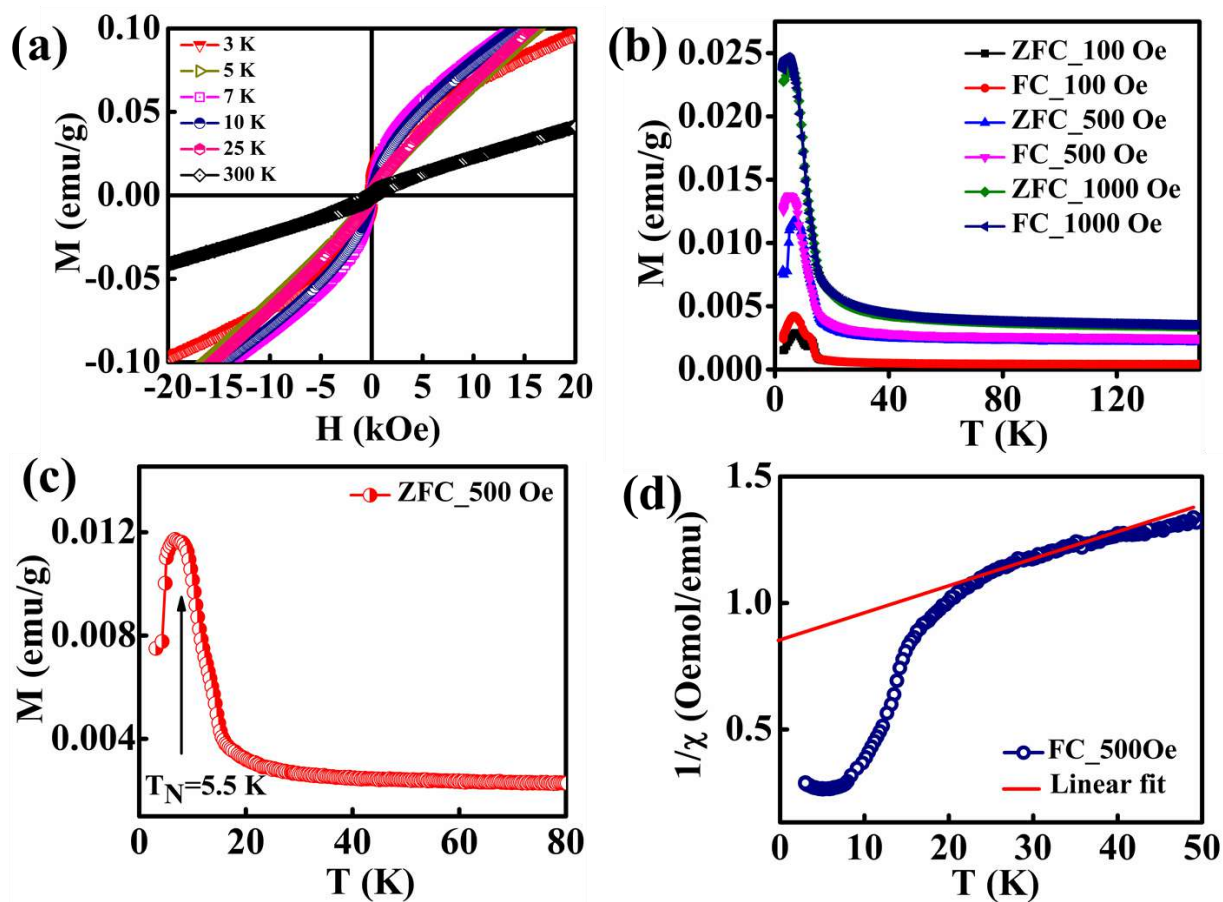


Figure 4.6. (a) M versus H at different temperatures, (b) M versus T at different fields, (c) Neel temperature from M-T plot at 500 Oe, and (d) CW plot in FC mode at 500 Oe

The temperature dependence of the molar magnetic susceptibility is explained by the Curie-Weiss law

$$\chi_{mol} = \frac{C}{T-\theta} \quad (1)$$

Where C is known as the Curie constant and θ as Weiss temperature, Figure 4.6d shows the Curie –Weiss plot of the material at 500 Oe. The paramagnetic region is fitted with C-W law,

from the fitted slope and intercept, we have calculated Curie constant (C) =1/slope and Curie temperature (θ) = - (y-intercept)/slope. The calculated parameters are shown in Table 4.1

Table 4.1. Data obtained from CW linear fit

	Slope (Oe mol emu ⁻¹ K ⁻¹)	y-intercept (Oe mol emu ⁻¹)	C (Oe ⁻¹ mol ⁻¹ emuK)	Weiss temperature(Θ) (K)	μ_{eff} ($\mu_{\text{B/F.U}}$)
CNS	4.24	460	0.235	-108.4	1.373

The negative value of Weiss temperature (θ) further confirms the AFM nature of the materials [37]. The effective paramagnetic moment from the linear fit was calculated by using the equation $\mu_{\text{eff}} = 2.827\sqrt{C} \mu_{\text{B}}$. The theoretical magnetic moment was spin only due to the orbital quenching [38], it is given by $\mu_{\text{eff}} = g\sqrt{S(S+1)} \mu_{\text{B}}$. In CNS, the transition metals Ni and Co contribute combined cationic magnetic moment. The effective moment calculated for all combinations of cations is listed in Table 4.2.

Table 4.2. All possible cationic combinations of the spin-only moment of CNS

	Co²⁺ (HS)	Co²⁺ (LS)	Co³⁺ (HS)	Co³⁺ (LS)
Ni²⁺ (HS)	4.75	3.31	5.65	2.82
Ni²⁺ (LS)	3.87	1.73	4.89	0
Ni³⁺ (HS)	2.44	4.24	6.30	3.87
Ni³⁺ (LS)	4.24	2.44	5.19	1.73

On comparing the experimental magnetic moment with cationic contribution, it was found that Co²⁺ and Ni²⁺ are in a low spin state. The cations Co²⁺ (S = 3/2) and Ni²⁺(S=1) generate AFM ordering [6]. The oxidation states Ni²⁺ and Co²⁺ were already confirmed through XPS analysis.

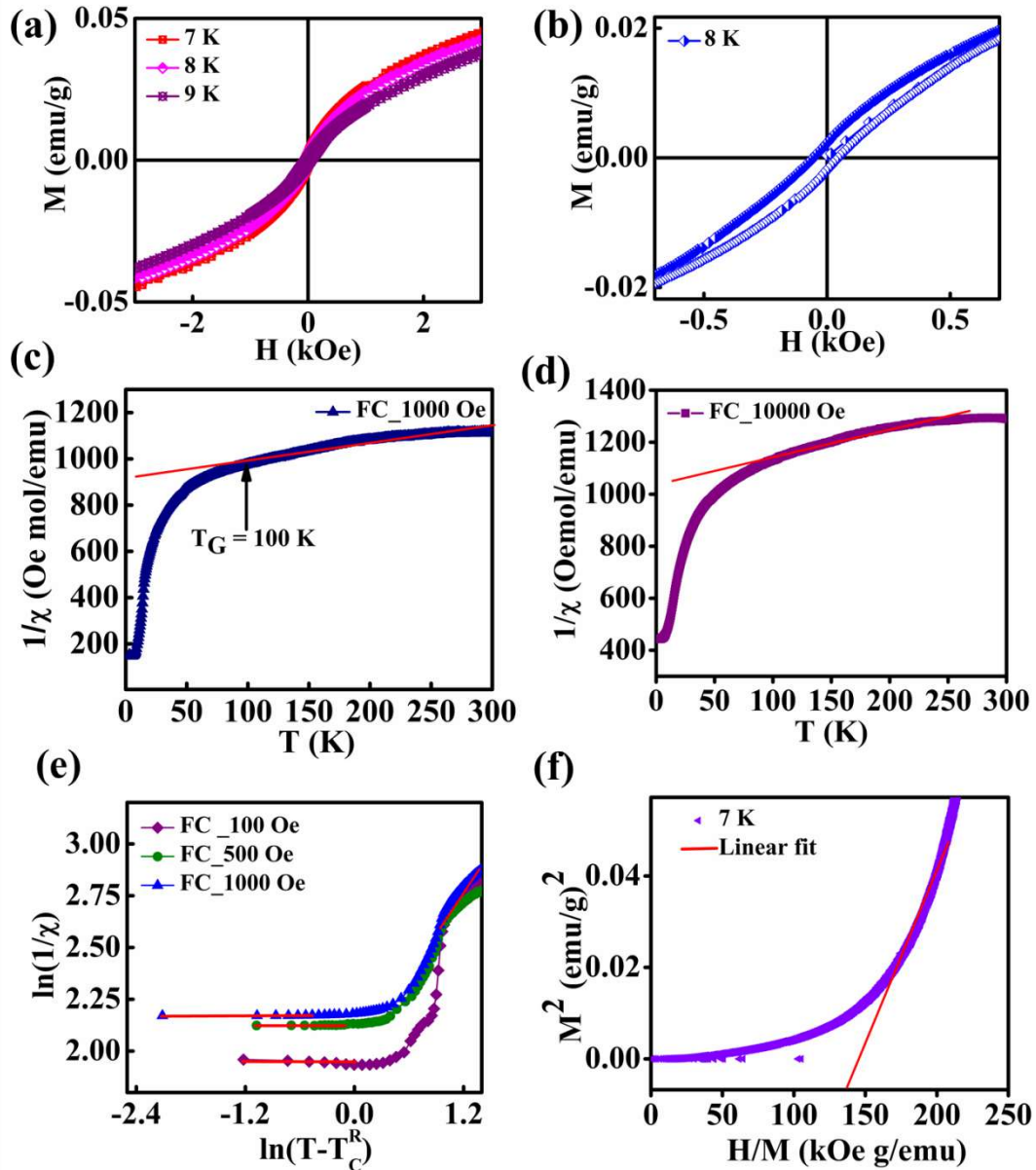


Figure 4.7 (a) M versus H plot at 7 K, 8 K and 9 K, (b) zoomed MH curve at 8 K, (c) & (d) linear fit on CW curve at 1000 Oe and 10000 Oe, (e) linear fit on $\ln(1/\chi)$ versus $\ln(T-T_C^R)$, and (f) Aroff's plot at 7 K

Figure 4.7a depicts the hysteresis loop of sample NCSS above T_N for temperatures 7 K, 8 K and 9 K, from Figure 4.7b it was clear that even at higher temperatures the material possesses a slight hysteresis loop instead of a PM curve. It confirms that the material has a different phase in between AFM and PM and the downward turn in the $1/\chi$ versus T is a major characteristic of the presence of Griffith-like phase [39]. From Figure 4.7c and d, for lower fields 100 Oe, and 1000 Oe the CW plot has a deviation from Curie Weiss behaviour at a particular temperature $T_G = 100$ K. The existence of the GP was due to the random distribution of ferromagnetic clusters in the PM matrix [35] below the Griffiths temperature

T_G . The Griffith-like phase at the lower field can be further analysed by the power law (equation 2)

$$\frac{1}{\chi} = (T - T_C^R)^{1-\lambda} \quad (2)$$

where λ ($0 \leq \lambda \leq 1$) is the magnetic susceptibility exponent and T_C^R is the critical temperature of random ferromagnetic clusters where susceptibility tends to diverge. In general, GP was observed in the range of temperature $T_C^R < T < T_G$, and in the present system the GP phase was observed in the range of temperature $5.5 \text{ K} < T < 100 \text{ K}$. As the applied magnetic field increases from 100 Oe to 10000 Oe, the downward deviation diminishes gradually and this is due to the polarization of the spins outside the cluster at higher fields [40]. Figure 4.7e shows the plot of $\ln 1/\chi$ versus $\ln(T-T_C^R)$ with linear fit at the GP and PM region. Because of the negative value of θ , T_C^R is approximated as T_C [41]. The slope of the fitted straight line in the GP regime gives λ_{GP} and it is close to 1 at all fields which confirm the GP in CNS. The linear fit at the PM region generates λ_{PM} close to zero (0.3 for 10000 Oe) at different fields. In long-range ordered magnetic materials, a spontaneous magnetization (M_S) is present. In CNS, the existence of ferromagnetic clusters does not lead to any long-range ordering and thereby no spontaneous magnetization [42]. The confirmation of spontaneous magnetization can be studied through Arrott plots [43]. Figure 4.7f shows M^2 versus H/M above T_N at 7 K, the negative y-intercept on the M^2 axis confirms the zero spontaneous magnetization and the GP phase in CNS.

4.1.2.2. Magnetic Properties of CFS

The transition metal substitution in materials can significantly influence the magnetic properties due to the change in electronic configuration that affects the magnetic moment and spin interactions within the material. The substitution can lead to changes in magnetic ordering, Curie temperature, and overall magnetic behaviour. The choice of the substituted TM plays a crucial role in tailoring the magnetic properties for spintronics application. Here we study the magnetic properties of Fe substituted at the Ni site of CoMSe_2 ($M = \text{Ni, Fe}$).

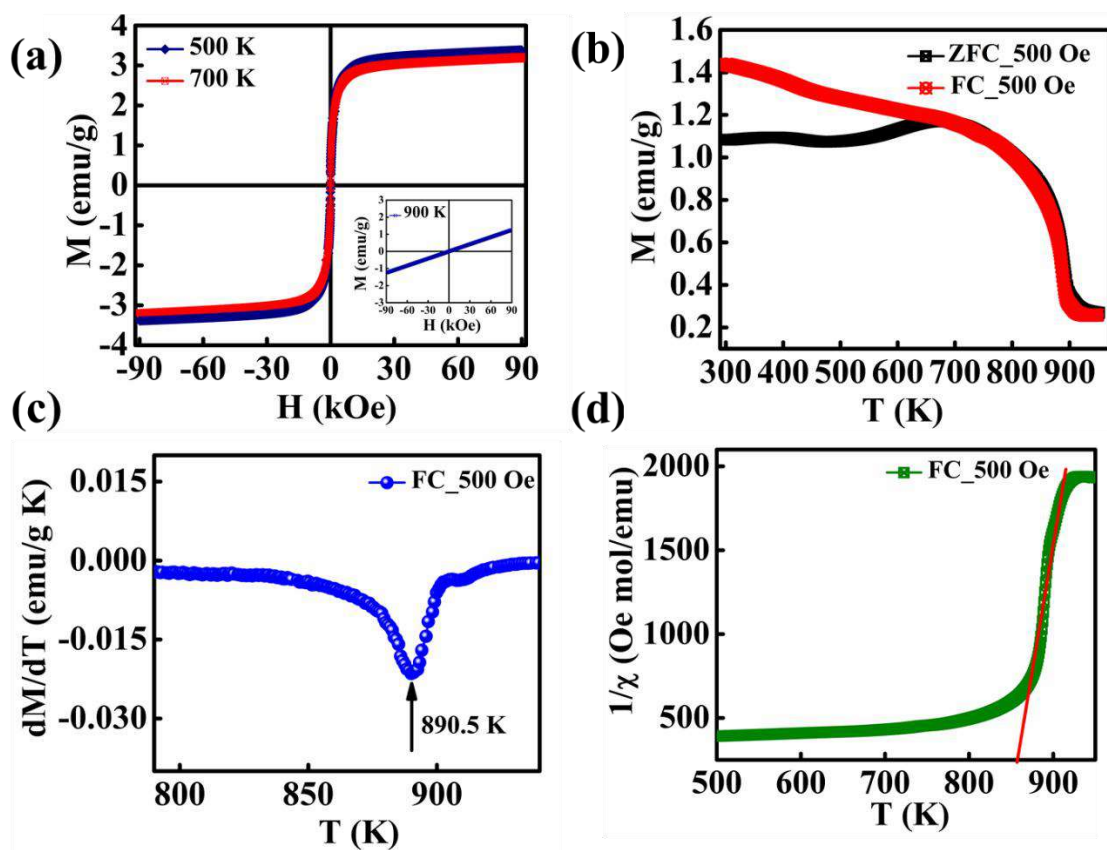


Figure 4.8. (a) $M-H$ data at 500 K and 700 K, (b) M versus T at 500 Oe, (c) dM/dT versus T at 500 Oe, (d) linear fit on the CW plot at 500 Oe

Figure 4.8a shows the $M-H$ plots of the material at different temperatures and it confirms that CFS has an FM nature below a particular temperature (the inset Figure shows the PM at 900 K). $M-T$ measurements were carried out to further study the associated magnetic properties, Figure 4.8b depicts the ZFC - FC magnetization curve measured from 300 K to 950 K at an applied field of 500 Oe. In the FM region, the bifurcation in ZFC and FC were observed and it corresponds to the thermomagnetic irreversibility near the transition temperature. The T_C value of approximately 890.5 K was determined from the point of inflection of the dM/dT versus the T curve (Figure 4.8c) in the FC mode at 500 Oe. Figure 4.8d shows the CW plot of CFS, from the linear fit we have calculated the Curie temperature, and effective magnetic moment, and the associated parameters. The positive value of Curie temperature ($\theta = 850.6$ K) further confirms the FM ordering in CFS and the experimentally obtained magnetic moment is $1.43 \mu_B$. The spin-only moment was calculated from all possible cationic combinations (table 4.3) and the down spins of Co^{2+} and Fe^{2+} contributed to the observed magnetic moment.

Table 4.3. All possible cationic combinations of spin only moment of CFS

	Co ²⁺ (HS)	Co ²⁺ (LS)	Co ³⁺ (HS)	Co ³⁺ (LS)
Fe ²⁺ (HS)	6.24	5.19	6.92	0
Fe ²⁺ (LS)	3.87	1.73	4.9	0
Fe ³⁺ (HS)	7.06	6.16	7.7	5.9
Fe ³⁺ (LS)	4.24	2.45	5.19	1.73

4.1.3. Thermoelectric properties

Temperature-dependent electronic and thermal transport measurements of the samples were recorded in the low-temperature range of 3 K to 300 K. Figure 4.9a shows the electrical conductivity (σ) of the materials and CFS has higher electrical conductivity compared with CNS. On decreasing the temperature from 300 K to 3 K the conductivity increases showing the metallic or heavily doped semiconductor nature. The increase in σ is associated with the suppression of electron-phonon and electron-electron scattering at low temperatures [44,45]. Hou et al reported that hollow sub-microsphere NiCoSe₂ exhibit an electrical conductivity of 10 S/cm [29] and here we got the value of 2.7×10^4 S/m. Compounds synthesized from direct element melting exhibit high crystallinity and density that lead to the enhancement in the conductivity of the material [46]. Increasing the carrier concentration (n) and carrier mobility (μ) of a material through doping or substitution can improve the electrical conductivity [47]. The substitution by Fe with a higher ionic radius than that of the Ni site enhanced the electrical conductivity of CFS due to the enhanced carrier mobility. With the help of the hall effect measurement room temperature μ of both samples was calculated and recorded in Table 4.4 From Figure 4.9b the Seebeck coefficient measurement, we found that both have electrons as the majority charge carriers and it increases with temperature.

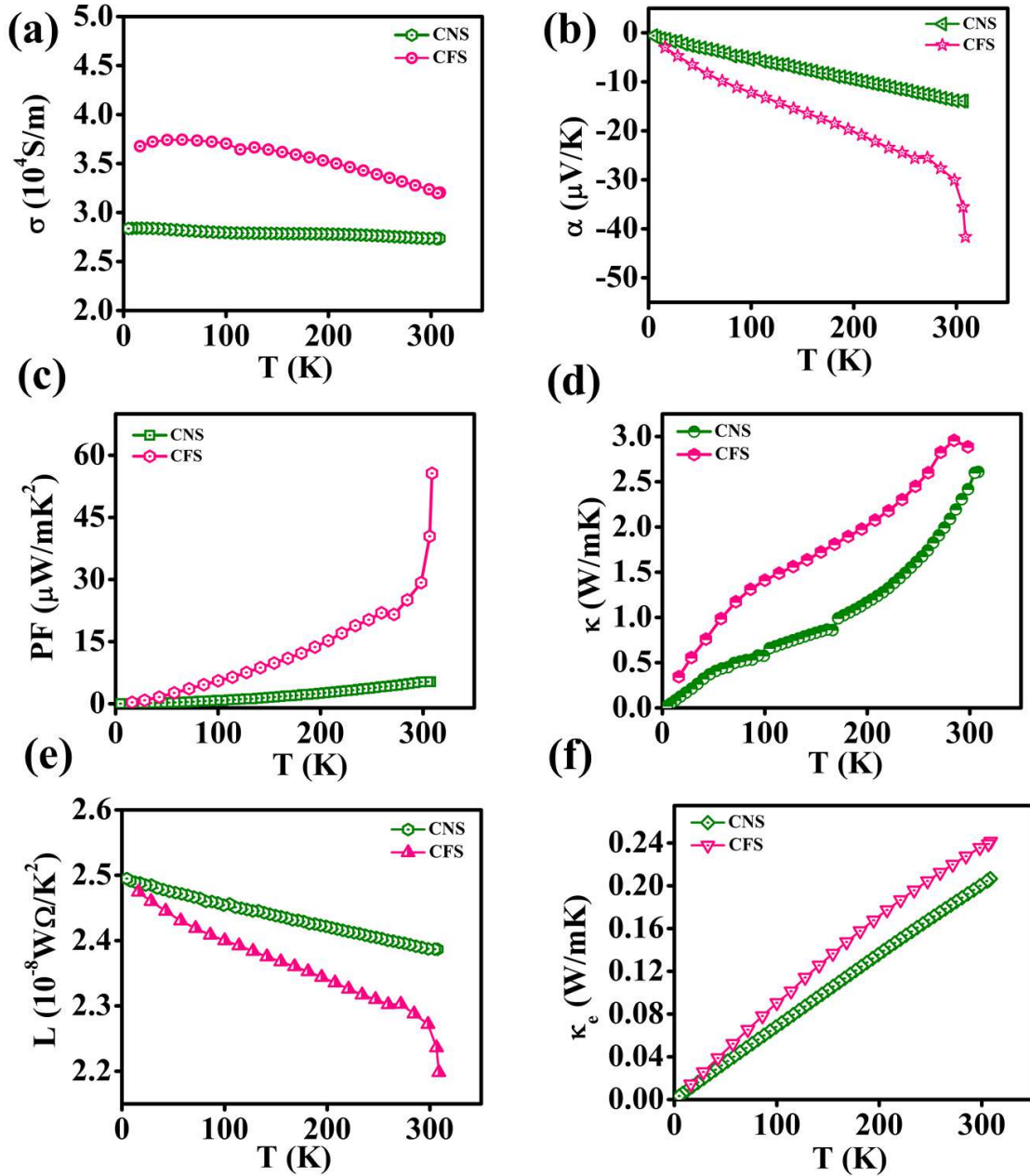


Figure 4.9. Temperature-dependent (a) electrical conductivity, (b) Seebeck coefficient, (c) power factor, (d) thermal conductivity, (e) Lorenz number and (f) electronic thermal conductivity

The Hall coefficient determined from the Hall effect measurement would also identify the type of carrier concentration. For n-type materials, the slope of transverse resistivity versus applied field gives a negative slope according to the Hall coefficient relation ($R_H = -1/ne$) [48]. Here the materials satisfy the inverse relationship between the electrical conductivity and Seebeck coefficient [49], and CFS has a higher S value compared with CNS. There are various techniques

Table 4.4. Calculated n , μ , and m^* at room temperature for CNS and CFS

	n (/cm ³)	μ (cm ² /V.s)	m^* (m_0)
CNS	1.06×10^{20}	16.08	0.006
CFS	10^{19}	200	0.23

has been introduced to enhance the thermopower of a TE material, which includes band convergence [50], density of states improvement[51], optimization of carrier concentration, resonant state [52] and energy filtering [51] etc. The relation connecting the Seebeck coefficient of metals or degenerate semiconductors with charge carrier concentration and effective mass is given by the Mott equation (equation 3) with the assumption of a parabolic band and energy-independent scattering [53].

$$\alpha = \frac{8\pi^2 k_B^2 T}{3qh^2} m^* \left(\frac{\pi}{3n}\right)^{2/3} \quad (3)$$

Where n is the carrier concentration, k_B is the Boltzmann constant, q is the electronic charge, h is the Planck constant and m^* is the density of state effective mass. Here the effective mass is calculated from the Seebeck coefficient and is named as Seebeck coefficient effective mass [54]. The room temperature m^* of the carriers can be calculated by using the Mott formula with the help of experimentally obtained Seebeck coefficient and the carrier concentration calculated from Hall effect measurement. The Fe in CFS has reduced the carrier concentration by 10 times that of CNS, according to the Mott equation α is directly proportional to the carrier effective mass and inversely proportional to $n^{2/3}$, which contributed to the thermopower [55]. The efficiency of a thermoelectric material can be quantified by power factor ($PF = \alpha^2 \sigma$), the PF of the synthesized materials increases with temperature (4.9c). The Fe-substituted compound has a PF of ~ 55 near room temperature, which is 10 times higher than that of CNS, the combined effect of S and σ pays to high PF. Figure 4.9d shows the low-temperature total thermal conductivity of CNS and CFS, it increases with temperature and CFS has a higher k . The total thermal conductivity is contributed mainly by phonons and electrons in a thermoelectric material and the increase in trend in thermal conductivity as a function of temperature can be associated with the phonon contribution [56]. The electronic part of thermal conductivity can be found with the help of Wiedemann-Franz law ($k_e = \sigma LT$), where L is the Lorenz number at a given T), The Lorenz number has the relation with the Seebeck coefficient by the equation $L = 1.5 + (|S|/116)$ [57], L is in 10^{-8}

$W\Omega/K^2$ and S is in $\mu V/K$. The estimated temperature-dependent L values were plotted in Figure 4.9e and they decrease with temperature in a range of $2.49 - 2.38 \times 10^{-8} W\Omega/K^2$ for CNS and $2.47-2.2 \times 10^{-8} W\Omega/K^2$ for CFS from 3 K to 300 K. The lattice thermal conductivity was obtained by subtracting k_e (Figure 4.9f) from k , Figure 4.10a shows that major players of thermal transport were phonons. In magnetic materials, the thermopower can be contributed by electrons/holes, phonons and magnons, but the major contribution comes from the actual charge carriers. Polash et al proposed that spin degree of freedom can also offer excess S to the diffused S in magnetic materials [58]. It was reported that in FM, AFM materials magnon electron drag (MED) results in the enhancement of thermopower. The coupling between the phonon and magnon will result in a momentum gradient on the magnon system and that can affect the electrons through s-d or p-d interaction. This makes a drag effect on the carrier electron or holes due to the transfer of the linear momentum [59]. Recent studies revealed that above T_C the paramagnons contribute to thermopower by similar drag effect through s-d exchange interaction [60]. The phonon and magnon effect on thermal transport is studied by heat capacity measurement techniques. Figure 4.10b depicts the heat capacity versus temperature plots for CNS and CFS, from the graph it is clear that at low temperature the heat capacity is mainly contributed by the phonons. The T^3 dependence on heat capacity is associated with the phonon heat transport and it reveals that magnon contribution was suppressed by the phonons in CNS (AFM) and CFS (FM). There is no evidence of the magnetic transition from FM to PM near 40 K in CNS, hence it confirms that below-room-temperature phonons are the heat carriers in these compounds. The material CFS has higher lattice thermal conductivity than CNS due to the phonon generation which increases with the temperature which was confirmed experimentally by the heat capacity measurements. Here at low temperatures, the heat capacity can be fitted by the relation (equation 4)

$$C_p = \gamma T + \beta T^3 \quad (4)$$

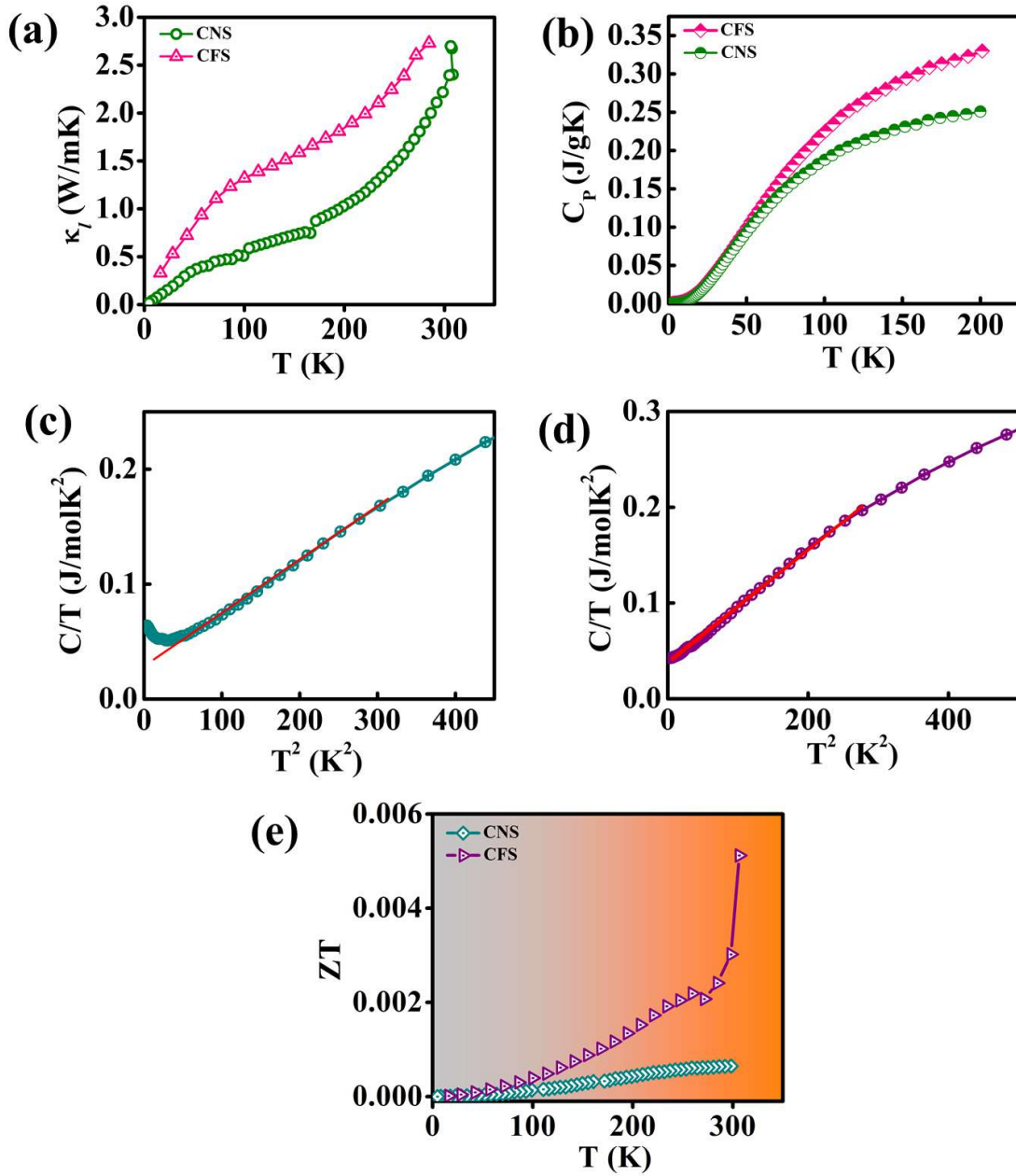


Figure 4.10. Temperature-dependent (a) lattice thermal conductivity, (b) specific heat capacity, (c) & (d) linear fit on C/T versus T^2 plots, (e) ZT versus T for CNS and CFS

Where γ connects with the electronic part and β with the phonon part of the heat capacity [61]. Figures 4.10c and d display the C/T versus T^2 fit, one can find the Debye temperature, $\theta_D = (12\pi^4 pR/5\beta)^{1/3}$ (p is the number of atoms according to the chemical formula, R is the molar gas constant) and density of states near E_F ($N(E_F)$) from $\gamma = \pi^2(k_B^2)N(E_F)/3$ (k_B is the Boltzmann's constant). The obtained Debye temperature and the density of states were

tabulated in Table 4.5, from which it is clear that CFS has a higher density of states (DOS) near E_F which increases the DOS effective mass and thereby the Seebeck coefficient.

Table 4.5. Calculated Debye temperature and density of states at E_F of CNS and CFS

	θ_D (K)	$N(E_F)$ ($eV^{-1} \text{ mole}^{-1}$)
CNS	232.4	7.4×10^{24}
CFS	258.3	1.2×10^{25}

From the measured transport properties the efficiency of the thermoelectric material ZT can be calculated, and Figure 4.10e shows the variation of ZT with temperature. The substitution of Fe at Ni site enhanced thermoelectric conversion efficiency 10 times. The enhanced electrical conductivity and Seebeck coefficient improved the thermoelectric efficiency of CFS on substitution.

4.2. Conclusion

The binary transition metal chalcogenide $CoMSe_2$ ($M = Ni, Fe$) is synthesized by a direct element melting route and its structural, electronic, magnetic and thermoelectric characteristics were investigated. The low-temperature magnetic and thermoelectric properties were carried out and it was observed that on substitution of Fe at the Ni site produced different magnetic ordering. The sample CNS exhibit AFM ordering with T_N as 5.5K, and CFS has an FM nature with a high temperature $T_C \sim 890.5$ K. The downward turn in the CW plot, power law analysis and Arrott plot confirm the presence of Griffith's like Phase (GP) in CNS and it is due to the random distribution of FM clusters in the PM matrix. The electrical and thermoelectric properties of the materials were analyzed at low temperatures. It was observed that both materials have electrons as the majority charge carrier which is confirmed through Seebeck coefficient measurement and Hall Effect analysis. The enhanced thermopower in CFS is due to the higher DOS effective mass. The heat capacity measurements reveal that phonons are responsible for the thermal transport in CFS. In magnetic semiconducting materials, MED can also contribute to the diffusion of thermopower. These materials can be considered as a base material, further doping or substitution at the cationic site can result in the enrichment of TE efficiency. In summary substitution by another TM results in 10 times enhancement of the thermoelectric efficiency at room temperature.

References

- [1] J. Puebla, J. Kim, K. Kondou, Y. Otani, Spintronic devices for energy-efficient data storage and energy harvesting, *Commun. Mater.* 1 (2020) 1–9.
- [2] X. Li, J. Yang, First-principles design of spintronics materials, *Natl. Sci. Rev.* 3 (2016) 365–381.
- [3] S. Mani, S. Ramaraj, S.M. Chen, B. Dinesh, T.W. Chen, Two-dimensional metal chalcogenides analogous NiSe₂ nanosheets and its efficient electrocatalytic performance towards glucose sensing, *J. Colloid Interface Sci.* 507 (2017) 378–385.
- [4] C. Tang, Z. Pu, Q. Liu, A.M. Asiri, X. Sun, Y. Luo, Y. He, In Situ Growth of NiSe Nanowire Film on Nickel Foam as an Electrode for High-Performance Supercapacitors, *ChemElectroChem.* 2 (2015) 1903–1907.
- [5] X. Qiu, P. Qiu, T. Deng, H. Huang, X. Du, X. Shi, L. Chen, Thermoelectric Properties of Nano-grained Mooihoekite Cu₉Fe₉S₁₆, *Zeitschrift Fur Anorg. Und Allg. Chemie.* 646 (2020) 1116–1121.
- [6] K.W. Shah, S.X. Wang, Y. Zheng, J. Xu, Solution-based synthesis and processing of metal chalcogenides for thermoelectric applications, *Appl. Sci.* 9 (2019) 1–20.
- [7] H. Wada, D. Kawasaki, Y. Maekawa, Magnetocaloric Effect and Magnetoresistance Due to Itinerant Electron Metamagnetic Transition in Co(S_{1-x}Se_x)₂, *IEEE Trans. Magn.* 50 (2014) 1–7.
- [8] S. Ogawa, Magnetic properties of 3d transition-metal dichalcogenides with the pyrite structure, *J. Appl. Phys.* 50 (1979) 2308–2311.
- [9] J.R. Neilson, T.M. McQueen, Bonding, ion mobility, and rate-limiting steps in deintercalation reactions with ThCr₂Si₂-type KNi₂Se₂, *J. Am. Chem. Soc.* 134 (2012) 7750–7757.
- [10] E. Zhang, J. Zhi, Y.C. Zou, Z. Ye, L. Ai, J. Shi, C. Huang, S. Liu, Z. Lin, X. Zheng, N. Kang, H. Xu, W. Wang, L. He, J. Zou, J. Liu, Z. Mao, F. Xiu, Signature of quantum Griffiths singularity state in a layered quasi-one-dimensional superconductor, *Nat. Commun.* 9 (2018) 4656.

- [11] P.Y. Chan, N. Goldenfeld, M. Salamon, Critical behavior of Griffiths ferromagnets, *Phys. Rev. Lett.* 97 (2006) 1–4.
- [12] C. Binek, W. Kleemann, Domainlike antiferromagnetic correlations of paramagnetic FeCl₂: A field-induced Griffiths phase?, *Phys. Rev. Lett.* 72 (1994) 1287–1290.
- [13] and L.L. Z. W. Ouyang, N. M. Xia, Y. Y. Wu, S. S. Sheng, J. Chen, Z. C. Xia, Short-range ferromagnetic correlations in the spin-chain compound Ca₃CoMnO₆, *Phy. Rev. B.* 84 (2002) 1–5.
- [14] R.R.& S.M. Krishanu Ghosh, Chandan Mazumdar², Griffiths phase behaviour in a frustrated antiferromagnetic intermetallic compound, *Sci. Rep.* 5 (2015) 1–10.
- [15] A. Karmakar, S. Majumdar, S. Kundu, T.K. Nath, S. Giri, A Griffiths-like phase in antiferromagnetic R_{0.5}Eu_{0.5}MnO₃ (R = Pr, Nd, Sm), *J. Phys. Condens. Matter.* 25 (2013) 1–8.
- [16] M.R. Shankar, A.N. Prabhu, A review on structural characteristics and thermoelectric properties of mid-temperature range Chalcogenide-based thermoelectric materials, Springer US, 2023.
- [17] U. Syafiq, E. Isotta, N. Ataollahi, K. Lohani, S. Luong, V. Trifiletti, O. Fenwick, P. Scardi, Facile and Low-Cost Fabrication of Cu/Zn/Sn-Based Ternary and Quaternary Chalcogenides Thermoelectric Generators, *ACS Appl. Energy Mater.* 5 (2022) 5909–5918.
- [18] S. Yamanaka, A. Kosuga, K. Kurosaki, Thermoelectric properties of Tl₉BiTe₆, *J. Alloys Compd.* 352 (2003) 275–278.
- [19] D. Chung, T.P. Hogan, M. Rocci-Lane, P. Brazis, J.R. Ireland, C.R. Kannewurf, M. Bastea, C. Uher, M.G. Kanatzidis, A New Thermoelectric Material: CsBi₄Te₆, *ChemInform.* 35 (2004) 105–112.
- [20] Y. Shi, C. Sturm, H. Kleinke, Chalcogenides as thermoelectric materials, *J. Solid State Chem.* 270 (2019) 273–279.
- [21] H. Kleinke, New bulk materials for thermoelectric power generation: clathrates and complex antimonides, *Chem. Mater.* 22 (2010) 604–611.
- [22] T.M. Tritt, H. Böttner, L. Chen, Thermoelectrics: Direct Solar Thermal Energy Conversion, *MRS Bull.* 33 (2008) 368–371.

- [23] R. Venkatasubramanian, E. Siivola, T. Colpitts, B. O'Quinn, Thin-film thermoelectric devices with high room-temperature figures of merit, *Nature*. 413 (2001) 597–602.
- [24] M. Cutler, J.F. Leavy, R.L. Fitzpatrick, Electronic transport in semimetallic cerium sulfide, 1964.
- [25] S.N. Zhang, T.J. Zhu, S.H. Yang, C. Yu, X.B. Zhao, Phase compositions, nanoscale microstructures and thermoelectric properties in $\text{Ag}_{2-y}\text{Sb}_y\text{Te}_{1+y}$ alloys with precipitated Sb_2Te_3 plates, *Acta Mater.* 58 (2010) 4160–4169.
- [26] S.N. Zhang, G.Y. Jiang, T.J. Zhu, X.B. Zhao, S.H. Yang, Doping effect on thermoelectric properties of nonstoichiometric AgSbTe_2 compounds, *Int. J. Miner. Metall. Mater.* 18 (2011) 352–356.
- [27] K.X. Chen, X.M. Wang, D.C. Mo, S.S. Lyu, Thermoelectric Properties of Transition Metal Dichalcogenides: From Monolayers to Nanotubes, *J. Phys. Chem. C*. 119 (2015) 26706–26711.
- [28] J. Xu, H. Li, B. Du, X. Tang, Q. Zhang, C. Uher, High thermoelectric figure of merit and nanostructuring in bulk AgSbTe_2 , *J. Mater. Chem.* 20 (2010) 6138–6143.
- [29] L. Hou, Y. Shi, C. Wu, Y. Zhang, Y. Ma, X. Sun, J. Sun, X. Zhang, C. Yuan, Monodisperse Metallic NiCoSe_2 Hollow Sub-Microspheres: Formation Process, Intrinsic Charge-Storage Mechanism, and Appealing Pseudocapacitance as Highly Conductive Electrode for Electrochemical Supercapacitors, *Adv. Funct. Mater.* 28 (2018) 1–12.
- [30] Y.Y. Sun, M.Y. Jiang, L.K. Wu, G.Y. Hou, Y.P. Tang, M. Liu, Ultra-thin NiFeSe nanosheets as a highly efficient bifunctional electrocatalyst for overall water splitting, *Sustain. Energy Fuels*. 4 (2020) 582–588.
- [31] Z. Qian, Y. Chen, Z. Tang, Z. Liu, X. Wang, Y. Tian, W. Gao, Hollow Nanocages of $\text{Ni}_x\text{Co}_{1-x}\text{Se}$ for Efficient Zinc–Air Batteries and Overall Water Splitting, *Nano-Micro Lett.* 11 (2019) 1–17.
- [32] NIST XPS Database, (n.d.). https://srdata.nist.gov/xps/main_search_menu.aspx.
- [33] H. Singh, A.K. Sinha, S.M. Gupta, M.N. Singh, H. Ghosh, Two step solid state synthesis and Synchrotron X-ray characterizations of ceramic Co_3TeO_6 ; an improper multiferroic *, *Condens. Matter Mater. Sci.* 6 (2015) 1–14.

- [34] Q.S. Jiang, W. Li, J. Wu, W. Cheng, J. Zhu, Z. Yan, X. Wang, Y. Ju, Electrodeposited cobalt and nickel selenides as high-performance electrocatalytic materials for dye-sensitized solar cells, *J. Mater. Sci. Mater. Electron.* 30 (2019) 9429–9437.
- [35] P. Ravikumar, B. Kisan, A. Perumal, Enhanced room temperature ferromagnetism in antiferromagnetic NiO nanoparticles, *AIP Adv.* 5 (2015) 1–4.
- [36] S. Matteppanavar, S. Rayaprol, A. V. Anupama, B. Angadi, B. Sahoo, Origin of room temperature weak-ferromagnetism in antiferromagnetic $\text{Pb}(\text{Fe}_{2/3}\text{W}_{1/3})\text{O}_3$ ceramic, *Ceram. Int.* 41 (2015) 11680–11686.
- [37] J. Xu, H. Li, B. Du, X. Tang, Q. Zhang, C. Uher, High thermoelectric figure of merit and nanostructuring in bulk AgSbTe_2 , *J. Mater. Chem.* 20 (2010) 6138–6143. <https://doi.org/10.1039/c0jm00138d>.
- [38] R. Revathy, M.R. Varma, K.P. Surendran, Effect of morphology and ageing on the magnetic properties of nickel nanowires, Elsevier Ltd, 2019.
- [39] J. Herrero-Albillos, L.M. García, F. Bartolomé, Observation of a Griffiths-like phase in the paramagnetic regime of ErCo_2 , *J. Phys. Condens. Matter.* 21 (2009) 1–9.
- [40] K. Ghosh, C. Mazumdar, R. Ranganathan, S. Mukherjee, Griffiths phase behaviour in a frustrated antiferromagnetic intermetallic compound, *Sci. Rep.* 5 (2015) 15801 1–8.
- [41] A. Karmakar, S. Majumdar, S. Kundu, T.K. Nath, S. Giri, A Griffiths-like phase in antiferromagnetic $\text{R}_0.5\text{Eu}_{0.5}\text{MnO}_3$ ($\text{R} = \text{Pr}, \text{Nd}, \text{Sm}$), *J. Phys. Condens. Matter.* 25 (2013) 0–8.
- [42] I.N. Bhatti, I.N. Bhatti, R.N. Mahato, M.A.H. Ahsan, Magnetic behavior, Griffiths phase and magneto-transport study in 3d based nano-crystalline double perovskite $\text{Pr}_2\text{CoMnO}_6$, *Phys. Lett. Sect. A Gen. At. Solid State Phys.* 383 (2019) 2326–2332.
- [43] S. Bustingorry, F. Pomiro, G. Aurelio, J. Curiale, Second-order magnetic critical points at finite magnetic fields: Revisiting Arrott plots, *Phys. Rev. B.* 93 (2016) 1–12.
- [44] H. Wu, J. Carrete, Z. Zhang, Y. Qu, X. Shen, Z. Wang, L.D. Zhao, J.Q. He, Strong enhancement of phonon scattering through nanoscale grains in lead sulfide thermoelectrics, *NPG Asia Mater.* 6 (2014) 1–11.

- [45] Z. Cheng, L. Liu, S. Xu, M. Lu, X. Wang, Temperature dependence of electrical and thermal conduction in single silver nanowire, *Sci. Rep.* 5 (2015) 1–12.
- [46] X. Mu, H. Zhou, D. He, W. Zhao, P. Wei, W. Zhu, X. Nie, H. Liu, Q. Zhang, Enhanced electrical properties of stoichiometric Bi_{0.5}Sb_{1.5}Te₃ film with high-crystallinity via layer-by-layer in-situ Growth, *Nano Energy.* 33 (2017) 55–64.
- [47] Q. Song, P. Qiu, H. Chen, K. Zhao, M. Guan, Y. Zhou, T.R. Wei, D. Ren, L. Xi, J. Yang, Z. Chen, X. Shi, L. Chen, Enhanced carrier mobility and thermoelectric performance in Cu₂FeSnSe₄ diamond-like compound via manipulating the intrinsic lattice defects, *Mater. Today Phys.* 7 (2018) 45–53.
- [48] J. Nag, D. Rani, J. Kangsabanik, D. Singh, R. Venkatesh, P.D. Babu, K.G. Suresh, A. Alam, Bipolar magnetic semiconducting behavior in VNbRuAl, *Phys. Rev. B.* 104 (2021) 1–7.
- [49] S. Ganeshan, M. Levin, Formalism for the solution of quadratic Hamiltonians with large cosine terms, *Phys. Rev. B.* 93 (2016) 1–32.
- [50] K.H. Lee, S. il Kim, H.S. Kim, S.W. Kim, Band Convergence in Thermoelectric Materials: Theoretical Background and Consideration on Bi-Sb-Te Alloys, *ACS Appl. Energy Mater.* 3 (2020) 2214–2223.
- [51] G. Tan, X. Zhang, S. Hao, H. Chi, T.P. Bailey, X. Su, C. Uher, V.P. Dravid, C. Wolverton, M.G. Kanatzidis, Enhanced Density-of-States Effective Mass and Strained Endotaxial Nanostructures in Sb-Doped Pb_{0.97}Cd_{0.03}Te Thermoelectric Alloys, *ACS Appl. Mater. Interfaces.* 11 (2019) 9197–9204.
- [52] L. Wang, X. Tan, G. Liu, J. Xu, H. Shao, B. Yu, H. Jiang, S. Yue, J. Jiang, Manipulating Band Convergence and Resonant State in Thermoelectric Material SnTe by Mn-In Codoping, *ACS Energy Lett.* 2 (2017) 1203–1207.
- [53] A. Suwardi, D. Bash, H.K. Ng, J.R. Gomez, D.V.M. Repaka, P. Kumar, K. Hippalgaonkar, Inertial effective mass as an effective descriptor for thermoelectrics: Via data-driven evaluation, *J. Mater. Chem. A.* 7 (2019) 23762–23769.
- [54] G.J. Snyder, A. Pereyra, R. Gurunathan, Effective Mass from Seebeck Coefficient, *Adv. Funct. Mater.* 32 (2022) 1–6.

- [55] E.M. Levin, Charge carrier effective mass and concentration derived from combination of Seebeck coefficient and Te 125 NMR measurements in complex tellurides, *Phys. Rev. B.* 93 (2016) 1–5.
- [56] B. Hamawandi, H. Mansouri, S. Ballikaya, Y. Demirci, M. Orlovská, N. Bolghanabadi, S.A. Sajjadi, M.S. Toprak, A Comparative Study on the Thermoelectric Properties of Bismuth Chalcogenide Alloys Synthesized through Mechanochemical Alloying and Microwave-Assisted Solution Synthesis Routes, *Front. Mater.* 7 (2020) 1–13.
- [57] A. Putatunda, D.J. Singh, Lorenz number in relation to estimates based on the Seebeck coefficient, *Mater. Today Phys.* 8 (2019) 49–55.
- [58] M.M.H. Polash, D. Moseley, J. Zhang, R.P. Hermann, D. Vashaee, Understanding and design of spin-driven thermoelectrics, *Cell Reports Phys. Sci.* 2 (2021).
- [59] Y. Zheng, T. Lu, M.M.H. Polash, M. Rasoulianboroujeni, N. Liu, M.E. Manley, Y. Deng, P.J. Sun, X.L. Chen, R.P. Hermann, D. Vashaee, J.P. Heremans, H. Zhao, Paramagnon drag in high thermoelectric figure of merit Li-doped MnTe, *Sci. Adv.* 5 (2019) 1–8.
- [60] M.M.H. Polash, F. Mohaddes, M. Rasoulianboroujeni, D. Vashaee, Magnon-drag thermopower in antiferromagnets: Versus ferromagnets, *J. Mater. Chem. C.* 8 (2020) 4049–4057.
- [61] Y. Ando, N. Miyamoto, K. Segawa, T. Kawata, I. Terasaki, Specific-heat evidence for strong electron correlations in the thermoelectric material (Na, Ca)Co₂O₄, *Phys. Rev. B - Condens. Matter Mater. Phys.* 60 (1999) 10580–10583.

Chapter 5

The Low-Temperature Thermoelectric Transport Behavior of AgSbTe₂

As the energy demand continues to grow, it is becoming increasingly important to find ways to use energy more efficiently and to transition to cleaner, more sustainable sources of energy. The way we use energy has significant implications for our environment, economy, and society. Fossil fuels, which currently provide the majority of the world's energy, are finite resources that are becoming more difficult and expensive to extract. Renewable energy resources are promising alternatives to fossil fuels, and they do not emit greenhouse gases during operation. Thermoelectric materials find application in the area of new energy resources; they have the ability to convert waste heat energy into useful electrical energy by using thermoelectric materials [1–3]. Nowadays, thermoelectric devices play a crucial role in the fields of electricity generation and refrigeration. The efficiency of thermoelectric material is expressed through the dimensional figure of merit $ZT = S^2\sigma T/k$, where S , σ , T , and k are the Seebeck coefficient, electrical conductivity, absolute temperature, and thermal conductivity, respectively [4]. In order to get a high ZT value, the thermoelectric material should possess high S , σ , and low k . The optimization of these parameters is attained through band engineering, defect mechanisms, and optimizing the carrier concentration, mobility, and scattering mechanisms within the material[5,6]. There is a recent trend in the search for silver-based chalcogenides as promising candidates for thermoelectric applications. Binary and ternary silver chalcogenides emerged as efficient thermoelectric materials near room temperature applications [7–10]. It was observed that various mechanisms, like doping, alloying, site defects, vacancies, nano-precipitates, dislocations, interfaces, and composite formation with other materials, enhance the thermoelectric properties of silver-based chalcogenides [11–14]. In comparison with conventional thermoelectric materials, these have glass-like thermal conductivity due to the strong bond anharmonicity and the enhanced phonon scattering at the nanostructures within the material [15–18].

Among the ternary silver chalcogenides, metastable AgSbTe₂ was found to be of considerable interest due to its attractive structural and transport properties. Despite having a simple chemical formula (Ag₁Sb₁Te₂) this material has complex variations in stoichiometry and crystal structure [19]. AgSbTe₂ can be the solid solution between Ag₂Te and Sb₂Te₃, the single-phased AgSbTe₂ can be found only in a composition range with a ratio of Ag₂Te/Sb₂Te₃ less than unity [20]. The thermodynamic stability of AgSbTe₂ still exists as a challenging matter, and based on the pseudo-binary phase diagram [21] of $x\text{Ag}_2\text{Te} - (1-x)$

Sb_2Te_3 with $x = 0.5$ is the stoichiometric δ - AgSbTe_2 . From the detailed investigation of the pseudo-binary phase diagrams of Ag_2Te and Sb_2Te_3 , it was observed that the exact nominal composition of thermodynamically stable AgSbTe_2 is nonexistent [10]. This metastable state normally decomposes into Ag_2Te and Sb_2Te_3 below 633 K, the precipitates of Ag_2Te or Sb_2Te_3 along with stoichiometric AgSbTe_2 are due to the equivalence of their formation energies [22],[23]. It is experimentally observed that the δ phase of AgSbTe_2 has off stoichiometry and is expressed as $\text{Ag}_2\text{Te} (1-x)/2 - \text{Sb}_2\text{Te}_3(1+x)/2 = \text{Ag}_{1-x}\text{Sb}_{1+x}\text{Te}_{2+x}$ and the only stable ternary phase is with x having a range of value of 0.06-0.28. [23] This ternary chalcocantimonate AgSbTe_2 generally crystallizes in a cubic rock salt structure with space group $\text{Fm}\bar{3}\text{m}$, where Ag/Sb/vacancies randomly occupy the Wyckoff position 4a (0.5, 0.5, 0.5) while Te atoms randomly occupy Wyckoff position 4b (0, 0, 0) [8]. It was observed that still metastable cubic δ phase can be found at room temperature,[8] and Sugar et al. report that the single phase of AgSbTe_2 exists in a wide range of stoichiometries[24]. Due to the intrinsic metastable nature of the cubic δ phase, generally, AgSbTe_2 is formed with Ag or Sb-rich secondary phases such as nano-scaled Ag_2Te and Sb_2Te_3 [25]. The presence of these secondary phases influences the thermal and electrical transport properties of the material in an observable manner [10].

The experimental details of the compound AgSbTe_2 is included in chapter 2, structure, composition, morphology and the electric, magnetic- thermal transport and thermoelectric properties were executed.

5.1. Results and discussion

5.1.1. Structure and morphology

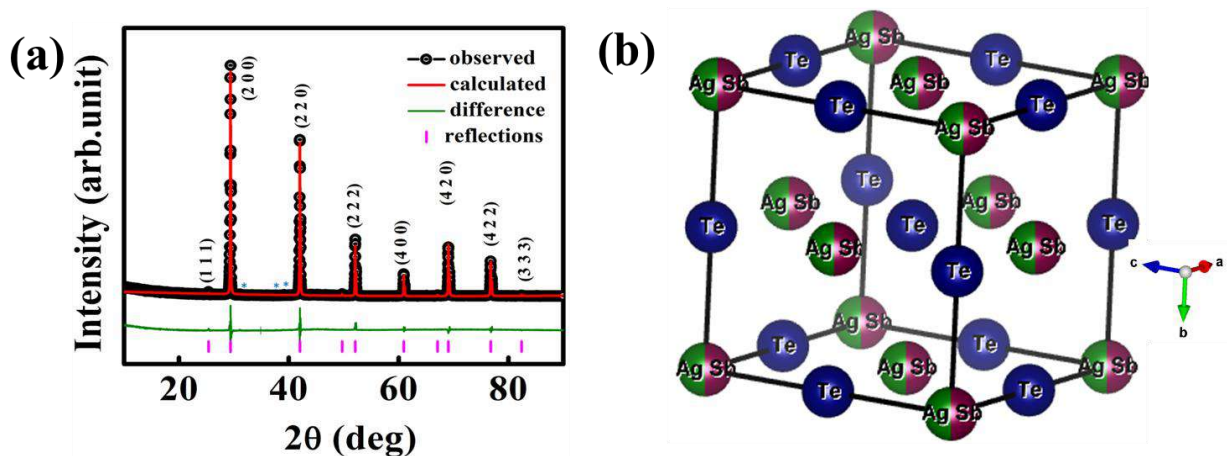


Figure 5.1. (a). Powder X-ray diffraction pattern of the as-synthesized sample; (b) Crystal structure of AgSbTe₂ from VESTA

The phase purity of the synthesized sample was analyzed by powder X-ray diffraction. The strong reflections were indexed by the cubic rock salt structure of AgSbTe₂ ($a = 6.06 \text{ \AA}$) having space group Fm-3m [19] and the weak secondary phase with Ag₂Te monoclinic phase [24] ($a = 8.09 \text{ \AA}$ $b = 4.48 \text{ \AA}$ $c = 8.96 \text{ \AA}$). Figure 5.1a shows the Rietveld-refined (GSAS 2 software) XRD data of the sample with a goodness of fit of 1.8, the obtained phase fraction of AgSbTe₂ is 95% and Ag₂Te is 5%. It confirms that the primary phase of the synthesized material at room temperature is AgSbTe₂, and the formation of the secondary phase is due to the slight energy difference between the meta-stable δ phase and the Ag₂Te/Sb₂Te₃ mixture [21]. Figure 5.1b shows the crystal structure of the face-centred cubic AgSbTe₂ with Ag⁺ and Sb³⁺ cations randomly occupied at the fcc cationic sublattice, while Te²⁻ was at the anionic sublattice [26,27]. Roychowdhury et al. report that AgSbTe₂ is a disordered material having two types of disorder that originate from the formation of impurity phases, Ag₂Te/Sb₂Te₃ and Ag/Sb cation disorder[24].

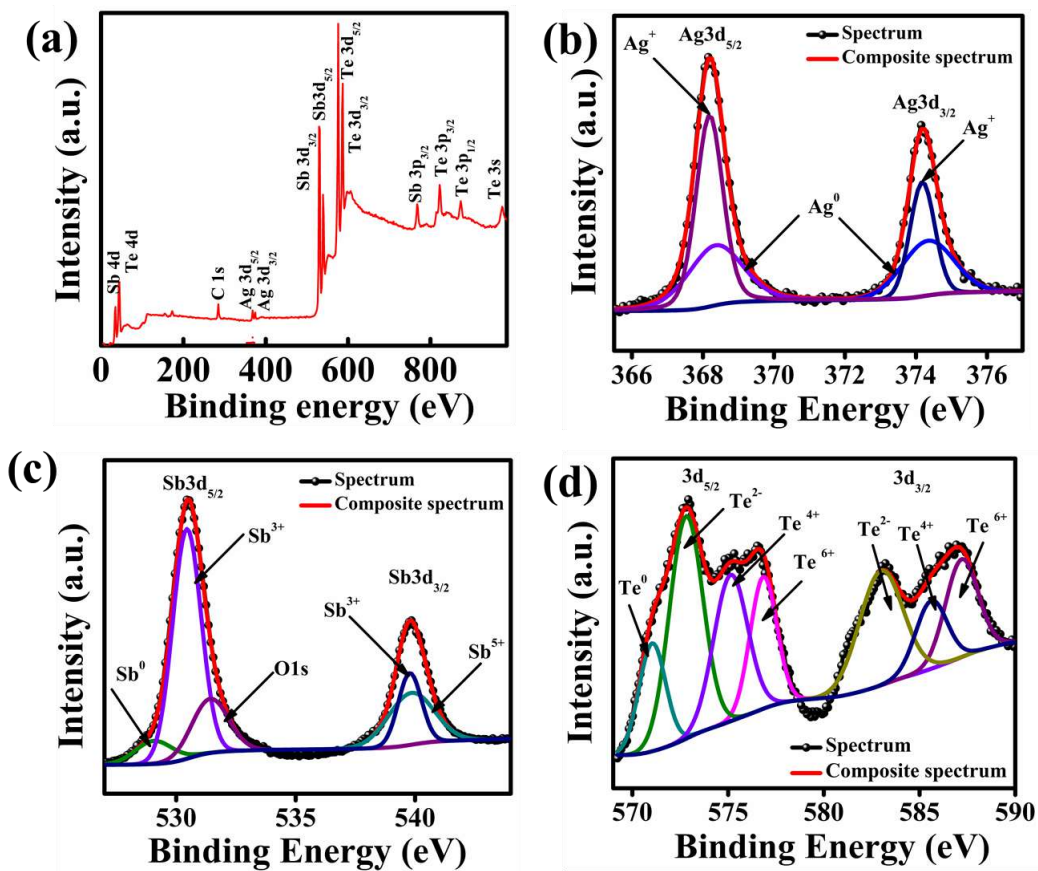
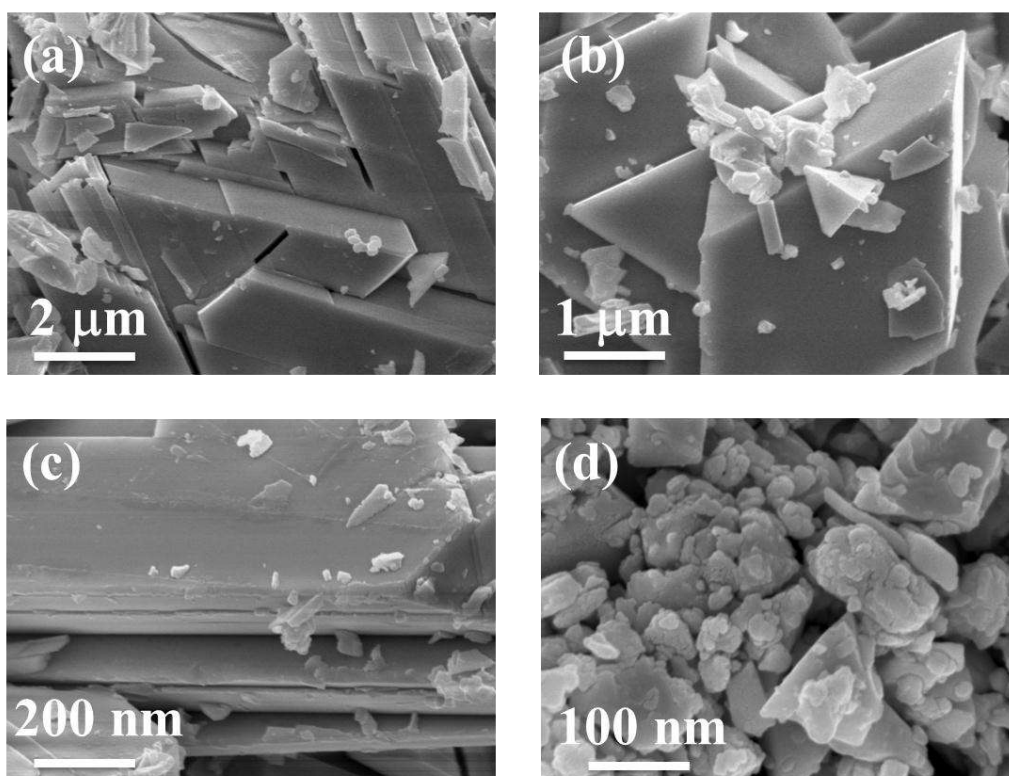


Figure 5.2. XPS spectra of the as-synthesized sample (a) Survey spectrum (b)-(d) high-resolution spectra of Ag, Sb, and Te respectively

The chemical composition and valence states of the constituent elements of the sample were analyzed from XPS spectra. Figure 5.2a shows the survey spectrum of the sample and confirms the presence of corresponding constituent elements. The oxidation states of the elements Ag, Sb, and Te were studied from their 3d core-level spectra. The strong doublet peaks (Figure 5.2b) fitted for Ag at binding energies of 368.3 eV and 374.3 eV correspond to Ag 3d_{5/2} and Ag 3d_{3/2} respectively, and the spin-orbit splitting of Ag is 6 eV with Ag⁺ oxidation state [28]. The peaks at 368.32 eV and 374.36 eV correspond to the Ag-Ag bonds [28]. The Figure 5.2c shows the Sb 3d spectrum, the doublet at 530.46 eV and 539.82 eV [29] are associated with 3d_{5/2} and 3d_{3/2} of Sb, and the corresponding spin-orbit splitting energy of 9.3 eV confirms the Sb³⁺ oxidation state. The presence of peaks at 528.9 eV and 540 eV corresponds to the Sb⁰ [28] and Sb⁵⁺ oxidation state; the O1s peak at binding energy 531.5 eV may be accompanied with the presence of Sb₂O₅ due to the surface oxidation of the material [30]. The Te 3d spectra contain four sub-peaks (Figure 5.2d), two of them centred at approximately 572.36 eV and 582.94 eV corresponding to 3d_{5/2} and 3d_{3/2} of Te²⁻, other two peaks are associated with the Te-Te bonds [28] of minor-phase monoclinic Ag₂Te.



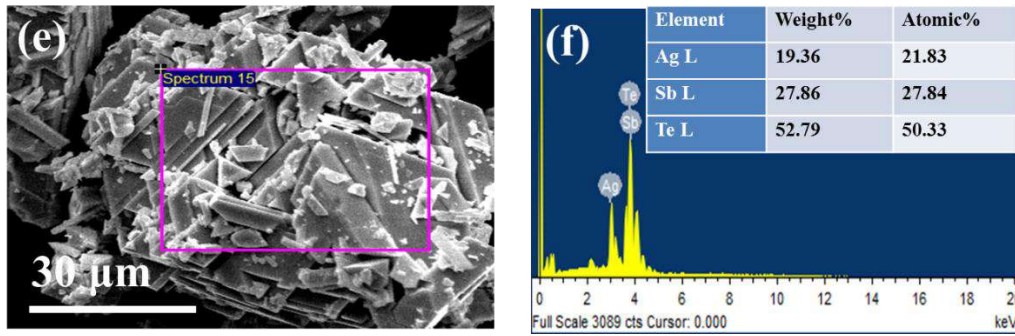


Figure 5.3. (a) - (d) SEM micrographs of the sample at different scale bars; (e)-(f) SEM-EDX of the sample

The microstructure composition and the surface morphology of the sample were investigated through EDX and SEM. Figure 5.3a-d shows the morphology of the samples at different scales. The density of the synthesized ingots was measured by the Archimedes principle and found to exhibit a density of ~ 97% of the theoretical crystallographic density. It was found that direct melted samples exhibit high relative density without the aid of densification techniques such as spark plasma sintering and hot pressing at elevated temperatures [11]. The compactness of the material was further confirmed through SEM analysis; Figures 5.3 a-c shows the microstructure of the samples with compacted sheet-like structures. Figure 5.3d reveals that micro- and nano-sized particles are randomly arranged on the plate-like structures of the direct-melted sample.

Table 5.1. Elemental the weight percentage of AgSbTe_2 calculated and obtained from SEM-EDX

Element	Actual weight%	Average weight%
Ag	22.24	20.61
Sb	25.11	26.86
Te	52.63	52.76

The local composition of the synthesized sample was determined through EDX analysis at different regions of the material under study. Figure 5.3f shows the EDX spectrum; the corresponding weight percentage and atomic percentage of each element were also marked. Table 5.1 compares the actual weight percentage calculated from its stoichiometric composition with the average weight percentage obtained from the SEM-EDX analysis. The microstructure composition was obtained as $\text{Ag}_{0.927}\text{Sb}_{1.07}\text{Te}_{2.005}$, and it confirms an off-stoichiometry from the actual composition with $x \sim 0.07$ [31]. Lee et al. report that the δ phase

was identified as Ag deficient and Sb rich, with composition inhomogeneity generated due to the formation of Ag_2Te within or near the cubic phase from excess Ag, [32] and here the monoclinic Ag_2Te [33] results in the off- stoichiometry.

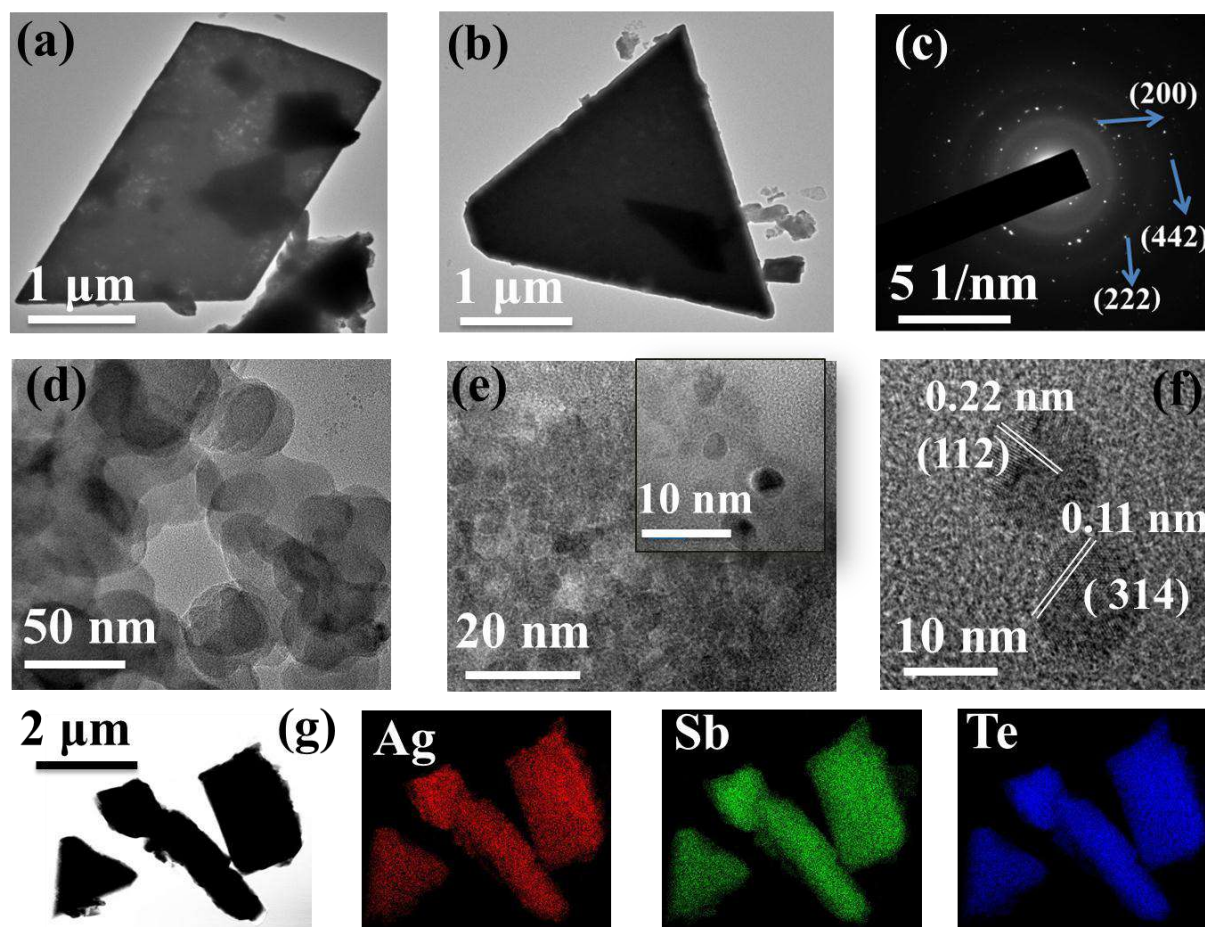


Figure 5.4. (a), (b), TEM images of AgSbTe_2 , (c) SAED pattern of the material under study; (d)- (e) Observed nanostructures in AgSbTe_2 , (f) HRTEM image of the sample confirms the Ag_2Te monoclinic phase and (g) TEM-EDS elemental mapping of the material

Various microstructures like plates, and triangular-shaped sheets (Figure 5.4a,b) were further confirmed through the TEM analysis. Figure 5.4c shows the TEM-SAED pattern of the material, and the planes exactly match the cubic phase of AgSbTe_2 . The clear evidence of nanoprecipitates in off-stoichiometric cubic AgSbTe_2 was found in both low- and high-resolution TEM images and is shown in d & e of Figure 5.4. The nanostructures in AgSbTe_2 emerged from the ordering of cations ($\text{Ag}^+/\text{Sb}^{3+}$) into nanoscale domains, [34,35] and previous studies reveal that AgSbTe_2 exist with secondary phases such as Ag_2Te , Sb_2Te_3 , or Ag-Sb rich nanodots. The nanoscale continuous precipitates of Ag_2Te can be observed within the Ag-deficient region of AgSbTe_2 [32] and conventional melted or hot-pressed samples

exhibit white and dark nanodots of Ag_2Te and Sb-rich regions (Sb_2Te_3) respectively [25,32]. The EDX composition confirms the Ag-deficient nature of the synthesized material, and the observed nanodots can be marked as the secondary phase Ag_2Te . Figure 5.4f shows the calculated d spacing of the planes in the nanodots; d spacing of 0.22 nm and 0.11 nm correspond to the planes (112) and (314) of the monoclinic Ag_2Te [24]. These nanostructures can modulate various electronic and thermal transport properties in the material. Figure 5.4g shows the TEM-EDS elemental mapping of the powdered sample, and it confirms the uniform distribution of all three constituent elements Ag, Sb and Te throughout the material on a micrometre scale.

5.1.2. Thermoelectric studies

The temperature-dependent electrical and thermal transport properties were carried out over the temperature range of 6 K to 300 K and are shown in Figures 5.5a-d. The resistivity curve has a minimum around a particular temperature $T_m \sim 95$ K (Figure 5.5a), and this minimum temperature indicates the transition from a normal semiconductor[36] to a heavily doped semiconductor or metal-like material. At low temperatures, the minimum resistivity in disordered materials arises due to the competition between the weak localization of electronic states and disorder-enhanced electron-electron interaction [36]. It was reported that pristine AgSbTe_2 has a $T_m \sim 61$ K, and the increase in this minimum temperature is a measure of disorder in this material [37], it indicates that the enhanced disorder is due to the localized states of Ag_2Te . On further increasing the temperature to 300 K, the material exhibits a heavily doped semiconducting nature with low electrical conductivity. The low-temperature electrical transport properties of the disordered semiconductors can be explained by the Variable Range Hopping Model (VRH) [37,38] and Mott found that at low temperatures the most probable transport process would not be the nearest neighbour hopping [39]. Mott's variable range hopping mechanism establishes the hopping conduction between localized states with energies concentrated within a narrow band ($\sim k_B T$) in the vicinity of Fermi level (E_F) at relatively low temperatures [40]. The hopping mechanism is associated with both thermally activated hopping over a potential barrier and phonon-assisted quantum mechanical hopping between the states [41]. According to the VRH model, the temperature dependence of electrical conductivity is expressed as $\sigma \propto \exp [-(T_0/T)^S]$, with $s = 1/(1+d)$, where d is the dimensionality of the system and T_0 is the characteristic hopping temperature [42]. The linear dependence of logarithmic σ on $T^{-1/4}$ is shown in Figure 5.5b, and it was observed that the off-stoichiometric AgSbTe_2 exhibits the VRH conduction in a temperature range of $13 \text{ K} < T$

< 84 K. Hatayama et al. pointed out that local structural defects due to the nanoclusters [43], small grain boundaries [44] and dangling bonds [45] can generate localized states within the band gap. Here, the disorder and inhomogeneity stem from the Ag₂Te nanostructures that create a structural difference from the actual one and lead to the dangling bonds. The carriers can tunnel between the localized states generated by this δ -AgSbTe₂/Ag₂Te system within the impurity energy band [38].

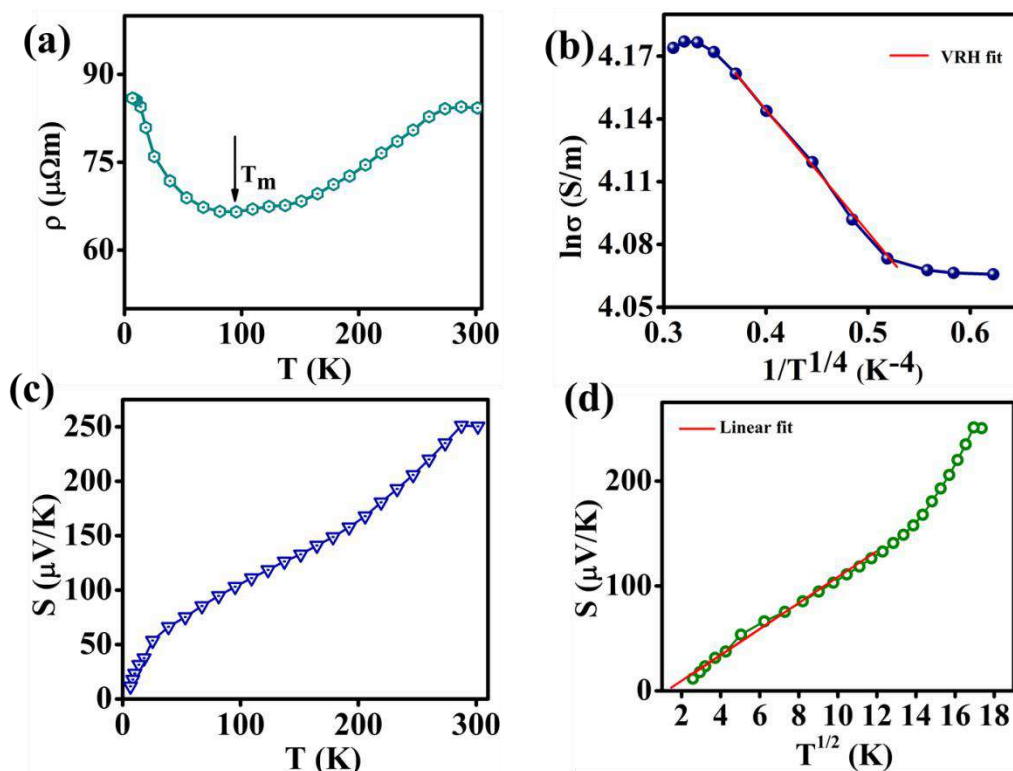


Figure 5.5. (a) Temperature dependence of electrical conductivity; (b) VRH fit on electrical conductivity versus T data ; (c) Temperature dependence of Seebeck coefficient; (d) VRH fit on the S versus T data

Figure 5.5c shows that the Seebeck coefficient (thermopower) increases with temperature and is positive over the entire range of temperatures. The positive value of S indicates that holes are the majority of charge carriers, and according to the previous reports, the p-type carriers are generated due to the Ag vacancies [46, 10]. Most of the studies report that the ternary chalcogenide AgSbTe₂ has a high S value in the range of 220 $\mu\text{V}/\text{K}$ - 300 $\mu\text{V}/\text{K}$. It is further enhanced through doping at various sites [10,47,48] and in the present study, the material attains a maximum value of thermopower around 251 $\mu\text{V}/\text{K}$ at room temperature. According to the VRH hopping model, the Seebeck coefficient follows the relation $S \sim T^{(d-1)/(d+1)}$ where d is the dimensionality of the system [49]. Figure 5.5d validates the S versus $T^{1/2}$ relation: when

the temperature approaches zero S exactly fits with $T^{1/2}$ and $S \rightarrow 0$ as $T \rightarrow 0$ [50,51] and it demonstrates that large S at the low temperature range is due to the hopping of holes [50,52].

The enhancement of the Seebeck coefficient in thermoelectric materials includes band engineering through lowering carrier concentration (n), enhancing effective mass, the energy filtering effect, and increasing scattering parameters [49]. Roychaowdhury et al. report that the high density of states' effective mass can contribute to the high Seebeck coefficient,[53] and that comes from the increase in density of states around the Fermi level. Hoang et al. found that the enhanced S value in AgSbTe_2 is due to the existence of the flat and multivalley valence band [54]. The cation disorder in Ag-Sb-Te-based materials has a vital role in transport properties due to the creation of localized electronic states near the Fermi level. In these disordered materials, the mobility edge separates the localized states from the extended states. When the mobility edge comes near the Fermi level, it results in a distortion in the electronic density of states, which enhances the Seebeck coefficient [55]. The Seebeck coefficient of the degenerate semiconductor or metal can be expressed by the Mott formula [56]

$$\alpha = \frac{8\pi^2 k_B^2 T}{3eh^2} m^* \left(\frac{\pi}{3n}\right)^{2/3}$$

Where n is the carrier concentration, k_B is the Boltzmann constant, e is the electronic charge, h is the Planck constant, and m^* is the density of the state effective mass. It shows that S is inversely proportional to the carrier concentration, and directly depends on the effective mass, and for a particular carrier concentration the Seebeck coefficient can increase with the scattering factor [57]. The presence of nanopores and nanograins in the matrix may enhance the scattering mechanism[58]. The carrier concentration (n) and carrier mobility (μ) were estimated from the Hall effect measurements at room temperature, and the positive slope of ρ_{xy} versus H further confirms the p-type carriers. The effective mass was calculated from the experimentally measured S and n , and the obtained S , n , μ , and m^* values were tabulated in Table 5.2. It was found that the material has an optimized carrier concentration that is required for a promising thermoelectric material and the effective mass slightly contributes to the high Seebeck coefficient at room temperature.

Table 5.2: Obtained values of n , μ , and m^* from Hall effect measurement and Mott equation.

T(K)	α ($\mu\text{V/K}$)	n ($/\text{cm}^3$)	μ ($\text{cm}^2\text{V}^{-1}\text{s}^{-1}$)	m^*/m_0
300K	251	2.5×10^{19}	29.70	1.1

A peak in the temperature-dependent thermopower was observed in thermoelectric materials with bipolar conduction mechanisms [59,60]. Goldsmid and Sharp formulated an analytical expression $E_g = 2eS_{\text{max}}T_{\text{max}}$ based on bipolar conduction, it connects the parameters band gap (E_g), maximum thermopower $|S_{\text{max}}|$ and maximum temperature T_{max} , where T_{max} is the temperature at which the thermopower attains a maximum value [61,62]. The bipolar conduction in the semiconducting materials comes from the thermal excitation of the electrons and holes across the band gap. The presence of minority charge carriers results in a variation in the trend of the Seebeck coefficient with increasing temperature, and the total Seebeck coefficient is the collective contribution from both charge carriers [62]. At low temperatures, the minority charge carriers will not contribute much to the Seebeck coefficient. The increase in temperature results in the broadening of Fermi distribution, which enhances the electrical conductivity due to the minority carriers and reduces the Seebeck coefficient. In p-type material, the generation of electrons at high temperatures results in a peak in the thermopower, and it is the simplest way to obtain the energy gap of the material from the temperature-dependent S data [62],[60]. The variation of the Seebeck coefficient with temperature from 6 K to 800 K was shown in Figure A.5.1, and the S_{max} was obtained from the peak of the curve. It was found that the material exhibits an energy gap of ~ 0.15 eV at a maximum temperature of 300 K, and AgSbTe_2 is widely accepted as a narrow band gap semiconductor[46]. Hoang et al. estimated the E_g at high temperatures from electrical conductivity measurements as 0.1 eV [54]. The dependence of $\rho(H)$ and $\rho(T)$ on VRH conductivity can be expressed in a single relation[38].

$$\ln \frac{\rho(H)}{\rho(0)} = t_1 \left(\frac{a}{L_H} \right)^4 \left(\frac{T_0}{T} \right)^{3/4}$$

Where $\frac{\rho(H)}{\rho(0)}$ is the ratio of electrical resistivity at the magnetic field to zero field, t_1 is the constant equal to 5/2016, a is the localization radius of the electron, $L_H = (ch/2\pi eH)^{1/2}$, and c is the speed of light.

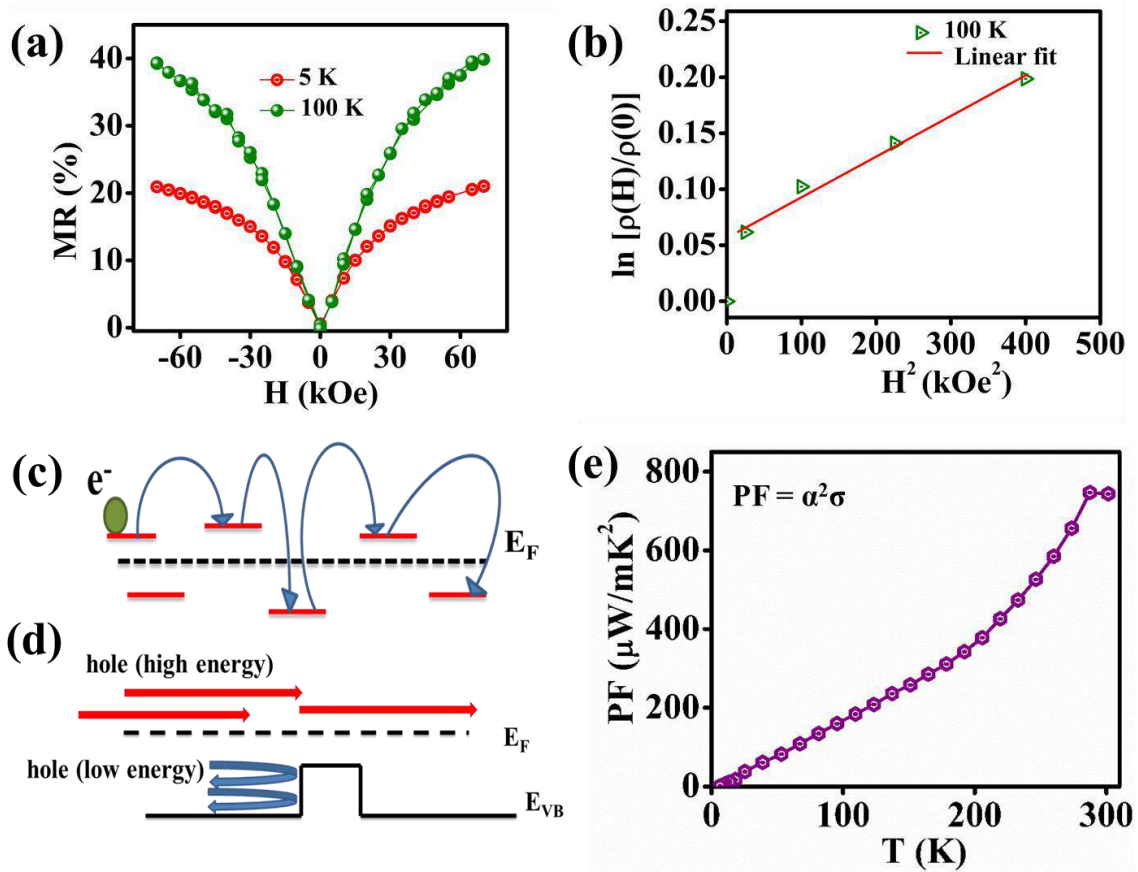


Figure 5.6. (a) Magnetoresistance versus magnetic field plot; (b) Linear fit on $\ln \rho (H)/\rho(0)$ versus H^2 , Schematic representation of (c) VRH mechanism, (d) Electron filtering mechanism, and (e) PF versus T plot

Linear magnetoresistance (LMR) is another interesting electronic property witnessed in inhomogeneous and disordered semiconductors [63–65]. Xu et al. found for the first time that nonmagnetic silver selenides and tellurides exhibit an unusual increase in resistance to magnetic fields and they show an unsaturated nature even at higher fields [66]. In inhomogeneous conductors, the LMR originates from the variation in the current path generated by the macroscopic spatial fluctuations of carrier mobility induced by the variation in material density and thickness [66,67]. The transverse magnetoresistance (applied magnetic field perpendicular to the current direction in the material) measurements were carried out up to 70 kOe at lower temperatures (5 K and 100 K). Figure 5.6a establishes clear evidence of unsaturating LMR in this disordered material, and it exhibits a high MR of 40% at 100K. The semiconductors with VRH conductivity obey the linear dependence of $\ln (\rho (H))/(\rho(0))$ with H^2 and are confirmed for 100K in Figure 5.6b and Figure 5.6c depicts the schematic representation of the VRH mechanism.

Another major factor behind the high α value in disordered material may be due to the electron filtering mechanism triggered by the nanoscale and microscale structures [68]. The energy filtering effect of carriers plays a major role in enhancing α ; in this effect, a barrier permits the high-energy carriers and scatters the low-energy carriers, [49] as demonstrated in figure 5.6d. The barriers were due to the naturally occurring or intentionally created interfaces between the matrix and nanoprecipitates. The Seebeck coefficient value is associated with the Fermi level of the material through the relationship

$$\alpha = -\frac{E_J - E_F}{k_B T}$$

Where E_J is the mean energy of the charge carriers and k_B is the Boltzmann constant. The Seebeck coefficient increases with an increase in quantity $|E_J - E_F|$ and it strictly depends on the relative shift of E_F concerning E_J . P-type semiconductors with energy barriers block the holes having low energy, which is very close to the Fermi level. It results in the accumulation of high-energy holes at the cold end and enhances the Seebeck coefficient [69]. In the present material, nanoprecipitates of Ag_2Te with AgSbTe_2 create an interface that acts as a scattering barrier for energy filtering of carriers and, thereby enhances the S value. Figure 5.6e represents the calculated temperature-dependent power factor ($\alpha^2\sigma$) [70] of $\text{Ag}_{0.927}\text{Sb}_{1.07}\text{Te}_{2.005}$ from the measured S and σ . It was observed that this particular composition has a power factor of $747 \mu\text{W}/\text{mK}^2$ near room temperature, and it comes from the Seebeck value.

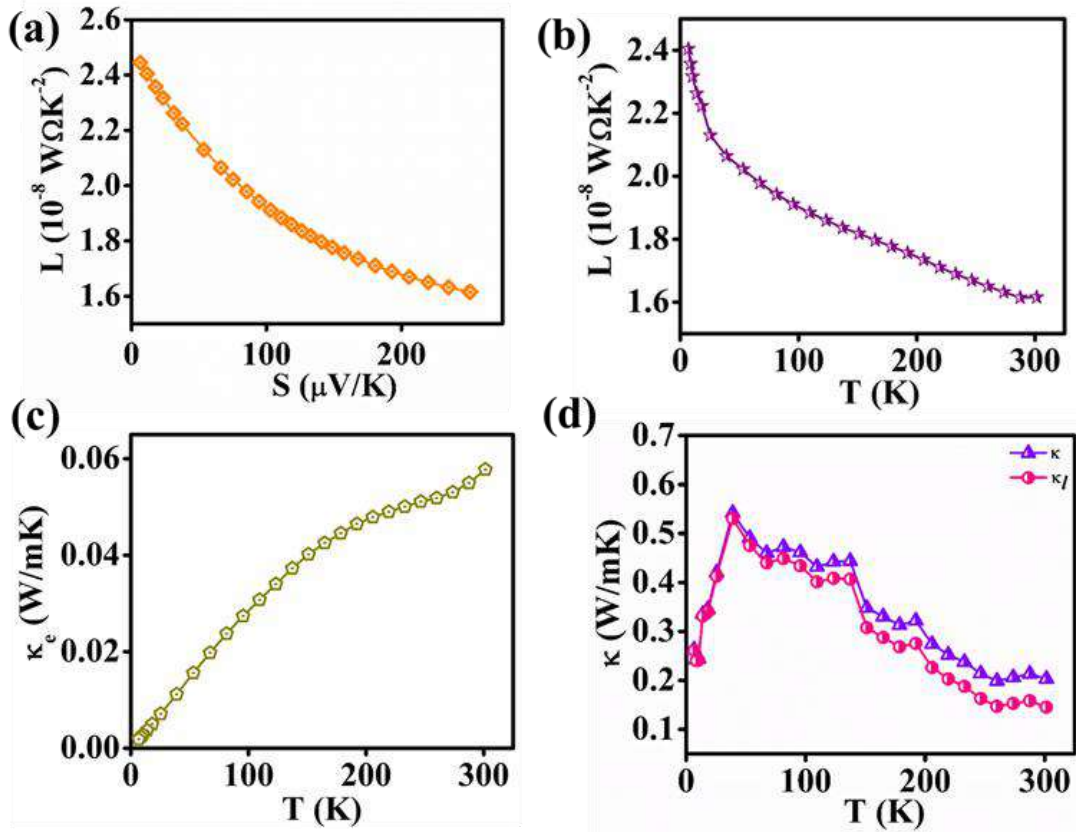


Figure 5.7. (a) Calculated Lorenz number from S ; (b) Variation of L with T ; Variation of (c) electronic thermal conductivity with T ; (d) total and lattice thermal conductivity with T

For metals (degenerate limit), the Lorenz number (L) is approximated as $2.44 \times 10^{-8} \text{ W}\Omega\text{K}^{-2}$, and in degenerate semiconductors, the approximate value of L is calculated from the expression [71] $L = 1.5 + \exp(-|S|/116)$, where L is in $10^{-8} \text{ W}\Omega\text{K}^{-2}$ and S is the Seebeck coefficient in $\mu\text{V}/\text{K}$. Figures 5.7 (a), and (b) show the variation of L with both the Seebeck coefficient and temperature; it decreases with increasing temperature due to various scattering, such as acoustic phonon scattering [71,72]. The total thermal conductivity of a material is the sum of its electronic thermal conductivity (k_e) and lattice thermal conductivity (k_l). The electronic part of the thermal conductivity (k_e) can be obtained with the help of the Wiedemann-Franz law ($k_e = L\sigma T$) and Figure 5.7c shows the temperature-dependent. The variation of total and lattice thermal conductivity of the sample is shown in Figure 5.7d, and it is found that the major part of the thermal conductivity comes from the lattice contribution. At low temperatures, the material has a T^3 -dependent thermal conductivity and attains a maximum of 0.5 W/mK at 40 K, then decreases with increasing temperature due to the dominant phonon scattering [10]. At room temperature, the total thermal conductivity of the material reduces to a glass-like thermal conductivity of 0.2 W/mK [73,74].

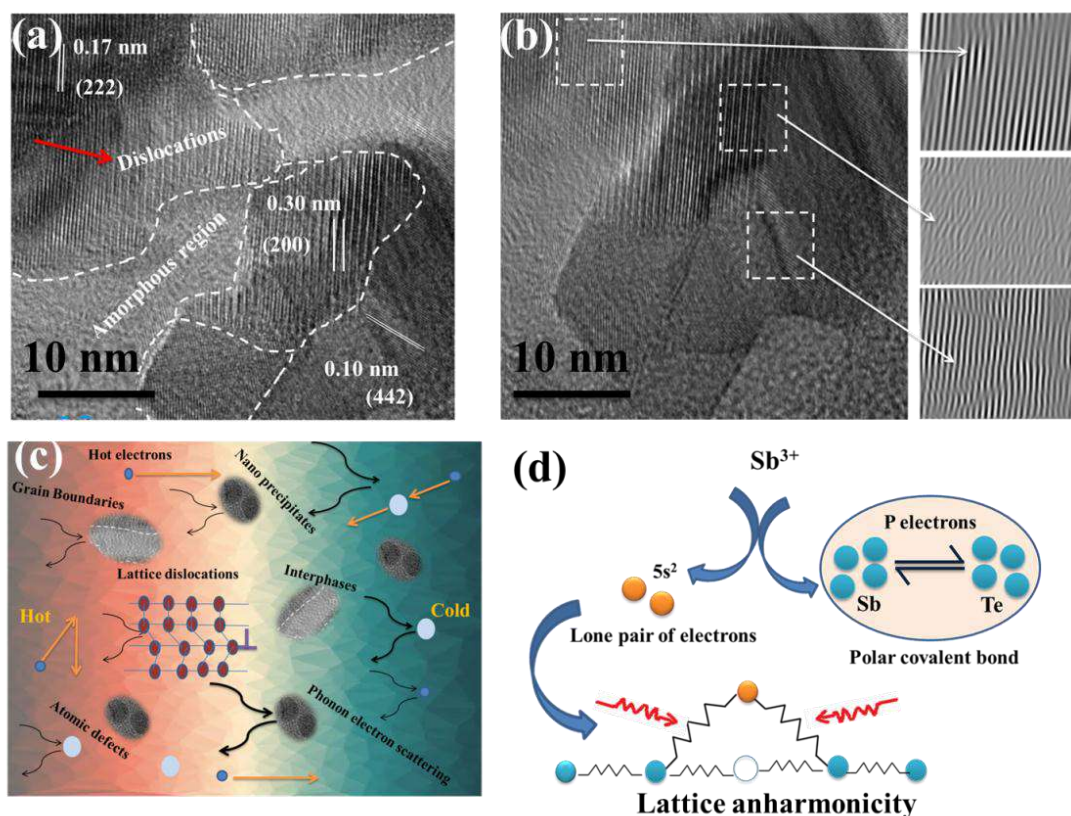


Figure 5.8. HRTEM images of the sample (a), amorphous, crystalline regions and dislocations; (b) IFFT of HRTEM images clearly shows the lattice dislocations; (c) schematic representation of phonon scattering mechanisms; and (d) 1D ball and spring model for phonon-phonon interaction

The low thermal conductivity of AgSbTe_2 -based materials was associated with phonon scattering at the structural disorder, point defects, nano inclusions, and strong lattice anharmonicity. The combination of crystalline, amorphous regions, and dislocations were noticeable in the high magnification TEM images of the sample in a and b of Figure 5.8. The boundaries were marked between the interphase of crystalline and amorphous regions, and the dislocations were visible in the Inverse Fast Fourier Transform (IFFT) of HRTEM images. Figure 5.8c confines various parameters that contribute to the phonon scattering in this material and concludes that the phonons encounter scattering at various interphases that include nanostructures, defects, dislocations, and boundaries [75,76].

In the cubic rock salt crystal structure of nominal AgSbTe_2 , the disordered distribution of Ag^+ and Sb^{3+} between the closely packed layers of Te ions contributes to the lattice anharmonicity [77,78]. Normally in the class of I-V-VI₂ (chalcoantimonates) materials, the nonbonding of

the exterior s and a fraction of the p electrons forms a shell of large radius, which leads to anharmonicity bonds in these compositions [79]. Figure 5.8d shows the proposed schematic representation of the 1D ball and spring model for phonon-phonon interaction with the bonding of Sb-Te [76]. In AgSbTe_2 , the Sb has a valence configuration of $5s^2 5p^3$, Sb^{3+} results in a lone pair of electrons ($5s^2$), and the p electrons of Sb and Te form a polar covalent bond and separately form the band. The competition between covalent bonding and lone pair repulsion results in the anharmonicity in lattice vibrations of these materials [76]. Tan et al. report that the overlapping of wave functions of the lone pair of electrons and the nearby valence electrons leads to the nonlinear repulsive electrostatic force [80]. The occupancy of chemically dissimilar atoms at the same crystallographic site generates distortion in the structure, and the differences in the local force constants of Ag^+ and Sb^{3+} induce phonon scattering in AgSbTe_2 [20,81].

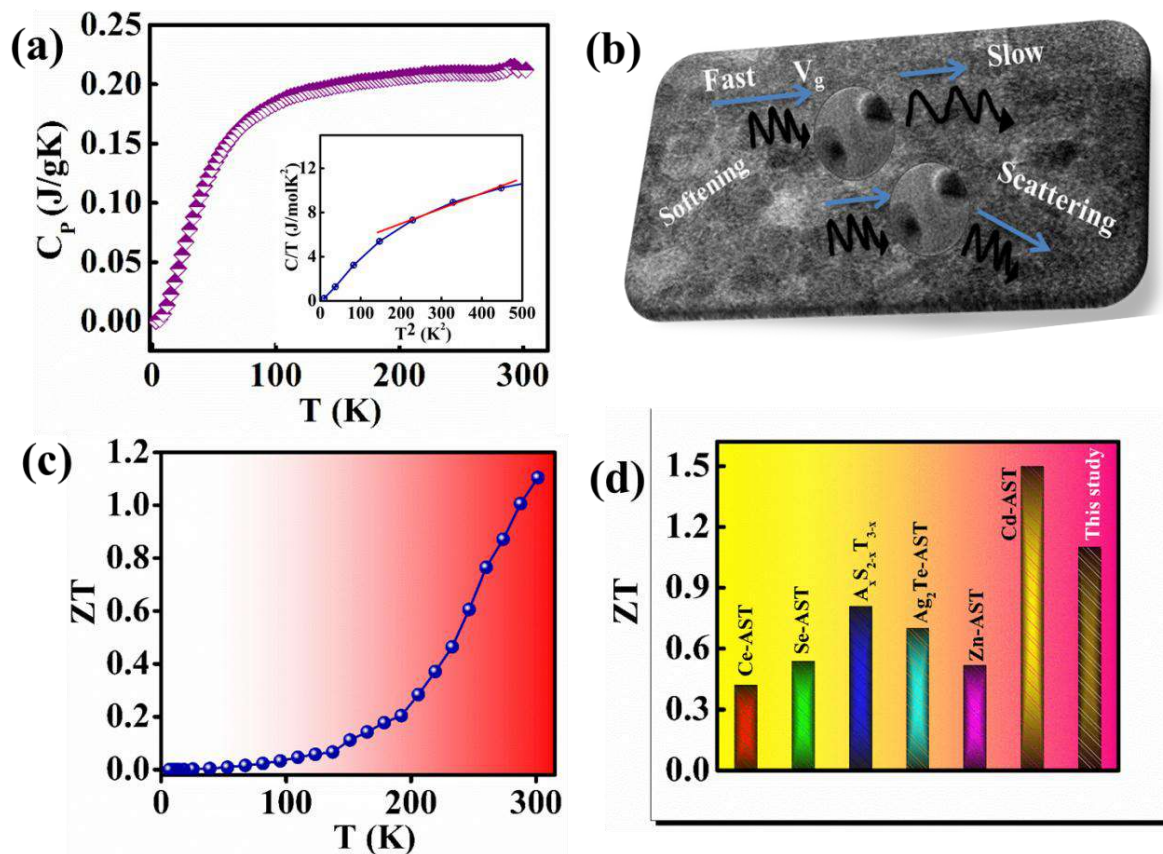


Figure 5.9. (a) Temperature-dependent heat capacity of the material (inset: C/T versus T^2 plot), (b) Schematic explanation for lattice softening, (c) Variation of ZT with temperature, (d) A comparison of ZT of the present material with previous reports

The spontaneous nanostructures, due to the cationic ordering, can scatter the phonons effectively [27] and the spontaneous nanostructures in the present material were confirmed

through TEM analysis, which scatters the phonons and reduces the lattice thermal conductivity remarkably. The low temperature heat capacity of the sample was measured under a high vacuum between 2 K and 300 K as shown in Figure 5.9a. In the heat capacity measurement, a known heat pulse is applied at each point of temperature, and the material and platform are heated to a temperature of $T_p(t)$. At the end of the heat pulse, the sample temperature relaxes to a particular temperature, T_0 , where T_0 is known as the heat sink temperature and is expressed by the relation[82]

$$T_p = T_0 + \Delta T \exp(-t/\tau)$$

Where τ is the time constant, and according to Dulong-petit law, the near room temperature heat capacity of the material was found to be 0.205 J/g K [33]. The experimental C_p value near room temperature was determined as 0.212 J/g K, and it is well in agreement with the theoretically calculated value. At low temperatures, the heat capacity of a nonmagnetic material can be expressed as the sum of the contributions from electrons and phonons,

$$C_p = \alpha T + \beta T^3$$

Where α and β are constants, in the expression, the first part corresponds to the electronic contribution, and the second part arises from the lattice contribution to the heat capacity. The density of states (DOS) at the Fermi level ($E = E_F$) can be calculated from the electronic part of heat capacity by using the expression[83]

$$\gamma = \frac{\pi^2}{3} (k_B^2) N(E_F)$$

Where k_B is the Boltzmann's constant and the material has a high density of states $1.1 \times 10^{27} \text{ eV}^{-1} \text{ mol}^{-1}$ at E_F , and it contributes to the enhancement in Seebeck coefficient through heavy carrier effective mass. At low temperatures, the data was fitted with C/T versus T^2 (inset of Figure 4.9a) and the Debye temperature was obtained from β by using the relation [84]

$$\theta_D = \left(\frac{12\pi^4 NR}{5\beta} \right)^{1/3}$$

Where N is the number of atoms per chemical formula, R is the molar gas constant. It was confirmed that from the linear fit of C/T versus T^2 , the material obeys the Debye T^3 law, and the estimated Debye temperature was ~ 91 K. Morelli et al. reported that the material AgSbTe_2 exhibits $\theta_D \sim 125\text{K}$ [85]. It was found that the reduction in Debye temperature was associated with the lattice softening in the material; the phonons met the softening (the

reduction in group velocity of phonons) and scattering at the nanostructures [86]. The various lattice defects, dislocations, and nanostructures change the phonon frequency in a disordered material, generating lattice softening that reduces the phonon speed and leads to phonon scattering [87]. The lattice softening reduces the overall thermal conductivity of the material, and that helps to tune the thermoelectric efficiency by introducing internal lattice strain [87]. Figure 5.9b shows the pictorial representation of lattice softening and scattering at nanoprecipitates.

The dimensionless figure of merit ZT of the present material was calculated from various measured parameters S , σ , and k using; the variation of ZT as a function of temperature is plotted in Figure 5.9c. At room temperature, the material exhibits a ZT of 1.1 and can be further increased by various defect engineering techniques. Figure 5.9d displays the comparison study of the ZT of doped AgSbTe_2 with the current material, and this nonstoichiometric compound has the highest ever reported ZT value at room temperature.

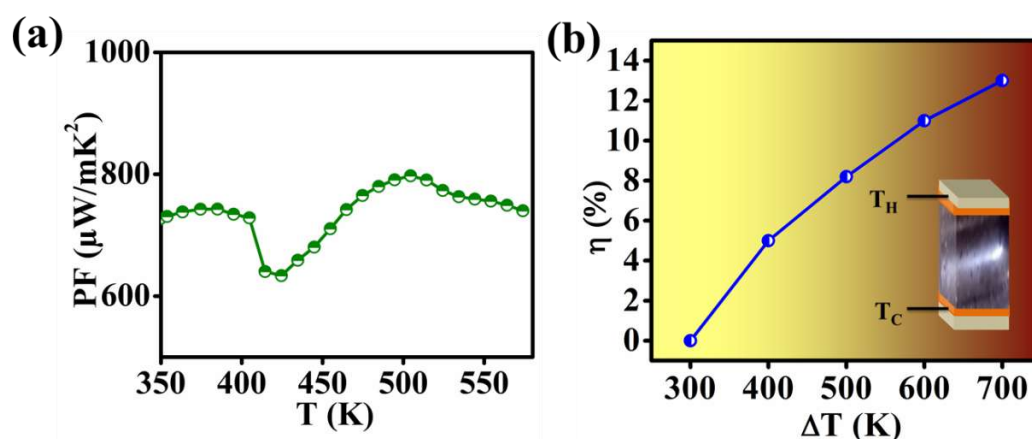


Figure 5.10. (a) High-temperature PF versus T; (b) Variation of calculated one-leg TE efficiency with ΔT

The high-temperature thermoelectric power factor (Figure 5.10a) reveals that this material can be applied to elevated-temperature TEGs. The single-leg TEG has an enhanced efficiency (η) of 12.5% (Figure 5.10b) at a temperature gradient of 700 K. On an application level, the thermoelectric materials should have temperature and mechanical stability, which was confirmed through thermogravimetric analysis and Vickers hardness measurement. The off-stoichiometric AgSbTe_2 has high thermal stability up to 841 K, and the endothermic dip in the DTA analysis of the material corresponds to the melting temperature in the range of 825 K and the peak at 713 K is due to the recrystallization of the material on cooling. Figures A.5.2.a, b represents the TGA and DTA data of the material. It was observed that the material

exhibits a high Vickers hardness[88] value H_v of $\sim 108.47 \text{ kgf/mm}^2$ and was found to be much higher when compared with conventional TE materials Bi_2Te_3 (63 kgf/mm^2) and PbTe (24 kgf/mm^2) [89].

5.2. Conclusion

Ternary chalcogenide AgSbTe_2 was synthesized by the direct melting of high-purity component elements, yielding a high-density material with a composition of $\text{Ag}_{0.927}\text{Sb}_{1.07}\text{Te}_{2.005}$. The metastable AgSbTe_2 crystallizes in the cubic phase with space group Fm-3m , with Ag and Sb randomly occupying the same site to contribute towards the unique transport properties. The presence of nanostructures of Ag_2Te was observed in SEM and confirmed through EDX composition analysis and HRTEM. At extremely low temperatures, this disordered material unveils a variable-range hopping mechanism due to the presence of localized states. The high Seebeck coefficient of the order of $251 \mu\text{V/K}$ at room temperature could be attributed to the high DOS near the E_F and electron filtering mechanisms triggered by the nanoscale structures of Ag_2Te . The energy gap of 0.15 eV was determined from the temperature-dependent thermopower data. The lower thermal conductivity (0.2 W/mK) at ambient temperature predominantly depends on the spontaneous cation ordering that formed nanostructures functioning as powerful phonon scattering centres. Additionally, the point defects, interfaces, and lattice anharmonicity, all contributed to the lessened thermal conductivity. The confirmation of the lattice relaxation in this disordered material was achieved by observing a decrease in the Debye temperature. At ambient temperature, a power factor of $741 \mu\text{W/mK}^2$ and ZT of 1.1 were achieved which increased with increasing temperature, reaching a calculated efficacy of 12.5% at a $\Delta T = 700 \text{ K}$.

Reference

- [1] T.M. Tritt, M.A. Subramanian, Thermoelectric Materials, Phenomena , and Applications : A Bird ' s Eye View, Mater. Res. Bull. 31 (2006) 188–198.
- [2] M.S. Dresselhaus, G. Chen, M.Y. Tang, R. Yang, H. Lee, D. Wang, Z. Ren, J.P. Fleurial, P. Gogna, New directions for low-dimensional thermoelectric materials, Adv. Mater. 19 (2007) 1043–1053. <https://doi.org/https://doi.org/10.1002/adma.200600527>.
- [3] G.J. Snyder, E.S. Toberer, Complex thermoelectric materials, Nat. Mater. 7 (2008) 101–110.
- [4] M.G. Kanatzidis, Ultralow thermal conductivity and high thermoelectric figure of merit in SnSe crystals, Nature. 508 (2014) 373–378.
- [5] S.N. Guin, K. Biswas, Sb deficiencies control hole transport and boost the thermoelectric performance of p-type AgSbSe₂, J. Mater. Chem. C. 3 (2015) 10415–10421.
- [6] P. Jood, R. Chetty, M. Ohta, Structural stability enables high thermoelectric performance in room temperature Ag₂Se, J. Mater. Chem. A. 8 (2020) 13024–13037.
- [7] J. Liang, T. Wang, P. Qiu, S. Yang, C. Ming, H. Chen, Q. Song, K. Zhao, T.R. Wei, D. Ren, Y.Y. Sun, X. Shi, J. He, L. Chen, Flexible thermoelectrics: From silver chalcogenides to full-inorganic devices, Energy Environ. Sci. 12 (2019) 2983–2990.
- [8] L.C. Yi Wu , Pengfei Qiu, Yuan Yu, Yifei Xiong, Tingting Deng, Oana Cojocaru-Miredin Matthias Wuttig, Xun Shi a, High-performance and stable AgSbTe₂-based thermoelectric materials for near room temperature applications, J.Mater. 8 (2022) 1095–1103.
- [9] A.J.E. Rettie, C.D. Malliakas, A.S. Botana, J.M. Hodges, F. Han, R. Huang, D.Y. Chung, M.G. Kanatzidis, Ag₂Se to KAg₃Se₂: Suppressing Order-Disorder Transitions via Reduced Dimensionality, J. Am. Chem. Soc. 140 (2018) 9193–9202.
- [10] S.N. Zhang, T.J. Zhu, S.H. Yang, C. Yu, X.B. Zhao, Improved thermoelectric properties of AgSbTe₂ based compounds with nanoscale Ag₂Te in situ precipitates, J. Alloy. Compd. 499 (2010) 215–220.
- [11] S. Singh, K. Hirata, D. Byeon, T. Matsunaga, O. Muthusamy, S. Ghodke, M. Adachi,

- Y. Yamamoto, M. Matsunami, T. Takeuchi, Investigation of Thermoelectric Properties of $\text{Ag}_2\text{S}_x\text{Se}_{1-x}$ ($x = 0.0, 0.2$ and 0.4), *J. Electron. Mater.* 49 (2020) 2846–2854.
- [12] J. Zhang, X. Qin, D. Li, C. Song, Y. Liu, H. Xin, T. Zou, Y. Li, Optimized thermoelectric properties of AgSbTe_2 through adjustment of fabrication parameters, *Electron. Mater. Lett.* 11 (2015) 133–137.
- [13] J.P. McHugh, W.A. Tiller, S.E. Haszko, J.H. Wernick, Phase diagram for the pseudobinary system $\text{Ag}_2\text{Te}-\text{Sb}_2\text{Te}_3$, *J. Appl. Phys.* 32 (1961) 1785.
- [14] S.Y. Tee, D. Ponsford, C.L. Lay, X. Wang, X. Wang, D.C.J. Neo, T. Wu, W. Thitsartarn, J.C.C. Yeo, G. Guan, T.C. Lee, M.Y. Han, Thermoelectric Silver-Based Chalcogenides, *Adv. Sci.* 9 (2022) 1–35.
- [15] G. Qin, X. Zhang, S. Yue, Z. Qin, H. Wang, Y. Han, M. Hu, Resonant bonding driven giant phonon anharmonicity and low thermal conductivity of phosphorene, *Phy. Rev. B.* 94 (2016) 1–11.
- [16] C.W. Li, J. Hong, A.F. May, D. Bansal, S. Chi, T. Hong, G. Ehlers, O. Delaire, Orbitally driven giant phonon anharmonicity in SnSe , *Nat. Phys.* 11 (2015) 1–8.
- [17] M.G. Kanatzidis, Nanostructured Thermoelectrics : The New Paradigm ?, *Chem.Mater.* 22 (2010) 648–659.
- [18] J.K. Lee, M.W. Oh, S.D. Park, B.S. Kim, B.K. Min, M.H. Kim, H.W. Lee, Improvement of Thermoelectric Properties through Controlling the Carrier Concentration of $\text{AgPb}_{18}\text{SbTe}_{20}$ Alloys by Sb Addition, *Electron. Mater. Lett.* 8 (2012) 659–663.
- [19] R. Mohanraman, R. Sankar, F.C. Chou, C.H. Lee, Y. Chen, R. Mohanraman, R. Sankar, F.C. Chou, C.H. Lee, Enhanced thermoelectric performance in Bi-doped p-type AgSbTe_2 compounds Enhanced thermoelectric performance in Bi-doped p-type AgSbTe_2 compounds, *J. Appl. Phys.* 163712 (2014) 16–21.
- [20] G. Ehlers, T. Hong, A. Huq, W. Tian, V.M. Keppens, B.C. Sales, Glass-like phonon scattering from a spontaneous nanostructure in AgSbTe_2 , *Nat. Nanotechnol.* 8 (2013) 445–451.
- [21] R. Marin, G.I.R. Brun, J. Tedenac, P.E. Bataillon, M. Cedex, Phase equilibria in the

- Sb₂Te₃-Ag₂Te system, *J.Mater.Sci.* 20 (1985) 730–735.
- [22] B. Legendre, G. Brun, B. Liautard, J.C. Tedenac, THE TERNARY SYSTEM SILVER-ANTIMONY-TELLURIUM. STUDY OF THE SUBTERNARY Sb,Tq-Ag, Te-Te, *Thermochim. Acta.* 131 (1988) 37–45.
- [23] P.M. WYZGA and K.T., Wojciechowski, Analysis of the Influence of Thermal Treatment on the Stability of Ag_{1-x}Sb_{1+x}Te_{2+x} and Se-Doped AgSbTe₂, *J.Electron.Mater.* 45 (2016) 1548–1554.
- [24] J.D. Sugar, D.L. Medlin, Precipitation of Ag₂Te in the thermoelectric material AgSbTe₂, *J. Alloy. Compd.* 478 (2009) 75–82.
- [25] S.N. Zhang, T.J. Zhu, S.H. Yang, C. Yu, X.B. Zhao, Phase compositions, nanoscale microstructures and thermoelectric properties in Ag_{2-y}Sb_yTe_{1+y} alloys with precipitated Sb₂Te₃ plates, *Acta Mater.* 58 (2010) 4160–4169.
- [26] S.P. Jae Ki Lee , Byungki Ryu, Sungjin Park, Ji Hee Son, Jongho Park, Jeongin Jang, Min-Wook Oh, Effect of microstructure on thermoelectric conversion efficiency in metastable δ -phase AgSbTe₂, *Acta Mater.* 222 (2021) 117443.
- [27] J. Ki, B. Ryu, S. Park, J. Hee, J. Park, J. Jang, M. Oh, S. Park, Effect of microstructure on thermoelectric conversion efficiency in metastable δ -phase AgSbTe₂, *Acta Mater.* 222 (2022) 117443.
- [28] S. Sahu, A. Manivannan, H. Shaik, G.M. Rao, S. Sahu, A. Manivannan, H. Shaik, G.M. Rao, Local structure of amorphous Ag₅In₅Sb₆₀Te₃₀ and In₃SbTe₂ phase change materials revealed by X-ray photoelectron and Raman spectroscopic studies Local structure of amorphous Ag₅In₅Sb₆₀Te₃₀ and 3 SbTe₂ phase change materials revealed by X-ray pho, *J. Appl. Phys.* 122 (2017) 1–6.
- [29] S.K. Pandey, S.K. Pandey, V. Awasthi, A. Kumar, U.P. Deshpande, S. Mukherjee, p-type conduction from Sb-doped ZnO thin films grown by dual ion beam sputtering in the absence of oxygen ambient, *J. Appl. Phys.* 114 (2013) 1–7.
- [30] Y. Liu, M. Li, S. Wan, K.H. Lim, Y. Zhang, M. Li, J. Li, M. Ib, Surface Chemistry and Band Engineering in AgSbSe₂: Toward High Thermoelectric Performance, *ACS Nano.* 17 (2023) 1–12.

- [31] P.M. WYZGA and K.T., Analysis of the Influence of Thermal Treatment on the Stability of $\text{Ag}_{1-x}\text{Sb}_{1+x}\text{Te}_{2+x}$ and Se-Doped AgSbTe_2 , *J. Electron. Mater.* 45 (2016) 1–8.
- [32] S.P. Jae Ki Lee , Byungki Ryu, Sungjin Park, Ji Hee Son, Jongho Park, Jeongin Jang, Min-Wook Oh, Effect of microstructure on thermoelectric conversion efficiency in metastable δ -phase AgSbTe_2 , *Acta Mater.* 222 (2021) 117443.
- [33] J.K. Lee, M.W. Oh, B. Ryu, J.E. Lee, B.S. Kim, B.K. Min, S.J. Joo, H.W. Lee, S.D. Park, Enhanced thermoelectric properties of AgSbTe_2 obtained by controlling heterophases with Ce doping, *Sci. Rep.* 7 (2017) 1–8.
- [34] G. Ehlers, T. Hong, A. Huq, W. Tian, V.M. Keppens, B.C. Sales, Glass-like phonon scattering from a spontaneous nanostructure in AgSbTe_2 , *Nat. Nanotechnol.* 8 (2013) 1–7.
- [35] T. Ghosh, S. Roychowdhury, M. Dutta, K. Biswas, High-Performance Thermoelectric Energy Conversion: A Tale of Atomic Ordering in AgSbTe_2 , *ACS Energy Lett.* 6 (2021) 2825–2837.
- [36] J.H. and K.B. Riddhimoy Pathak¹, Lin Xie², Subarna Das, Tanmoy Ghosh, Animesh Bhui, Kapildeb Dolui, Dirtha Sanyal, Vacancy Controlled Nanoscale Cation Ordering Leads to High Thermoelectric Performance, *Energy Environ. Sci.* 16 (2023) 3110–
- [37] S. Roychowdhury, T. Ghosh, R. Arora, M. Samanta, L. Xie, Enhanced atomic ordering leads to high thermoelectric performance in AgSbTe_2 , *Science* (80-.). 727 (2021)
- [38] O. Ivanov, M. Yaprincev, Variable-range hopping conductivity in Lu-doped Bi_2Te_3 , *Solid State Sci.* 76 (2018) 111–117.
- [39] L. Zhang, Z. Tang, Polaron relaxation and variable-range-hopping conductivity in the giant-dielectric-constant material $\text{CaCu}_3\text{Ti}_4\text{O}_{12}$, *Phy. Rev. B.* 174306 (2004) 1–6.
- [40] L. Essaleh, S.M. Wasim, G. Marín, C. Rincón, S. Amhil, J. Galibert, Mott type variable range hopping conduction and magnetoresistance in p -type CuIn_3Te_5 semiconductor compound, *J. Appl. Phys.* 122 (2017) 015702.
- [41] Y. Huang, S. Chiu, Z. Zhu, Z. Li, J. Lin, Y. Huang, S. Chiu, Z. Zhu, Z. Li, J. Lin, Variable-range-hopping conduction processes in oxygen deficient polycrystalline ZnO

- films Variable-range-hopping conduction processes in oxygen deficient polycrystalline ZnO films, *J. Appl. Phys.* 107 (2010) 063715.
- [42] K.H. Kim, S. Lara-avila, H. He, H. Kang, S.J. Hong, M. Park, J. Eklöf, K. Moth, S. Matsushita, K. Akagi, S. Kubatkin, Probing variable range hopping lengths by magneto conductance in carbonized polymer nanofibers, *Sci. Rep.* 8 (2018) 1–7.
- [43] S. Hatayama, Y. Shuang, P.J. Fons, Y. Saito, V. Alexander, Cr-Triggered Local Structural Change in Cr₂Ge₂Te₆ Phase Change Material, *ACS Appl.Mater. Interfaces.* 11 (2019) 43320–43329.
- [44] K. Xu, M. Yao, J. Chen, P. Zou, Y. Peng, F. Li, X. Yao, Effect of crystallization on the band structure and photoelectric property of SrTiO₃ sol e gel derived thin fi lm, *J. Alloy. Compd.* 653 (2015) 7–13.
- [45] A. Phys, H. Lu, Y. Guo, H. Li, Modeling of surface gap state passivation and Fermi level de-pinning in solar cells Modeling of surface gap state passivation and Fermi level de-pinning in solar cells, *J. Appl. Phys.* 114 (2019) 222106.
- [46] J.P.H. Jovic, V, Measurements of the energy band gap and valence band structure of AgSbTe₂, *J.Phys.Rev.B.* 77 (2008) 245204.
- [47] H. Wu, S. Chen, T. Ikeda, G.J. Snyder, Reduced thermal conductivity in Pb-alloyed AgSbTe₂ thermoelectric materials, *Acta Mater.* 60 (2012) 6144–6151.
- [48] H. Wang, J.F. Li, M. Zou, T. Sui, Synthesis and transport property of AgSb Te₂ as a promising thermoelectric compound, *Appl. Phys. Lett.* 93 (2008) 202106.
- [49] L. Wang, X. Zhang, L. Zhao, Evolving Strategies Toward Seebeck Coefficient Enhancement, *Acc.Mater.Res.* 4 (2023) 448–456.
- [50] and M.K. K. Suekuni, K. Tsuruta, T. Ariga, Variable-range-hopping conduction and low thermal conductivity in chalcogenide spinel Cu_yFe₄Sn₁₂X₃₂ (X S , Se), *J. Appl. Phys.* 109 (2017) 083709.
- [51] O.E. Parfenov, F.A. Shklyaruk, On the Temperature Dependence of the Thermoelectric Power in Disordered Semiconductors, *Semiconductors.* 41 (2007) 1021–1026.
- [52] P. Zvyagin, On the Theory of Hopping Transport in Disordered Semiconductors,

- Phys.Stat.Sol. 58 (1973) 443–449.
- [53] S. Roychowdhury, R. Panigrahi, S. Perumal, K. Biswas, Ultrahigh Thermoelectric Figure of Merit and Enhanced Mechanical Stability of p-type $\text{AgSb}_{1-x}\text{Zn}_x\text{Te}_2$, ACS Energy Lett. 2 (2017) 349–356.
- [54] K. Hoang, S.D. Mahanti, J.R. Salvador, M.G. Kanatzidis, Atomic Ordering and Gap Formation in Ag-Sb-Based Ternary Chalcogenides, Phy. Rev.Lett. 99 (2007) 1–4.
- [55] J.P. Heremans, Enhancement of Thermoelectric Efficiency in PbTe by Distortion of the Electronic Density of States, Science (80-.). 321 (2008) 554–557.
- [56] J. Lee, S. Choi, W. Seo, Y. Lim, H. Lee, I. Kim, Thermoelectric properties of Spark Plasma Sintered $\text{In}_x\text{Yb}_y\text{La}_{0.3-x-y}\text{Co}_4\text{Sb}_{12}$ skutterudite system, Renew.Energy. 42 (2012) 36–40.
- [57] J.P. Heremans, C.M. Thrush, D.T. Morelli, J.P. Heremans, C.M. Thrush, D.T. Morelli, Thermopower enhancement in PbTe with Pb precipitates Thermopower enhancement in PbTe with Pb precipitates, J. Appl. Phys. 98 (2005) 063703.
- [58] B. Du, H. Li, J. Xu, X. Tang, C. Uher, Enhanced thermoelectric performance and novel nanopores in AgSbTe_2 prepared by melt spinning, J.Solid.State.Chem. 184 (2011) 109–114.
- [59] A. Hmood, A. Kadhim, H.A. Hassam, Superlattices and Microstructures Yb-doped SnTe semimetal thin films deposited by thermal evaporation : Structural , electrical, and thermoelectric properties, Superlattices Microstruct. 76 (2014) 36–45.
- [60] J.H. Son, M.W. Oh, B.S. Kim, S.D. Park, B.K. Min, M.H. Kim, H.W. Lee, Effect of ball milling time on the thermoelectric properties of p-type $(\text{Bi}, \text{Sb})_2\text{Te}_3$, J. Alloy. Compd. 566 (2013) 168–174.
- [61] A. Hmood, A. Kadhim, M.A. Mahdi, H.A. Hassan, ScienceDirect Structural, characterization and electrical properties of $\text{AgPb}_m\text{SbTe}_{m+2}$ compounds synthesized through a solid-state microwave technique, Int. J. Hydrog. Energy. 41 (2016) 5048–5056.
- [62] H.J. Goldsmid, J.W. Sharp, Estimation of the Thermal Band Gap of a Semiconductor from Seebeck Measurements, J.Electron.Mater. 28 (1999) 1–4.

- [63] R. Xu, A. Husmann, T.F. Rosenbaum, M.L. Saboungi, J.E. Enderby, P.B. Littlewood, Large magnetoresistance in non-magnetic silver chalcogenides, *Nature*. 390 (1997) 57.
- [64] M.-L.S. A. Husmann, J. B. Betts, G. S. Boebinger, A. Migliori, T. F. Rosenbaum, Megagauss sensors, *Nature*. 417 (2002) 421–424.
- [65] J. Hu, T.F. Rosenbaum, Classical and quantum routes to linear magnetoresistance, *Nat.Mater.* 7 (2008) 697–700.
- [66] S. Tong, D. Pan, X. Wang, Z. Yu, Unsaturated linear magnetoresistance effect in high-quality free-standing InSb single-crystal nanosheets, *J.Phys.D: Appl.Phys.* 53 (2020) 1–9.
- [67] N. V Kozlova, N. Mori, O. Makarovsky, L. Eaves, Q.D. Zhuang, A. Krier, Linear magnetoresistance due to multiple- electron scattering by low-mobility islands in an inhomogeneous conductor, *Nat.Commun.* 3 (2012) 1–5.
- [68] J.M.O. Zide, D. Vashaee, Z.X. Bian, G. Zeng, J.E. Bowers, A. Shakouri, A.C. Gossard, Demonstration of electron filtering to increase the Seebeck coefficient in In_{0.53}Ga_{0.47}As/In_{0.53}Ga_{0.28}Al_{0.19}As superlattices, *Phy. Rev. B*. 74 (2006) 205335.
- [69] T. Hong, C. Guo, D. Wang, B. Qin, C. Chang, Enhanced thermoelectric performance in SnTe due to the energy filtering effect introduced by Bi₂O₃, *Mater. Today Energy*. 25 (2022) 100985.
- [70] S. Roychowdhury, R. Panigrahi, S. Perumal, K. Biswas, Ultrahigh Thermoelectric Figure of Merit and Enhanced Mechanical Stability of p - type AgSb_{1-x}Zn_xTe₂, *ACS Energy Lett.* 2 (2017) 349–356.
- [71] A. Das, A. Chauhan, V. Trivedi, M. Tiadi, R. Kumar, M. Battabyal, D.K. Satapathy, Effect of iodine doping on the electrical, thermal and mechanical properties of SnSe for thermoelectric applications, *Phys.Chem.Chem.Phys.* 23 (2021) 4230–4239.
- [72] R.W. McKinney, P. Gorai, E.S. Toberer, Search for new thermoelectric materials with low Lorenz number, *J. Mater. Chem. A*. 5 (2017) 17302–17311.
- [73] L. Ferrer-argemi, Z. Yu, J. Kim, N. V Myung, J. Lim, J. Lee, Silver content dependent thermal conductivity and thermoelectric properties of electrodeposited antimony telluride thin films, *Sci. Rep.* 9 (2019) 1–8.

- [74] S.S. Ragimov, A.E. Babayeva, A.I. Aliyeva, On the thermal conductivity of AgSbTe₂ and Ag_{0.82}Sb_{1.18}Te_{2.18}, *Low Temp.Phys.* 44 (2018) 1–4.
- [75] H. Wang, H. Hu, N. Man, C. Xiong, Y. Xiao, Band flattening and phonon-defect scattering in cubic SnSe-AgSbTe₂ alloy for thermoelectric enhancement, *Mater. Today Phys.* 16 (2020) 100298.
- [76] V. Vijay, S. Harish, J. Archana, M. Navaneethan, Cation disorder and bond anharmonicity synergistically boosts the thermoelectric performance of p-type AgSbSe₂, *CrystEngComm.* 23 (2021) 5522–5530.
- [77] Y.S.-H. Christopher E. Carlton, Ricardo De Armas, Jie Ma, Andrew F. May, Olivier Delaire, Natural nanostructure and superlattice nanodomains in AgSbTe₂, *J. Appl. Phys.* 115 (2014) 1–7.
- [78] B. Min, B. Kim, M. Oh, B. Ryu, J. Lee, S. Joo, S. Park, H. Lee, H. Lee, Effect of La-doping on AgSbTe₂ Thermoelectric Compounds, *J. Korean Phys. Soc.* 68 (2016) 164–169.
- [79] J. Ki, B. Ryu, S. Park, J. Hee, J. Park, J. Jang, M. Oh, S. Park, Effect of microstructure on thermoelectric conversion efficiency in metastable δ -phase AgSbTe₂, *Acta Mater.* 222 (2022) 117443.
- [80] G. Tan, L. Zhao, M.G. Kanatzidis, Rationally Designing High-Performance Bulk Thermoelectric Materials, *Chem.Rev.* 116 (2016) 12123–12149.
- [81] L. Ye, K. Hoang, A.J. Freeman, S.D. Mahanti, J. He, T.M. Tritt, M.G. Kanatzidis, First-principles study of the electronic, optical, and lattice vibrational properties of AgSbTe₂, *Phy. Rev. B.* 77 (2008) 1–6.
- [82] B. Jonas, T. Brink, K. Tsuchiya, F. Meng, G. Wilde, K. Albe, Low temperature heat capacity of a severely deformed metallic glass, *Phy. Rev.Lett.* 112 (2014) 1–5.
- [83] J.J. Hamilton, E.L. Keatley, H.L. Ju, A.K. Raychaudhuri, V.N. Smolyaninova, R.L. Greene, Low-temperature specific heat of La_{0.67}Ba_{0.33}MnO₃ and La_{0.8}Ca_{0.2}MnO₃, *Phy. Rev.B.* 54 (1996) 926–929.
- [84] E.S.R.Gopal, *Specific heat at low temperatures*, 1st ed., Plenum Press, 1966.
- [85] D.T. Morelli, V. Jovovic, *Intrinsically Minimal Thermal Conductivity in Cubic I - V -*

VI 2 Semiconductors, 035901 (2008) 16–19.

- [86] G. Tan, S. Hao, R.C. Hanus, X. Zhang, S. Anand, T.P. Bailey, A.J.E. Rettie, X. Su, C. Uher, V.P. Dravid, G. Je, C. Wolverton, M.G. Kanatzidis, High Thermoelectric Performance in SnTe –AgSbTe₂ Alloys from Lattice Softening, Giant Phonon–Vacancy Scattering, and Valence Band Convergence, *ACS Energy Lett.* 3 (2018) 705–712.
- [87] R. Hanus, M.T. Agne, A.J.E. Rettie, Z. Chen, G. Tan, D. Young, M.G. Kanatzidis, Y. Pei, P.W. Voorhees, G.J. Snyder, Lattice softening significantly reduces thermal conductivity and leads to high thermoelectric efficiency, *Adv. Mater. Lett.* 31 (2019) 1–21.
- [88] H. Liu, X. Zhang, W. Li, Y. Pei, Advances in thermoelectric (GeTe)_x(AgSbTe₂)_{100-x}, *Chinese Phys. B.* 31 (2022) 1–9.
- [89] H. Kim, P. Dharmiah, S. Hong, Thermoelectric Properties of Texture-Controlled Fabricated by Gas-Atomization and Hot-Extrusion Processes, *J. Electron. Mater.* 47 (2018) 3119–3126.

Chapter 6

Summary and Outlook

Global power shortages create a difficult situation as energy demands rise. The decline of traditional fossil fuel resources generates concerns about energy security and environmental consequences. There is a distinct shift of focus toward renewable energy sources to address this issue by utilizing cleaner alternatives. To resolve the need for electrical power while avoiding environmental harm, a comprehensive plan that integrates innovation, efficiency, and sustainable behaviours is required. Inorganic compounds, particularly chalcogenides, play an important role in thermoelectric applications. Ongoing research strives to find novel materials with high figures of merit to replace traditional thermoelectric materials. Because of their unique magnetic and transport properties, transition metal ternary chalcogenides are of particular interest. An exhaustive examination is carried out on the fundamental mechanism that impacts different characteristics in transition metal chalcogenides. The main focus of the present work was on the synthesis of new materials and the examination of their thermoelectric and magnetic functions at low temperatures.

The current thesis begins by providing an introduction to energy consumption, including a comprehensive explanation of the theory, methods, and importance of transition metal-based ternary chalcogenides as materials with thermoelectric and magnetic properties. *Chapter 2* deals with the experimental methods. In **Chapter 3** discusses the synthesis of Zintl phase BaVSe_3 using two distinct approaches: one involving the combination of constituent elements, and the other utilizing a novel synthesis process that ensures phase purity and reduces the time required for synthesis. The first method results in BaVSe_3 with a secondary phase BaSe_3 (BVS: BS) and the newly introduced route results in the phase pure BaVSe_3 (BVS). Through the analysis of magnetic properties, it was confirmed that these materials have an intrinsic glassy and Griffith-like nature. The magnetoresistance studies reveal that BVS has butterfly magneto resistance at extremely low temperatures (<11 K) in the longitudinal direction. The inherent magnetic properties arise from its quasi-1-dimensional form and the robust interaction between the electrons in the E_g and A_{1g} energy levels. The thermoelectric investigations validated that electrons were the predominant charge carriers in both materials. However, the higher thermopower in the pure-phase BVSe_3 can be attributed to the higher effective mass of the carriers. Additionally, thermal transport is mostly governed by phonons. BVS demonstrated a maximum ZT value of 0.008, which is fourfold

greater than that of BVS: BS near room temperature. FM transition metal chalcogenides show great potential for use in thermoelectric power production and spintronics.

Chapter 4 deals with the synthesis of new materials, CoNiSe_2 (CNS) and CoFeSe_2 (CFS), through direct melting of the precursors at elevated temperatures. The replacement of Fe at the Ni location improves the thermoelectric capabilities and demonstrates distinct magnetic features. CNS exhibited antiferromagnetic (AFM) ordering with a T_N of 5.5 K. On the other hand, CFS has an FM nature with a high-temperature T_C of ~ 890.5 K. The reported power factor of CFS is 55.64 W/mK^2 , which is attributed to its high Seebeck coefficient and ZT value of 0.005 at near ambient temperatures. Heat capacity investigations on these materials validate that, at low temperatures, the thermal voltage is mostly influenced by phonon-electron drag rather than the magnon component. The substitution doping at transition metal sites provides an opportunity to improve the thermoelectric characteristics of the material.

Chapter 5 is focused on the synthesis of spontaneously nanostructured AgSbTe_2 as a promising candidate for future-generation thermoelectric materials. The work revealed various mechanisms that contribute to the enrichment of the thermoelectric properties of this material. A fraction of variation in the local composition ($\text{Ag}_{0.927}\text{Sb}_{1.07}\text{Te}_{2.005}$) of this material generates a noticeable change in its properties. A Seebeck coefficient of $251 \mu\text{V/K}$ and a power factor of $741 \mu\text{W/mK}^2$ at near ambient temperature is attained with this composition. It also exhibited a low thermal conductivity of 0.2 W/mK arising from phonon scattering at various defects that led to a high ZT of 1.1 at room temperature. The calculated efficacy of 12.5% at a $\Delta T = 700 \text{ K}$ makes it an efficient candidate for future-generation thermoelectric applications due to its remarkable thermoelectric and mechanical properties.

Overall, the investigations involved examining the basic mechanisms and pathways that enhance the effectiveness of transition metal ternary chalcogenides for thermoelectric and magnetic applications using various methods. This work also outlines innovative processes for designing such compounds and presented advanced techniques for studying these materials for extracting exceptional performance for future power generation and spintronics.

Appendix

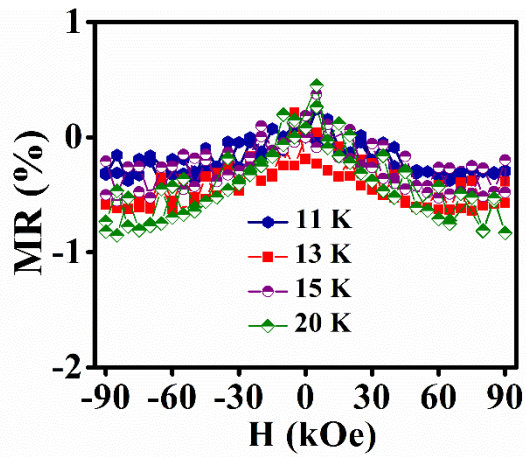


Figure A.3.1. MR versus H at 11 K, 13 K, 15 K and 20 K

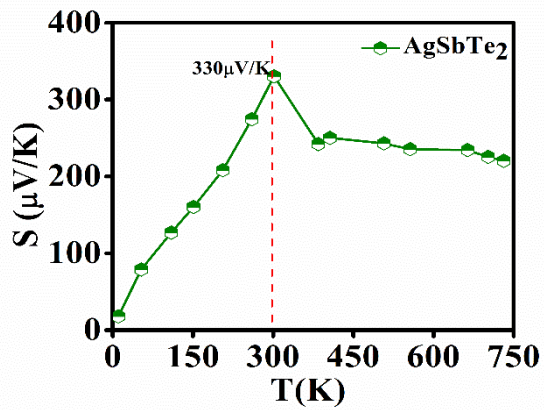


Figure A.5.1. Variation of S with T

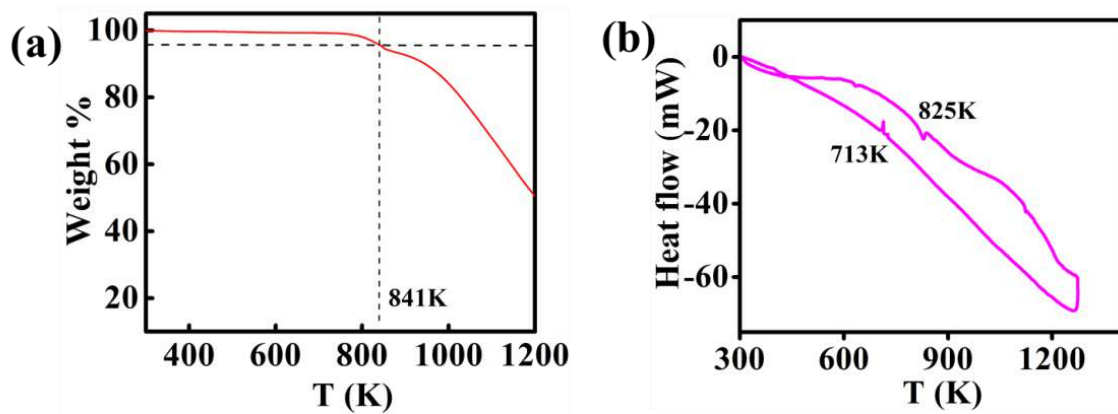


Figure A.5.2. (a) TGA and (b) DTA of the material

ANNEXURE

1. Characterization Techniques

The crystal structure of synthesized samples was analysed by Powder X-ray diffraction techniques, (Philips X'pert pro-X-ray diffractometer) using Cu-K α radiation with wavelength 1.5406Å in the 2 θ range 20° - 90° with a step size 0.005°. XRD data was refined by using the software GSAS. The composition and oxidation states were analysed through X-ray photoelectron spectroscopy (PHI 5000 Verasprobe II) and the peaks were fitted by Multi-pack software. The morphology of the synthesized samples was investigated by scanning electron microscopy (SEM (JEOL JSM-5600LV, Tokyo, Japan), and the homogeneity of the sample was analyzed by high-resolution transmission electron microscopy (HRTEM (FEI Tecnai F20, operated at 300 kV). The elemental mapping of the samples was done by TEM-EDS, SEM -EDAX. Various magnetic measurements were carried out using a vibrating magnetometer (VSM) attached to the physical property measurement system (PPMS, Dynacool, Quantum Design). The low-temperature electrical transport and thermal transport measurements were done through the thermal transport option (TTO) and electrical transport option (ETO) of PPMS.

1.1. Structural and Morphology Characterization

1.1.1. X-ray powder diffraction (XRD)

The room temperature powder diffraction patterns of the synthesized samples were recorded by X-ray diffractometer (Empyrean 3, PANalytical) using Cu-K α radiation with wavelength 1.5406Å in the 2 θ range 20° — 90° with a step size of 0.005°. The powder X-ray diffraction [1] technique is based on the principle of diffraction of X-rays from the electrons in a crystalline solid. The high-energy electron beams are aimed into a target metal and the collision results in the dislodging of core electrons, higher energy electrons will fall into that vacancy and those results in the production of X-rays. When monochromatic X-rays fall into a crystal the electrons get scattered and are recorded by a detector. Figure 2a shows the schematic diagram of the X-ray diffractometer.

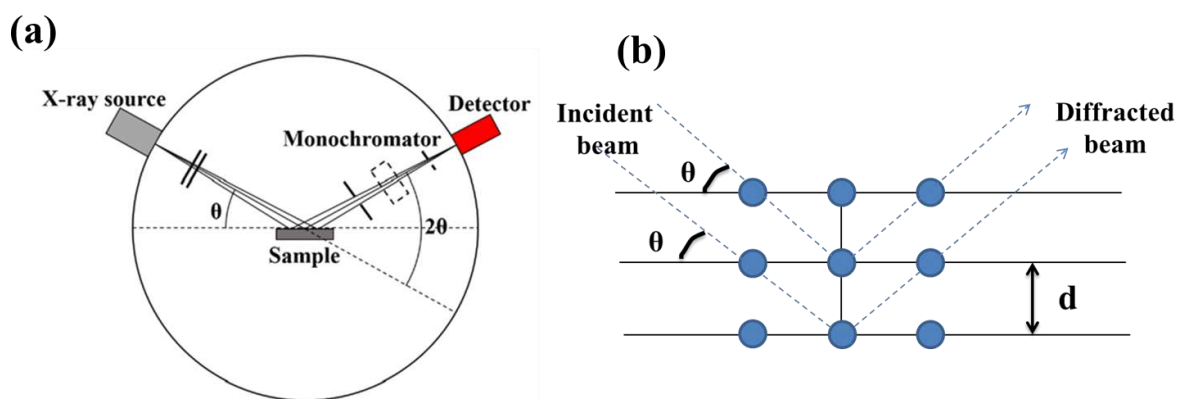


Figure 2. (a) X-ray diffractometer, (b) Bragg's diffraction

The fundamental to XRD is Bragg's diffraction (Figure 2b), according to Bragg's law, the condition for constructive interference in a crystal lattice occurs when the path difference between the X-rays scattered by adjacent crystal plane is a multiple of the wavelength and it is mathematically expressed as

$$2d\sin\theta_{hkl} = n\lambda$$

Where d is the spacing between the crystal planes, θ is the angle of incidence, n is an integer and λ is the wavelength of X-rays. The XRD data can be analysed by the Rietveld refinement method and it is based on the least squares approach in which a theoretical profile will fit with the experimental data. Various experimental parameters were refined to get an exact fit between the experimental and theoretical data. Here we are using the GSAS 2 software for the refinement studies.

1.1.2. X-ray photoelectron spectroscopy

The surface elemental composition of synthesized samples was analyzed using X-ray photoelectron spectroscopy (XPS, PHI 5000 Versa probe II, ULVAC-PHI Inc., USA) equipped with monochromatic Al $K\alpha$ X-ray source of energy 1486.6 eV. X-ray photoelectron spectroscopy is a surface-sensitive analytical study and it determines the surface sensitivity and the chemical state information from the identification of the constituent elements [2]. Figure 3a shows the XPS instrument and the photoelectron emission and the energy level diagram is depicted in Figures 3b & c.

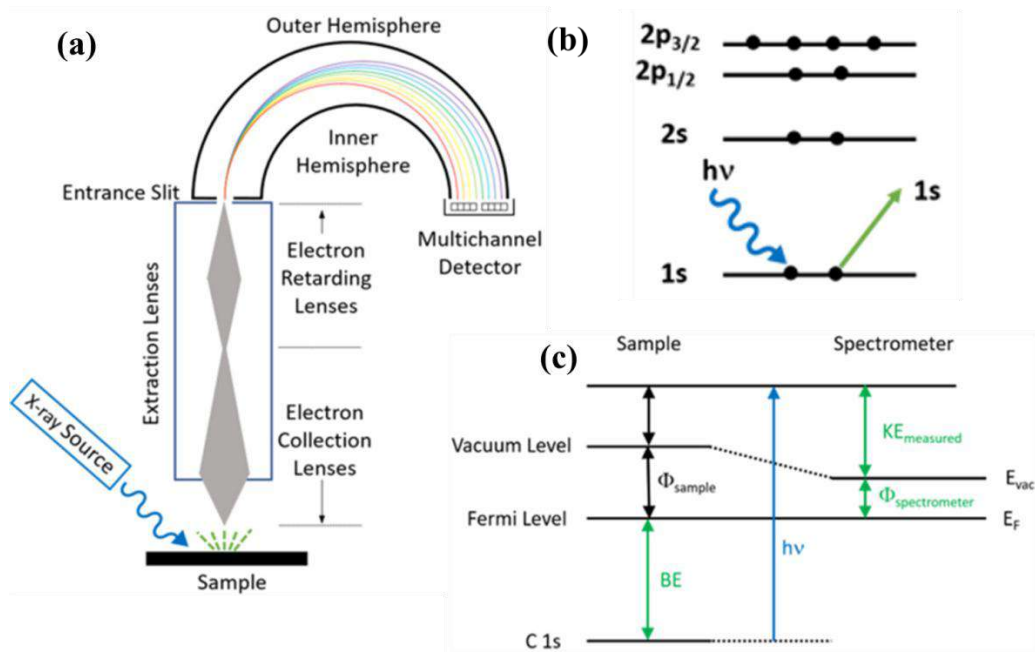


Figure 3. (a) XPS instrument, (b) photoelectron emission, (c) energy level diagram illustrates the basis XPS equation.

XPS is based on the photoelectric effect in which the material is irradiated with soft X-rays and the kinetic energy of the emitted electrons (photoelectrons) is recorded. The incident energy ($h\nu$) of the X-ray is expressed in terms of binding energy (BE), kinetic energy (KE) and spectrometer work function (ϕ_{spec}) as

$$h\nu = \text{BE} + \text{KE} + \phi_{\text{spec}}$$

The binding energy can be obtained from this relation and it is demonstrated in the figure c)

1.1.3 Scanning electron microscopy

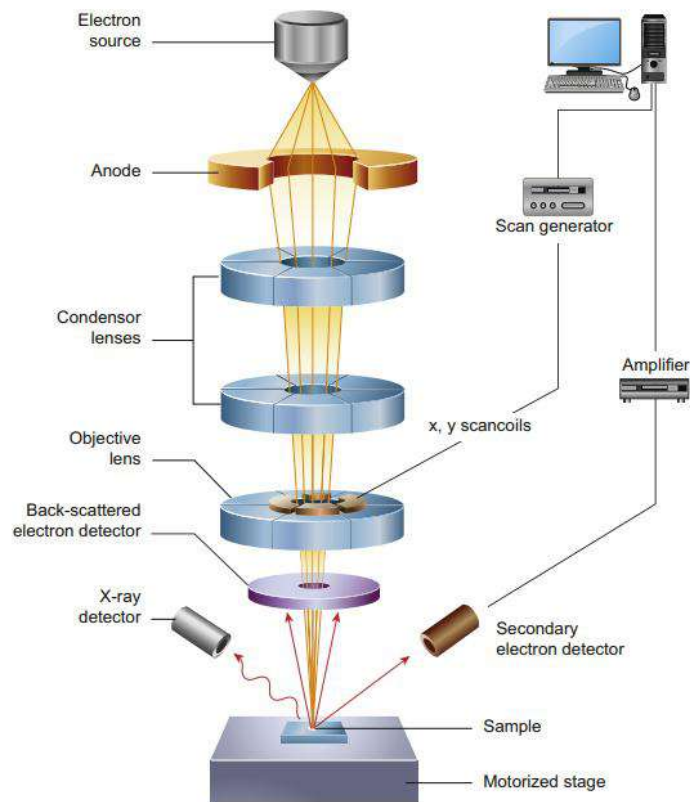


Figure 4. Schematics of scanning electron microscopy

The microstructure and local composition of the synthesized samples at room temperature under vacuum were investigated by scanning electron microscopy (Zeiss EVO 18 cryo-SEM, operating voltage of 15 kV). The SEM (Figure 4) involves the scanning of a sample's surface with a focused electron beam. When the beam interacts with the sample, it generates signals such as secondary electrons, backscattered electrons, diffracted backscattered electrons and X-rays. The secondary electrons and backscattered electrons are normally used for imaging samples, secondary electrons are most valuable for displaying morphology and topography on samples and backscattered electrons are most valuable for illustrating contrasts in composition in multiphase samples. The characteristic X-rays produced by each element help to identify the corresponding constituent of the material [3].

1.1.4. Transmission electron microscopy

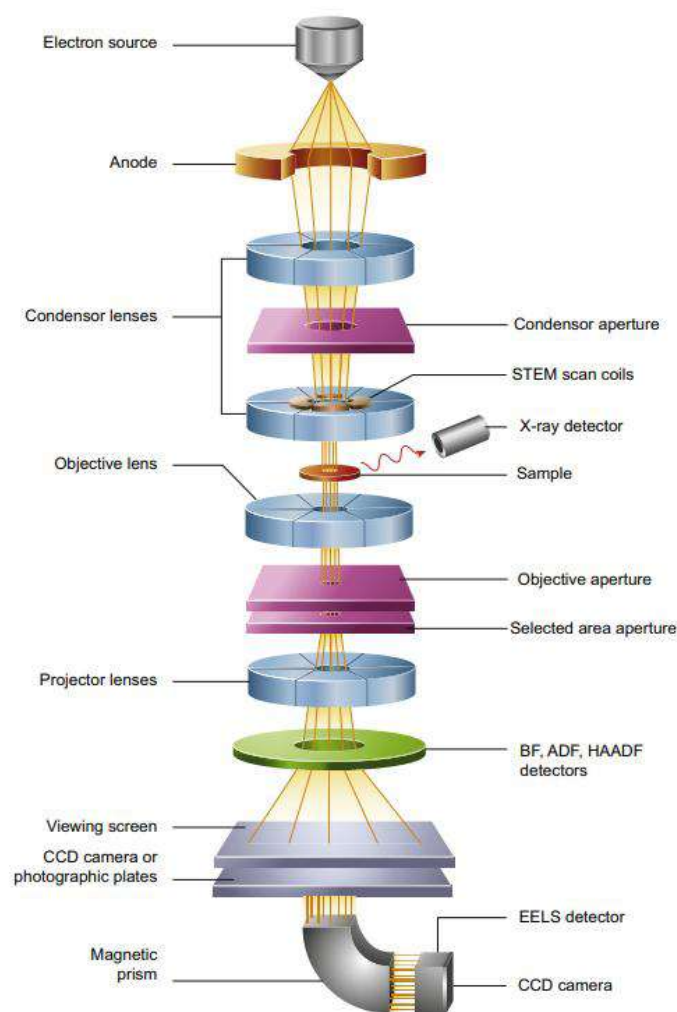


Figure 5. Schematic representation of transmission electron microscopy

The high-resolution transmission electron microscopy (HRTEM (FEI Tecnai F20, operated at 300 kV) and the elemental mapping of the samples can also be done by TEM-EDS. The TEM (Figure 5) works on the principle of transmitting electrons through a thin film and it gives detailed images of internal structures at the nano-scale by using the wave nature of electrons. The TEM techniques generally include conventional imaging in bright field (BF) and dark field (DF) mode, high-resolution imaging (HRTEM) and energy-dispersive X-ray spectroscopy (EDS) [3]. The Fast Fourier Transform (FFT) of HRTEM images were used to find the interplanar distance of the crystal planes.

1.2. Magnetic and transport Characterization

Physical Property Measurement System (PPMS)



Figure 6. Physical property measurement system (Quantum Design)

The magnetic and various transport studies were carried out using the PPMS Dynacool (Quantum design 9T, USA) (Figure 6). This instrument is designed to measure various physical properties that include DC, AC magnetization, electrical, thermal transport, heat capacity etc[4].

3.2.1. Magnetic characterization

The magnetic measurements were carried out in PPMS using VSM (Vibrating sample magnetometer) standard (9T, 1.8 K-400 K) and oven (9T, 300 K- 950 K) options. The VSM [5] works on Faraday's law of electromagnetic induction and it mainly consists of a VSM linear motor for vibrating the sample, a coil set puck and the associated electronics for the data extraction, the figure shows the schematic representation of VSM. The sample to be measured is attached to the end of the sample rod and placed in a magnetic field. Figure 7 shows the structure of VSM.

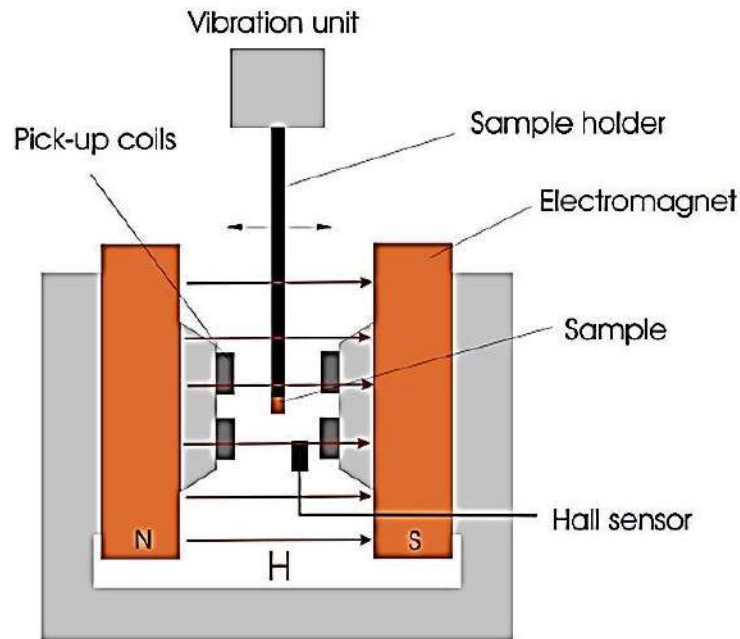


Figure 7. Schematic diagram of VSM

The change in magnetic flux will generate an induced emf in the pickup coil and it is expressed as $V_{\text{coil}} = d\phi/dt$, where ϕ is the magnetic flux. The induced emf is related to the magnetic moment (m) through the equation $V_{\text{coil}} = 2\pi f C m A \sin(2\pi f t)$, A is the amplitude of oscillation, C is the coupling constant and f is the frequency of oscillation. By measuring the induced current that determines the magnetization of the material under study.

1.2.3. Transport properties

Here we have calculated the carrier concentration by the Hall effect method with the help of the Electrical Transport Option (ETO)[6] in PPMS. The four-terminal geometry is used to measure the resistance of the material; in this method, two leads pass the current through the sample and two different terminals measure the corresponding voltage. Ohm's law is used to calculate the resistance (R), and resistivity (ρ) is calculated with the help of the sample's geometrical parameters ($\rho = RA/l$, where A is the area of cross-section, l is the voltage lead separation). For the Hall Effect measurement, the voltage leads are connected perpendicular to the current direction under a transverse magnetic field (Figure 8 a & b).

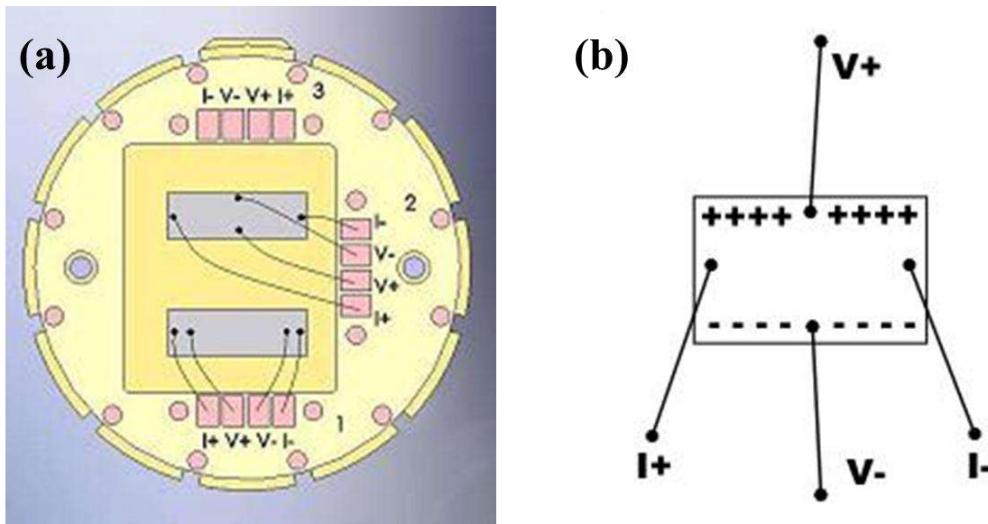


Figure 8. (a) Four probe connection for Hall effect measurement in sample puck (channel 2),
 (b) Schematic diagram of Hall effect connection

The force experienced by the charged particle in a transverse magnetic field (B) perpendicular to both field and direction of motion is expressed as $F=q(v \times B)$, and this force creates a potential across the sample and it is termed as Hall voltage (V_H) and the Hall coefficient is expressed as $R_H = V_H A / I B$, it is related to the carrier concentration (n) by the equation $R_H = -1/ne$ and its sign determines the type carriers. The Hall coefficient can be easily obtained from the measured R by $R_H = RA / IB$.

3.2.4. Thermoelectric measurements

The Thermal Transport Option (TTO) [7] of the PPMS enables the measurement of electrical conductivity, thermal conductivity and Seebeck coefficient (S) over the range of temperature 3K- 350 K under high vacuum. The thermoelectric figure of merit (ZT) of the sample is also recorded. A four-probe geometry is used for the measurement, heat ($Q_{+/-}$) is applied at the one end of the sample by a running current, T_{hot} and T_{cold} are measured at the thermometer shoes and also the voltage gradient is recorded to calculate the S . Electrical resistivity is also recorded concerning the flow of current through the sample and heat exits through the cold foot. Figure 9 shows the connection of the sample in the TTO option.

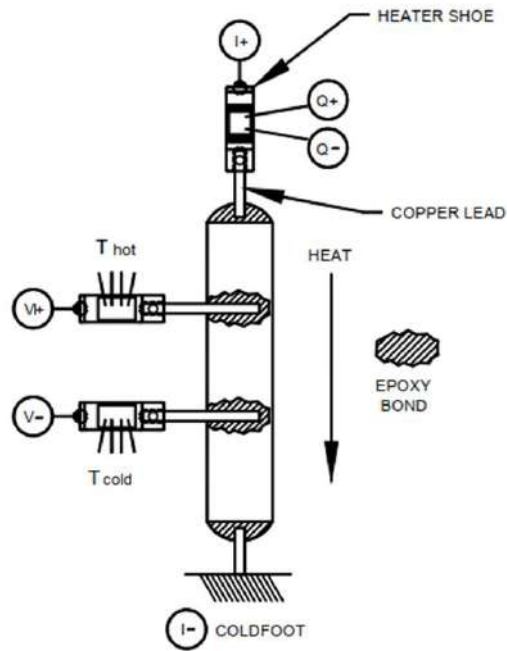


Figure 9. Schematic diagram of TTO sample connection

1.2.5. Heat Capacity Measurement

The heat capacity module in the PPMS measures the heat capacity at constant pressure in the range of temperature (1.8 K to 300 K). During the measurement, a known amount of heat at constant power is applied to the sample for a fixed time and it is also removed from the sample, the heat capacity is measured by recording the change in temperature. It is expressed as $C_p = dQ/dT$. Figure 10 shows the thermal connection between a sample and the sample platform[7].

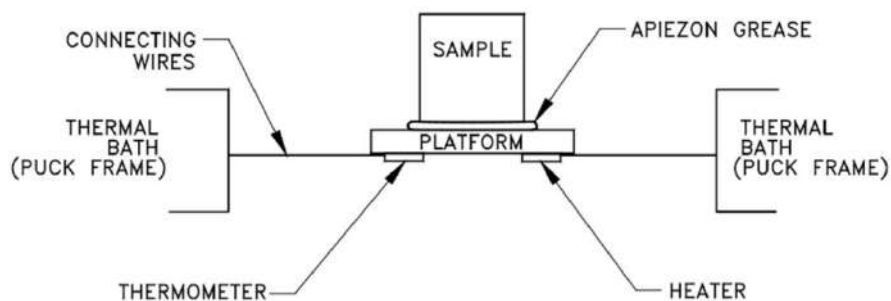


Figure 10. Thermal connection of sample and sample platform in Heat capacity option

Two analysis models can be used in heat capacity measurements the simple model and the tau model. In a simple model, we assume that the sample and the sample platform are in good

thermal contact with each other and in this model the temperature T of the platform as a function of time is given by

$$C_{\text{total}} dT/dt = -K_w (T - T_b) + P(t)$$

Where C_{total} is the total heat capacity of the sample and sample platform, K_w is the thermal conductance of the supporting wires; T_b is the temperature of the thermal bath (puck frame); and $P(t)$ is the power applied by the heater. Whenever the thermal contact between the sample and holder is poor then the software uses the two-tau model and the given equations explain this model.

$$C_{\text{platform}} dT_p/dt = -K_w (T_p(t) - T_b) + K_g (T_s(t) - T_p(t)) + P(t)$$

$$C_{\text{sample}} dT_s/dt = -K_g (T_s(t) - T_p(t))$$

Where C_{platform} is the heat capacity of the sample platform, C_{sample} is the heat capacity of the sample and K_g is the thermal conductance between the two due to the grease. $T_p(t)$ and $T_s(t)$ are the platform and sample temperature.

ABSTRACT

Name of the Student: **Chinnu V. Devan**

Registration No: **10PP19A39027**

Faculty of Study: **Physical Sciences**

Year of Submission: **2024**

AcSIR academic centre/CSIR Lab: **CSIR-National Institute for Interdisciplinary Science and Technology (CSIR-NIIST)**

Name of the Supervisor(s): **Dr. Biswapriya Deb**

Title of the thesis: **Investigation of Thermoelectric and Magnetic properties of Transition metal-based Chalcogenides**

The transition metal chalcogenides (TMCs) have significant interest in the arenas of thermoelectrics (TE) and spintronics due to their unique electronic, thermal and magnetic properties. The present thesis consists of three working chapters. The introduction chapter (*Chapter 1*) gives an overview of thermoelectrics and magnetism. It highlights the need for thermoelectric power generation, materials for both TE, magnetic applications and various mechanisms that enhance the efficiency of TE materials. The *Chapter 2* deals with the experimental methods. In *Chapter 3*, the novel solid-state method was introduced to synthesize quasi-one-dimensional and phase-pure BaVSe₃. The ferromagnetic BaVSe₃ exhibits unique magnetic characteristics such as glassy behaviour, a Griffiths-like phase, and butterfly magnetoresistance at low temperatures. A comparison study on thermoelectrics reveals that phase pure BaVSe₃ has a maximum ZT value of 0.008, which is fourfold greater than that of impurity-phased BaVSe₃. *Chapter 4* discusses the synthesis, magnetic and thermoelectric studies of selenium-based TMCs CoMSe₂ (Ni, Fe). The Fe substitution at the Ni site enhanced electrical conductivity, and Seebeck coefficient and resulted in a PF of 55 $\mu\text{W}/\text{mK}^2$. The improved mobility, density of states near EF and phonon generation contributed to the improvement in various transport properties in CFS and resulted in a 10 times increase in thermoelectric efficiency (ZT) of the material. *Chapter 5*, examines the impact of micro/nanostructure on the thermoelectric characteristics of nonstoichiometric AgSbTe₂. The composition also exhibited a low thermal conductivity of 0.2 W/mK arising from phonon scattering at various defects that led to a high ZT of 1.1 at room temperature. The high thermal, and mechanical stability and calculated efficacy of 12.5% at a $\Delta T = 700$ K promise this material for future TE module generation. The overall summary and future outlook of the thesis are outlined in *Chapter 6*. The novel materials developed in this thesis have exotic magnetic and thermoelectric properties at low temperatures. The multifunctional nature of these TMCs can find applications in the fields of both thermoelectrics and magnetic electronics.

Details of the publications emanating out of the thesis work

1. **Chinnu V. Devan**, Anoop A. Nair, Ramany Revathy, Biswapriya Deb, Manoj Raama Varma, “Exotic magnetic properties in Zintl phase BaVSe_3 : A theoretically supported experimental investigation” *New J.Chem.*, 2023, 47
2. **Chinnu V. Devan**, Manoj Raama Varma and Biswapriya Deb, Magnetic and thermoelectric properties of quasi-one-dimensional BaVSe_3 , *Journal of Magnetism and Magnetic Materials*, 2024, 599, 172110, DOI: 10.1016/j.jmmm.2024.17211
3. **Chinnu V. Devan**, Mahima M. Kurian, Santhosh P. N., Manoj Raama Varma, Biswapriya Deb, A low-temperature thermoelectric transport study of non-stoichiometric AgSbTe_2 , *Phys. Chem. Chem. Phys.*, 2024, <https://doi.org/10.1039/D4CP01171F>
4. **Chinnu V. Devan**, Manoj Raama Varma, Biswapriya Deb, The synthesis, magnetic and thermoelectric studies of CoMSe_2 (M = Ni, Fe) (Manuscript under preparation).

Details of the publications not related to the thesis work

1. **Chinnu V Devan**, Biswapriya Deb, Manoj Raama Varma, Magnetic Properties of Undoped and Bi-doped LaMnO_3 , ECS Transactions, 107, 12047, 2022
2. Mahima M. Kurian, Ranjana R. Das, **Chinnu V. Devan**, Manoj Raama Varma, P.N. Santhosh, Exchange bias effect and inhomogeneous magnetism in $6\text{H Ba}_3\text{CoFeRuO}_9$: Role of structural site disorder, *Journal of Magnetism and Magnetic Materials*, 568, 170372, 2023
3. J Mini, N Joseph, R Sugathan, **C V Devan**, IA Al-Omar, M R Varma, S Thomas, Structural and magnetic properties of Ni-substituted Y-type $\text{Ba}_{0.5}\text{Sr}_{1.5}\text{Zn}_{2-x}\text{Ni}_x\text{Fe}_{12}\text{O}_{22}$ (x = 0, 0.5, 1.0, and 1.5) hexaferrite, *Journal of Materials Science: Materials in Electronics*, 34, 194, 2023

List of papers presented in International or National Conference

1. **Chinnu V Devan**, Shabir Ali P C, Biswapriya Deb, Manoj Raama Varma, Thermoelectric and magnetic study on vanadium diselenide, 3rd International Conference on Advanced Functional Materials (ICAFM), CSIR-NIIST, during December 9-10, 2019
2. **Chinnu V Devan**, Biswapriya Deb, Manoj Raama Varma, Bi doped LaMnO_3 for thermoelectric and spintronic applications, 5th National Symposium on Shaping the Energy Future: Challenges & Opportunities, August 27, 2021
3. **Chinnu V Devan**, Biswapriya Deb, Manoj Raama Varma, Magnetic Properties of Undoped and Bi-doped LaMnO_3 , ICTSGS, November 29, 2021
4. **Chinnu V Devan**, Anoop A. Nair, Ramany Revathy, Biswapriya Deb, Manoj Raama Varma, “Exotic Magnetic Properties in Zintl Phase BaVSe_3 : A Theoretically Supported Experimental Investigation, Recent Advances in the Physics of Materials, December 9-10, 2021
5. **Chinnu V Devan**, Manoj Raama Varma, Biswapriya Deb, Low-temperature thermoelectric properties of AgSbTe_2 and multiphysics simulation on $\text{AgSbTe}_2\text{-Bi}_2\text{Te}_3$ thermoelectric generator, National symposium on radiation and photochemistry, January 5-9, 2023
6. **Chinnu V Devan**, Anoop A. Nair, Ramany Revathy, Biswapriya Deb, Manoj Raama Varma, “Exotic Magnetic Properties in Zintl Phase BaVSe_3 : A Theoretically Supported Experimental Investigation, AMMT, February 23-24, 2023

Thermoelectric and Magnetic Study on Vanadium Diselenide

Chinnu V Devan,^{1,2} Shabir Ali P C,^{1,2} Biswapriya Deb,^{1,2} Manoj Raama Varma^{1,2*}

¹Materials Science and Technology Division, CSIR- National Institute for Interdisciplinary Science and Technology Division (CSIR-NIIST), Industrial Estate P.O., Thiruvananthapuram -695019, India

²Academy of Scientific and Innovative Research (AcSIR), CSIR-HRDC Campus, Ghaziabad, Uttar Pradesh- 201002, India

*E-Mail: manoj@niist.res.in

The use of energy in day to day life has grown in rapid way, and conserving energy to meet the energy demand is the need of today. Thermoelectric materials have been considered as an alternative clean energy technology that can realize direct conversion between heat and electricity. Waste heat recovery is an environment-friendly way to preserve resources and increase energy efficiency [1]. Thermoelectric materials are characterized by material figure of merit, ZT. It depends on the Seebeck coefficient, temperature, electrical conductivity and thermal conductivity. The metal chalcogenide systems consist of inorganic compounds of oxygen, sulphur, selenium and tellurium with metals and semimetals is an interesting area of research. The present work is focused on the synthesis and characterization of Vanadium diselenide (VSe₂). VSe₂ is a transition metal chalcogenide showing semiconducting nature and having positive Seebeck coefficient. In the present study VSe₂ is synthesized by solid-state reaction [2]. Magnetic and thermoelectric properties were carried out. By doping VSe₂ with various elements can improve the thermoelectric properties.

References

[1] Xiaojian Tan, Hongxiang Wang, Guoqiang Liu Jacques G. Noudem , Haoyang Hu ,Jingtao Xu ,Hezhu Shao ,Jun Jiang,Materials Today Physics 7(2018)35 44

[2] Michel Bayard and M.J.Sienko, Journal of Solid State Chemistry, 19,325-329 (1976)

Low Temperature Thermoelectric Properties of AgSbTe₂ and Multiphysics simulation on AgSbTe₂-Bi₂Te₃ Thermoelectric Generator

Chinnu V. Devan^{1,3},

Manoj Raama Varma^{1,3}, Biswapriya Deb^{2,3}

¹*Materials Science and Technology Division, CSIR- National Institute for Interdisciplinary Science and Technology (NIIST), Thiruvananthapuram- 695019, Kerala, India*

²*Photosciences and Photonics, Chemical science and Technology Division, CSIR- National Institute for Interdisciplinary Science and Technology (NIIST), Thiruvananthapuram- 695019, Kerala, India*

³*Academy of Scientific and Innovative Research (AcSIR), Ghaziabad-201002, India*

Email:biswapriya.deb@niist.res.in

There is an upcoming competition in the search of new energy resources due to their scarcity. The development of reliable and nonpolluting energy is our major concern. With the increasing awareness of the reduction of global energy resources welcome alternative methods for power generation [1]. Thermoelectric power generation is healthy candidate with wide range of applications and advantages. Thermoelectric devices are able to convert unusable heat energy to useful electrical energy. There are interesting researches on AgSbTe₂ as a promising thermoelectric material[2]. The phase pure polycrystalline AgSbTe₂ synthesized through solid state route from its constituent elements. The structural and thermoelectric properties were analysed experimentally through various measurements. It crystallizes in cubic structure with space group Fm3m. It exhibit high positive seebeck coefficient (330μV/K) and low thermal conductivity (0.82W/m.K) at room temperature. Spontaneous nanostructures lowers thermal conductivity and generates ZT~0.42 at 300K. The hall measurement further confirms the holes were the majority charge carriers and obtains carrier concentration in the order of 10¹⁸/cm³. The results suggest that AgSbTe₂ is a promising material for thermoelectric generator(TEG). By using Comsol simulation, a 16×16 AgSbTe₂-Bi₂Te₃ TEG were simulated and output characteristics were calculated.

References

¹ Lee Gilgeun, Ha Gookhyun, Journal of electronic materials, **2014**, 43, 6

² Heng Wang, Jing-Feng Li, Minmin Zou, and Tao Sui, Applied Physics Letters, **2008**, 93, 202106

Magnetic Properties of Undoped and Bi doped LaMnO₃

Chinnu V Devan^{1,3}, Biswapriya Deb^{2,3}, Manoj Raama Varma^{1,3}

¹*Materials Science and Technology Division, CSIR- National Institute for Interdisciplinary Science and Technology (NIIST), Thiruvananthapuram- 695019, Kerala, India*

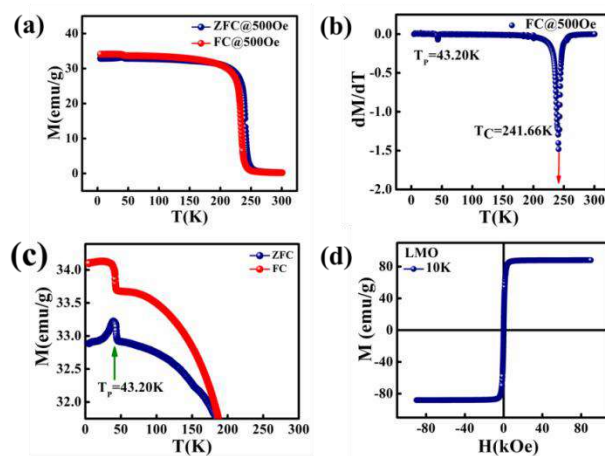
²*Photosciences and Photonics, Chemical science and Technology Division, CSIR- National Institute for Interdisciplinary Science and Technology (NIIST), Thiruvananthapuram- 695019, Kerala, India*

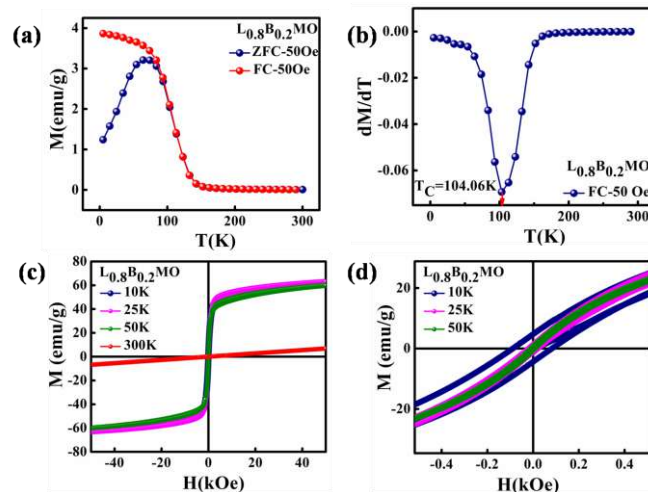
³*Academy of Scientific and Innovative Research (AcSIR), Ghaziabad-201002, India*

*E-Mail: manoj@niist.res.in

Perovskite materials have wide range of applications in the area of spintronics and thermoelectricity. Among manganites LaMnO₃ is a well studied simple perovskite system due to its interesting magnetic and transport properties. Most of the investigation is concentrated on the properties of A site hole-doped (A=Ca, Sr, Ba etc) LaMnO₃. Previous studies report undoped LaMnO₃ as an antiferromagnetic (AFM) insulator having Mn³⁺ oxidation state. It arises from the superexchange AFM interactions between Mn³⁺ ions. Here, we have synthesized LaMnO₃ and La_{1-x}Bi_xMnO₃ (x=0.1, 0.2) from La₂O₃, Bi₂O₃ and MnO₂ through three step heating process by conventional solid state route. It crystallizes in orthorhombic phase with space group pbnm, structural and magnetic properties were also investigated with increasing Bi content. The lattice parameters and unit cell volume has changed slightly on doping. The saturating hysteresis loops confirm ferromagnetic (FM) nature with transition temperature T_c=241.66K and have high magnetization with small coercive field. From Curie Weiss plot at 500Oe gives C-W temperature(θ) as 233.68K, the positive value of θ is another justification for the FM material. The ferromagnetic order may be due to the evolution of oxygen stoichiometry, during synthesize the material can be oxidized, leading to the presence of both Mn³⁺ and Mn⁴⁺ results double exchange ferromagnetic interactions between Mn³⁺ and Mn⁴⁺ ions [1]. There is a peak in the zero field cooled (ZFC) magnetization at a temperature (T_p) 43.20K, the presence of cusp in ZFC is an indication of glassy nature. Epitaxial LaMnO₃ films [2] exhibit a similar peak in previous report and identified as glassy nature. The magnetization versus temperature measurement is

carried out at different field confirms the ferromagnetic ordering. The variation of oxygen content plays a major role in the magnetic properties of manganites. Generally hole doping at the cationic La site with Sr, Ba, Ca generates unusual magnetic properties like colossal magneto resistance (CMR) and ferromagnetic property in LaMnO_3 . La site doped with Bi results in noticeable magnetic properties, it has similar ionic radius and valency as that of La. It belongs to the orthorhombic crystal symmetry with pbnm space group, similar to undoped LaMnO_3 . The transition temperature (T_C) changes with Bi substitution, $T_C = 157.16\text{K}$ for $x=0.1$ and $T_C = 104.06\text{K}$ for $x=0.2$. At low temperatures it shows ferromagnetic nature and above T_C transforms into paramagnetic phase. The linear fit of the $1/\chi$ vs T gives positive CW temperatures for doped system. From previous reports Bi substitution act like divalent ions similar to Ba or Sr [3]. LaMnO_3 with $x=0.1$ concentration of Bi shows minute splitting in ZFC-FC curve at low temperature at 500Oe field. There is a visible bifurcation in the ZFC-FC curve for $x=0.2$ doped LaMnO_3 and observed a cusp in the ZFC magnetization at low temperature. The bifurcation and the cusp are the primary features of glassy like behaviour and also it shows [4] spin glass like behavior in Bi doped LaMnO_3 . The synthesized undoped and Bi doped LaMnO_3 exhibit ferromagnetic nature instead of antiferromagnetic behavior, which is confirmed from various magnetic measurements and there exist exotic magnetic property like glassy nature.





Reference

- [1] F. Prado, R.D. Sánchez, A. Caneiro, M.T. Causa, M. Tovar, Discontinuous evolution of the highly distorted orthorhombic structure and the magnetic order in $LaMnO_{3\pm\delta}$ perovskite, *J. Solid State Chem.* 146 (1999) 418–427. <https://doi.org/10.1006/jssc.1999.8386>.
- [2] Y.M. Liang, Z.J. Wang, Y. Bai, Y.J. Wu, X.K. Ning, X.F. Xiao, X.G. Zhao, W. Liu, Z.D. Zhang, Interface-induced transition from a cluster glass state to a spin glass state in $LaMnO_3/BiFeO_3$ heterostructures, *J. Mater. Chem. C.* 7 (2019) 2376–2384. <https://doi.org/10.1039/c9tc00172g>.
- [3] T. Ogawa, A. Sandhu, M. Chiba, H. Takeuchi, Y. Koizumi, Electrical and magnetic properties of $La_{1-x}Bi_xMnO_3$, *J. Magn. Magn. Mater.* 290–291 (2005) 933–936. <https://doi.org/10.1016/j.jmmm.2004.11.29>.
- [4] D.P. Joseph, J.W. Lin, N.P. Kumar, W.C. Chen, J.G. Lin, Isovalent Bi^{3+} substitution induced structural and magnetic transitions in $LaMnO_3$, *J. Magn. Magn. Mater.* 418 (2016) 68–75. <https://doi.org/10.1016/j.jmmm.2016.02.003>.

Observation of Cluster glass and Griffith like phase in BaVSe₃

Chinnu V. Devan^{1,2}, Anoop A. Nair³, Ramany Revathy^{4,5}, Biswapriya Deb^{1,2,*},

Manoj Raama Varma^{2,4,*}

¹*Photosciences and Photonics, Chemical science and Technology Division, CSIR- National Institute for Interdisciplinary Science and Technology (NIIST), Thiruvananthapuram- 695019, Kerala, India*

²*Academy of Scientific and Innovative Research (AcSIR), Ghaziabad-201002, India*

³*School of Physics (SoP), Indian Institute of Science Education and Research, Thiruvananthapuram- 695551, Kerala, India*

⁴*Materials Science and Technology Division, CSIR- National Institute for Interdisciplinary Science and Technology (NIIST), Thiruvananthapuram- 695019, Kerala, India*

⁵*Department of Physics, St. John's College, Anchal, Kollam, Kerala, India*

Zintl phases are a special class of complex structures having general formula A-M-Q, where A is the alkali metal, alkaline earth metal or rare earth metal, M stands for transition metal and Q is the main group element [1]. Chalcogen based Zintl phases find applications in the area of spintronics and thermoelectric power generation. The magnetic properties of zintl phase BaVSe₃ were studied experimentally through various magnetic measurements. It is synthesized through solid state method from the constituent elements. It crystallizes in the hexagonal structure with space group P6₃/mmc, a secondary phase BaSe₃ is identified in the synthesized sample. The system exhibits a paramagnetic (PM) to ferromagnetic (FM) transition at a transition temperature T_C=40.81K. The experimentally obtained effective magnetic moment is 1.02μ_B and positive Curie Weiss temperature confirms the FM ordering. The exotic magnetic properties like glassy nature and Griffith like phase behaviour observed in the material. The existence of randomly oriented FM clusters generates cluster glass nature in the material. The presence of a hysteresis loop at temperatures above T_C provides evidence for the existence of the Griffiths-like phase. The reason for the same can be attributed to the persistence of FM or AFM clusters in the PM matrix [2]. The theoretical band structure studies were carried out by using DFT analysis and it confirms the metallic nature of the material.

References

1. A. Balvanz, S. Baranets, S. Bobev, Synthesis, structural characterization, and electronic structure of the novel Zintl phase Ba₂ZnP₂, *Acta Cryst.* 76 (2020) 869–873.
4. R.B. Griffiths, Nonanalytic Behavior Above the Critical Point in a Random Ising Ferromagnet, *Phys. Rev. Lett.* 23 (1969) 563–890.

Manuscript no.: (To be inserted by the organisers)

THERMOELECTRIC PROPERTIES OF AgSbTe₂ AND MULTIPHYSICS SIMULATION ON AgSbTe₂-Bi₂Te₃ THERMOELECTRIC GENERATOR

Chinnu V. Devan^{1,3},

Manoj Raama Varma^{2,3}, Biswapriya Deb^{1,3}

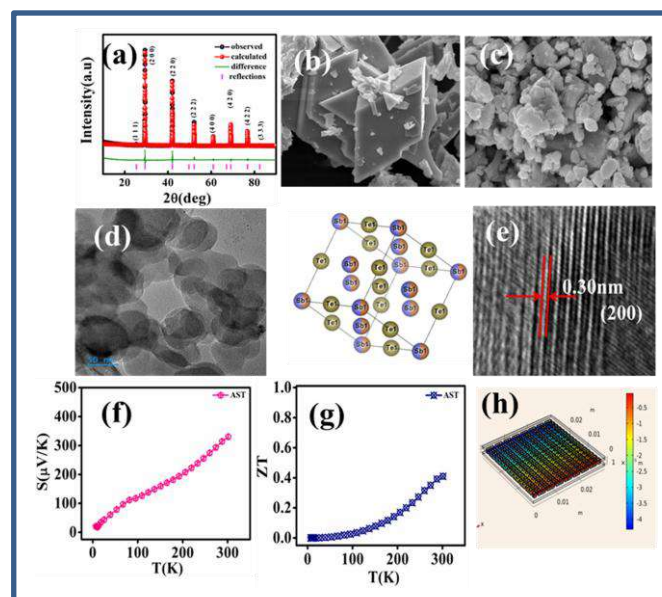
¹ *Photoscience and Photonics Section, Chemical science and Technology Division, CSIR- National Institute for Interdisciplinary Science and Technology (NIIST), Thiruvananthapuram- 695019, Kerala, India*

² *Materials Science and Technology Division, CSIR- National Institute for Interdisciplinary Science and Technology (NIIST), Thiruvananthapuram- 695019, Kerala, India*

³ *Academy of Scientific and Innovative Research (AcSIR), Ghaziabad-201002, India*

Email:chinnusept3@gmail.com

Developing reliable and nonpolluting energy generators is crucial for sustainability. Thermoelectric devices are solid-state systems that can convert waste heat energy to useful electrical energy without moving parts. A phase-pure polycrystalline AgSbTe₂ is synthesized from its constituent elements via a solid-state route. The material showed a cubic structure with space group Fm3m and exhibited a high positive Seebeck coefficient (330 μV/K) and low thermal conductivity (0.82W/m.K) at room temperature. Spontaneous nanostructuring minimizes the thermal conductivity that leads to a ZT~0.42 at 300K. The hall measurement further confirms that the material is p-type with carrier concentration ~10¹⁸/cm³, which is promising for a thermoelectric generator. A 16×16 AgSbTe₂-Bi₂Te₃ TEG was simulated using COMSOL, and different device characteristics are presented in detail.



References

¹ Lee Gilgeun, Ha Gookhyun, Journal of electronic materials, **2014**, 43, 6

² Heng Wang, Jing-Feng Li, Minmin Zou, and Tao Sui, Applied Physics Letters, **2008**,93, 202106


 Cite this: *New J. Chem.*, 2023, 47, 97

Exotic magnetic properties in Zintl phase BaVSe₃: a theoretically supported experimental investigation†

 Chinnu V. Devan,^{ab} Anoop A. Nair,^{ib} c Ramany Revathy,^{de} Biswapriya Deb^{ib} *^{ab} and Manoj Raama Varma^{ib} *^{bd}

The magnetic properties of Zintl phase barium vanadium selenide (BaVSe₃) were investigated experimentally and theoretically. BaVSe₃, synthesized through a solid-state route, crystallized into a hexagonal structure with the space group *p63/mmc*. A secondary phase of barium selenide (BaSe₃) was also formed during the synthesis along with BaVSe₃. The BaVSe₃ crystal system exhibited a Curie temperature (T_C) of 40.81 K. Exotic magnetic phenomena like the glassy nature and the Griffiths-like phase were observed in BaVSe₃ for the first time. The experimentally observed effective magnetic moment was less than the spin-only moment due to the nonmagnetic secondary phase. The crystal structure, lattice parameters, DOS, spin-polarized charge density calculations, T_C and effective magnetic moment were theoretically studied using density functional theory (DFT) as implemented in Quantum ESPRESSO and via the atomistic simulation code VAMPIRE. DFT and atomistic simulations give an insight into the localization of magnetic moment on the V⁴⁺ ions, the metallic nature, and the occurrence of ferromagnetism in BaVSe₃ which has been observed experimentally.

 Received 18th August 2022,
Accepted 15th November 2022

DOI: 10.1039/d2nj04129d

rsc.li/njc

1. Introduction

Zintl phases are a special class of complex structures with the general formula A–T–Q, where A is an alkali metal or an alkaline earth metal, T is a transition metal, and Q is the main group element.¹ These intermetallic phases satisfy the Zintl–Klemm concept in which the electropositive atoms act as electron donors and electronegative atoms act as valence-electron acceptors. This donor–acceptor system leads to a valence-balanced condition.² Transition metal compounds exhibit a paramagnetic (PM) to ferromagnetic (FM) transition at particular temperatures, leading to some exciting phenomena like colossal magnetoresistance (CMR)³ due to the critical

FM fluctuations about T_C .⁴ This property finds applications in device components like the magnetic reading head. CMR was initially observed in manganese-based oxides and recent reports suggest its presence in alloys and chalcogenides.^{5,6}

BaVSe₃, having a hexagonal perovskite-like structure with the general formula BaVX₃ (with X = S, Se), satisfies the Zintl–Klemm concept.⁷ Among the above-mentioned BaVX₃ compounds, BaVS₃ has been extensively studied.⁸ BaVS₃ shows a metal to insulator transition at a temperature of 70 K, a hexagonal to orthorhombic structural transition at 240 K and antiferromagnetic (AFM) ordering below 30 K.⁷ The selenium (Se) ions, being larger than the sulphur (S) ions, lead to orbital overlap in BaVSe₃ and generate a condition synonymous to one where BaVS₃ is under high pressure.⁹ BaVSe₃ exhibits a structural transition from hexagonal to orthorhombic at a temperature of ~310 K.^{10,11}

Ternary chalcogenides with the general formula BaMX₃ (M = Ti, V, Nb or Ta and X = S or Se) exhibit a quasi-one-dimensional structure. At room temperature, BaVS₃ crystallizes in the CsNiCl₃ structure having a space group of *p63/mmc* with a linear chain of vanadium atoms formed by the face sharing of VS₆ octahedra. In this structure the unidimensionality arises from the short intrachain V–V (vanadium–vanadium) distance (2.805 Å) and a long interchain V–V separation (6.724 Å).¹² The ideal quasi-one-dimensional nature is represented by vanadium ion chains that are slightly distorted, forming a

^a Photosciences and Photonics, Chemical science and Technology Division, CSIR-National Institute for Interdisciplinary Science and Technology (NIIST), Thiruvananthapuram-695019, Kerala, India

^b Academy of Scientific and Innovative Research (AcSIR), Ghaziabad-201002, India. E-mail: manoj@niist.res.in, biswapriya.deb@niist.res.in; Fax: +91-471-2491712; Tel: +91-471-2515478, +91-471-2515377

^c School of Physics (SoP), Indian Institute of Science Education and Research, Thiruvananthapuram-695551, Kerala, India

^d Materials Science and Technology Division, CSIR-National Institute for Interdisciplinary Science and Technology (NIIST), Thiruvananthapuram-695019, Kerala, India

^e Department of Physics, St. John's College, Anchal, Kollam, Kerala, India

† Electronic supplementary information (ESI) available. See DOI: <https://doi.org/10.1039/d2nj04129d>

zig-zag pattern along the crystallographic *c* axis. BaVSe₃ also exhibits a metallic ferromagnetic nature and is considered to be an example of an itinerant electron magnet possessing a 1D structure;¹³ hence its primary application is in the field of spintronics.¹⁴ Sugiyama *et al.* reported that the V moments align ferromagnetically along the *c*-axis but they slightly canted towards the *a*-axis by 28° and are coupled antiferromagnetically.¹⁵ Recently, several studies have been conducted on the spin-glass behavior and the long-range AFM ordering in dilute metallic alloys and layered transition metal chalcogenides.^{16–19} Magnetic materials with glassy behavior are characterized by randomness, competing interactions and geometrical frustrations, which lead to the freezing of magnetic moments below a temperature denoted as the freezing temperature (T_f).²⁰ These metastable ground states are structurally similar to the glassy state.²¹

Materials exhibiting glassy behavior are categorized into several classes based on the observed density of magnetic moments. Canonical spin-glass (SG) materials exhibit a small magnetic moment density and can be considered as single magnetic impurities being dispersed in a nonmagnetic host. These materials indicate a phase transition that is brought about due to the strong interaction and cooperative spin freezing present in them. These magnetic systems have some frozen-in structural disorder and do not have any well-defined long-range order as observed in FM and AFM systems. These systems exhibit a freezing transition with order in which the spins are correlated to form clusters which are oriented in random directions.²² Cluster glass (CG) materials exhibit large magnetic moment densities, resulting from local magnetic moment and frustration between the neighboring magnetic clusters.²¹ This state can be distinguished from SG by the presence of clusters originating due to short-range magnetic ordering at temperatures near T_C .²² When the density of magnetic moments of a material overcomes the glassy limit, it results in long-range magnetic order. Such magnetic materials exhibit a transition from the PM state to an ordered state at a transition temperature before the glassy appearance at T_f . The PM, SG and CG states lack the long-range magnetic ordering.^{20–23}

Nowadays intense research and development (R&D) is underway to understand the Griffiths-like phase (GP) observed in different magnetic materials.²⁴ Griffith first observed the GP in randomly diluted Ising ferromagnetic systems. In such systems, magnetization fails to be an analytical function of magnetic field at temperatures between the Curie–Weiss temperature and the Griffiths temperature.²⁵ The reasons for the origin of the GP vary from one material to another, some of which are phase separation, the presence of cluster sizes ranging from nanometers to micrometers and competition for intra–interlayer magnetic interactions.²⁶ In most of the materials the GP arises due to the occurrence of short-range ordered FM clusters in the PM region.²⁷ In manganese oxide-based materials,²⁸ quenched disorder plays an essential role in GP formation. In the case of 4f electron alloys²⁹ the origin of the GP is associated with inherent disorder and competition between the Ruderman–Kittel–Kasuya–Yosida (RKKY) interaction and the Kondo effect.

In the present investigation, we synthesized polycrystalline Zintl phase BaVSe₃ with BaSe₃ as the secondary phase through a solid-state method and carried out detailed structural and magnetic investigations. The present study establishes the glassy behavior of BaVSe₃ with the secondary phase of BaSe₃ for the first time. The GP is another area of interest in the present system. The existence of this phenomenon is established through different magnetic property evaluation techniques. In addition to experimental techniques, we also employ DFT and atomistic simulations to probe the electronic and magnetic nature of the material. The band structure, density of states, effective magnetic moment and the Curie temperature of the synthesized material were theoretically investigated through DFT analysis.

2. Experimental section

2.1. Synthesis

Polycrystalline BaVSe₃ was synthesized *via* a solid-state reaction route using the precursors Ba, V and Se. The components of the precursors, *i.e.*, Ba rods (99.99%), V pieces (99.7%) and Se granules (99.999%), were purchased from Alfa Aesar. The synthesis was done in three steps: at first Ba and Se were weighed in a 1 : 1 ratio under a nitrogen atmosphere in a glove box with 1 ppm oxygen level and moisture level, sealed under vacuum (10^{-4} Torr) in quartz tubes and annealed at 600 °C for 2 days. In the second step VSe₂ was prepared *via* the same solid-state route, with a heat treatment of the evacuated and sealed quartz tube at 750 °C for 8 days. The obtained pieces were ground and then subjected to recrystallization for an extended duration of 8 days at 750 °C. The synthesized material from the first step and VSe₂ were mixed with Se in the required stoichiometry in a glove box with ideal conditions and sealed under vacuum in quartz tubes. The tubes were then heated at 950 °C for 100 hours. The obtained powder was crushed and pelletized for characterization using various techniques.

2.2. Characterization techniques

The crystal structure of the synthesized BaVSe₃ was analyzed by utilizing the powder X-ray diffraction technique (XRD, Bruker D8 Advance diffractometer) using Cu-K α radiation with a wavelength of 1.5406 Å in the 2θ range of 10°–90° with a step size of 0.005°. The Rietveld refinements of the XRD patterns were done by using GSAS-EXPGUI software. The elemental analysis was carried out using X-ray photoelectron spectroscopy (PHI 5000 Versaprobe II) and the peaks were fitted by using Multi-Pak software. Magnetic measurements were carried out using a vibrating sample magnetometer (VSM) attached to the physical property measurement system (PPMS DynaCool, Quantum Design, USA).

2.3. Computational details

The spin-polarized DFT calculations are carried out using Quantum ESPRESSO, the plane-wave pseudopotential (PW + PP) code. The converged values for the *K*-point grid, the kinetic energy cut-off of the wave function and the kinetic energy cut-off for charge density are $8 \times 8 \times 8$, 80 Ry and 640 Ry, respectively,

and are used in conducting the SCF (self-consistent field) calculations. The approximation involved was the GGA-PBE (generalized gradient approximation-Perdew–Burke–Ernzerhof) exchange–correlation functional with the KJPAW (Kresse–Joubert projector augmented wave) pseudopotential. The GGA-KJPAW pseudopotential is acquired from the Quantum ESPRESSO repository of pseudopotentials and is used for our calculations as it is reasonably accurate and inexpensive in terms of the computational power required. The denser grid for NSCF (non-self-consistent field) calculations is taken to be $16 \times 16 \times 16$. The geometry is relaxed using the BFGS (Broyden–Fletcher–Goldfarb–Shanno) algorithm. The constraint involved keeping the lattice parameters (a , b , c , α , β and γ) equal to the ones obtained from the XRD measurement and moving the ions so as to obtain the minimum energy structure with the forces on the atoms reduced (shown in Fig. S1, ESI†). The electronic structure calculated *via* DFT resembles the experimentally obtained lattice and at the same time the relaxation (by varying the positions of atoms) minimizes the effect of strains that may exist in the unit cell. The DFT+ U methodology, which is based on the Hubbard model, can be used to reduce the electron delocalization, but we were not able to tune the U parameter based on an experimentally observed physical quantity (like the bandgap). Since the system is metallic, the DFT+ U methodology was not followed in our simulations. The Curie temperature is simulated *via* the atomistic simulation code VAMPIRE which implements the 3D Heisenberg model.

The atomistic spin model used in VAMPIRE is based on the spin Hamiltonian, which describes the fundamental spin-dependent interactions at the atomic level (neglecting the effects of potential and kinetic energy and electron correlations). The spin Hamiltonian is defined as

$$\hat{H} = \sum_{i < j} J_{ij} S_i \cdot S_j - k_2 \sum_i S_z^2 - \mu_S \sum_i B_{\text{app}} \cdot S_i$$

The three terms describe the exchange, uniaxial anisotropy and applied field contributions, respectively. Important parameters are the Heisenberg exchange J_{ij} , the anisotropy constant k_2 and the atomic spin moment μ_S . S_i is a unit vector which describes the orientation of the local spin moment. In most magnetic materials the exchange interactions are the dominant contribution, usually by two orders of magnitude, and give rise to the atomic ordering of the spin directions. For ferromagnetic materials (parallel alignment of spins), $J_{ij} > 0$, while for anti-ferromagnetic materials (antiparallel alignment of spins), $J_{ij} < 0$.

3. Results and discussion

3.1. Crystal structure

The indexed XRD spectra of the synthesized BaVSe_3 are shown in Fig. S2 in the ESI,† and the Rietveld refined XRD pattern is shown in Fig. 1(a). The existence of the secondary phase of BaSe_3 is also evident from the XRD data.

Hulliger *et al.*³⁰ reported the formation of BaSe_3 from its constituent elements at temperatures between 500 °C and 700 °C and remained stable even after prolonged heat

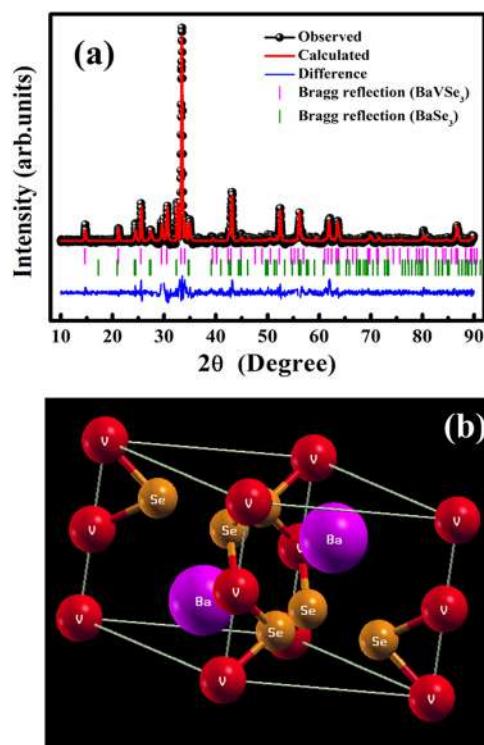


Fig. 1 (a) Rietveld refined XRD pattern of BaVSe_3 and (b) a graphical representation of the BaVSe_3 unit cell obtained from the refined XRD data.

treatment. The presence of secondary phases is common in solid-state synthesized materials from constituent elements.³¹ The primary phase BaVSe_3 belongs to the hexagonal crystal system with a space group of $p63/mmc$ and the other phase, BaSe_3 , belongs to the tetragonal system with a space group of $p421m$. The goodness of fit factor of the refinement (χ^2) is obtained as 1.66. The lattice parameters of BaVSe_3 are $a = b = 6.9944 \text{ \AA}$ and $c = 5.8577 \text{ \AA}$. The α , β and γ angles are 90° , 90° , and 120° , respectively. From the Rietveld refinement, the phase fraction obtained for BaVSe_3 is 76.21% and for the secondary phase it is 23.79%. A crystallographic information file (CIF) is created from the Rietveld refined XRD data using the software Crystal Maker (version 2.7.3). A graphical representation with the labeling of Ba, V and Se is shown in Fig. 1(b), where the barium, vanadium and selenium (Se) ions are labeled with purple, red and orange spheres, respectively. The Wyckoff symbols and the initial fractional coordinates are given in Table 1. The structure from the CIF file is subjected to constrained relaxation prior to conducting the DFT calculations. The procedure for the same is detailed in the ESI.†

3.2. X-ray photoelectron spectroscopy

X-ray photoelectron spectroscopy (XPS) studies of polycrystalline BaVSe_3 were carried out to observe the oxidation state and chemical composition of the sample. The binding energies are corrected with the reference energy of 284.60 eV (C 1s). Fig. 2(a)–(c) shows the peak fitted high-resolution spectra of Ba, V, and Se, respectively. Fig. 2(a) depicts the deconvolution of

Table 1 The Wyckoff symbols and positions (in fractional coordinates) of one instance of Ba, V and Se as is present in the CIF file created from refined XRD data

Atoms	Wyckoff symbols	x coordinate	y coordinate	z coordinate
Ba	2c	0.33333	0.66667	0.25
Se	6h	0.82735	0.65470	0.25
V	2a	0	0	0

the Ba $3d_{5/2}$ peak, fitted with two curves at binding energies of 781.27 eV and 779.35 eV, representing the Ba^{2+} and Ba^0 states, respectively.³² In $BaVSe_3$, vanadium exists in the V^{4+} state; however, the presence of V^{5+} may indicate the surface oxidation³³ and the formation of V_2O_5 on the top 5 nm layer of $BaVSe_3$. However, the presence of V_2O_5 is not observed in XRD, indicating that the formation of V_2O_5 is negligible and does not influence the properties of the considered system. Fig. 2(c) shows the deconvoluted spectra of Se. It has a lower binding energy of 54.36 eV due to Se^{2-} ³² and a higher binding energy of 55.90 eV corresponding to the Se^0 state.³² Hulliger *et al.*³⁰ reported that $BaSe_3$ has the ionic formula of $Ba^{2+}Se^0Se_2^{1-}$, where Se^0 corresponds to the formation of the secondary phase, $BaSe_3$, and is confirmed by the Rietveld refinement of XRD spectra.

3.3. Magnetic properties

The magnetic hysteresis ($M-H$) loops were recorded at different temperatures in the field ranging from -90 kOe to $+90$ kOe. Fig. 3(a) shows the $M-H$ loops recorded at different temperatures

such as 2 K, 10 K, 25 K and 43 K. Up to 25 K, the MH loop shows FM nature, and the $M(H)$ loop at 43 K shows PM behavior, which profoundly indicates the FM to PM transition at a critical temperature (*i.e.*, Curie temperature, T_C) between 25 K and 43 K.

However, the hysteresis loops below T_C exhibit unsaturated magnetization even at a higher field of 90 kOe. Usually this kind of unsaturated magnetization is due to the presence of AFM moments.³⁴ Also, an unsaturated $M-H$ loop is one of the criteria for magnetic systems with glassy behavior.³⁵ Fig. 3(a) clearly demonstrates the above-mentioned unsaturated nature of magnetization and is a profound indication of a frustrated ferromagnetic system.³⁶ In the magnified view of the hysteresis (shown in Fig. 3(b)), a non-zero coercivity (H_C) and remanent magnetization (M_R) at temperatures of 2 K, 10 K, and 25 K can be observed. Here, H_C and M_R are observed to decrease with an increase in temperature. Another parameter of interest is the anisotropy constant (K) since it depends strongly on temperature.³⁷ In Table 2, H_C , saturation magnetization (M_S) and M_R are presented. The reduction in coercivity can be a direct consequence of the reduction in effective magnetic anisotropy with an increase in temperature.³⁸ According to the Néel model of anisotropy, the magnetic energy barrier³⁹ is given in eqn (1) as

$$H_C = \frac{2K}{M_S} \quad (1)$$

The calculated values of K at different temperatures are given in Table 2. The anisotropy constant is observed to decrease with increasing temperature.³⁹

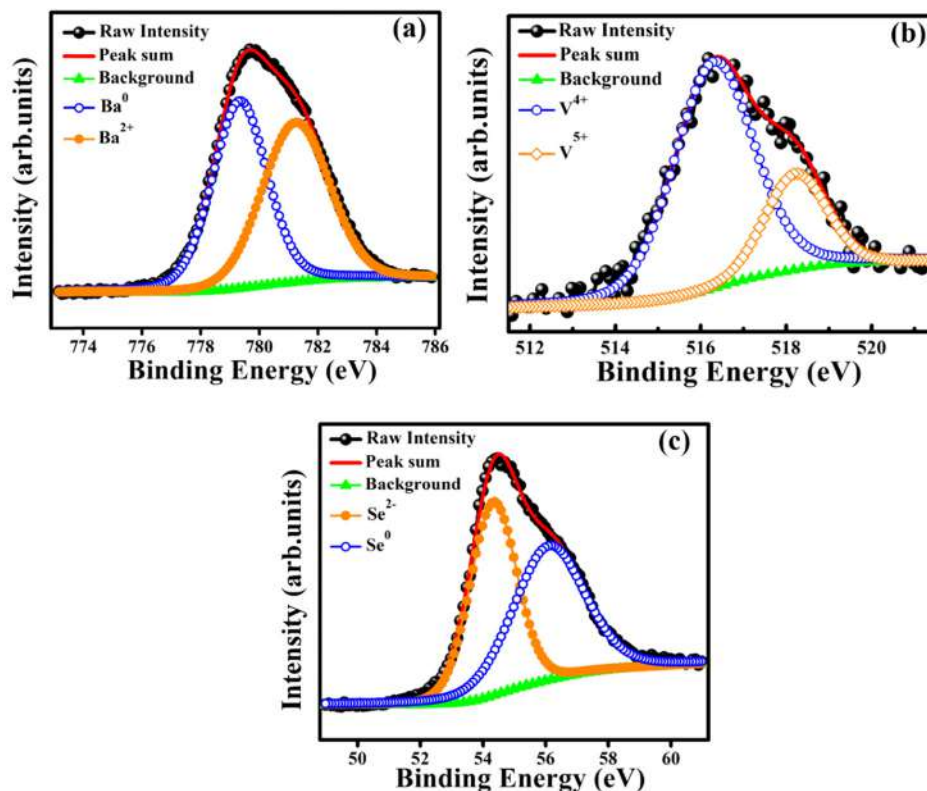


Fig. 2 Deconvoluted high resolution XPS spectra of elements (a) Ba, (b) V and (c) Se.

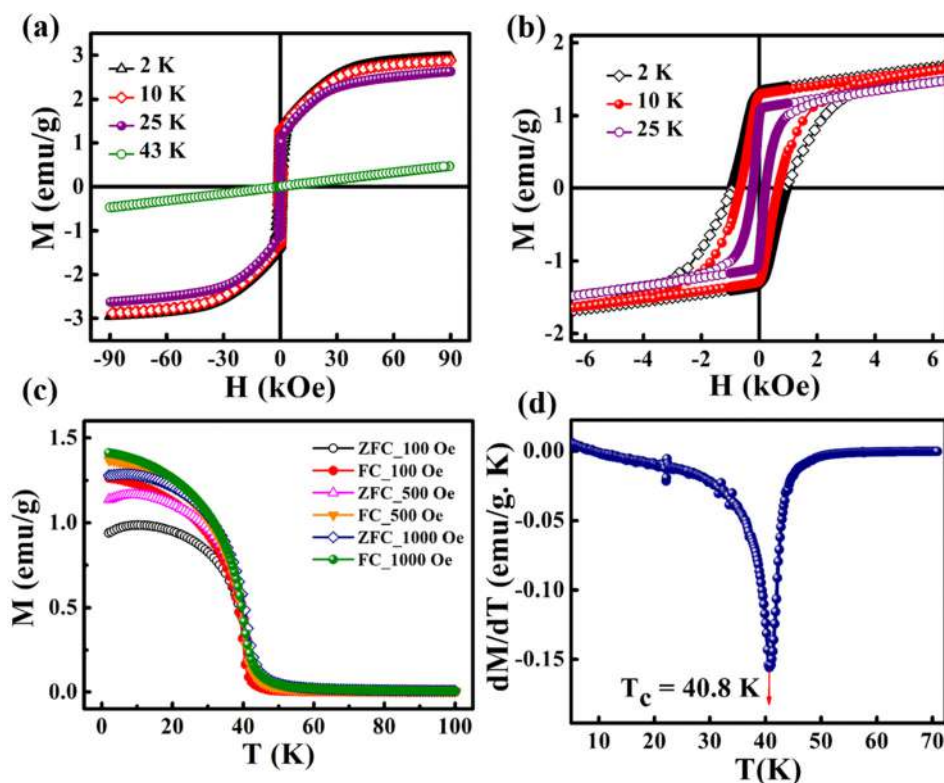


Fig. 3 (a) M - H loops recorded at different temperatures, (b) zoomed-in view of (a), (c) M - T curves recorded at different magnetic fields, and (d) the dM/dT versus T plot.

The temperature-dependent magnetization of the material is studied in the temperature range of 2–100 K at different field strengths. The zero-field cooled (ZFC) and field cooled (FC) magnetization *versus* temperature (M - T) curves were recorded under different field conditions. In ZFC, the material is cooled to 2 K in the absence of an external magnetic field and subsequently warmed from 2 K to 300 K by applying the required field; the required data are collected during the warming process. In FC, the M - T measurement was carried out in the presence of a constant field with cooling the sample from 300 K to 2 K. Fig. 3(c) shows the M - T curves of BaVSe₃ under the influence of 100 Oe, 500 Oe and 1000 Oe fields, indicating that there is a split in ZFC and FC at low temperatures. This bifurcation in the M - T curves was not suppressed by the applied strong magnetic fields, which is an indication of glassy behavior.⁴⁰ Fig. S3 in the ESI,[†] shows the observed cusp in ZFC at lower fields.

The transition temperature, T_C , is obtained from the minimum of the dM/dT versus T plot. Below T_C , the material exhibits FM ordering and a paramagnetic behavior is observed above T_C .

Table 2 Comparison of H_C , M_S and M_R

T (K)	H_C (kOe)	M_S (emu g ⁻¹)	M_R (emu g ⁻¹)	$K = \frac{M_S H_C}{2}$
2	1.00	2.80	1.32	1409.80
10	0.67	2.22	1.29	748.80
25	0.23	1.38	1.07	161.30

Fig. 3(d) shows the dM/dT vs. T plot of BaVSe₃ and the T_C obtained is 40.81 K. This is in good agreement with previous reports by Kelber *et al.* ($T_C = 41$ K)¹¹ and Akrap *et al.* ($T_C = 43$ K).⁹ Some recent reports of 2D magnetic materials exhibit low T_C values (below 50 K).^{41–43} But the Curie temperature of ferromagnetic materials is dependent on the size and shape effects of nanoparticles.^{44,45} These results indicate that the presence of nonmagnetic BaSe₃ did not affect the properties of BaVSe₃ much. Since V is a first-row transition metal, orbital angular momentum does not contribute to the total magnetic moment due to orbital quenching.³⁷ Hence, the magnetic moment for these metals originates from electron spin-only magnetic moment and is given by

$$\mu_{\text{eff}} = g_s \sqrt{S(S+1)} \mu_B \text{ per F.U.} \quad (2)$$

where S is the spin angular momentum quantum number and the Lande g factor, g_s , has a value of 2.

In BaVSe₃, vanadium is the only element that contributes to magnetism. The spin-only magnetic moment for V⁴⁺ calculated from eqn (2) is 1.73 μ_B per F.U. Since eqn (2) represents a scenario in which spins are non-interacting, the magnetic properties of BaVSe₃ are also obtained *via* a DFT calculation. DFT involves solving the many-body Schrödinger equation. Hence it reveals the interactions between the ions in a crystal system. The spin-polarized bands (the calculation procedure is mentioned in Section S4.1 of the ESI[†]) crossing the Fermi level (0 eV) at Gamma and other high-symmetry points (Fig. 4(a))

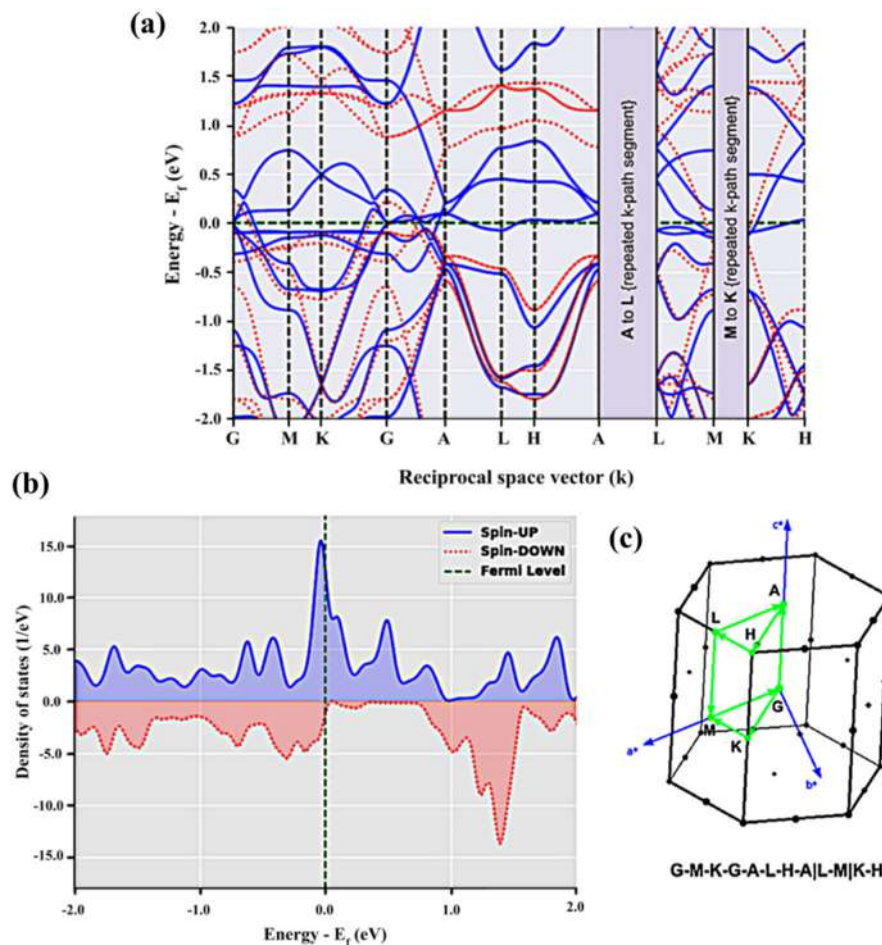


Fig. 4 (a) The spin-polarized band structure of BaVSe₃. The blue (solid-line) and red (dotted-line) bands indicate the spin-up and spin-down channels, respectively (the green dashed line indicates the Fermi level at zero). (b) The spin-polarized density of states (DOS) of BaVSe₃ near the Fermi level. (c) The *k*-path (for band structure calculations) taken through the Brillouin zone.

indicate the metallic nature of the material. This is also evident from the peaking of spin-polarized DOS (the calculation procedure is mentioned in Section S4.2 of the ESI[†]) near the Fermi level (given in Fig. 4(b)). The room temperature electrical conductivity (120 S m⁻¹) measurements further confirm the metallic nature of the material (S5(c), ESI[†]). The spike seen in the spin-up DOS near the Fermi level can be attributed to the dispersion-less nature of the spin-up bands. The spin-polarized band structure is obtained along the *k*-path “G-M-K-G-A-L-H-A|L-M|K-H” (where the letters stand for the high symmetry points) as given in Fig. 4(c), where hexagonal BaVSe₃ is considered. The magnetic moment of the unit cell was also calculated from the DOS using eqn (3):

$$\mu = \mu_B \int_E [n^+(E) - n^-(E)] \cdot dE \quad (3)$$

where μ represents the net magnetic moment, μ_B is the Bohr magneton, $n^+(E)$ and $n^-(E)$ are the DOS values of spin-up states and spin-down states, respectively, and dE is the increase in energy (integrating variable). The integration was done over the entire range of the calculated energy values from $-\infty$ to 0

(since the energy values are shifted with respect to the Fermi level), which turned out to be $1.73\mu_B$ per unit cell. The atomic moments are calculated by carrying out the spin-polarized DFT calculations. The moments on individual atoms of Ba, Se and V are $-0.0058\mu_B$, $-0.0759\mu_B$ and $+1.0460\mu_B$, respectively. The magnetic moment on vanadium ions ($1.046\mu_B$) is two orders of magnitude greater than that present on the other ionic species (Ba²⁺ and Se²⁻). The total magnetic moment is calculated by summing up the contributions of all the atomic moments, and it results in a value of $1.73\mu_B$ which is equivalent to the one obtained from the DOS calculation.

The spin-polarized charge density distribution (Fig. 5) is calculated to understand the distribution of spins inside the crystal (Section S4.3, ESI[†]). The charge with a positive spin polarity is localized around the vanadium atom (Fig. 5(a-d)) as observed from the iso-surface plot (iso-value = 0.022) shown in Fig. 5(d). The spin-polarized charge density distribution is also found to be different on the two vanadium atoms (Fig. 5(d)) in the BaVSe₃ unit cell.

From Fig. S6 (ESI[†]), the experimental effective magnetic moment is calculated from the C-W fit by using eqn (4):

$$\mu_{\text{eff}} = 2.827\sqrt{\chi^T} \mu_B \text{ per F.U.} \quad (4)$$

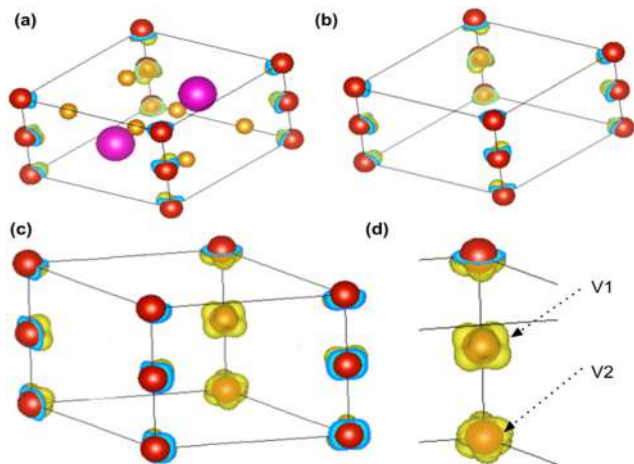


Fig. 5 The spin-polarized charge density plots of (a) the BaVSe_3 unit cell (Ba – pink, V – red, Se – orange), (b) BaVSe_3 unit cell with the V atoms visible, (c) BaVSe_3 unit cell (zoomed-in) and (d) vanadium ions with electron distribution iso-surface (yellow) which are magnified.

Here χ^T is the reciprocal of the slope of the linear fit, k_B is the Boltzmann constant and N_A is the Avogadro number. The paramagnetic μ_{eff} calculated from the C–W linear fit is $1.02\mu_B$ per F.U. Yamaski *et al.* reported the μ_{eff} of BaVSe_3 as $1.42\mu_B$ per F.U.¹³ The reduction in the magnetic moment may have occurred due to the disorder induced by the secondary phase BaSe_3 . The C–W temperature (θ) obtained is 17 K. The positive value of θ confirms that the material is ferromagnetic below T_C .

The FM to PM transition of BaVSe_3 is also investigated *via* atomistic simulations. The exchange interaction constant (J) is obtained as $+0.392 \times 10^{-21}$ J per atom. The positive value of J is also indicates that the material is ferromagnetic in nature. The atomistic simulation of the Curie temperature using VAMPIRE yielded a value of 41.01 K (shown in Fig. 6(a) and (b)). The initial spin distribution for the calculation involved assigning a moment of $1.046\mu_B$ to the V ions arranged in a pattern as shown in Fig. 6(c).

The simulation required the dimensions of the magnetic unit cell (a , b and c), damping constant, exchange-matrix value, atomic-spin-moment and the uniaxial-anisotropy constant. The magnetic unit cell was taken in accordance with the distribution of local moments (located mostly on the vanadium ions in the unit cell of the crystal) obtained from the DFT calculations. The distribution of local magnetic moments resembled a hexagonal magnetic unit cell with the parameter values of a , b and c of 7 Å, 7 Å, and 3 Å, respectively. The magnetic unit cell is not equivalent to the crystallographic unit (repeating unit with a specific composition of elements) as it takes into consideration the local spin magnetic moment (localized on the atoms) and is defined as the smallest repeating spin configuration. Hence, the magnetic unit cell parameters (a , b and c) mentioned here are different from those defined for the unit cell of the BaVSe_3 crystal. Since the support for unit cells with non-orthogonal cell vectors is not implemented in VAMPIRE,⁴⁶ the magnetic unit cell was considered as an orthorhombic unit cell (as shown in Fig. 6(c)) with the a , b , and c parameters taken as 7 Å, 7 Å, and 3 Å.

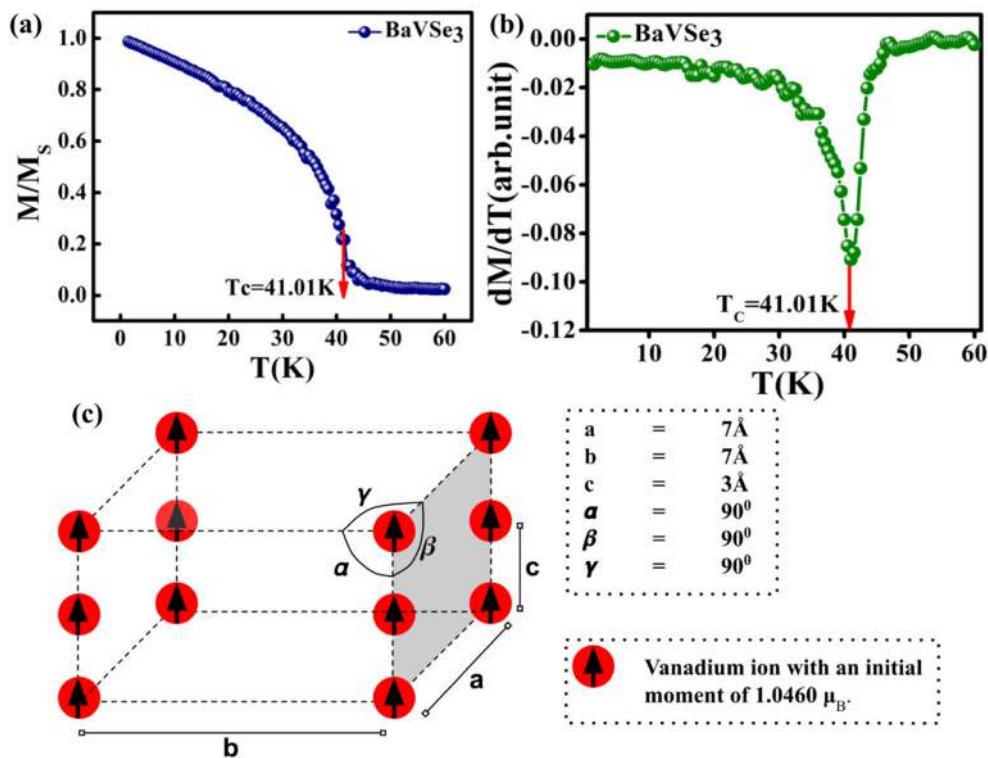


Fig. 6 (a) M – T curve obtained from the atomistic simulation, (b) dM/dT vs. T curve obtained from the simulated M – T curve, and (c) the initial spin configuration chosen for the BaVSe_3 unit cell for the Curie temperature simulation.

The atomic magnetic moment is given as $1.0460\mu_B$, the value of the local magnetic moment for vanadium obtained from DFT. The initial magnetic configuration as given in Fig. 6(c) is taken to be similar to that in the DFT configuration. The damping constant, uniaxial-anisotropy constant and exchange matrix value are provided as 1.0, 6.39×10^{-30} J per atom, and 0.392×10^{-21} J per atom, respectively. To get an estimate of the exchange matrix value, eqn (5) was used.

$$J = \frac{3k_B T_C}{\varepsilon n} \quad (5)$$

Here k_B , T_C , ε , and n represent the Boltzmann constant, Curie temperature, correction factor related to spin stiffness, and the number of interactions, respectively.⁴⁷ The values for the same are provided as $k_B = 1.3806 \times 10^{-23}$ m² kg s⁻² K⁻¹, $T_C = 40.8$ K (experimental observation), $\varepsilon = 0.719$ (for a 3D Heisenberg system having a simple cubic-like lattice⁴⁷), and $n = 6$ (since the magnetic unit cell approximated as orthorhombic).

In most of the substituted manganites there is magnetic inhomogeneity at temperatures above T_C , and Griffith initially explained it for disordered magnetic systems.⁴⁸⁻⁵⁰ It is defined for randomly diluted Ising ferromagnets and this phase appears as ferromagnetic clusters in a paramagnetic matrix above T_C .²⁴ This theory was first introduced for explaining the CMR, magnetic susceptibility, and heat capacity in $\text{La}_{0.7}\text{Ca}_{0.3}\text{MnO}_3$.⁵¹ The downturn deviation from standard PM behavior in the inverse susceptibility graph at lower applied fields is a hallmark of the presence of the GP.⁵² It is due to the short-range FM ordering in the PM region. However, on increasing the applied magnetic field the anomaly in the C-W plot softens and attains the classical C-W behavior.⁵³

According to the concept of GP there is always a finite probability of finding FM clusters with randomly distributed spins in the temperature range $T_C < T < T_G$, where T_C is the C-W temperature and T_G is the Griffiths temperature at which the deviation in χ^{-1} occurs. In the Griffiths phase spontaneous magnetization is absent due to the lack of long-range FM order.⁵⁴ Further, Bray extended the concept of GP and at present the GP is observed in the region $T_C^R < T < T_G$, where T_C^R is the critical temperature of the random FM at which the

susceptibility starts to diverge.⁵⁵ So the GP is the area between completely ordered states above T_C^R and the disordered state below T_G . In general, T_C^R is considered as the C-W temperature, Θ . Hence, the GP is defined as the region of the PM phase where the magnetic clusters are generated.⁵⁶

Fig. 7(a) shows the χ^{-1} versus T behavior under the influence of various field strengths of 100 Oe, 1000 Oe, 3000 Oe and 10 000 Oe. It can be seen that there is a visible downturn in the variation of χ^{-1} above the temperature T_C . The retention of this anomaly up to a field strength of 10 000 Oe indicates that higher fields are required for its suppression. The linear fit of the C-W plot at fields of 3000 Oe and 10 000 Oe is depicted in Fig. 7(b). The fit exhibited a T_G value of 116 K and a Θ value of 17 K. The GP is observed in this temperature range. On increasing the field to 10 000 Oe the linear fit overlaps with the PM region, confirming the disappearance of FM clusters in the PM region. This is due to the fact that the increase in field leads to the magnetization of the spins which are outside the clusters or the masking FM signal by the enhanced PM background.⁵²

The susceptibility of the GP at low applied fields follows a power-law, which is formulated in eqn (6).

$$\frac{1}{\chi} = (T - T_C^R)^{1-\lambda} \quad (6)$$

Here λ is the magnetic susceptibility exponent with a value that lies between 0 and 1, and T_C^R is the random critical temperature. Based on the value of λ , the GP and PM phases can be distinguished. When $\lambda = 1$, it corresponds to GP behavior and $\lambda = 0$ is indicative of the PM state. T_C^R is the random critical temperature at which the C-W law yields a λ value close to zero above T_G , and in the present case the Θ can be considered as T_C^R .⁵⁷ In Fig. 8(a) the linear region of the graph $\ln(\chi^{-1})$ versus $\ln(T - T_C^R)$ is fitted with a power law. The λ values for lower and higher fields are calculated from the slope of the fitted straight line in the GP region. The λ_{GP} value decreases from 0.99 to 0.94 when the applied field increases from 100 Oe to 10 000 Oe. This is in good agreement with the required range. This confirms the presence of the GP in this Zintl phase compound and the high value of λ_{GP} indicates the prominence

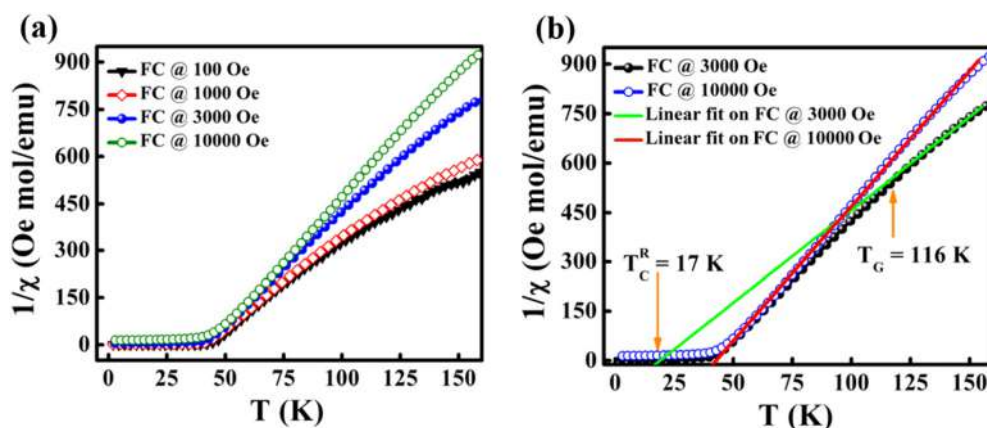


Fig. 7 (a) C-W plot at different fields and (b) C-W plot with linear fit in the PM region.

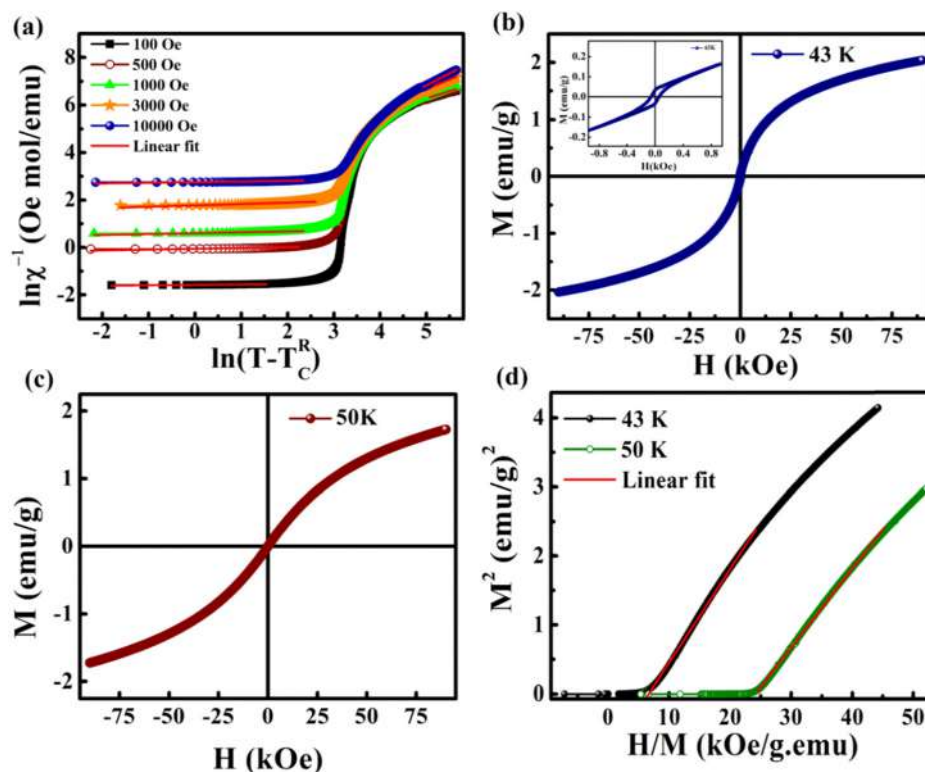


Fig. 8 (a) GP analysis, (b) M - H loop at 43 K, (c) M - H loop at 50 K and (d) Arrott plot.

of the GP. The linear fit in the paramagnetic region ($T > T_G$) at higher fields (10 000 Oe) shows a reduction in the λ_{PM} value to 0.12 and this is due to the decrease in the size of the clusters in the PM region under large fields. On increasing the field, the exponent value gets reduced (this is a signature of GP behavior), as higher fields are needed to remove the ferromagnetic clusters in the paramagnetic matrix. Here, the $M(H)$ measurements above T_C also show FM-like behavior with small loops as shown in Fig. 8(b) and (c) and its inset. This hysteresis above and below T_G is due to the presence of FM or AFM clusters in the GP regime.

Another major analysis technique used to probe for the presence of the GP is the Arrott plot, in which the square of magnetization (M^2) is plotted as a function of H/M .⁵⁸ Fig. 8(d) shows the Arrott plot at 43 K, which is well above T_C^R (17 K) and below T_G (116 K). The extrapolation of linear fit in the M^2 versus H/M plot exhibits a negative y-intercept. This indicates the absence of spontaneous magnetization (*i.e.* $M_S = 0$) above T_C . The absence of M_S in the GP regime is an indirect characteristic of the Griffiths-like phase in BaVSe₃. Hence, the Arrott plot analysis further confirms the presence of the GP in BaVSe₃.

The foremost measurement that indicates a glassy-like nature is the AC susceptibility measurement.⁵⁹ The AC susceptibility measurements are carried out by varying the temperature from 22 K to 44 K at frequencies of 177 Hz, 555 Hz and 777 Hz. Fig. 9(a) depicts the real part of AC susceptibility (χ') vs. temperature at different frequencies. The temperature at which the peak point occurs in the χ' vs. T plot is the freezing temperature (T_f). χ' has a peak at T_f as shown in Fig. 9(a) and

it shifts towards the right when the frequency is increased. This frequency dependent shift indicates the glassy nature of the material. The three models introduced to explain the T_f shift are the Arrhenius law, Vogel-Fulcher (V-F) law and critical scaling approach.^{19,21,60,61} When the spin-glass material is cooled from a paramagnetic state, it results in a random configuration initially. The spins will locally optimize their respective orientations over longer length scales, which defines the time growing correlation length, ξ .⁶² Let us assume that τ_0 represents the spin relaxation time, E_a is the activation energy, T_{SG} represents the critical spin glass ordering temperature in which the frequency tends to zero, z is the dynamical critical exponent, ν represents the critical exponent of spin correlation length, and $\xi = \left(\frac{T_f - T_{SG}}{T_{SG}}\right)^{-\nu}$.⁶³ The relationship between relaxation time τ and reduced temperature is given by $t = \frac{T_f - T_{SG}}{T_{SG}}$. The τ is associated with the frequency (f) at which the single-spin flip occurs and is given by $\tau = 1/2\pi f$. The relaxation time is obtained from the experiments and the other parameters are calculated by fitting the experimental data with the concerned model.

The first model is the Arrhenius law⁶⁴ represented by eqn (7).

$$\tau = \tau_0 \cdot e^{\frac{E_a}{k_B T_f}} \quad (7)$$

Similarly, the V-F law is defined by the relationship represented in eqn (8), and the critical scaling approach is given by the

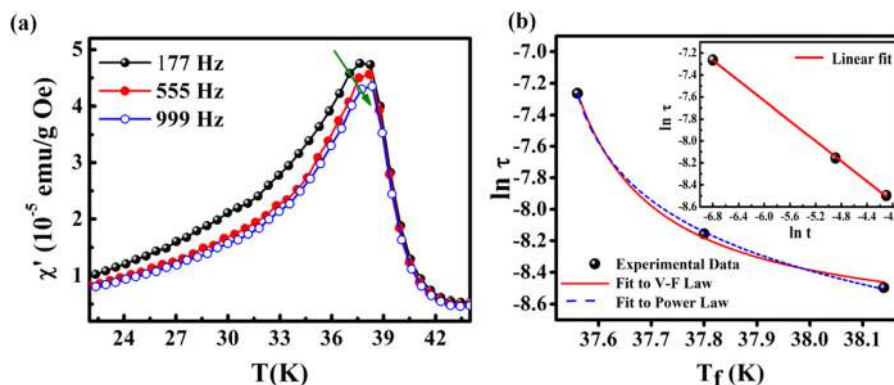


Fig. 9 Frequency dependence of the (a) real component of AC-magnetic susceptibility and (b) relaxation time τ versus maximum spin-freezing temperature T_f fitted to the VF law (solid line) and power law (dashed line). The inset shows linear fitted $\ln(\tau)$ versus $\ln(t)$, where reduced temperature $t = (T_f - T_{SG})/T_{SG}$ and the solid line is the linear fit.

relationship in eqn (9).⁶⁵

$$\tau = \tau_0 \cdot e^{\frac{E_a}{k_B(T_f - T_{SG})}} \quad (8)$$

$$\tau = \tau_0 \left[\frac{T_f}{T_{SG}} - 1 \right]^{z\nu} \quad (9)$$

For spin-glass nature to be evident in a system, the τ_0 must be in the range of 10^{-10} to 10^{-13} seconds and the value of $z\nu$ should be between 4 and 12.⁶⁵ Another parameter of interest is the Mydosh parameter (g) which determines the relative temperature shift of T_f with frequency, which is given by the relationship shown in eqn (10).

$$g = \frac{\Delta T_f}{T_f \log(\Delta f)}. \quad (10)$$

The g value for spin glasses lies between 0.005 and 0.08 and for superparamagnetic materials this value is greater than 2.⁶⁶ If the g value is in between those of the above two classes of materials, then the system exhibits a cluster glass nature. In the present case, the g value obtained is 0.1, which lies in the value range of cluster glasses. The Arrhenius model is omitted because the fit does not converge with the experimental data. Therefore, the other two models are considered and are fitted to the experimental data. Fig. 9(b) shows the $\ln(\tau)$ versus T_f graph and the data are fitted using both the V-F model and the critical power law model. The parameter values obtained using the V-F model are $E_a/k_B = 0.243 \pm 0.011$, $T_0 = 37.401 \pm 0.001$ K and $\tau_0 = 1.522 \times 10^{-4}$ s. From the dynamical scaling analysis, T_{SG} and the critical exponent $z\nu$ are obtained as 37.518 ± 0.012 K and 0.459 ± 0.008 , respectively. From this analysis the higher value of τ_0 and lower value of $z\nu$ confirm the slower spin flipping mechanism and the existence of randomly oriented ferromagnetic clusters rather than atomic-level randomness.⁶⁷

4. Conclusion

BaVSe₃, a Zintl phase crystal system, is synthesized through a solid-state reaction by vacuum sealing and controlled atmosphere

heat treatment. The secondary phase associated with it has been identified as nonmagnetic BaSe₃. The crystal structure was analyzed experimentally *via* XRD and theoretically by using DFT simulations. The magnetic measurements indicate that the present material has an FM to PM transition at a T_C of 40.81 K. The effective magnetic moment calculated was $1.02\mu_B$, which is less than the reported values due to the influence of the nonmagnetic impurity phase. We report the occurrence of glassy nature and the Griffiths-like phase in the BaVSe₃ crystal system for the first time. The glassy nature is probed and confirmed *via* AC magnetic susceptibility measurements. The presence of a hysteresis loop at temperatures above T_C provides evidence for the existence of the Griffiths-like phase. The reason for the same can be attributed to the persistence of FM or AFM clusters in the PM matrix. The spin-polarized DFT calculations (without the inclusion of spin-orbit coupling) are carried out to analyze the electronic and magnetic properties of the material. The spin-polarized band structure is a reason for the metallic nature. The crossing of the Fermi level (E_F) by the bands of both spin channels is also a reason. The Curie temperature is theoretically obtained as 41.6 K by using the atomistic simulation suite software VAMPIRE. The effective magnetic moment calculated from the DOS is $1.73\mu_B$, and the spin-polarized charge density distribution confirms the localization of magnetic moments on the V⁴⁺ ions and it is found to be different on the two vanadium ions present within the same BaVSe₃ unit cell.

Conflicts of interest

There are no conflicts of interest to declare.

Acknowledgements

C. V. D. acknowledges the support of University Grants Commission (UGC), India, for granting a research fellowship. R. R. is thankful to the Kerala State Council for Science, Technology and Environment (KSCSTE), Kerala, India for granting a junior research fellowship. The authors acknowledge the measurement facilities in different labs of CSIR-NIIST. M. R. V. and

B. D. are thankful to the Science and Engineering Research Board, Department of Science and Technology, New Delhi, India for funding this research through the Project EMR/2017/004539(Ver-1) dated 06/05/2019.

References

- 1 A. Balvanz, S. Baranets and S. Bobev, *Acta Crystallogr.*, 2020, **76**, 869–873.
- 2 S. M. Kauzlarich, *Materials*, 2019, **12**, 10–12.
- 3 Y. Tokura, *Rep. Prog. Phys.*, 2006, **69**, 797–851.
- 4 A. J. Millis, P. B. Littlewood and B. I. Shraiman, *Phys. Rev. Lett.*, 1995, **74**, 5144–5147.
- 5 S. Jin, T. H. Tiefel, M. McCormack, R. A. Fastnacht, R. Ramesh and L. H. Chen, *Science*, 1994, **264**, 413–415.
- 6 A. P. Ramirez, R. J. Cava and J. Krajewski, *Nature*, 1997, **386**, 156–159.
- 7 N. J. Poulsen, *Mater. Res. Bull.*, 1998, **33**, 313–322.
- 8 A. W. R. A. Gardner and M. Vlasse, *Acta Crystallogr., Sect. B*, 1969, **25**, 781–787.
- 9 A. Ana, S. Vladan, H. Mirta, M. Miljak, N. Bariši, H. Berger and L. Forró, *Phys. Rev. B: Condens. Matter Mater. Phys.*, 2008, **78**, 1–11.
- 10 D. Grieger, L. Boehnke and F. Lechermann, *J. Phys. D: Appl. Phys.*, 2010, **22**, 275601.
- 11 J. Kelber, A. H. Reis, A. T. Aldred and M. H. Muller, *J. Solid State Chem.*, 1979, **30**, 357–364.
- 12 J. Gopalakrishnan and K. S. Nanjundaswamy, *Bull. Mater. Sci.*, 1983, **5**, 287–306.
- 13 T. Yamasaki, S. Giri, H. Nakamura and M. Shiga, *J. Phys. Soc. Jpn.*, 2001, **70**, 1768–1771.
- 14 J. Dijkstra, C. F. van Bruggen, C. Haas and R. A. de Groot, *Phys. Rev. B: Condens. Matter Mater. Phys.*, 1989, **40**, 7973–7976.
- 15 J. Sugiyama, W. Higemoto, D. Andreica, F. O. Kenji, E. Nocerino, M. Månsson, Y. Sassa, R. Gupta, R. Khasanov, H. Ohta and H. Nakamura, *Phys. Rev. B: Condens. Matter Mater. Phys.*, 2021, **103**, 1–10.
- 16 Z. Huang, B. Wolfgang, S. Mankovsky, P. Svitlana, H. Ebert and K. K. Reinhard, *J. Solid State Chem.*, 2006, **179**, 2067–2078.
- 17 D. Yuan, N. Liu, K. Li, S. Jin, J. Guo and X. Chen, *Inorg. Chem.*, 2017, **56**, 13187–13193.
- 18 C. P. H. Lei, E. S. Bozin and K. Wang, *Phys. Rev. B: Condens. Matter Mater. Phys.*, 2011, **84**, 3–6.
- 19 B. Wang, Z. Guo, F. Sun, J. Deng, J. Lin, D. Wu and W. Yuan, *J. Solid State Chem.*, 2019, **272**, 126–130.
- 20 J. A. Mydosh, *Spin Glasses: An Experimental Introduction*, 1993.
- 21 G. Benka, A. Bauer, P. Schmakat, S. Säubert, M. Seifert, P. Jorba and C. Pfleiderer, *Condens. Matter*, 2020, 1–14.
- 22 S. Mukherjee, R. Ranganathan, P. Anilkumar and P. Joy, *Phys. Rev. B: Condens. Matter Mater. Phys.*, 1996, **54**, 9267–9274.
- 23 K. Binder and A. P. Young, *Rev. Mod. Phys.*, 1986, **58**, 801–976.
- 24 P. R. Mandal and T. K. Nath, *Mater. Res. Express*, 2015, **2**, 66101.
- 25 R. B. Griffiths, *Phys. Rev. Lett.*, 1969, **23**, 563–890.
- 26 K. Ghosh, C. Mazumdar, R. Ranganathan and S. Mukherjee, *Sci. Rep.*, 2015, **5**, 15801.
- 27 Y. Öner and A. Guler, *J. Appl. Phys.*, 2013, **141**, 5–8.
- 28 E. D. J. Burgy, M. Mayr, V. Martin-Mayor and A. Moreo, *Phys. Rev. Lett.*, 2001, **87**, 277202.
- 29 A. H. C. Neto, G. Castilla and B. A. Jones, *Phys. Rev. Lett.*, 1998, **81**, 3531–3534.
- 30 F. Hulliger and T. Siegrist, *Cryst. Struct. BaSe₂ BaSe₃*, 1981, **36b**, 14–15.
- 31 S. K. Bux, A. Zevalkink, J. G. Snyder, J. P. Fluerial, O. Janka, D. Uhl and S. Kauzlarich, *J. Mater. Chem. A*, 2014, **2**, 215–220.
- 32 NIST XPS Data base, URL: https://srdata.nist.gov/xps/main_search_menu.aspx.
- 33 G. Silversmit, D. Depla, H. Poelman, G. B. Marin and R. De Gryse, *Surf. Sci.*, 2006, **600**, 3512–3517.
- 34 M. Motin Seikh, V. Caignaert, O. I. Lebedev and B. Raveau, *Solid State Commun.*, 2014, **180**, 52–55.
- 35 J. Kroder, J. Gooth, W. Schnelle, G. H. Fecher and C. Felser, *AIP Adv.*, 2019, **55327**, 0–5.
- 36 V. Kumar, R. Kumar, K. Singh, S. K. Arora, I. V. Shvets and R. Kumar, *J. Appl. Phys.*, 2014, **116**, 1–6.
- 37 S. Blundell, *Mag. Condens. Matter*, 2001, 128–129.
- 38 N. A. Spaldin, *Magnetic materials: fundamentals and applications*, 2011.
- 39 S. Upadhyay, K. Parekh and B. Pandey, *J. Alloys Compd.*, 2016, **678**, 478–485.
- 40 H. Neuendorf and W. Gunßer, *J. Magn. Magn. Mater.*, 1997, **173**, 117–125.
- 41 Z. Zheng, K. Ren, Z. Huang, Z. Zhu, K. Wang, Z. Shen and J. Yu, *Semicond. Sci. Technol.*, 2021, **36**, 1–9.
- 42 Z. Guan and S. Ni, *ACS Appl. Mater. Interfaces*, 2020, **12**, 53067–53075.
- 43 S. Wang and J. Yu, *J. Supercon. Nov. Magn.*, 2018, **31**, 2789–2795.
- 44 L. Fei Cao, D. Xie, M. Xing Guo, H. S. Park and T. Fujita, *Trans. Nonferrous Met. Soc. China*, 2007, **17**, 1451–1455.
- 45 R. Revathy, M. R. Varma and K. P. Surendran, *Mater. Res. Bull.*, 2019, **120**, 110576.
- 46 VAMPIRE software manual, <https://vampire.york.ac.uk/>.
- 47 R. F. L. Evans, W. J. Fan, P. Churemart, T. A. Ostler, M. O. A. Ellis and R. W. Chantrell, *J. Phys.: Condens. Matter*, 2014, **26**, 103202.
- 48 Y. E. Samoshkina, M. V. Rautskii, E. A. Stepanova, D. S. Neznakhin, N. V. Andreev and V. I. Chichkov, *J. Exp. Theor. Phys.*, 2017, **125**, 1090–1095.
- 49 G. G. L. A. N. Ulyanov, N. E. Pismenova and D. S. Yang, *J. Alloys Compd.*, 2015, **618**, 607–608.
- 50 R. M. Eremina, I. V. Yatsyk, Y. M. Mukovskii and A. L. H. A. Krug Von Nidda, *JETP Lett.*, 2007, **85**, 51–54.
- 51 M. B. Salamon, P. Lin and S. H. Chun, *Phys. Rev. Lett.*, 2002, **88**, 1972031–1972034.
- 52 E. D. A. Tozri, *J. Alloys Compd.*, 2019, **783**, 718–728.
- 53 P. Tong, B. Kim, D. Kwon, T. Qian, S. I. Lee, S. W. Cheong and B. G. Kim, *Phys. Rev. B: Condens. Matter Mater. Phys.*, 2008, **77**, 1–7.
- 54 S. O. Manjunatha, A. Rao, P. Poornesh, W. J. Lin and Y. K. Kuo, *Phys. B: Condens. Matter*, 2016, **498**, 82–91.
- 55 A. J. Bray and M. A. Moore, *J. Phys. C: Solid State Phys*, 1984, **17**(23), L613.
- 56 H. S. Nair, D. Swain, N. Hariharan, S. Adiga, C. Narayana and S. Elizabeth, *J. Appl. Phys.*, 2011, **110**, 123919.

- 57 A. K. N. M. K. Majee and P. A. Bhohe, *J. Magn. Magn. Mater.*, 2019, **485**, 112–117.
- 58 I. N. Bhatti, I. N. Bhatti, R. N. Mahato and M. A. H. Ahsan, *Phys. Lett. A*, 2019, **383**, 2326–2332.
- 59 C. A. M. Mulder, A. J. Van Duynveldt and J. A. Mydosh, *Phys. Rev. B: Condens. Matter Mater. Phys.*, 1982, **25**, 515–518.
- 60 G. Balaji, G. Wilde, J. Weissmüller, N. S. Gajbhiye and V. K. Sankaranarayanan, *Phys. Status Solidi B*, 2004, **241**, 1589–1592.
- 61 G. F. Goya, H. R. Rechenberg and V. Sagredo, *J. Magn. Magn. Mater.*, 2001, **226–230**, 1298–1299.
- 62 E. Vincent and V. Dupuis, *Springer Series in Materials Science*, 2018, vol. 275, pp. 31–56.
- 63 P. Bag, K. Somesh and R. Nath, *J. Magn. Magn. Mater.*, 2020, **497**, 165977.
- 64 J. Souletie and J. L. Tholence, *Phys. Rev. B: Condens. Matter Mater. Phys.*, 1985, **32**, 516–519.
- 65 P. Bag, P. R. Baral and R. Nath, *Phys. Rev. B*, 2018, **98**, 1–10.
- 66 R. Yadav and S. Elizabeth, *J. Appl. Phys.*, 2015, **117**, 53902.
- 67 M. Viswanathan and P. S. A. Kumar, *Phys. Rev. B: Condens. Matter Mater. Phys.*, 2009, **80**, 3–6.



Research article

Magnetic and thermoelectric properties of quasi-one-dimensional BaVSe₃Chinnu V. Devan^{a,c}, Manoj Raama Varma^{b,c,*}, Biswapriya Deb^{a,c,**}^a Centre for Sustainable Energy Technologies (C-SET), CSIR- National Institute for Interdisciplinary Science and Technology (NIIST), Thiruvananthapuram 695019, Kerala, India^b Materials Science and Technology Division, CSIR- National Institute for Interdisciplinary Science and Technology (NIIST), Thiruvananthapuram 695019, Kerala, India^c Academy of Scientific and Innovative Research (AcSIR), Ghaziabad 201002, India

ARTICLE INFO

Keywords:

BaVSe₃BaSe₃

Thermoelectric

Spintronics

Magnetotransport

ABSTRACT

Quasi-one-dimensional (Q1D) materials possess extraordinary magnetic and transport characteristics, which render them of critical importance. In this study, we present the synthesis of phase pure Q1D BaVSe₃ via a novel heat treatment process and analyze its low-temperature thermoelectric, magnetotransport, and magnetic properties. A comparison is made between this phase pure system and the BaVSe₃ infused with the secondary BaSe₃ phase that we previously reported to determine the potential effect of impurities on the magnetic and thermoelectric properties. Our previous study covered the experimental and theoretical investigation on the exotic magnetic properties of BaVSe₃ with BaSe₃. In phase pure BaVSe₃, at T_C ~ 41.2 K, a paramagnetic to ferromagnetic transition with a magnetic moment of 1.74 μ_B from V⁴⁺ was observed, consistent with calculated values. At very low temperatures (<117 K), the material behaved like glass, showed Griffiths-like behavior and spin valve-like butterfly magnetoresistance (BMR). Experiments indicate that these exotic magnetic properties are caused by the interaction between the A_{1g} and t_{2g} levels of the V 3d orbital and their spin orientation. Magnetic frustration in these materials is caused by V-V inter and intra chain interactions in the 1D spin chains of V. Q1D BaVSe₃ (BVS) demonstrated n-type thermoelectricity with a thermoelectric figure of merit of ~ 0.008, 4 × greater than BaVSe₃:BaSe₃ (BVS: BS) at room temperature. The thermal transport is determined to be primarily phonon-dependent. The magnetic property studies disclosed that this FM transition metal chalcogenide can contribute to low-temperature spintronics.

1. Introduction

Transition metal chalcogenides (TMCs) are at the forefront of research in energy applications, providing potential paths for technological growth. These compounds demonstrate distinctive electronic characteristics that render them crucial in the endeavour to develop energy-efficient storage devices, including supercapacitors [1], batteries [2], and thermoelectric generators [3]. Recently, TMCs were shown to have exceptional magnetic properties, involving harnessing electron spin for information storage and processing [4,5]. The interdisciplinary study of TMCs may hasten the development of creative solutions in sustainable energy and information technologies.

Thermoelectric applications at cryogenic temperatures are crucial [6] for converting waste heat into electrical power at temperatures falling below -150 °C [7–9]. This is particularly significant in

environments associated with space exploration, superconducting technologies, and certain industrial processes [10]. The primary obstacle is the identification of materials that possess elevated thermoelectric efficiency even at such low temperatures. Presently, research is underway to investigate exotic materials that may improve the efficiency of thermoelectric devices, Berri et al [11] proposed the first principles calculations on thermoelectric materials. The objective of low-temperature spintronics is to manipulate and utilize electron spins to store and process information. Magnetic materials [12,13] demonstrate improved spin coherence and minimal thermal noise at extremely low temperatures, thereby enabling precise manipulation of electron spin [14]. Spin-based technologies such as spin valves, magnetic tunnel junctions, and spin transistors operate more reliably at low temperatures [15]. Some novel materials, such as certain semiconductors and topological insulators were introduced to push the boundaries of low-

* Corresponding author at: Materials Science and Technology Division, CSIR- National Institute for Interdisciplinary Science and Technology (NIIST), Thiruvananthapuram 695019, Kerala, India.

** Corresponding author at: Academy of Scientific and Innovative Research (AcSIR), Ghaziabad 201002, India.

E-mail addresses: manoj@niist.res.in (M. Raama Varma), biswapriya.deb@niist.res.in (B. Deb).

<https://doi.org/10.1016/j.jmmm.2024.172110>

Received 23 January 2024; Received in revised form 10 April 2024; Accepted 30 April 2024

Available online 1 May 2024

0304-8853/© 2024 Elsevier B.V. All rights reserved.

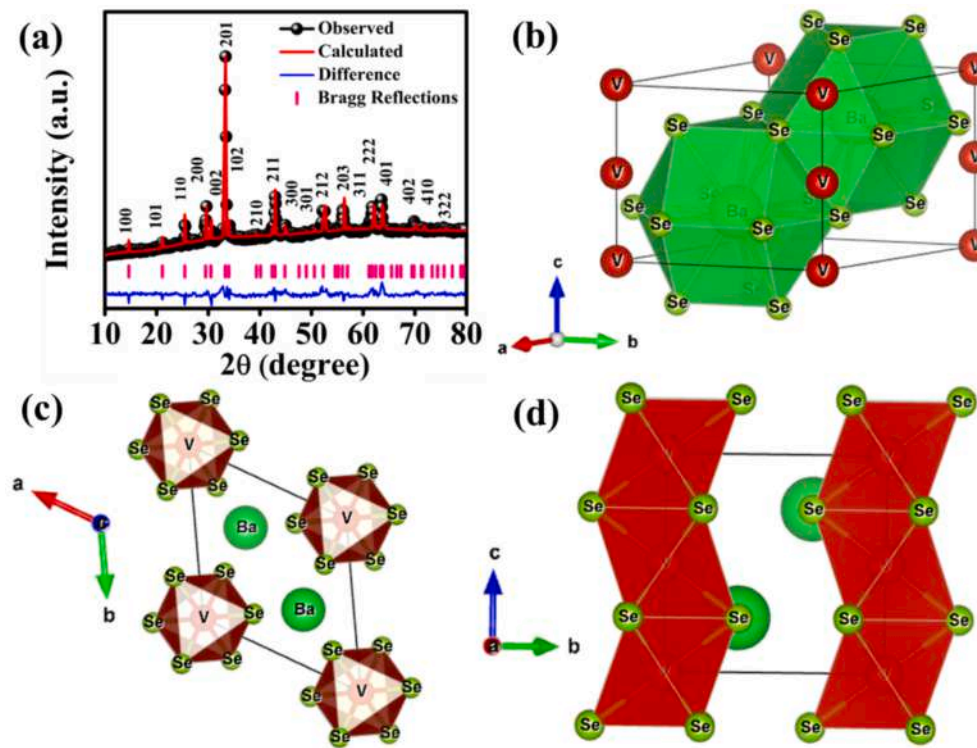


Fig. 1. (a) Rietveld refined XRD pattern of the sample, (b) – (d) Crystal structure of $BaVSe_3$ with different orientations.

temperature spintronics [16] and energy harvesting [17].

A survey of the TMCs reveals that their anisotropic physical properties emerge from their anisotropic structural arrangements of the layers or chains of atoms with weak interlayer bonding [18]. The Q1D materials are low dimensional solids comprised of linear chains of metal (M) atoms extended along one of the crystal axis and the unidimensionality arises from the comparison between the M–M inter-chain and intra-chain bond length [18]. Researchers reported spin glass behaviour [19,20], long-range antiferromagnetism (AFM) [21,22], linear ferromagnetism (FM), Griffiths-like nature [23] and superconductivity [24] for transition metal chalcogenides. Kelber et. al synthesized $BaVSe_3$ that crystallizes in a hexagonal phase with space group $p63/mmc$ with a ferromagnetic ordering below 41 K [25]. Yamasaki et al investigated the magnetic and thermoelectric properties of $BaVSe_3$ [26]. It exhibited a phase transition from hexagonal to orthorhombic symmetry at ~ 310 K, and resulted in a zigzag distortion in the V chains [27]. The crystal distortions at low temperatures could generate unusual physical properties in this class of compounds [28]. It is well established that achieving an adequate thermoelectric output is difficult because it requires the optimization of interdependent parameters, however, extensive research is now being conducted on the thermoelectric characteristics of many materials [29]. Consequently, ongoing research initiatives are dedicated to the development of novel ferromagnetic systems and their unusual magnetic characteristics [30]. The current study presents the synthesis of phase pure BVS and analyzes its thermoelectric, magnetotransport, and low-temperature magnetic properties. A comparative analysis was conducted between our prior investigations involving the formation of BVS: BS [28].

2. Experimental section

2.1. Synthesis of BVS

High-purity precursor elements Ba (99.99 %, rods), V (99.7 %, plates), and Se (99.999 %, shots) (Alfa Aesar) were taken in the stoichiometric ratio under a nitrogen environment in the Glove box with

more than 2 ppm oxygen and moisture level in quartz tubes. Following this, the sample tubes were deposited in a furnace after being sealed under a high vacuum (10^{-4} Torr). With a 24-hour ramp-up, the furnace temperature was maintained at 973 K for the next twenty-four hours. The temperature was raised to 1073 K in a 24-hour ramp immediately following the initial phase, annealed for three days, and then cooled to room temperature. For phase analysis, the molten samples were reduced to powder, subsequently pressed into rectangular pellets, and sintered at 973 K for 6 h to facilitate diverse transport investigations. Using the Archimedes method, the pellets' specific gravity was determined to be 95 %.

2.2. Characterization

The Powder X-ray diffraction techniques (Empyrean 3, PANalytical X-ray diffractometer) were employed to analyze the phase identification of the synthesized BVS. The diffraction utilized $Cu-K\alpha$ radiation with a wavelength of 1.5406 \AA within the 2θ range of 10° – 90° , with a step size of 0.005° . The GSAS-EXPGUI software was used to perform Rietveld refinements on the XRD pattern. By employing scanning electron microscopy (SEM-EDS, Zeiss EVO 18 cryo-SEM, operating voltage of 15 kV), the composition and surface morphology were examined. High-resolution transmission electron microscopy (HRTEM, FEI Tecnai F20, operated at 300 kV) was utilized to validate the crystallinity and phase. Thermal transport and magnetic transport experiments were carried out utilizing the physical property measuring system's (PPMS Dynacool, Quantum Design, USA) thermal transport option (TTO) and electrical transport option (ETO), respectively.

3. Results and discussion

3.1. Crystal structure and surface studies

The phase and purity of the synthesized samples were analyzed by X-ray diffraction (XRD) measurements, Fig. 1 (a) shows the Rietveld refined XRD data of the obtained material with a goodness of fit (χ^2) 2.2.

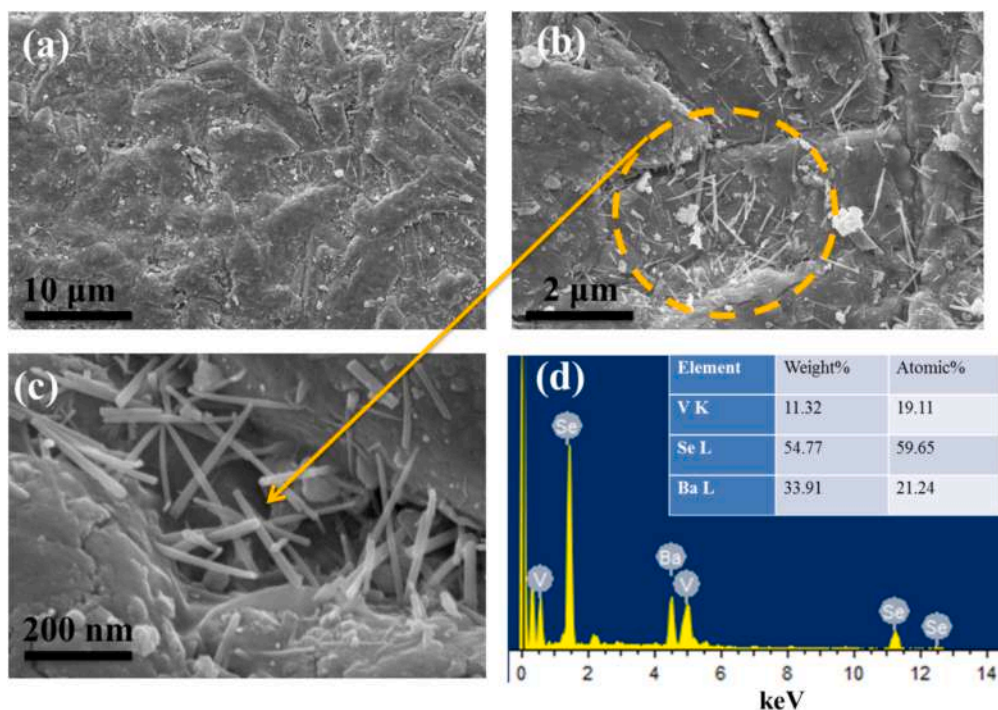


Fig. 2. Scanning electron microscopy images of the pellet sample (a) on a 10 μm scale, (b) associated needle-shaped crystals on the surface of the sample (2 μm scale), (c) needle-shaped crystals with nanometer diameter on a 200 nm scale, (d) EDS spectrum of the sample.

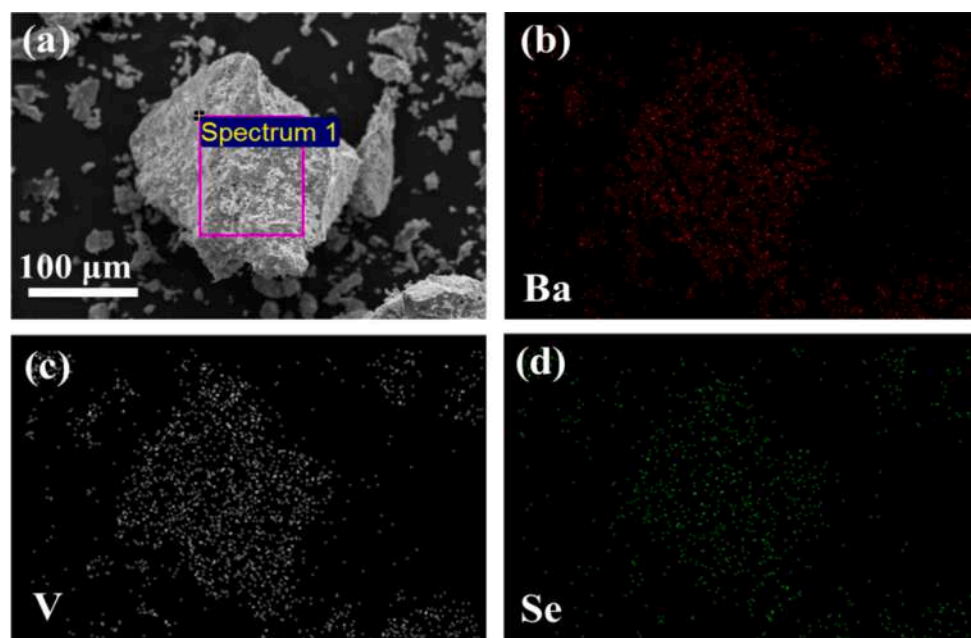


Fig. 3. (a)-(d), Elemental mapping of the sample at a micrometre scale, constituent elements Ba, V, Se were mapped.

All diffraction peaks can be indexed into hexagonal crystal structure [JCPDS no: 00-033-0186] with space group (p63/mmc having lattice parameters $a = b = 7.00067 \text{ \AA}$, and $c = 5.86133 \text{ \AA}$; $\alpha, \beta = 90^\circ$, and $\gamma = 120^\circ$). The data indicated that the implementation of a novel thermal treatment procedure aided the production of pure phase BaVSe_3 , in contrast to the previously documented method [31], which resulted in the formation of BaVSe_3 with BaSe_3 impurities. The crystal structure of hexagonal BaVSe_3 is depicted in Fig. 1b. In this structure, the Ba atoms are surrounded by 12 Se atoms, while the V atoms form face-shared VSe_6 octahedra, as illustrated in Fig. 1c. The material's one-dimensional

nature arises from the presence of elongated chains of V atoms aligned along the crystallographic c-axis (as shown in Fig. 1d). Each V atom is surrounded by face-sharing Se octahedra [2532]. Typically, in BaVSe_3 , the intra-chain V-V distance is 2.9310 \AA and the inter-chain V-V distance is 6.999 \AA [33], which ensures the structural unidimensionality and weak van der Waal interactions [32,34]. The SEM analysis revealed a highly compact and dense microstructure of the synthesized sample, as depicted in Fig. 2(a)-(b). Fig. 2(c) displays the presence of needle-shaped crystals between 100–200 nm in diameter. Kelber et al. [25] were the first to report the synthesis and growth of needle-shaped crystals in

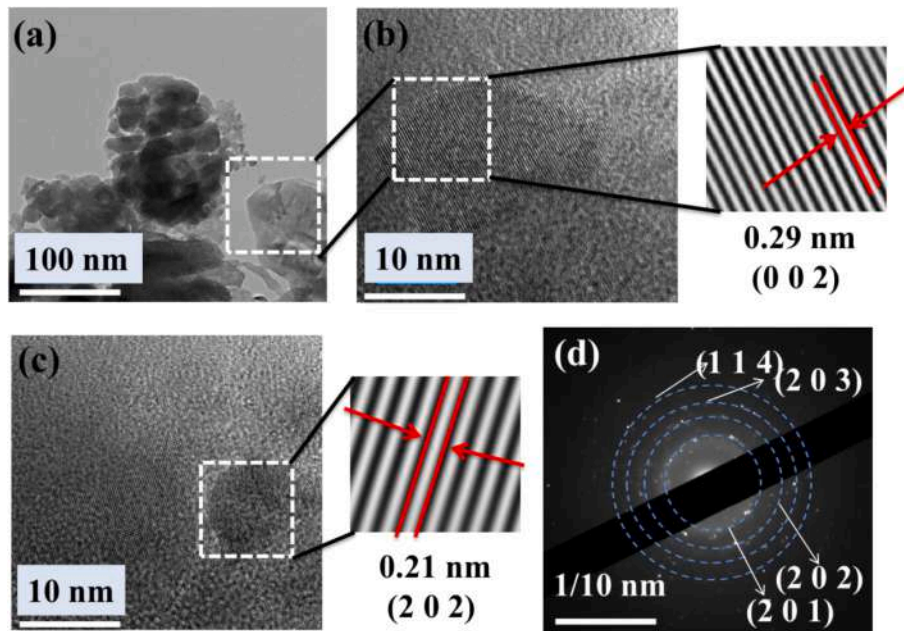


Fig. 4. (a)TEM image of the synthesized material, (b) & (c) the HRTEM images with crystal planes and the corresponding d spacing were marked, (d) SAED pattern of the material.

BaVSe₃. This growth is attributed to the structure of the Q1D material. Fig. 2d displays the EDS spectrum, indicating the weight and atomic fraction of each element in the developed material that is redisplayed in the figure inset. The local composition of the material aligns well with the expected stoichiometry. Fig. 3a displays the mapping of the constituent elements Ba, V, and Se. The distribution of all elements appeared homogeneous. The microstructure and homogeneity of the previously reported BVS: BS is presented in Fig. S1, revealing a similar

compact topography of the pellets and the presence of needle-shaped crystals.

The transmission electron microscope was used to further examine the nano/microstructure of the melted sample. Fig. 4a illustrates the coexistence of nanostructures and microstructures. The material's polycrystalline nature was verified using HRTEM analysis (Fig. 4(b)–(d)), and the identification of the planes was achieved by comparing them with the d spacing obtained from the XRD data. The d-spacing of

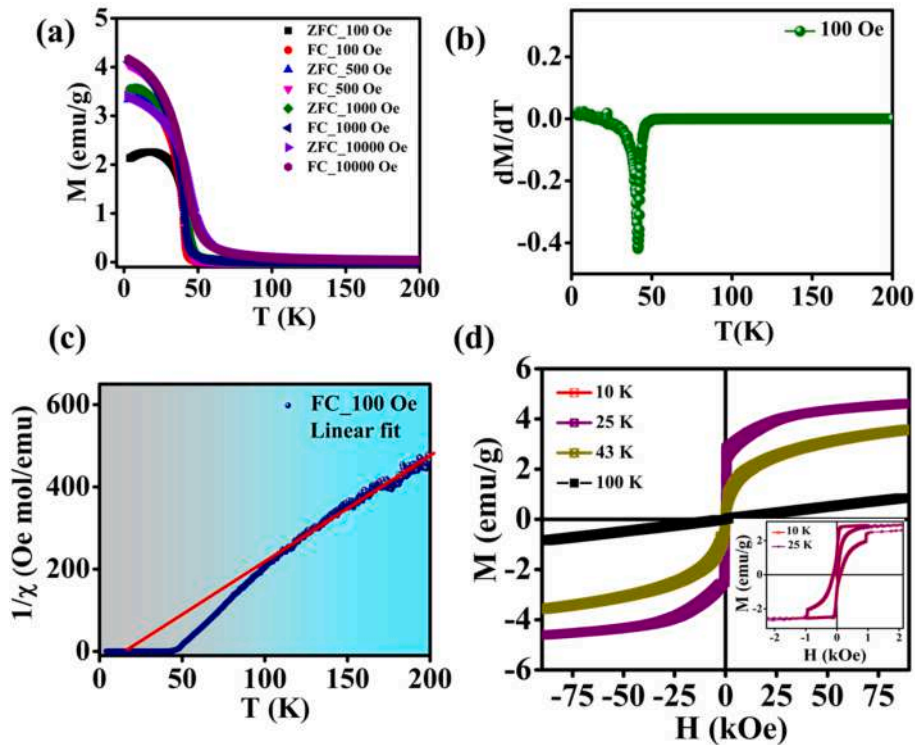


Fig. 5. (a) Temperature-dependent ZFC and FC magnetization of BaVSe₃ at different fields, (b) dM/dT versus T plot at an applied field of 100 Oe, (c) Linear fit on the Curie-Weiss plot at 100 Oe, (d) M versus H at different temperatures (inset depicts the enlarged loop at 10 K and 25 K).

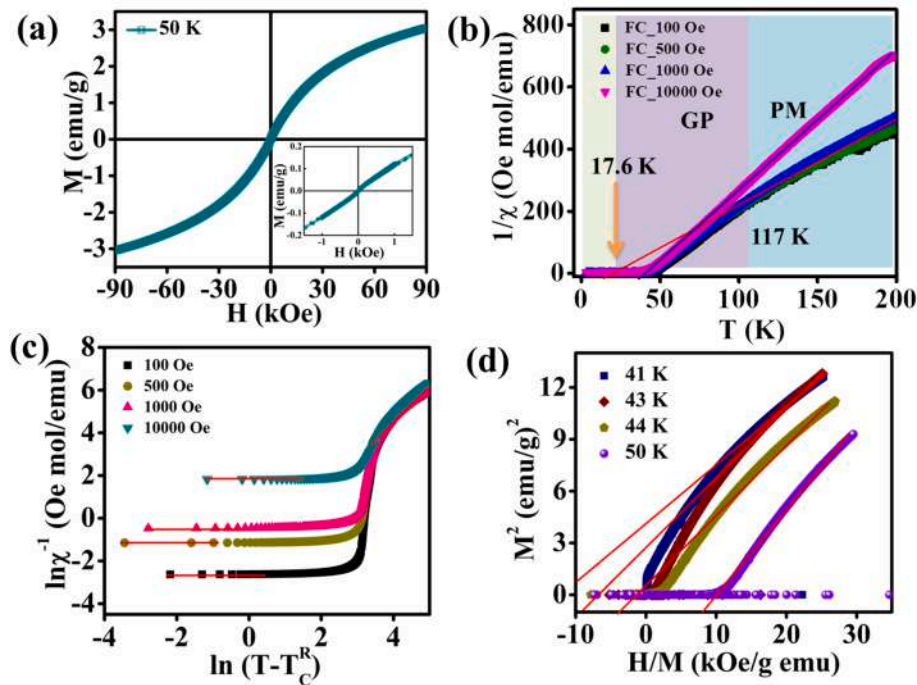


Fig. 6. (a) Hysteresis loop at 50 K (inset of the figure shows the minute loop) (b) GP analysis by the linear fit on the CW plot at different fields (c) $\ln(1/\chi)$ versus $\ln(T - T_C^R)$ at different fields (d) Arrott plot (M^2 versus H/M) at 41 K, 43 K, 44 K and 50 K.

the planes in the sample was calculated with the help of GATAN microscopy suite software and the d-spacing of 0.29 nm and 0.21 nm was corresponding to the planes (002) and (202) respectively. The ring diffraction pattern in the selected area diffraction (SAED) was indexed to the corresponding crystal planes of hexagonal BVS. From SAED, it was observed that the present material has some randomly distributed single-crystalline zones along with the utmost polycrystalline nature.

3.2. Magnetic properties

Our previous investigation explored the experimental and theoretical magnetic characterizations of BaVSe_3 with impurity phase. The material exhibited FM to PM transition at 40.8 K, Griffith's like phase and cluster glass nature at extremely low temperature. The previous studies on this material did not find any signature of these exotic magnetic properties and our study on magnetic properties on this Q-1D BaVSe_3 highlights the unusual presence of these magnetic properties. The temperature-dependent magnetization measurements were conducted on the material in the absence of an external magnetic field (zero field cooled, ZFC) and in the presence of a field (field cooled, FC) at various field strengths (100 Oe, 500 Oe, 1000 Oe & 10,000 Oe). It was observed that the material undergoes a transition from paramagnetic (PM) to ferromagnetic (FM) behaviour at a critical temperature (T_C), as depicted in Fig. 5a. The temperature T_C may be determined by analyzing the dM/dT vs T curve (Fig. 5b). For the synthesized BVS, T_C is measured to be 41.2 K, which is consistent with previous reports [25,35,36]. The magnetization of the bifurcated ZFC-FC curve exhibits a rising tendency. At extremely low temperatures, a distinct cusp is detected in the ZFC curve, which serves as an indication of the glassy behaviour of magnetic materials [36], a clear observation of bifurcation of ZFC-FC at 100 Oe is depicted in Fig. S2. According to Zheng et al., the observable difference between the zero field cooling (ZFC) and field cooling (FC) curves is caused by the spin glass or cluster glass properties resulting from magnetic anisotropy or magnetic frustrations [37].

To gain a deeper comprehension of the magnetic properties of the recently produced BVS, we have examined the Curie Weiss plot, which represents the reciprocal of magnetic susceptibility ($1/\chi$) as a function of

temperature (T) [38]. The linear regression analysis (shown in Fig. 5c) conducted on the PM region of the plot allows for the determination of the Curie-Weiss temperature ($\theta = -y_{\text{int}}/\text{slope}$) and the effective magnetic moment ($\mu_{\text{eff}} = 2.82\sqrt{1/\text{slope}}$) [39]. The theoretical effective moment can be determined using the formula $\mu_{\text{eff}} = g\sqrt{S(S+1)}$, where $g = 2$ represents the Lande factor. The calculated value of μ_{eff} is $1.73 \mu_B$. The experimentally obtained values for θ and μ_{eff} were 17.6 K and $1.74 \mu_B$, respectively. The effective magnetic moment values closely correspond to the predicted value, and the positive indication of the Curie-Weiss temperature indicates the presence of ferromagnetic ordering in the material at low temperatures. The M vs H graph (Fig. 5d), obtained by varying the applied magnetic field from -9 T to 9 T, at various temperatures both below and above T_C , provides more evidence supporting the transition from PM to FM behaviour.

It was noted that this material exhibits a hysteresis loop even above the critical temperature T_C , as seen in Fig. 6a and the inset shows an enlarged view of the loop with extremely low coercivity. Additionally, the magnetization curve only becomes fully linear at high temperatures. The recent findings indicate that the presence of magnetic inhomogeneity in the PM region of specific systems might be referred to as the Griffiths phase (GP). Ghosh et al. state that GP can occur due to the existence of finite-sized FM clusters in the PM matrix above T_C , as well as phase separation and conflicting magnetic interactions within and between layers in the material [40]. The GP was defined within the temperature range $T_C < T < T_G$, with T_G representing the upper boundary of this phase and referred to as the Griffiths temperature. BVS is classified as a quasi-one-dimensional van der Waals material [41], and the presence of magnetic interaction between the layers can cause this compound to exhibit inhomogeneity. The deviation observed in the $1/\chi$ vs T plot at low fields, as indicated by the Curie-Weiss fit [42] provides additional evidence supporting the existence of the GP phase. The decrease in $1/\chi$, as indicated by the deviation from a linear fit on the Curie-Weiss law (Fig. 6b), suggests that the transition temperature (T_G) for this material is approximately 117 K. Furthermore, this material exhibits a GP phase within the temperature range of $17.6 \text{ K} < T < 117 \text{ K}$, which is distinct from both the PM and FM phases. We have previously documented that the material BVS, even with the presence of a

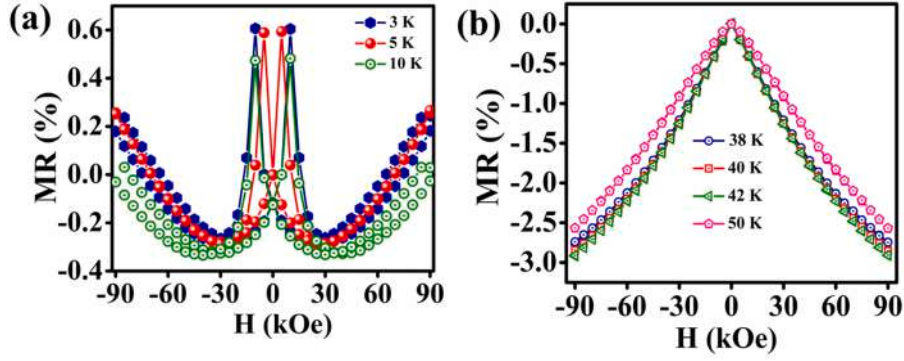


Fig. 7. MR versus H at (a) 3 K, 5 K and 10 K, (b) 38 K, 40 K, 42 K and 50 K.

secondary phase, also demonstrates the GP phase within a similar temperature range. This finding provides more evidence that the GP phase is an inherent characteristic of BVS. It became apparent that when the field was increased to 10,000 Oe, the decrease in $1/\chi$ could be attributed to the masking of FM clusters by the PM matrix or the saturation of the FM clusters at higher fields [43]. The power law at low temperatures is employed to analyze the Griffiths singularity, which is denoted as [38]

$$\ln\left(\frac{1}{\chi}\right) = \ln(T - T_C^R)^{1-\lambda}$$

The susceptibility exponent λ ($0 < \lambda < 1$) represents the strength GP. A value close to 1 indicates the presence of GP, whereas a value close to 0 corresponds to PM phase. T_C^R is the critical temperature of random FM clusters, at which the susceptibility tends to diverge and approximated to 0 [43]. Fig. 6c shows the plot of $\ln(T - T_C^R)$ versus $\ln\left(\frac{1}{\chi}\right)$ at different magnetic fields (100 Oe, 500 Oe, 1000 Oe, 10,000 Oe). The gradient of the linearly fitted curve in the GP region yields a λ value of 0.99, while the linear fit in the PM region yields a λ value of 0.01. This confirms the GP behaviour of the synthesized material. Materials with GP do not exhibit any long-range magnetic ordering above T_C and do not display spontaneous magnetization. This could be investigated by measuring $M(H)$ at different temperatures above and below T_C . The spontaneous magnetization (M_s) can then be determined by performing a linear regression on the Arrott plot (M^2 vs H/M) [44]. The value of M_s is determined by the intercept on the M^2 axis obtained through extrapolation of data from the strong magnetic field, which is illustrated in Fig. 6d. The Arrott plot has a positive y-intercept at a temperature (41 K) below T_C and a negative intercept on the M^2 axis at temperatures above T_C . This observation validates the absence of long-range order and the zero M_s [45]. The magnetic properties of these 1D spin chain materials are determined by the disparity in the strength of inter-chain exchange interaction and intra-chain coupling. The former is two to three orders of magnitude more than the latter [46]. The unique magnetic properties seen in ABX_3 compounds can be attributed to the complex spin arrangements resulting from frustrated antiferromagnetic interactions and geometric magnetic frustration arising from the ordering of spin chains in the triangular lattice [47].

The magnetic and electrical characteristics of BVS mostly depend on the transition metal V. In octahedral coordination, the V 3d level splits into e_g and t_{2g} multiplets [28]. The t_{2g} energy levels are further split into a lower doublet (d_{xy} , d_{yz}^2) and a higher singlet (d_z^2) as a result of the elongation of the VSe_6 octahedra along the crystallographic c axis. Within the V chains, the direct overlap of the closest d_z^2 orbitals results in the formation of a broad conduction band. The adjacent lower doublets indirectly overlap in the same direction, facilitated by the hybridization with intervening Se 3p orbitals. The doublets can divide at lower temperatures because of the orthorhombic distortion, which is referred to as

the cooperative Jahn-Teller distortion [48]. The material exhibits structural disorder at low temperatures, which arises from the Jahn-Teller distortion. This disorder is responsible for the emergence of the GP phase and other unique magnetic properties [49]. The present repeated study on the synthesis and magnetic characterization of $BaVSe_3$ reveals that the exhibited GP phase and glassy nature are its intrinsic magnetic characteristics; it strengthens our previous results on this particular material.

3.3. Magnetotransport studies

The magnetotransport studies of BVS were conducted using an applied magnetic field of ± 9 T across a temperature range of 3 K to 300 K. The magnetoresistance of a material is quantified by the equation $MR = [R(H) - R(0)]/R(0)$, where $R(H)$ and $R(0)$ represent the resistance of the material in the presence and absence of a magnetic field, respectively [50].

Fig. 7a and 7b depict the longitudinal MR of the synthesized $BaVSe_3$ at various temperatures. $BaVSe_3$ exhibits distinct magnetic behaviour when the temperature is increased. At extremely low temperatures, the material demonstrates a remarkable butterfly-shaped magnetoresistance (BMR), it is commonly encountered in compounds exhibiting a hysteresis loop. In this case, the MR exhibits two equal upward resistance states, resulting in the formation of two crossing peaks at a magnetic field strength of 1 Tesla. Prior research indicates that the majority of FM materials exhibit a BMR on a scale of 0.1 % [51]. In contrast, the current material demonstrates a BMR on the scale of 0.6 % at 3 K, which subsequently decreases with increasing temperature. The BMR is typically observed in materials having strong crystalline or magnetic anisotropy at low temperatures. However, the specific cause of BMR can differ between different materials, BMR is widely observed in longitudinal resistance measurements and can be explained by Ohm's law. The longitudinal and transverse MR in a magnetic material is determined by the magnetization in the x (M_x) and y (M_y) directions. The current is applied along the x-axis and transverse voltage is measured along the y direction. The equation for the MR in amorphous or polycrystalline magnetic material could be expressed as,

$$R_{xx} = R_1 + A_1 M_x^2 \text{ (longitudinal)} \quad (1)$$

and

$$R_{xy} = R_1 M_z + A_1 M_x M_y \text{ (transverse)} \quad (2)$$

where R_1 and A_1 are material parameters linked with the anomalous Hall effect and anisotropic MR respectively [52]. In longitudinal MR the quadratic term $M_x^2(H)$ (Eq. (1)) leads to two equal states of MR, the switching between $-M_{x0}$ and M_{x0} creates peaks and valleys, that result in BMR. It is worth noting that there have been no previous reports on the BMR in this van der Waals material BVS. Several studies have

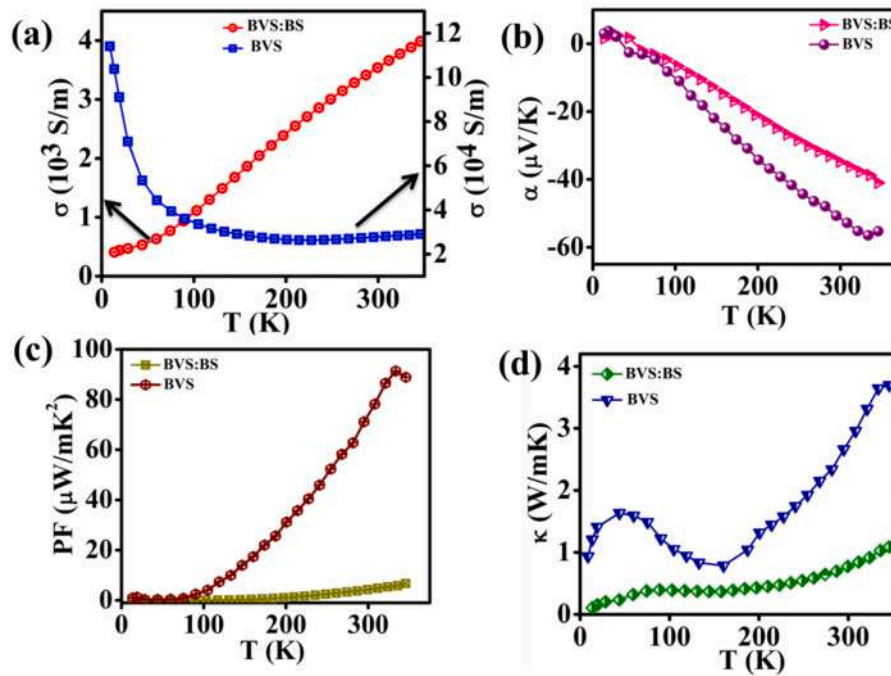


Fig. 8. Temperature-dependent (a) electrical conductivity, (b) Seebeck coefficient, (c) Power factor and (d) thermal conductivity of both BVS and BVS: BS.

examined the behaviour of the BMR in van der Waals materials. Ohta et al. revealed that the observed BMR in the van der Waals Fe_5GeTe_2 FM material is caused by the interaction between magnons and electrons, specifically due to magnetic fluctuations at the Fe(1) site at temperatures around 100 K [51]. The atypical MR observed in van der Waals CrI_3 layers is triggered by the presence of strong or weak electron scattering, leading to fluctuations in magnetization between neighbouring layers [53]. The presence of the BMR in the triangular lattice of AFM Ag_2CrO_2 is observable exclusively when a magnetic field is applied parallel to the c-axis that arises from the pronounced uniaxial anisotropy [54]. Herak et al. conducted the initial investigation of the magnetic anisotropy in BVS and its corresponding uniaxial symmetry in the FM state [36]. The longitudinal MR studies revealed that as the temperature increases, BVS undergoes a transformation from a spin valve-like BMR to a negative MR at 11 K. The MR investigations conducted on individual crystals of BVS demonstrate a shift in the MR behaviour throughout the temperature range of 8 K to 15 K [55]. This change to negative MR is illustrated in Fig. S3 and Fig. 7b. At low temperatures, FM metals exhibit a negative MR due to electron-spin scattering. The applied magnetic field strengthens the effective field acting on the localized spins, which suppresses spin fluctuations and consequently reduces the material's resistivity [55,56]. At normal temperatures, the magnetism weakens and shows a positive MR due to the dominance of orbital effects [57]. The Fig. S4 shows the MR in transverse mode and it confirms the absence of BMR in the material for transverse measurement. The significant BMR seen in these layered chalcogenides is a result of the inherent magnetic interaction between the E_g and A_{1g} electrons, as well as the crystallographic characteristics. The layered structure also enables the spin valve like mechanism in this compound, the V-Se chains are separated by the Ba atoms and this arrangement replicates the intrinsic spin valve like structure. The switching of magnetization between these layers contributes to BMR [58]. The strong in-plane anisotropy in quasi one dimensional chalcogenides has strong influence on various properties that includes electrical, magnetic and optical [59]. The strong in-plane anisotropy due to the VSe_6 along c-axis also contributes to this MR. The strong magnetic anisotropy in BaVSe_3 can be confirmed from the bifurcation in ZFC-FC curve [60]. The origin of BMR in materials like layered chalcogenides

and Q1D materials is an area of active research. The spin valve like MR [61] has potential applications in magnetic memory devices.

3.4. Thermoelectric studies

The efficiency of a thermoelectric material is determined in terms of the dimensionless figure of merit (ZT), $ZT = S^2\sigma T / (k_e + k_p)$, where α is the Seebeck coefficient, σ is the electrical conductivity, T is the absolute temperature, k_e is the electronic thermal conductivity and k_l is the lattice thermal conductivity of the material [3]. We investigated the thermoelectric properties of two samples: phase pure BVS and a previously reported BVS: BS (impurity phase) [31]. The purpose of our investigation was to gain a better understanding of the influence of impurities on thermoelectric capabilities. The temperature-dependent electrical conductivity of the material was measured between 8 K to 350 K temperature ranges as shown in Fig. 8a. The two materials exhibited entirely different electrical responses to the temperature variations. The electrical conductivity of BVS demonstrates the characteristics of a degenerate semiconductor while the material BVS: BS has normal semiconductor properties. The resistivity curve of the phase pure material closely resembles that of the BaVSe_3 single crystals described by Akarp et al. [55] and its order of magnitude was one-order less. We noted that the presence of impurity yielded 10-fold lower electrical conductivity in BVS: BS compared to BVS. Grieger et al [62] reports that the electronic structure of BaVSe_3 is contributed by V^{4+} valence, considered as a $3d^1$ compound. It contains A_{1g} -like orbital pointing along the V chain direction as well as two E_g -like orbitals pointing in between the neighboring Se ions and three band model is introduced for the explanation of the electronic properties of this material [62].

The scattering of electrons at the interfaces and defects disrupt the pathway for electron conduction [63], which consequently leads to a decrease in electrical conductivity in BVS: BS [64]. Both materials have a negative Seebeck coefficient, indicating n-type conduction that increases with temperature (Fig. 8b). The near room temperature Seebeck coefficient of BVS and BVS: BS was measured as -35 and $-14 \mu\text{W}/\text{mK}^2$ respectively. A similar trend in α is observed for both materials resembling the single crystal behaviour. The low-temperature peak at 20 K can be attributed to the combined effects of phonon drag and magnon

Table 1

Experimentally obtained room temperature values of n , μ and m^* of the materials.

	n (/cm ³)	μ (cm ² /V.s)	m^* (m_0)
BVS	10 ¹⁸	470	0.001
BVS: BS	10 ¹⁷	55.3	0.0001

contribution [65]. The decrease of the Seebeck coefficient in semi-conducting materials can be associated with the generation of minority carriers at higher temperatures [66]. In BVS the electrical conductivity and Seebeck coefficient follow the general inverse trend and where as in BVS: BS, the presence of a secondary phase disturbs this trend. Table 1 shows the calculated values of carrier concentration mobility and effective mass of the samples at room temperature, the effective mass is calculated by using the Mott equation.

The Seebeck coefficient and the carrier concentration of metals and degenerate semiconductors could be linked by the Mott equation [67],

$$\alpha = \frac{8\pi^2 k_B^2 T}{3eh^2} m^* \left(\frac{\pi}{3n}\right)^{2/3} \quad (3)$$

where n is the carrier concentration, k_B is the Boltzmann constant, e is the electronic charge, h is the Planck constant and m^* is the density of state effective mass. An increase in the energy dependence of either $\mu(E)$ or $n(E)$ can improve the Seebeck coefficient of a material. A higher value of $\mu(E)$ corresponds to a distinct electron scattering mechanism, while a higher value of $n(E)$ can be achieved by manipulating the density of states [68]. The Mott equation reveals that the effective mass of BVS at room temperature is larger than that of BVS: BS. This difference in effective mass is responsible for the increase in thermopower.

The power factor (PF = $S^2\sigma$) of the materials was determined from the measured σ and S values and plotted against temperature in Fig. 8c.

A peak PF of 92 $\mu\text{W}/\text{mK}^2$ at 335 K was obtained for BVS, surpassing the equivalent BVS: BS values by a significant margin (5.81 $\mu\text{W}/\text{mK}^2$). Fig. 8d displays the total thermal conductivity vs temperature graph. The materials exhibit distinct thermal conductivity characteristics at extremely low temperatures. The total thermal conductivity is expressed as,

$$k = k_e + k_p \quad (4)$$

where the lattice thermal conductivity is denoted by k_p , while k_e is the electronic contribution. The electronic thermal conductivity can be determined by employing the Wiedemann-Franz law ($k_e = L\sigma T$, where L is the Lorenz number). In a degenerate semiconductor, the relationship between L and the Seebeck coefficient is given by the equation $L = 1.5 + (|\alpha|/116)$ [69], where L is in $10^{-8} \text{ W}\Omega/\text{K}^2$ and S is in $\mu\text{V}/\text{K}$. The temperature-dependent variations in L are shown in Fig. 9a for both materials. The Lorenz number [70] decreases as the temperature increases, and the BVS: BS material exhibits a greater L value. The thermal current in thermoelectric materials can be reduced by the phonon-mediated process, electron–electron scattering, and inelastic electron–phonon scattering [71]. Fig. 9b depicts the computed electronic thermal conductivity, with the dominant contribution to thermal conductivity originating from the phonons (Fig. 9c). At extremely low temperatures (<80 K), BVS exhibited a T^3 dependence on thermal conductivity, which subsequently increases with temperature as a result of phonon generation. The T^3 dependence on k originates from the heat capacity of the phonons [72] and the dominant boundary scattering [73]. In general, the reduction in thermal conductivity of a material is associated with the impurities or imperfections in the crystal structure [74].

The presence of lattice defects and secondary phase in BVS: BS significantly reduces the overall thermal conductivity compared to BVS due to phonon scattering. The presence of a chain-like structure in the

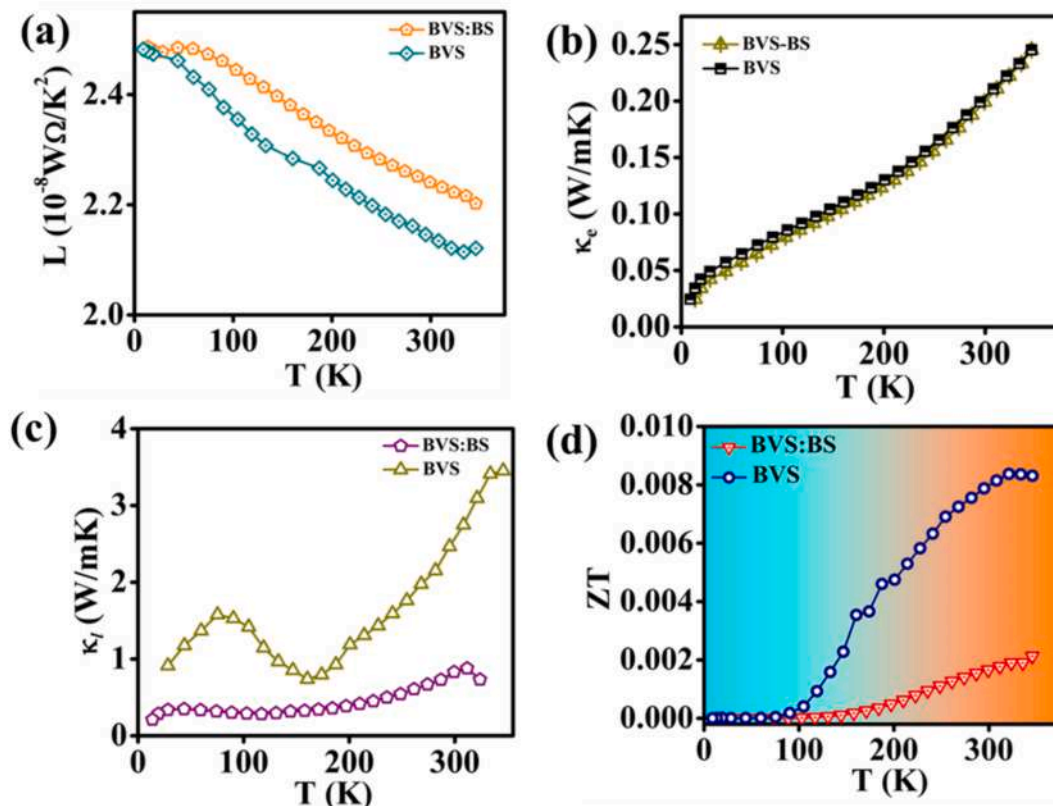


Fig. 9. (a) Temperature dependence of Lorenz number, (b) electronic thermal conductivity, (c) lattice thermal conductivity and (d) thermoelectric figure of merit of the samples.

layered TMCs increases the thermal conductivity [75] whereas the existence of an impurity phase may affect the Q1D characteristics of BVS. The thermoelectric figure of merit of the materials was determined based on the measured values of σ , k , and S . Fig. 9d illustrates the changes in the thermoelectric figure of merit (ZT) that increased with temperature for both materials. The phase pure BVS exhibits ZT values about four times higher than that of BVS: BS.

4. Conclusion

A novel solid-state method was used to synthesize quasi-one-dimensional and phase-pure BVS. The synthesized material displayed a hexagonal crystal structure with the $p6_3/mmc$ space group. The unidimensionality resulted from the V chains being arranged in a long chain formation along the crystallographic c -axis. The magnetic and thermoelectric properties of pure BVS and the previously described BVS: BS compound were studied to reveal the basic mechanism of a couples thermal and electrical transport. Based on the thorough examination of the magnetic data, it has been shown that this material undergoes a transition from a ferromagnetic to a paramagnetic state at a temperature of ~ 41 K. The observed PM magnetic moment of $1.74 \mu_B$ closely matches the calculated value of $1.73 \mu_B$. BVS exhibits unique magnetic characteristics such as a glassy behaviour, a Griffiths-like phase, and butterfly magnetoresistance at low temperatures, similar to BVS: BS, demonstrating that BVS possesses inherent magnetic properties that arise from its quasi-one-dimensional form and the robust interaction between the electrons in the E_g and A_{1g} energy levels. The thermoelectric investigations validated that electrons were the predominant charge carriers in both materials. However, the higher thermopower in the pure-phase BVS can be attributed to the higher effective mass of the carriers. Additionally, thermal transport is mostly governed by phonons. BVS demonstrated a maximum ZT value of 0.008, which is fourfold greater than that of BVS.

CRedit authorship contribution statement

Chinnu V. Devan: Writing – original draft, Investigation, Formal analysis. **Manoj Raama Varma:** Writing – original draft, Formal analysis, Conceptualization. **Biswapriya Deb:** Writing – review & editing, Supervision, Resources, Project administration.

Declaration of competing interest

The authors declare that they have no known competing financial interests or personal relationships that could have appeared to influence the work reported in this paper.

Data availability

Data will be made available on request.

Acknowledgement

C.V.D. acknowledges the support of the University Grants Commission (UGC), India, for granting a research fellowship. The authors acknowledge the measurement facilities obtained from different labs of CSIR-NIIST. The authors M.R.V. and B.D. are thankful to the Science and Engineering Research Board, Department of Science and Technology, New Delhi, India for funding this research through Project EMR/2017/004539 (Ver-1) dated 06/05/2019. MRV also thanks CSIR HRD Group for the CSIR Emeritus Scientist Project.

Appendix A. Supplementary data

Supplementary data to this article can be found online at <https://doi.org/10.1016/j.jmmm.2024.172110>.

References

- [1] S. Palchoudhury, K. Ramasamy, J. Han, P. Chen, A. Gupta, Transition metal chalcogenides for next-generation energy storage, *Nanoscale Adv.* 5 (2023) 2724–2742, <https://doi.org/10.1039/d2na00944g>.
- [2] H. Alnaqbi, O. El-Kadri, M.A. Abdelkareem, S. Al-Asheh, Recent Progress in Metal-Organic Framework-Derived Chalcogenides (MX; X = S, Se) as Electrode Materials for Supercapacitors and Catalysts in Fuel Cells, *Energies*. 15 (2022), <https://doi.org/10.3390/en15218229>.
- [3] H. Wang, H. Hu, N. Man, C. Xiong, Y. Xiao, X. Tan, G. Liu, J. Jiang, Band flattening and phonon-defect scattering in cubic SnSe–AgSbTe2 alloy for thermoelectric enhancement, *Mater. Today Phys.* 16 (2021) 100298, <https://doi.org/10.1016/j.mtphys.2020.100298>.
- [4] N. Zibouche, A. Kuc, J. Musfeldt, T. Heine, Transition-metal dichalcogenides for spintronic applications, *Ann. Phys.* 526 (2014) 395–401, <https://doi.org/10.1002/andp.201400137>.
- [5] B.K.U. Chida, Transport phenomena in spin caloritronics, *Proc. Jpn. Acad., Ser. B*. 97 (2021) 69–88, <https://doi.org/10.2183%2Fpjab.97.004>.
- [6] Y. Liu, J.R. Riba, M. Moreno-Eguilaz, J. Sanllehi, Application of Thermoelectric Generators for Low-Temperature-Gradient Energy Harvesting, *Appl. Sci.* 13 (2023), <https://doi.org/10.3390/app13042603>.
- [7] T. Wang, T. Huo, H. Wang, C. Wang, Quaternary chalcogenides: Promising thermoelectric material and recent progress, *Sci. China Mater.* 63 (2020) 8–15, <https://doi.org/10.1007/s40843-019-9467-2>.
- [8] M. Ibáñez, D. Cadavid, R. Zamani, N. García-Castelló, V. Izquierdo-Roca, W. Li, A. Fairbrother, J.D. Prades, A. Shavel, J. Arbiol, A. Pérez-Rodríguez, J.R. Morante, A. Cabot, Composition control and thermoelectric properties of quaternary chalcogenide nanocrystals: The case of stannite Cu₂CdSnSe₄, *Chem. Mater.* 24 (2012) 562–570, <https://doi.org/10.1021/cm2031812>.
- [9] K.X. Chen, X.M. Wang, D.C. Mo, S.S. Lyu, Thermoelectric Properties of Transition Metal Dichalcogenides: From Monolayers to Nanotubes, *J. Phys. Chem. c*. 119 (2015) 26706–26711, <https://doi.org/10.1021/acs.jpcc.5b06728>.
- [10] S.R. Harutyunyan, V.H. Vardanyan, A.S. Kuzanyan, V.R. Nikoghosyan, S. Kunii, K. S. Wood, A.M. Gulian, Thermoelectric cooling at cryogenic temperatures, *Appl. Phys. Lett.* 83 (2003) 2142–2144, <https://doi.org/10.1063/1.1610810>.
- [11] S. Berri, Thermoelectric properties of A2BCl6: A first principles study, *J. Phys. Chem. Solids*. 170 (2022) 110940, <https://doi.org/10.1016/j.jpcs.2022.110940>.
- [12] C.V. Devan, B. Deb, M.R. Varma, Magnetic Properties of Undoped and Bi-Doped LaMnO₃, *ECS Trans.* 107 (2022) 12047–12053, <https://doi.org/10.1149/10701.12047ecst>.
- [13] P.N.S. Mahima, M. Kurian, R.R. Das, C.V. Devan, M.R. Varma, C.V. Colin, Exchange bias effect and inhomogeneous magnetism in 6H Ba₃CoFeRuO₉: Role of structural site disorder, *J. Magn. Mater.* 568 (2023) 1–4, <https://doi.org/10.1016/j.jmmm.2023.170372>.
- [14] A. Hirohata, K. Yamada, Y. Nakatani, L. Prejbeanu, B. Diény, P. Pirro, B. Hillebrands, Review on spintronics: Principles and device applications, *J. Magn. Mater.* 509 (2020), <https://doi.org/10.1016/j.jmmm.2020.166711>.
- [15] E. Elahi, G. Dastgeer, P.R. Sharma, S. Nisar, M. Suleman, M.W. Iqbal, M. Imran, M. Aslam, A. Imran, A brief review on the spin valve magnetic tunnel junction composed of 2D materials, *J. Phys. d: Appl. Phys.* 55 (2022), <https://doi.org/10.1088/1361-6463/ac8816>.
- [16] J. Puebla, J. Kim, K. Kondou, Y. Otani, Spintronic devices for energy-efficient data storage and energy harvesting, *Commun. Mater.* 1 (2020) 1–9, <https://doi.org/10.1038/s43246-020-0022-5>.
- [17] M. Massetti, F. Jiao, A.J. Ferguson, D. Zhao, K. Wijeratne, A. Würger, J. L. Blackburn, X. Crispin, S. Fabiano, Unconventional Thermoelectric Materials for Energy Harvesting and Sensing Applications, *Chem. Rev.* 121 (2021) 12465–12547, <https://doi.org/10.1021/acs.chemrev.1c00218>.
- [18] J. Gopalakrishnan, K.S. Nanjundaswamy, Transition metal chalcogenides exhibiting quasi-one-dimensional behaviour, *Bull. Mater. Sci.* 5 (1983) 287–306, <https://doi.org/10.1007/BF02744043>.
- [19] L. Duan, X.C. Wang, J. Zhang, J.F. Zhao, L.P. Cao, W.M. Li, R.Z. Yu, Z. Deng, C. Q. Jin, Synthesis, structure, and properties of Ba₉Co₃Se₁₅ with one-dimensional spin chains, *Chinese Phys. b*. 29 (2020) 1–6, <https://doi.org/10.1088/1674-1056/ab69ea>.
- [20] F. Sun, Z. Guo, N. Liu, D. Wu, J. Lin, E. Cheng, T. Ying, S. Li, W. Yuan, Cs_{0.9}Ni_{3.1}Se₃: A Ni-Based Quasi-One-Dimensional Conductor with Spin-Glass Behavior, *Inorg. Chem.* 57 (2018) 3798–3804, <https://doi.org/10.1021/acs.inorgchem.7b03143>.
- [21] D. Yuan, N. Liu, K. Li, S. Jin, J. Guo, X. Chen, Structure Evolution and Spin-Glass Transition of Layered Compounds AlFeSe₂ (A = Na, K, Rb), *Inorg. Chem.* 56 (2017) 13187–13193, <https://doi.org/10.1021/acs.inorgchem.7b01937>.
- [22] H. Lei, E.S. Bozin, K. Wang, C. Petrovic, Antiferromagnetism in semiconducting KFe_{0.85}Ag_{1.15}Te₂ single crystals, *Phys. Rev. b*. 84 (2011) 2–5, <https://doi.org/10.1103/PhysRevB.84.060506>.
- [23] E. Zhang, J. Zhi, Y.C. Zou, Z. Ye, L. Ai, J. Shi, C. Huang, S. Liu, Z. Lin, X. Zheng, N. Kang, H. Xu, W. Wang, L. He, J. Zou, J. Liu, Z. Mao, F. Xiu, Signature of quantum Griffiths singularity state in a layered quasi-one-dimensional superconductor, *Nat. Commun.* 9 (2018) 4656, <https://doi.org/10.1038/s41467-018-07123-y>.
- [24] W. Bronger, K. Klepp, P. Müller, The magnetic structure of TlFe₃Te₃, *J. Less-Common Met.* 106 (1985) 301–303, [https://doi.org/10.1016/0022-5088\(85\)90267-X](https://doi.org/10.1016/0022-5088(85)90267-X).
- [25] J. Kelber, A.H. Reis, A.T. Aldred, M.H. Mueller, O. Massenet, G. DePasquali, G. Stucky, Structural and magnetic properties of “one-dimensional” barium vanadium triselenide, *J. Solid State Chem.* 30 (1979) 357–364, [https://doi.org/10.1016/0022-4596\(79\)90248-2](https://doi.org/10.1016/0022-4596(79)90248-2).

- [26] T. Yamasaki, S. Giri, H. Nakamura, M. Shiga, E. Procedures, *Magnetism of BaVSe₃*, *J. Phys. Soc. Japan*. 70 (2001) 1768–1771, <https://doi.org/10.1143/JPSJ.70.1768>.
- [27] A. Akrap, V. Stevanović, M. Herak, M. Miljak, N. Barišić, H. Berger, L. Forró, Transport and magnetic properties of BaVSe₃, *Phys. Rev. B - Condens. Matter Mater. Phys.* 78 (2008) 1–11, <https://doi.org/10.1103/PhysRevB.78.235111>.
- [28] A.M. and M.T. M. Nakamura, Sekiyama, A.H. Namatame, A. Fujimori, H. Yoshihara, T. Ohtani, Metal-semiconductor transition and Luttinger-liquid behavior in quasi-one-dimensional BaVS₃ studied by photoemission spectroscopy, *Phys. Rev. B*. 49 (1994) 16193–16201. <https://doi.org/https://doi.org/10.1103/PhysRevB.49.16191>.
- [29] S. Berri, First principle analysis of structural, electronic, optical, and thermoelectric characteristics of Ba₃CaTa₂O₉ complex perovskite, *Emergent Mater.* 5 (2022) 1849–1857, <https://doi.org/10.1007/s42247-021-00331-1>.
- [30] M.Y. Kim, S.J. Park, G.Y. Kim, S.Y. Choi, H. Jin, Designing efficient spin Seebeck-based thermoelectric devices via simultaneous optimization of bulk and interface properties, *Energy Environ. Sci.* 14 (2021) 3480–3491, <https://doi.org/10.1039/d1ee00667c>.
- [31] C.V. Devan, A.A. Nair, R. Revathy, B. Deb, M.R. Varma, Exotic magnetic properties in Zintl phase BaVSe₃: a theoretically supported experimental investigation, *New J. Chem.* 47 (2022) 97–108, <https://doi.org/10.1039/d2nj04129d>.
- [32] V. Ilakovac, M. Guarise, M. Griioni, T. Schmitt, K. Zhou, L. Braicovich, G. Ghiringhelli, V.N. Strocov, H. Berger, Opening of a Peierls gap in BaVS₃ probed by *v* L3 edge resonant inelastic x-ray scattering, *J. Phys. Condens. Matter*. 25 (2013), <https://doi.org/10.1088/0953-8984/25/50/505602>.
- [33] A. Akrap, V. Stevanović, M. Herak, M. Miljak, N. Barišić, H. Berger, L. Forró, Transport and magnetic properties of BaVSe₃, *Phys. Rev. B*. 78 (2008) 1–11, <https://doi.org/10.1103/PhysRevB.78.235111>.
- [34] C.P. Sujith, S. Joseph, T. Mathew, V. Mathew, Ab initio investigation of the structural and electronic properties of tantalum thallium chalcogenides TaTlX₃ (X = S, Se), *J. Solid State Chem.* 315 (2022) 3–7, <https://doi.org/10.1016/j.jssc.2022.123534>.
- [35] N.J. Poulsen, Rietveld refinement and magnetic properties of polycrystalline (Ba, K)VSe₃ and BaV(S, Se)₃, *Mater. Res. Bull.* 33 (1998) 313–322, [https://doi.org/10.1016/S0025-5408\(97\)00218-3](https://doi.org/10.1016/S0025-5408(97)00218-3).
- [36] M. Herak, M. Miljak, A. Akrap, L. Forró, H. Berger, Magnetic anisotropy of paramagnetic and ferromagnetically ordered state of single crystal BaVSe₃, *J. Phys. Soc. Japan*. 77 (2008) 1–4, <https://doi.org/10.1143/JPSJ.77.093701>.
- [37] N. Thi Dung, Y. Pham, D.S. Lam, N. Van Dang, A.G. Gamzatov, A.M. Aliev, D. H. Kim, S.C. Yu, T.D. Thanh, Critical behavior of polycrystalline Pr_{0.7}Ca_{0.1}Sr_{0.2}MnO₃ exhibiting the crossover of first and second order magnetic phase transitions, *J. Mater. Res. Technol.* 9 (2020) 12747–12755, <https://doi.org/10.1016/j.jmrt.2020.09.013>.
- [38] A. Tozri, E. Dhahri, Structural and magnetotransport properties of (La, Pr) -Ba manganites, *J. Alloy. Compd.* 783 (2019) 718–728, <https://doi.org/10.1016/j.jallcom.2018.12.303>.
- [39] J. Minia, N. Joseph, R. Sugathan, C.V. Devan, I. Al-Omari, Manoj, R. Varma, S. Thomas, Structural and magnetic properties of Ni-substituted Y-type Ba_{0.5}Sr_{1.5}Zn_{2-x}Ni_xFe₁₂O₂₂ (x = 0, 0.5, 1.0, and 1.5) hexaferrite, *J. Mater. Sci. Mater. Electron.* 34 (2023) 1–11. <https://doi.org/https://doi.org/10.1007/s10854-022-09638-z>.
- [40] K. Ghosh, C. Mazumdar, R. Ranganathan, S. Mukherjee, Griffiths phase behaviour in a frustrated antiferromagnetic intermetallic compound, *Nat. Publ. Gr.* 5 (2015) 1–10, <https://doi.org/10.1038/srep15801>.
- [41] C.P. Sujith, S. Joseph, T. Mathew, V. Mathew, Ab initio investigation of the structural and electronic properties of tantalum thallium chalcogenides TaTlX₃ (X = S, Se), *J. Solid. State. Chem.* 315 (2023) 3–7, <https://doi.org/10.1016/j.jssc.2022.123534>.
- [42] I. Noor, I. Noor, R. Nath, M.A.H. Ahsan, Magnetic behavior, Griffiths phase and magneto-transport study in 3 d based nano-crystalline double perovskite Pr₂CoMnO₆, *Phys. Lett. A*. 383 (2019) 2326–2332, <https://doi.org/10.1016/j.physleta.2019.04.036>.
- [43] R. Revathy, M.R. Varma, K.P. Surendran, Observation of Cluster Glass and Griffiths-like Phase in Fe₃O₄ Nanostructures, *Phys. Status Solidi*. 2000341 (2021) 1–12, <https://doi.org/10.1002/psb.202000341>.
- [44] H.K. Dara, D. Patra, G.P. Moharana, S.N. Sarangi, Evidence of weak itinerant ferromagnetism and Evidence of weak itinerant ferromagnetism and Griffiths like phase in MnFeGe, *J. Phys.: Condens. Matter*. 35 (2023) 1–9, <https://doi.org/10.1088/1361-648X/acc0ac>.
- [45] H.S. Nair, D. Swain, N. Hariharan, S. Adiga, C. Narayana, S. Elizabeth, Griffiths phase-like behavior and spin-phonon coupling in double perovskite Tb₂NiMnO₆, *J. Appl. Phys.* 110 (2011) 123919, <https://doi.org/10.1063/1.367167>.
- [46] L. Duan, X. Wang, J. Zhang, J. Zhao, L. Cao, Synthesis, structure, and properties of Ba₉Co₃Se₁₅ with one-dimensional spin chains * Synthesis, structure, and properties of Ba₉Co₃Se₁₅ with one-dimensional spin chains *, *Chinese Phys. B*. 29 (2020) 1–6, <https://doi.org/10.1088/1674-1056/ab69ea>.
- [47] A.P. Mihai, J.P. Attané, A. Marty, P. Warin, Y. Samson, Electron-magnon diffusion and magnetization reversal detection in FePt thin films, *Phys. Rev. B - Condens. Matter Mater. Phys.* 77 (2008) 1–4, <https://doi.org/10.1103/PhysRevB.77.060401>.
- [48] M.T.M. Nakamura, A. Sekiyama, H. Namatame, A. Fujimori, H. Yoshihara, T. Ohtani, A. Misu, Metal-semiconductor transition and Luttinger-liquid behavior in quasi-one-dimensional GaVS₃ studied by photoemission spectroscopy, *Phys. Rev. B*. 49 (1994).
- [49] P.R. Mandal, T.K. Nath, Evolution of Griffiths phase in hole doped double perovskite La_{2-x}Sr_xCoMnO₆ (x = 0.0, 0.5, and 1.0), *Mater. Express*. 2 (2015) 1–14, <https://doi.org/10.1088/2053-1591/2/6/066101>.
- [50] D.D. Sarma, E.V. Sampathkumaran, S. Ray, R. Nagarajan, S. Majumdar, A. Kumar, G. Nalini, T.N. Guru Row, Magnetoresistance in ordered and disordered double perovskite oxide, Sr₂FeMoO₆, *Solid State Commun.* 114 (2000) 465–468, [https://doi.org/10.1016/S0038-1098\(00\)00079-X](https://doi.org/10.1016/S0038-1098(00)00079-X).
- [51] T. Ohta, M. Tokuda, S. Iwakiri, K. Sakai, B. Driesen, Y. Okada, K. Kobayashi, Y. Niimi, Butterfly-shaped magnetoresistance in van der Waals ferromagnet Fe₅GeTe₂, *AIP Adv.* 11 (2021), <https://doi.org/10.1063/9.0000067>.
- [52] H.T. Wu, T. Min, Z.X. Guo, X.R. Wang, On universal butterfly and antisymmetric magnetoresistances, *Front. Phys.* 10 (2022) 1–10, <https://doi.org/10.3389/fphy.2022.1068605>.
- [53] D.R. Klein, D. MacNeill, J.L. Lado, D. Soriano, E. Navarro-Moratalla, K. Watanabe, T. Taniguchi, S. Manni, P. Canfield, J. Fernández-Rossier, P. Jarillo-Herrero, Probing magnetism in 2D van der Waals crystalline insulators via electron tunneling, *Science* (80-). 360 (2018) 1218–1222. <https://doi.org/10.1126/science.aar3617>.
- [54] H. Taniguchi, M. Watanabe, M. Tokuda, S. Suzuki, E. Imada, T. Ibe, T. Arakawa, H. Yoshida, H. Ishizuka, K. Kobayashi, Y. Niimi, Butterfly-shaped magnetoresistance in triangular-lattice antiferromagnet Ag₂CrO₂, *Sci. Rep.* 10 (2020) 1–7, <https://doi.org/10.1038/s41598-020-59578-z>.
- [55] A. Ana, V. Stevanović, M. Herak, M. Miljak, N. Barišić, H. Berger, L. Forró, Transport and magnetic properties of BaVSe₃, *Phys. Rev. B*. 78 (2008) 1–11, <https://doi.org/10.1103/PhysRevB.78.235111>.
- [56] H. Yamada, S. Takada, Negative Magnetoresistance of Ferromagnetic Metals due to Spin Fluctuations, *Prog. Theor. Phys.* 48 (1972) 1828–1848, <https://doi.org/10.1143/ptp.48.1828>.
- [57] T. Nie, W. Zhao, K.L. Wang, Engineering Magnetoresistance in Mn_xGe_{1-x} System for Magnetic Sensor Application, in: *Magn. Sensors - Dev. Trends Appl.*, 2017: pp. 65–87. <https://doi.org/10.5772/intechopen.70206>.
- [58] Q.X.J.W. Pan, P. Lu, J.F. Ihlefeld, S.R. Lee, E.S. Choi, Y. Jiang, Electrical-current-induced magnetic hysteresis in self-assembled vertically aligned La₂/3Sr₁/3MnO₃: ZnO-nanopillar composites, *Phys. Rev. Mater.* 2 (2018) 1–17, <https://doi.org/10.1103/PhysRevMaterials.2.021401>.
- [59] A. Patra, C.S. Rout, Anisotropic quasi-one-dimensional layered transition-metal trichalcogenides: Synthesis, properties and applications, *RSC Adv.* 10 (2020) 36413–36438, <https://doi.org/10.1039/d0ra07160a>.
- [60] V. Nagpal, S. Chaudhary, P. Kumar, S.S. Patnaik, Ferromagnetic Clusters and Griffiths Singularity in Magnetic Weyl Semimetal Co₃Sn₂S₂, *SSRN Electron. J.* (2022) 1–13, <https://doi.org/10.2139/ssrn.4157377>.
- [61] S. Singh, R. Rawat, S.E. Muthu, S.W. Dásouza, E. Suard, A. Senyshyn, S. Banik, P. Rajput, S. Bhardwaj, A.M. Awasthi, R. Ranjan, S. Arumugam, D.L. Schlageel, T. A. Lograsso, A. Chakrabarti, S.R. Barman, Spin-valve-like magnetoresistance in Mn₂NiGa at room temperature, *Phys. Rev. Lett.* 109 (2012) 1–5, <https://doi.org/10.1103/PhysRevLett.109.246601>.
- [62] D. Grieger, L. Boehnke, F. Lechermann, Electronic correlations in vanadium chalcogenides :BaVSe₃ versus BaVS₃, *J. Phys.: Condens. Matter*. 22 (2010) 1–16, <https://doi.org/10.1088/0953-8984/22/27/275601>.
- [63] K. Bin Masood, U. Farooq, J. Singh, Evolution of the structural, dielectric and electrical transport properties of Bi₂Te₃ nano-sticks synthesized via polyol and solvothermal routes, *Phys. B Condens. Matter*. 588 (2020) 412183, <https://doi.org/10.1016/j.physb.2020.412183>.
- [64] J.D. Musah, A.M. Ilyas, A. Novitskii, I. Serhienko, K.O. Egbo, G. Saianand, V. Khovaylo, S. Kwofie, K.M. Yu, V.A.L. Roy, Effective decoupling of seebeck coefficient and the electrical conductivity through isovalent substitution of erbium in bismuth selenide thermoelectric material, *J. Alloys Compd.* 857 (2021), <https://doi.org/10.1016/j.jallcom.2020.157559>.
- [65] L.F. Ana Akrap, Vladan Stevanović, Mirna Herak, Marko Miljak, Neven Barišić, Helmut Berger, Transport and magnetic properties of BaVSe₃, *Phys. Rev. B - Condens. Matter Mater. Phys.* 78 (2008) 1–11.
- [66] P.G. Burke, B.M. Curtin, J.E. Bowers, A.C. Gossard, Minority carrier barrier heterojunctions for improved thermoelectric efficiency, *Nano Energy*. 12 (2015) 735–741, <https://doi.org/10.1016/j.nanoen.2015.01.037>.
- [67] S. Watanabe, M. Ohno, Y. Yamashita, T. Terashige, H. Okamoto, J. Takeya, Validity of the Mott formula and the origin of thermopower in π -conjugated semicrystalline polymers, *Phys. Rev. B*. 10 (2019) 1–7, <https://doi.org/10.1103/PhysRevB.100.241201>.
- [68] O. Ivanov, M. Yaprincev, Variable-range hopping conductivity in Lu-doped Bi₂Te₃, *Solid State Sci.* 76 (2018) 111–117, <https://doi.org/10.1016/j.solidstatesciences.2017.12.012>.
- [69] A. Das, A. Chauhan, V. Trivedi, M. Tiadi, R. Kumar, M. Battabyal, D.K. Satapathy, Effect of iodine doping on the electrical, thermal and mechanical properties of SnSe for thermoelectric applications, *Phys. Chem. Chem. Phys.* 23 (2021) 4230–4239, <https://doi.org/10.1039/D0CP06130A>.
- [70] Z. Luo, J. Tian, S. Huang, M. Srinivasan, J. Maassen, Y.P. Chen, X. Xu, Large Enhancement of Thermal Conductivity and Lorenz Number in Topological Insulator Thin Films, *ACS Nano*. 12 (2018) 1120–1127, <https://doi.org/10.1021/acsnano.7b06430>.
- [71] S.D. Sawtelle, M.A. Reed, Temperature-dependent thermal conductivity and suppressed Lorenz number in ultrathin gold nanowires, *Phys. Rev. B*. 99 (2019) 1–11, <https://doi.org/10.1103/PhysRevB.99.054304>.
- [72] M. Yao, C. Opeil, S. Wilson, M. Zebbarjadi, Experimental determination of phonon thermal conductivity and Lorenz ratio of single-crystal bismuth telluride, *MRS Commun.* 7 (2017) 922–927, <https://doi.org/10.1557/mrc.2017.118>.

- [73] Z. Tian, K. Esfarjani, J. Shiomi, A.S. Henry, G. Chen, On the importance of optical phonons to thermal conductivity in nanostructures, *Appl. Phys. Lett.* 99 (2011) 1–4, <https://doi.org/10.1063/1.3615709>.
- [74] D.T. Morelli, J.P. Heremans, G.A. Slack, Estimation of the isotope effect on the lattice thermal conductivity of group IV and group III-V semiconductors, *Phys. Rev. B - Condens. Matter Mater. Phys.* 66 (2002) 1953041–1953049, <https://doi.org/10.1103/PhysRevB.66.195304>.
- [75] J. Philip, P.D. Shima, B. Raj, Enhancement of thermal conductivity in magnetite based nanofluid due to chainlike structures, *Appl. Phys. Lett.* 91 (2007) 1–4, <https://doi.org/10.1063/1.2812699>.



Cite this: DOI: 10.1039/d4cp01171f

A low-temperature thermoelectric transport study of non-stoichiometric AgSbTe_2 †

 Chinnu V. Devan,^{ad} Mahima M. Kurian,^b Santhosh P. N.,^b Manoj Raama Varma^{ib}*^{cd} and Biswapriya Deb^{ib}*^{ad}

In recent times, considerable attention has been given to examining the impact of micro/nanostructure on the thermoelectric characteristics of nonstoichiometric AgSbTe_2 . The present investigation employed direct melting of elements that produced p-type AgSbTe_2 with spontaneous nanostructuring due to cation ordering. The product predominantly features an Ag-deficient $\text{Ag}_{0.927}\text{Sb}_{1.07}\text{Te}_{2.005}$ phase with monoclinic Ag_2Te nanoprecipitates and exhibits a degenerate semiconductor-like behavior with an energy band gap of 0.15 eV. A Seebeck coefficient of $251 \mu\text{V K}^{-1}$ and a power factor of $741 \mu\text{W m}^{-1} \text{K}^{-2}$ at near ambient temperature are attained with this composition. The variable range hopping (VRH) and linear magnetoresistance (LMR) confirmed that the low-temperature transport followed a VRH between the localized states. The composition also exhibited glass like thermal conductivity of $0.2 \text{ W m}^{-1} \text{K}^{-1}$ arising from phonon scattering at all-scale hierarchical structures that led to a high ZT of 1.1 at room temperature. The direct melted ingots show a high relative density of $\sim 97\%$, Vickers hardness H_v of $\sim 108.5 \text{ kgf mm}^{-2}$, and excellent thermal stability, making them an attractive choice for TEGs.

 Received 20th March 2024,
 Accepted 11th May 2024

DOI: 10.1039/d4cp01171f

rsc.li/pccp

1. Introduction

As the demand for energy continues to grow, it is becoming increasingly important to find ways to use energy more efficiently and to transition to cleaner, more sustainable sources of energy. The way we use energy has significant implications for our environment, economy, and society. Fossil fuels, which currently provide the majority of the world's energy, are finite resources that are becoming more difficult and expensive to extract. Renewable energy resources are promising alternatives to fossil fuels, and they do not emit greenhouse gases during operation. Thermoelectric materials find applications in the area of new energy resources; they have the ability to convert waste heat energy into useful electrical energy by using thermoelectric materials.^{1–3} Nowadays, thermoelectric devices play a crucial role in the fields of electricity generation and

refrigeration. The efficiency of a thermoelectric material is expressed through the dimensional figure of merit $ZT = S^2\sigma T/k$, where S , σ , T , and k are the Seebeck coefficient, electrical conductivity, absolute temperature, and thermal conductivity, respectively.⁴ The optimization of these parameters S , σ , and k is achieved through band engineering, defect mechanisms, and optimizing the carrier concentration, mobility, and scattering mechanisms within the material.^{5,6} There is a recent trend in the search for silver-based chalcogenides as promising candidates for thermoelectric applications. Binary and ternary silver chalcogenides have emerged as efficient thermoelectric materials for near room temperature applications.^{7–10} It was observed that various mechanisms, like doping, alloying, site defects, vacancies, nano-precipitates, dislocations, interfaces, and composite formation with other materials, enhance the thermoelectric properties of silver-based chalcogenides.^{11–14} On comparing with conventional thermoelectric materials, these have glass-like thermal conductivity due to the strong bond anharmonicity and the enhanced phonon scattering at the nanostructures within the material.^{15–18} Among the ternary silver chalcogenides, metastable AgSbTe_2 was found to be of considerable interest due to its attractive structural and transport properties. Despite having a simple chemical formula ($\text{Ag}_1\text{Sb}_1\text{Te}_2$) this material has complex variations in stoichiometry and crystal structure.¹⁹ This ternary chalcoantimonate AgSbTe_2 generally crystallizes in a cubic rock salt structure with space group $Fm\bar{3}m$, where Ag/Sb/vacancies randomly occupy Wyckoff position 4a (0.5, 0.5, 0.5) while Te atoms randomly

^a Centre for Sustainable Energy Technology (C-SET), CSIR-National Institute for Interdisciplinary Science and Technology (NIIST), Thiruvananthapuram- 695019, Kerala, India. E-mail: biswapriya.deb@niist.res.in; Fax: +91-471-2491712; Tel: +91-471-2515478, +91-471-2515377

^b Department of Physics, Indian Institute of Technology Madras (IITM), Chennai 600036, India

^c Materials Science and Technology Division, CSIR-National Institute for Interdisciplinary Science and Technology (NIIST), Thiruvananthapuram-695019, Kerala, India. E-mail: mailto:manojraamavarma@gmail.com

^d Academy of Scientific and Innovative Research (AcSIR), Ghaziabad-201002, India

† Electronic supplementary information (ESI) available. See DOI: <https://doi.org/10.1039/d4cp01171f>

occupy Wyckoff position 4b (0, 0, 0).⁸ The thermodynamic stability of AgSbTe₂ still exists as a challenging matter, and based on the pseudo-binary phase diagram²⁰ of $x\text{Ag}_2\text{Te}-(1-x)\text{Sb}_2\text{Te}_3$ with $x = 0.5$ being the stoichiometric $\delta\text{-AgSbTe}_2$. It is experimentally observed that the δ phase of AgSbTe₂ has off stoichiometry and is expressed as $\text{Ag}_2\text{Te}_{(1-x)/2}\text{-Sb}_2\text{Te}_{3(1+x)/2} = \text{Ag}_{1-x}\text{Sb}_{1+x}\text{Te}_{2+x}$ and the only stable ternary phase is with x having a range of values of 0.06–0.28.^{21,22} From the detailed investigation of the pseudo binary phase diagrams of Ag₂Te and Sb₂Te₃, it was witnessed that the exact nominal composition of thermodynamically stable AgSbTe₂ is nonexistent.¹⁰ This metastable state normally decomposes into Ag₂Te and Sb₂Te₃ below 633 K, and the precipitates of Ag₂Te or Sb₂Te₃ along with stoichiometric AgSbTe₂ are due to the equivalence of their formation energies.^{23,24} Continuous research on this specific material concluded that metastable cubic δ phase can be found at room temperature,⁸ and Sugar *et al.* report that the single phase of AgSbTe₂ exists in a wide range of stoichiometries.^{25,26} Doping at various sites like Sb or Te is considered as one of the adopted strategies for the control of secondary phase Ag₂Te, and the doping of Zn,²⁷ Cd²⁸ at the Sb site and Se at the Te site²⁹ reduced the Ag₂Te impurity phase generation. From the current research on this metastable material, it was found that various stoichiometry results in different thermoelectric properties and achieving a stable AgSbTe₂ is still a tough task for practical applications.⁸ The presence of these secondary phases influences the thermal and electrical transport properties of the material in an observable manner.¹⁰ The previous studies outline the outstanding thermoelectric properties and diverse characteristics of the metastable compound AgSbTe₂. It was found that nonstoichiometric AgSbTe₂ displays high figure of merit in the temperature range 500–800 K and the majority of studies highlight the high temperature TE properties of this compound.¹ The doping or induced vacancy at various sites of AgSbTe₂ enhances the ZT and a few compositions display high ZT near room temperature. Here the present study primarily investigates the low temperature transport properties of the nonstoichiometric AgSbTe₂ with spontaneous nanostructures of Ag₂Te. The thermal and mechanical stability of the present material is comparatively higher with respect to other chalcogenides. Moreover, the glass like thermal conductivity contributed to a high ZT value of 1.1 for Ag_{0.927}Sb_{1.07}Te_{2.005} at room temperature. This study may validate the TE properties of previously reported metastable compound AgSbTe₂.

2. Experimental details

2.1 Material synthesis and characterization

AgSbTe₂ compounds were synthesized from high-purity elements Ag (99.99%, Alfa Aesar), Sb (99.99%, Alfa Aesar), and Te (99.99%, Alfa Aesar) through direct melting. The elements were weighed according to stoichiometry and loaded into the quartz tube under vacuum (10^{-5} mbar). The sealed ampoules were first heated at 1073 K for 10 h and the obtained ingot was further heat treated at 773 K for 72 h, then cooled to room

temperature over 24 h. The heat treatment resulted in high-density dark silvery-shaded metallic ingots. A part of the sample was ground for structure and morphology analysis; rectangular samples were cut and polished into a dimension of 10 mm \times 3 mm \times 2 mm for various transport measurements. The characterization techniques are included in the ESI.†

3. Results and discussion

The phase purity of the synthesized sample was analyzed by powder X-ray diffraction. The strong reflections were indexed to the cubic rock salt structure of AgSbTe₂ ($a = 6.06$ Å) having space group $Fm\bar{3}m$ ¹⁹ and the weak secondary phase with Ag₂Te monoclinic phase²⁵ ($a = 8.09$ Å, $b = 4.48$ Å, $c = 8.96$ Å). Fig. 1 shows the Rietveld-refined (GSAS 2 software) XRD data of the sample with a goodness of fit of 1.8; the obtained phase fraction of AgSbTe₂ is 95% and Ag₂Te is 5%. This confirms that the primary phase of the synthesized material at room temperature is AgSbTe₂, and the formation of the secondary phase is due to the slight energy difference between the meta stable δ phase and the Ag₂Te/Sb₂Te₃ mixture.²⁰ Fig. 1b shows the crystal structure of the face centered cubic AgSbTe₂ with Ag⁺ and Sb³⁺ cations randomly occupied at the fcc cationic sublattice, while Te²⁻ was at the anionic sublattice.^{30,31} Roychowdhury *et al.* report that AgSbTe₂ is a disordered material having two types of disorder that originate from the formation of impurity phases, Ag₂Te/Sb₂Te₃ and Ag/Sb cation disorder.²⁵

The chemical composition and valence states of the constituent elements of the sample were analyzed from XPS spectra. Fig. 2a shows the survey spectrum of the sample and confirms the presence of corresponding constituent elements. The oxidation states of the elements Ag, Sb, and Te were studied from their 3d core-level spectra. The strong doublet peaks (Fig. 2b) fitted for Ag at binding energies of 368.3 eV and 374.3 eV correspond to Ag 3d_{5/2} and Ag 3d_{3/2}, respectively, and the spin-orbit splitting of Ag is 6 eV with Ag⁺ oxidation state.³² The peaks at 368.32 eV and 374.36 eV correspond to the Ag–Ag bonds.³² Fig. 1d shows the Sb 3d spectrum, the doublets at 530.46 eV and 539.82 eV³³ are associated with 3d_{5/2} and 3d_{3/2} of Sb, and the corresponding spin-orbit splitting energy of 9.3 eV confirms the Sb³⁺ oxidation state. The presence of peaks at 528.9 eV and 540 eV corresponds to the Sb⁰³² and Sb⁵⁺ oxidation state; the O1s peak at binding energy 531.5 eV may be accompanied by the presence of Sb₂O₅ due to the surface oxidation of the

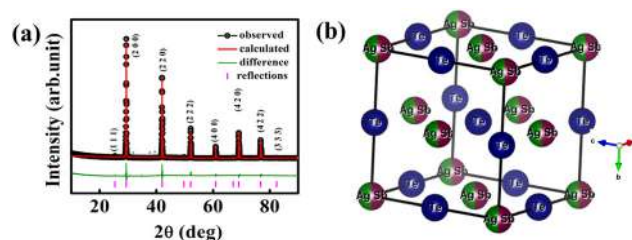


Fig. 1 (a) Powder X-ray diffraction pattern of the as-synthesized sample; (b) crystal structure of AgSbTe₂ from VESTA.

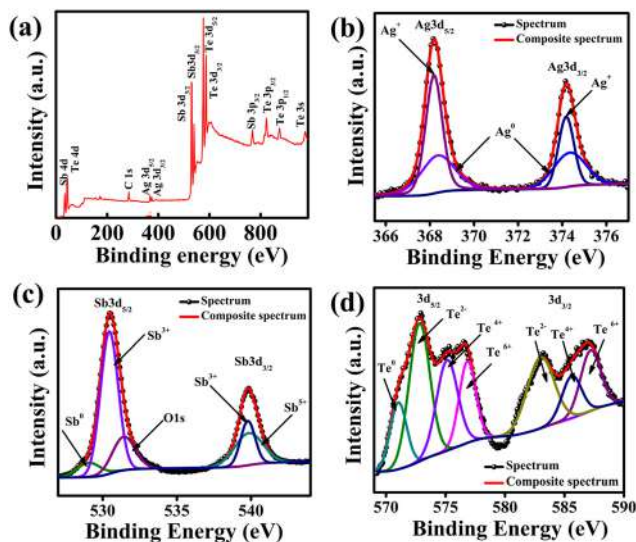


Fig. 2 XPS spectra of the as-synthesized sample: (a) survey spectrum and (b)–(d) high-resolution spectra of Ag, Sb, and Te, respectively.

material.³⁴ The Te 3d spectra contain four sub-peaks; two of them centered at approximately 572.36 eV and 582.94 eV correspond to $3d_{5/2}$ and $3d_{3/2}$ of Te^{2-} , and the other two peaks are associated with the Te–Te bonds³² of minor-phase monoclinic Ag_2Te .

The microstructure composition and the surface morphology of the sample were investigated through EDX and SEM. Fig. 3a–d shows the morphology of the samples at different scales. The density of the synthesized ingots was measured by the Archimedes principle and found to exhibit a density $\sim 97\%$

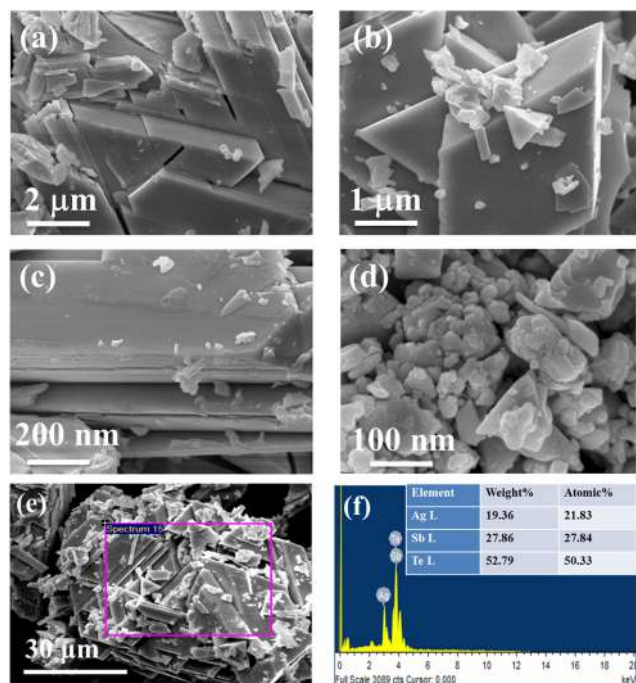


Fig. 3 (a)–(d) SEM micrographs of the sample at different scale bars; (e) and (f) SEM-EDX of the sample.

of the theoretical crystallographic density (7.16 g cm^{-3}). It was found that direct melted samples exhibit high relative density without the aid of densification techniques such as spark plasma sintering and hot pressing at elevated temperatures.¹¹ The compactness of the material was further confirmed through SEM analysis; Fig. 3a–c shows the microstructure of the samples with compacted sheet-like structures. Fig. 3d clearly reveals that micro- and nano-sized particles randomly arranged on the plate-like structures of the direct-melted sample. The local composition of the synthesized sample was determined through EDX analysis at different regions of the material under study. Fig. 3b shows the EDX spectrum; the corresponding weight percentage and atomic percentage of each element were also marked. Table S1 (ESI[†]) compares the actual weight percentage calculated from its stoichiometric composition with the average weight percentage obtained from the SEM-EDX analysis. The microstructure composition was obtained as $\text{Ag}_{0.927}\text{Sb}_{1.07}\text{Te}_{2.005}$, and it confirms an off-stoichiometry from the actual composition with $x \sim 0.07$.²⁴ Lee *et al.* report that the δ phase was identified as Ag deficient and Sb rich, with composition inhomogeneity generated due to the formation of Ag_2Te within or near the cubic phase from excess Ag,³⁵ and here the monoclinic Ag_2Te ³⁶ results in off-stoichiometry. Wyzga *et al.*²⁴ reported this material with a composition $\text{Ag}_{0.94}\text{Sb}_{1.06}\text{Te}_{2.06}$, which was associated with Ag_2Te inclusions and the present synthesized material has a stoichiometry very close to that of the above-mentioned one (Table 1).

Various micro structures like plates, and triangular-shaped sheets (Fig. 4a and b) were further confirmed through the TEM analysis. Fig. 4c shows the TEM-SAED pattern of the material, and the planes exactly match the cubic phase of AgSbTe_2 . Clear evidence of nanoprecipitates in off-stoichiometric cubic AgSbTe_2 was found in both low- and high-resolution TEM images and is shown in Fig. 4d and e of Fig. 4. The nanostructures in AgSbTe_2 emerged from the ordering of the cations ($\text{Ag}^+/\text{Sb}^{3+}$) into nanoscale domains,^{37,38} and previous studies reveal that AgSbTe_2 exists with secondary phases such as Ag_2Te , Sb_2Te_3 , or Ag–Sb rich nano dots. The nanoscale continuous precipitates of Ag_2Te can be observed within the Ag-deficient region of AgSbTe_2 ³⁵ and conventional melted or hot-pressed samples exhibit white and dark nanodots of Ag_2Te and Sb-rich regions (Sb_2Te_3), respectively.^{26,35} The EDX composition confirms the Ag-deficient nature of the synthesized material; and the observed nano dots can be marked as the secondary phase Ag_2Te . Fig. 4f shows the calculated d spacing of the planes in the nanodots; d spacings of 0.22 nm and 0.11 nm correspond to the planes (112) and (314) of the monoclinic Ag_2Te .²⁵ These nanostructures can modulate various electronic and thermal transport properties in the material. Fig. 4g shows the TEM-EDS

Table 1 Elemental weight percentage of AgSbTe_2 calculated and obtained from SEM-EDX

Element	Actual weight (%)	Average weight (%)
Ag	22.24	20.61
Sb	25.11	26.86
Te	52.63	52.76

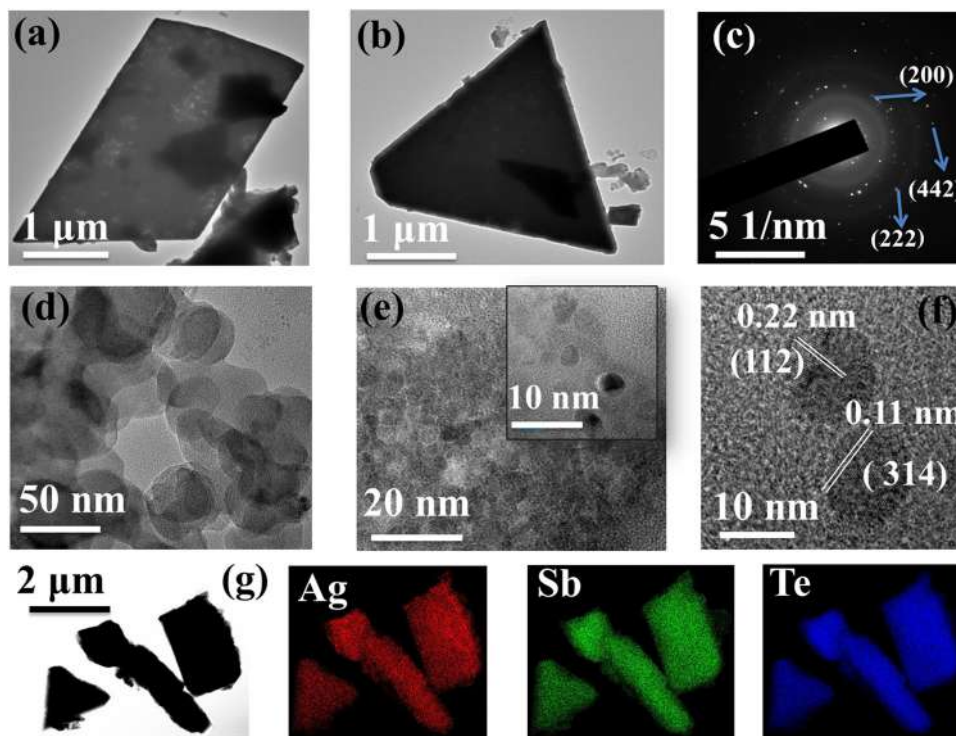


Fig. 4 (a) and (b) TEM images of AgSbTe_2 , and (c) SAED pattern of the material under study; (d) and (e) observed nanostructures in AgSbTe_2 , (f) HRTEM image of the sample confirming the Ag_2Te monoclinic phase, and (g) TEM-EDS elemental mapping of the material.

elemental mapping of the powdered sample, and it confirms the uniform distribution of all three constituent elements Ag, Sb and Te throughout the material on a micrometer scale.

The temperature-dependent electrical and thermal transport properties were carried out over the temperature range of 6 K to 300 K and are shown in Fig. 5a–d. Fig. 5a shows the temperature dependent resistivity data, and Fig. S1 (ESI[†]) depicts the normalized resistivity data $\rho(T)/\rho(T_m)$ versus temperature. The resistivity curve has a minimum around a particular temperature $T_m \sim 95$ K, and this minimum temperature indicates the transition from a normal semiconductor³⁹ to a heavily doped semiconductor or metal-like material. At low temperatures, the minimum resistivity in disordered materials arises due to the competition between the weak localization of electronic states and disorder-enhanced electron–electron interaction.³⁹ It was reported that pristine AgSbTe_2 has a $T_m \sim 61$ K, and the increase in this minimum temperature is a measure of disorder in this material,²⁸ which indicates that the enhanced disorder is due to the emerged localized states. On further increasing the temperature to 300 K, the material exhibits a heavily doped semiconducting nature with low electrical conductivity. The low-temperature electrical transport properties of the disordered semiconductors can be explained by the variable range hopping model (VRH)^{28,40} and Mott found that at low temperatures the most probable transport process would not be the nearest neighbour hopping.⁴¹ Mott's variable range hopping mechanism establishes the hopping conduction between localized states with energies concentrated within a narrow band ($\sim k_B T$) in the vicinity of the Fermi level (E_F) at relatively low temperature.⁴² The hopping mechanism is

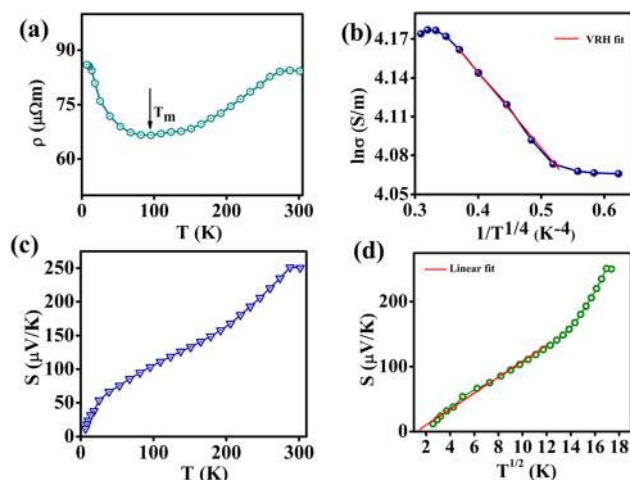


Fig. 5 (a) Temperature dependence of electrical conductivity; (b) VRH fit on electrical conductivity versus T data; (c) temperature dependence of Seebeck coefficient; (d) VRH fit on the S versus T data.

associated with both thermally activated hopping over a potential barrier and phonon-assisted quantum mechanical hopping between the states.⁴³ According to the VRH model, the temperature dependence of electrical conductivity is expressed as $\sigma \propto \exp[-(T_0/T)^S]$, with $S = 1/(1 + d)$, where d is the dimensionality of the system and T_0 is the characteristic hopping temperature.⁴⁴ The linear dependence of logarithmic σ on $T^{-1/4}$ is shown in Fig. 5b, and it was observed that the off-stoichiometric AgSbTe_2 exhibits VRH conduction in a temperature range of $13 \text{ K} < T <$

84 K. Hatayama *et al.* pointed out that local structural defects due to the nanoclusters,⁴⁵ small grain boundaries⁴⁶ and dangling bonds⁴⁷ can generate localized states within the band gap. Here, the disorder and inhomogeneity stem from the Ag₂Te nanostructures that create a structural difference from the actual one and lead to the dangling bonds.

Fig. 5c shows that the Seebeck coefficient increases with temperature and is positive over the entire range of temperatures. The positive value of S indicates that holes are the majority charge carriers, and according to the previous reports, the p-type carriers are generated due to the Ag vacancies.^{10,48} Most of the studies report that the ternary chalcogenide AgSbTe₂ has a high S value in the range of 220–300 $\mu\text{V K}^{-1}$. It is further enhanced through doping at various sites^{10,49,50} and in the present study, the material attains a maximum value of thermopower around 251 $\mu\text{V K}^{-1}$ at room temperature. According to the VRH hopping model, the Seebeck coefficient follows the relation $S \sim T^{(d-1)/(d+1)}$ where d is the dimensionality of the system.⁵¹ Fig. 5d validates the S versus $T^{1/2}$ relation: when the temperature approaches zero, S fits with $T^{1/2}$ and $S \rightarrow 0$ as $T \rightarrow 0$ ^{52,53} and it demonstrates that large S at the low temperature range is due to the hopping of holes.^{52,54} The enhancement of the Seebeck coefficient in thermoelectric materials includes band engineering through lowering carrier concentration (n), enhancing effective mass, the energy filtering effect, and increasing scattering parameters.⁵¹ Roychowdhury *et al.* report that the high density of states effective mass can contribute to the high Seebeck coefficient,²⁷ and that comes from the increase in density of states around the Fermi level. Hoang *et al.* found that the enhanced S value in AgSbTe₂ is due to the existence of the flat and multivalley valence band.⁵⁵ The cation disorder in Ag–Sb–Te-based materials has a vital role in transport properties due to the creation of localized electronic states near the Fermi level. In these disordered materials, the mobility edge separates the localized states from the extended states. When the mobility edge comes near the Fermi level, it results in a distortion in the electronic density of states, which enhances the Seebeck coefficient.⁵⁶ The Seebeck coefficient of the degenerate semiconductor or metal can be expressed by the Mott formula⁵⁷

$$S = \frac{8\pi^2 k_B^2 T}{3eh^2} m^* \frac{\pi^{2/3}}{3n}$$

where n is the carrier concentration, k_B is the Boltzmann constant, e is the electronic charge, h is the Planck constant, and m^* is the density of states effective mass. This shows that S is inversely proportional to the carrier concentration, and directly depends on the effective mass, and for a particular carrier concentration the Seebeck coefficient can increase with the scattering factor.⁵⁸ The presence of nanopores and nanograins in the matrix may enhance the scattering mechanism.⁵⁹ The carrier concentration (n) and carrier mobility (μ) were estimated from the Hall effect measurements at room temperature, and the positive slope of ρ_{xy} versus H further confirms the p-type carriers. The effective mass was calculated from the experimentally measured S and n , and the obtained S , n , μ , and m^* values are tabulated in Table 2. It was found that the material has an

Table 2 Obtained values of n , μ , and m^* from Hall effect measurement and Mott equation

T (K)	S ($\mu\text{V K}^{-1}$)	n (cm^{-3})	μ ($\text{cm}^2 \text{V}^{-1} \text{s}^{-1}$)	m^*/m_0
300 K	251	2.5×10^{19}	29.70	1.1

optimized carrier concentration that is required for a promising thermoelectric material.

A peak in the temperature-dependent thermopower was observed in thermoelectric materials with bipolar conduction mechanisms.^{60,61} Goldsmid and Sharp formulated an analytical expression $E_g = 2eS_{\text{max}}T_{\text{max}}$ on the basis of bipolar conduction, which connects the parameters band gap (E_g), maximum thermopower $|S_{\text{max}}|$ and maximum temperature T_{max} , where T_{max} is the temperature at which the thermopower attains a maximum value.^{62,63} The presence of minority charge carriers results in a variation in the trend of the Seebeck coefficient with increasing temperature, and the total Seebeck coefficient is the collective contribution from both charge carriers.⁶³ At low temperatures, the minority charge carriers will not contribute much to the Seebeck coefficient. The increase in temperature results in the broadening of the Fermi distribution, which enhances the electrical conductivity due to the minority carriers and reduces the Seebeck coefficient. In p type materials, the generation of electrons at high temperatures results in a peak in the thermopower, and this is the simplest way to obtain the energy gap of the material from the temperature-dependent S data.^{61,63} The variation of the Seebeck coefficient with temperature from 6 K to 800 K is shown in S2 (ESI[†]), and the S_{max} was obtained from the peak of the curve. It was found that the material exhibits an energy gap of ~ 0.15 eV at a maximum temperature 300 K, and AgSbTe₂ is widely accepted as a narrow band gap semiconductor.⁴⁸ Hoang *et al.* estimated the E_g at high temperatures from electrical conductivity measurements as 0.1 eV.⁵⁵ The dependence of $\rho(H)$ and $\rho(T)$ on VRH conductivity can be expressed in a single relation.⁴⁰

$$\ln \frac{\rho(H)}{\rho(0)} = t_1 \left(\frac{a}{L_H} \right)^4 \left(\frac{T_0}{T} \right)^{3/4}$$

where $\frac{\rho(H)}{\rho(0)}$ is the ratio of electrical resistivity at magnetic field to zero field, t_1 is a constant equal to 5/2016, a is the localization radius of the electron, $L_H = (ch/2\pi eH)^{1/2}$, and c is the speed of light.

Linear magnetoresistance (LMR) is another interesting electronic property witnessed in inhomogeneous and disordered semiconductors.^{64–66} Xu *et al.* found for the first time that nonmagnetic silver selenides and tellurides exhibit an unusual increase in resistance to magnetic fields and they show an unsaturating nature even at higher fields.⁶⁷ In inhomogeneous conductors, the LMR originates from the variation in the current path generated by the macroscopic spatial fluctuations of carrier mobility induced by the variation in material density and thickness.^{67,68} The transverse magnetoresistance (applied magnetic field perpendicular to the current direction in the material) measurements were carried out up to 70 kOe at lower temperatures (5 K and 100 K). Fig. 6a establishes clear evidence

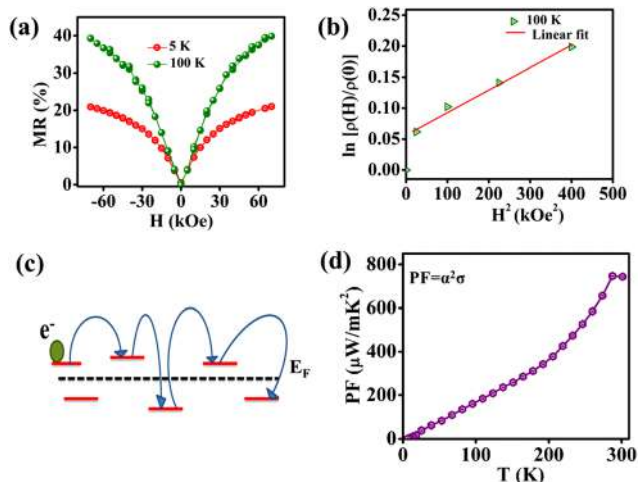


Fig. 6 (a) Magnetoresistance versus magnetic field plot; (b) linear fit on $\ln \rho(H)/\rho(0)$ versus H^2 , schematic representation of the (c) VRH mechanism, and (d) PF versus T plot.

of unsaturating LMR in this disordered material, and it exhibits a high MR of 40% at 100 K. The semiconductors with VRH conductivity obey the linear dependence of $\ln(\rho(H)/\rho(0))$ with H^2 and are confirmed for 100 K in Fig. 6b and c depicts the schematic representation of the VRH mechanism. Fig. 6d represents the calculated temperature-dependent power factor ($S^2\sigma$)²⁷ of $\text{Ag}_{0.927}\text{Sb}_{1.07}\text{Te}_{2.005}$ from the measured S and σ . It was observed that this particular composition has a power factor of $747 \mu\text{W m}^{-1} \text{K}^{-2}$ near room temperature, and it comes from the Seebeck value.

For metals (degenerate limit), the Lorenz number (L) is approximated as $2.44 \times 10^{-8} \text{ W } \Omega \text{ K}^{-2}$, and in degenerate semiconductors, the approximate value of L is calculated from the expression⁶⁹ $L = 1.5 + \exp(-|S|/116)$, where L is in $10^{-8} \text{ W } \Omega \text{ K}^{-2}$ and S is the Seebeck coefficient in $\mu\text{V K}^{-1}$. Fig. 7(a) and (b) show the variation of L with both the Seebeck coefficient and

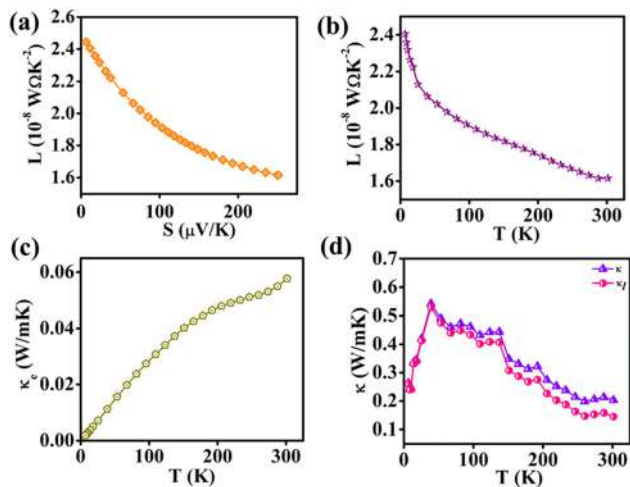


Fig. 7 (a) Calculated Lorenz number from S ; (b) variation of L with T ; variation of (c) electronic thermal conductivity with T ; (d) total and lattice thermal conductivity with T .

temperature; it decreases with increasing temperature due to various scattering, such as acoustic phonon scattering.^{69,70} The total thermal conductivity of a material is the sum of its electronic thermal conductivity (k_e) and lattice thermal conductivity (k_l). The electronic part of the thermal conductivity (k_e) can be obtained with the help of the Wiedemann–Franz law ($k_e = L\sigma T$) and Fig. 7c shows the temperature dependent k_e . The variation of total and lattice thermal conductivity of the sample is shown in Fig. 7d, and it is found that the major part of the thermal conductivity comes from the lattice contribution. At low temperatures, the material has a T^3 -dependent thermal conductivity and attains a maximum of $0.5 \text{ W m}^{-1} \text{ K}^{-1}$ at 40 K, then decreases with increasing temperature due to the dominant phonon scattering.¹⁰ At room temperature, the total thermal conductivity of the material reduces to a glass-like thermal conductivity of $0.2 \text{ W m}^{-1} \text{ K}^{-1}$.^{71,72} The ternary chalcogenide AgSbTe_2 is commonly reported with a thermal conductivity of $0.6\text{--}0.7 \text{ W m}^{-1} \text{ K}^{-1}$,⁷³ and Ag vacancy controlled $\text{Ag}_{0.98}\text{SbTe}_2$ exhibits room temperature thermal conductivity of $0.33 \text{ W m}^{-1} \text{ K}^{-1}$.³⁹

The low thermal conductivity of AgSbTe_2 -based materials was associated with phonon scattering at the structural disorder, point defects, nano inclusions, and strong lattice anharmonicity. The combination of crystalline, amorphous regions, and dislocations were clearly noticeable in the high magnification TEM images of the sample in a and b of Fig. 8. The boundaries were marked between the interphase of the crystalline and amorphous regions, and the dislocations were evidently visible in the Inverse Fast Fourier Transform (IFFT) of HRTEM images. Fig. 8c confines various parameters that contribute to the phonon scattering in this material and concludes that the phonons encounter scattering at various interphases that include nanostructures, defects, dislocations, and boundaries.^{74,75}

In the cubic rock salt crystal structure of nominal AgSbTe_2 , the disordered distribution of Ag^+ and Sb^{3+} between the closely

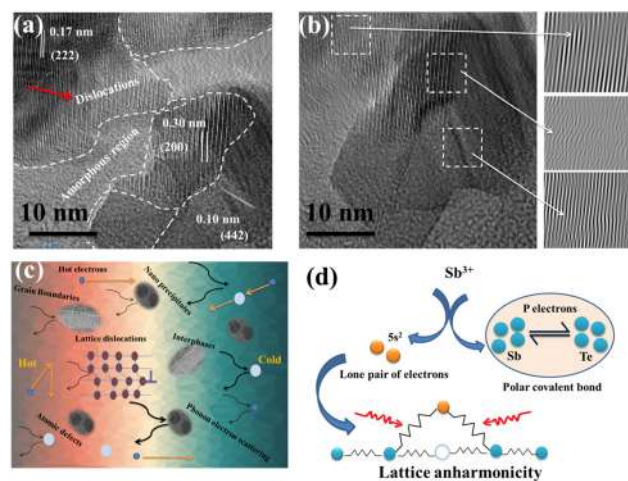


Fig. 8 HRTEM images of the sample (a), amorphous, crystalline regions and dislocations; (b) IFFT of the HRTEM images clearly showing the lattice dislocations; (c) schematic representation of the phonon scattering mechanisms; and (d) 1D ball and spring model for phonon–phonon interaction.

packed layers of Te ions contributes to the lattice anharmonicity.^{76,77} Normally in the class of I–V–VI₂ (chalcocyanates) materials, the nonbonding of the external s and a part of the p electrons forms a shell of large radius, which leads to anharmonicity bonds in these compositions.⁷⁸ Fig. 8d shows the proposed schematic representation of the 1D ball and spring model for phonon–phonon interaction with the bonding of Sb–Te.⁷⁵ In AgSbTe₂, the Sb has a valence configuration of 5s² 5p³, Sb³⁺ results in a lone pair of electrons (5s²), and the p electrons of Sb and Te form a polar covalent bond and separately form the band. The competition between covalent bonding and lone pair repulsion results in the anharmonicity in lattice vibrations of these materials.⁷⁵ Tan *et al.* report that the overlapping of wave functions of the lone pair of electrons and the nearby valence electrons leads to the nonlinear repulsive electrostatic force.⁷⁹ The occupancy of chemically dissimilar atoms at the same crystallographic site generates distortion in the structure, and the differences in the local force constants of Ag⁺ and Sb³⁺ induce phonon scattering in AgSbTe₂.^{22,80} The spontaneous nanostructures, due to the cationic ordering, can scatter the phonons effectively³¹ and the spontaneous nanostructures in the present material were confirmed through TEM analysis, which scatters the phonons and reduces the lattice thermal conductivity remarkably. A comparison study with the reported literature^{10,28,36,39,76,81} (Fig. S3, ESI†) concludes that the present composition exhibits extremely low thermal conductivity.

The low temperature heat capacity of the sample was measured under high vacuum between 2 K and 300 K, as shown in Fig. 9a. In the heat capacity measurement, a known heat pulse is applied at each point of temperature, and the material and platform are heated to a temperature of $T_p(t)$. At the end of the heat pulse, the sample temperature relaxes to a particular temperature, T_0 , where T_0 is known as the heat sink temperature and is expressed by the relation⁸²

$$T_p = T_0 + \Delta T \exp\left(-\frac{t}{\tau}\right)$$

where τ is the time constant, Fig. 9a shows the variation of measured heat capacity with temperature, and according to Dulong–Petit law, the near room temperature heat capacity of the material was found to be 0.205 J g⁻¹ K⁻¹.³⁶ The experimental C_p value near room temperature was determined as 0.212 J g⁻¹ K⁻¹, and it is well in agreement with the theoretically calculated value. At low temperatures the heat capacity of a nonmagnetic material can be expressed as the sum of the contributions from electrons and phonons,

$$C_p = \alpha T + \beta T^3$$

where α and β are constants, in the expression, the first part corresponds to the electronic contribution, and the second part arises from the lattice contribution to the heat capacity. The density of states (DOS) at the Fermi level ($E = E_F$) can be calculated from the electronic part of the heat capacity by using the expression⁸³

$$\alpha = \frac{\pi^2}{3} (k_B^2) N(E_F)$$

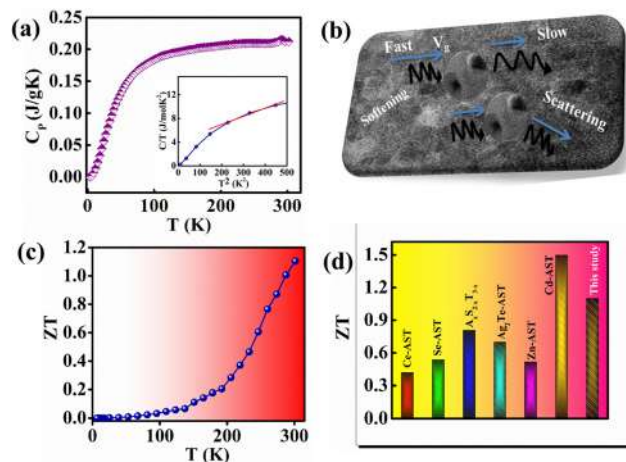


Fig. 9 (a) Temperature-dependent heat capacity of the material (inset: C/T versus T^2 plot), (b) schematic explanation for lattice softening, (c) variation of ZT with temperature, (d) a comparison of ZT of the present material with previous reports.

where k_B is the Boltzmann's constant and the material has a high density of states 1.1×10^{27} eV⁻¹ mol⁻¹ at E_F , and it contributes to the enhancement in Seebeck coefficient through heavy carrier effective mass. At low temperatures, the data was fitted with C/T versus T^2 (inset of Fig. 9a) and the Debye temperature was obtained from β by using the relation⁸⁴

$$\theta_D = \left(\frac{12\pi^4 NR}{5\beta}\right)^{\frac{1}{3}}$$

where N is the number of atoms per chemical formula, and R is the molar gas constant. It was confirmed that from the linear fit of C/T versus T^2 , the material obeys the Debye T^3 law, and the estimated Debye temperature was ~ 91 K. Morelli *et al.* reported that the material AgSbTe₂ exhibits $\theta_D \sim 125$ K.⁸⁵ It was found that the reduction in Debye temperature was associated with the lattice softening in the material; the phonons met the softening (the reduction in group velocity of phonons) and scattering at the nanostructures.⁸⁶ The various lattice defects, dislocations, and nanostructures change the phonon frequency in a disordered material, generating lattice softening that reduces the phonon speed and leads to phonon scattering.⁸⁷ The lattice softening reduces the overall thermal conductivity of the material, and that helps to tune the thermoelectric efficiency by introducing internal lattice strain.⁸⁸ Fig. 9b shows the pictorial representation of lattice softening and scattering at nanoprecipitates.

The dimensionless figure of merit ZT of the present material was calculated from various measured parameters S , σ , and k using $\frac{S^2 \sigma T}{k}$, and the variation of ZT as a function of temperature is plotted in Fig. 9c. At room temperature, the material exhibits a ZT of 1.1 and it can be further increased by various defect engineering techniques. Fig. 9d displays the comparison study of the ZT of doped AgSbTe₂ with the current material, and this nonstoichiometric compound has the highest ever reported ZT value at room temperature. Fig. S5a and b (ESI†)

Table 3 A comparison of the room temperature S and ZT values of the present study with previous reports

No.	Composition	Seebeck coefficient ($\mu\text{V K}^{-1}$)	ZT
1	AgSbTe_2	200 ⁹² Gainza <i>et al.</i>	0.12
2	$\text{Ag}_0.7\text{Sb}_{1.12}\text{Te}_2$	70 ⁹³ Gonjal <i>et al.</i>	0.2
3	$(\text{AgSbTe}_2)_{0.9}(\text{Ag}_2\text{Te})_{0.1}$	210 ⁹⁴ Lee <i>et al.</i>	0.2
4	$\text{Ag}_{0.88}\text{Sb}_{1.04}\text{Te}_2$	200 ⁵⁰ Wang <i>et al.</i>	0.5
5	$\text{Ag}_{0.83}\text{Sb}_{1.06}\text{Te}_2$	220 ⁵⁰ Wang <i>et al.</i>	0.6
6	AgSbTe_2	260 ⁵⁰ Wang <i>et al.</i>	0.7
7	$\text{Ag}_{0.98}\text{SbTe}_2$	235 ⁹⁵ Pathak <i>et al.</i>	0.85
8	$\text{Ag}_{0.99}\text{SbTe}_2$	250 ⁹⁶ Pathak <i>et al.</i>	0.5
9	$\text{Ag}_{0.99}\text{Na}_{0.01}\text{SbTe}_{2.02}$	275 ⁹⁰ Du <i>et al.</i>	0.55
10	$\text{AgBi}_{0.05}\text{Sb}_{0.95}\text{Te}_2$	200 ⁹⁷ Mohanraman <i>et al.</i>	0.4
11	$\text{Ag}_{0.9}\text{Sb}_{1.1}\text{Te}_{2.1}$	250 ⁸ Wu <i>et al.</i>	0.5
12	$\text{Ag}_{0.927}\text{Sb}_{1.07}\text{Te}_{2.005}$	251 this study	1.1

show the measured thermal conductivity and ZT of the material with error bars. The temperature-dependent TE properties of AgSbTe_2 demonstrate a $ZT > 1$ spanning the temperature range of 500 K to 700 K.⁸ Recent studies on AgSbTe_2 have shown that the presence of Ag vacancies leads to a $ZT < 1$ at ambient temperature, but reaches its greatest value of 2.3 at 573 K.³⁹ The high temperature high pressure synthesis method contributed a ZT of 1.07 at 513 K,⁸⁹ anion vacancies in Na-doped AgSbTe_2 bring about low thermal conductivity and enhanced ZT of 1.5 at 650 K.⁹⁰ The alloy of SnSe– AgSbTe_2 was found with $ZT \sim 1$ at a high temperature of 820 K.⁷⁴ The other Ag–Sb–Te based chalcogenides, $\text{AgSb}_{0.96}\text{Zn}_{0.04}\text{Te}_2$ with $ZT \sim 1.9$ at 585 K,⁹¹ $\text{AgSbTe}_{1.85}\text{Se}_{0.15}$ has a $ZT \sim 2.1$ at 573 K,²⁹ and Cd doped AgSbTe_2 unveil ZT as 2.6 at 573 K.²⁸ The present composition naturally exhibits a comparatively high room temperature ZT due to the enhanced Seebeck coefficient and the extreme low thermal conductivity due to the all-scale hierarchical structures. The previous exploration notifies that non-stoichiometric AgSbTe_2 obtained from natural or induced methods resulted in promising thermopower. Table 3 depicts a comparison study on the reported room temperature S and ZT value with the present study.

The high-temperature thermoelectric power factor reveals that this material can be applied to elevated temperature TEGs. The single-leg TEG has an enhanced efficiency of 12.5% at a temperature gradient of 700 K. On an application level, thermoelectric materials should have temperature and mechanical stability, which can be confirmed through thermogravimetric analysis and Vickers hardness measurement. The off-stoichiometric

AgSbTe_2 has high thermal stability up to 841 K, and the endothermic dip in the DTA analysis of the material corresponds to the melting temperature in the range of 825 K and the peak at 713 K is due to the recrystallization of the material on cooling. Fig. S6a and b (ESI[†]) represent the TGA and DTA data of the material. It was observed that the material exhibits a high Vickers hardness⁹⁸ value H_v of ~ 108.47 kgf mm^{-2} and was found to be much higher when compared with conventional TE materials Bi_2Te_3 (63 kgf mm^{-2}) and PbTe (24 kgf mm^{-2}) (Fig. 10).⁹⁹

4. Conclusion

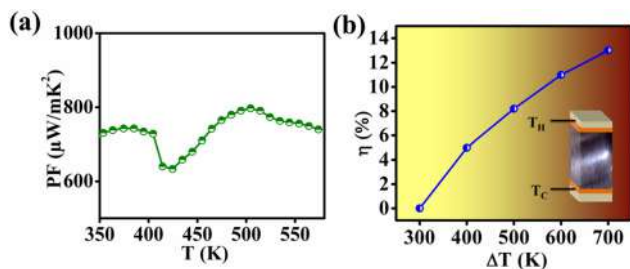
Ternary chalcogenide AgSbTe_2 was synthesized by the direct melting of high-purity component elements, yielding a high-density material with a composition of $\text{Ag}_{0.927}\text{Sb}_{1.07}\text{Te}_{2.005}$. The metastable AgSbTe_2 crystallizes in the cubic phase with space group $Fm\bar{3}m$, with Ag and Sb randomly occupying the same site to contribute towards the unique transport properties. The presence of nanostructures of Ag_2Te was observed in SEM, and confirmed through EDX composition analysis and HRTEM. At extremely low temperatures, this disordered material unveils a variable-range hopping mechanism due to the presence of localized states. The high Seebeck coefficient of the order of 251 $\mu\text{V K}^{-1}$ at room temperature could be attributed to the high DOS near the E_F and electron filtering mechanisms triggered by the nanoscale structures of Ag_2Te . The energy gap of 0.15 eV was determined from the temperature-dependent thermopower data. The lower thermal conductivity (0.2 $\text{W m}^{-1} \text{K}^{-1}$) at ambient temperature predominantly depends on the spontaneous cation ordering that formed nanostructures functioning as powerful phonon scattering centers. Additionally, the point defects, interfaces, and lattice anharmonicity all contributed to the lessened thermal conductivity. The confirmation of the lattice relaxation in this disordered material was achieved by observing a decrease in the Debye temperature. At ambient temperature, a power factor of 741 $\mu\text{W m}^{-1} \text{K}^{-2}$ and ZT of 1.1 were achieved, which increased with increasing temperature, reaching a calculated efficacy of 12.5% at $\Delta T = 700$ K.

Author contributions

Chinnu V. Devan: experimentation/data collection, initial drafting/editing, Mahima M Kurian: data collection/acquisition, writing review, P. N. Santhosh: writing review and editing, Manoj Raama Varma: conceptualization, drafting, data interpretation, revising, Biswapriya Deb: conceptualization, drafting, data interpretation, revising.

Conflicts of interest

The authors declare no conflict of interest.

**Fig. 10** (a) High temperature PF versus T ; (b) variation of the calculated one-leg TE efficiency with ΔT .

Acknowledgements

C. V. D. acknowledges the support of University Grants Commission (UGC), India, for granting a research fellowship. The authors acknowledge the measurement facilities obtained from different labs of CSIR-NIIST. The author P. N. S. acknowledges DST FIST-Phase II funding for the PPMS (SR/FST/PSII-038/2016) and DST-SERB for project funding [CRG/2022/006367] the measurement facilities obtained from IIT Madras. The authors M. R. V. and B. D. are thankful to the Science and Engineering Research Board, Department of Science and Technology, New Delhi, India for funding this research through the Project EMR/2017/004539 (Ver-1) dated 06/05/2019. MRV also thanks CSIR HRD Group for CSIR Emeritus Scientist Project.

References

- 1 T. M. Tritt and M. A. Subramanian, Thermoelectric Materials, Phenomena, and Applications: A Bird's Eye View, *Mater. Res. Bull.*, 2006, **31**, 188–198.
- 2 M. S. Dresselhaus, G. Chen, M. Y. Tang, R. Yang, H. Lee, D. Wang, Z. Ren, J. P. Fleurial and P. Gogna, New directions for low-dimensional thermoelectric materials, *Adv. Mater.*, 2007, **19**, 1043–1053.
- 3 G. J. Snyder and E. S. Toberer, Complex thermoelectric materials, *Nat. Mater.*, 2008, **7**, 101–110.
- 4 M. G. Kanatzidis, Ultralow thermal conductivity and high thermoelectric figure of merit in SnSe crystals, *Nature*, 2014, **508**, 373–378.
- 5 S. N. Guin and K. Biswas, Sb deficiencies control hole transport and boost the thermoelectric performance of p-type AgSbSe₂, *J. Mater. Chem. C*, 2015, **3**, 10415–10421.
- 6 P. Jood, R. Chetty and M. Ohta, Structural stability enables high thermoelectric performance in room temperature Ag₂Se, *J. Mater. Chem. A*, 2020, **8**, 13024–13037.
- 7 J. Liang, T. Wang, P. Qiu, S. Yang, C. Ming, H. Chen, Q. Song, K. Zhao, T. R. Wei, D. Ren, Y. Y. Sun, X. Shi, J. He and L. Chen, Flexible thermoelectrics: From silver chalcogenides to full-inorganic devices, *Energy Environ. Sci.*, 2019, **12**, 2983–2990.
- 8 Y. Wu, P. Qiu, Y. Yu, Y. Xiong, T. Deng, L. Chen, M. Wuttig and X. Shi, High-performance and stable AgSbTe₂-based thermoelectric materials for near room temperature applications, *J. Mater. Chem.*, 2022, **8**, 1095–1103.
- 9 A. J. E. Rettie, C. D. Malliakas, A. S. Botana, J. M. Hodges, F. Han, R. Huang, D. Y. Chung and M. G. Kanatzidis, Ag₂Se to KAg₃Se₂: Suppressing Order-Disorder Transitions via Reduced Dimensionality, *J. Am. Chem. Soc.*, 2018, **140**, 9193–9202.
- 10 S. N. Zhang, T. J. Zhu, S. H. Yang, C. Yu and X. B. Zhao, Improved thermoelectric properties of AgSbTe₂ based compounds with nanoscale Ag₂Te in situ precipitates, *J. Alloys Compd.*, 2010, **499**, 215–220.
- 11 S. Singh, K. Hirata, D. Byeon, T. Matsunaga, O. Muthusamy, S. Ghodke, M. Adachi, Y. Yamamoto, M. Matsunami and T. Takeuchi, Investigation of Thermoelectric Properties of Ag₂S_xSe_{1-x} (x = 0.0, 0.2 and 0.4), *J. Electron. Mater.*, 2020, **49**, 2846–2854.
- 12 J. Zhang, X. Qin, D. Li, C. Song, Y. Liu, H. Xin, T. Zou and Y. Li, Optimized thermoelectric properties of AgSbTe₂ through adjustment of fabrication parameters, *Electron. Mater. Lett.*, 2015, **11**, 133–137.
- 13 J. P. McHugh, W. A. Tiller, S. E. Haszko and J. H. Wernick, Phase diagram for the pseudobinary system Ag₂Te-Sb₂Te₃, *J. Appl. Phys.*, 1961, **32**, 1785.
- 14 S. Y. Tee, D. Ponsford, C. L. Lay, X. Wang, X. Wang, D. C. J. Neo, T. Wu, W. Thitsartarn, J. C. C. Yeo, G. Guan, T. C. Lee and M. Y. Han, Thermoelectric Silver-Based Chalcogenides, *Adv. Sci.*, 2022, **9**, 1–35.
- 15 G. Qin, X. Zhang, S. Yue, Z. Qin, H. Wang, Y. Han and M. Hu, Resonant bonding driven giant phonon anharmonicity and low thermal conductivity of phosphorene, *Phys. Rev. B*, 2016, **94**, 1–11.
- 16 C. W. Li, J. Hong, A. F. May, D. Bansal, S. Chi, T. Hong, G. Ehlers and O. Delaire, Orbitally driven giant phonon anharmonicity in SnSe, *Nat. Phys.*, 2015, **11**, 1–8.
- 17 M. G. Kanatzidis, Nanostructured Thermoelectrics: The New Paradigm?, *Chem. Mater.*, 2010, **22**, 648–659.
- 18 J. K. Lee, M. W. Oh, S. D. Park, B. S. Kim, B. K. Min, M. H. Kim and H. W. Lee, Improvement of Thermoelectric Properties through Controlling the Carrier Concentration of AgPb₁₈SbTe₂₀ Alloys by Sb Addition, *Electron. Mater. Lett.*, 2012, **8**, 659–663.
- 19 R. Mohanraman, R. Sankar, F. C. Chou, C. H. Lee, Y. Chen, R. Mohanraman, R. Sankar, F. C. Chou and C. H. Lee, Enhanced thermoelectric performance in Bi-doped p-type AgSbTe₂ compounds Enhanced thermoelectric performance in Bi-doped p-type AgSbTe₂ compounds, *J. Appl. Phys.*, 2014, 163712.
- 20 R. Marin, G. I. R. Brun, J. Tedenac, P. E. Bataillon and M. Cedex, Phase equilibria in the Sb₂Te₃-Ag₂Te system, *J. Mater. Sci.*, 1985, **20**, 730–735.
- 21 P. M. Wyzga and K. T. Wojciechowski, Analysis of the Influence of Thermal Treatment on the Stability of Ag_{1-x}Sb_{1+x}Te_{2+x} and Se-Doped AgSbTe₂, *J. Electron. Mater.*, 2016, **45**, 1548–1554.
- 22 G. Ehlers, T. Hong, A. Huq, W. Tian, V. M. Keppens and B. C. Sales, Glass-like phonon scattering from a spontaneous nanostructure in AgSbTe₂, *Nat. Nanotechnol.*, 2013, **8**, 445–451.
- 23 B. Legendre, G. Brun, B. Liautard and J. C. Tedenac, The ternary system silver-antimony-tellurium. Study of the sub-ternary Sb, Tq-Ag, Te-Te, *Thermochim. Acta*, 1988, **131**, 37–45.
- 24 P. M. Wyzga and K. T. Wojciechowski, Analysis of the Influence of Thermal Treatment on the Stability of Ag_{1-x}Sb_{1+x}Te_{2+x} and Se-Doped AgSbTe₂, *J. Electron. Mater.*, 2016, **45**, 1548–1554.
- 25 J. D. Sugar and D. L. Medlin, Precipitation of Ag₂Te in the thermoelectric material AgSbTe₂, *J. Alloys Compd.*, 2009, **478**, 75–82.
- 26 S. N. Zhang, T. J. Zhu, S. H. Yang, C. Yu and X. B. Zhao, Phase compositions, nanoscale microstructures and

- thermoelectric properties in $\text{Ag}_{2-y}\text{Sb}_y\text{Te}_{1+y}$ alloys with precipitated Sb_2Te_3 plates, *Acta Mater.*, 2010, **58**, 4160–4169.
- 27 S. Roychowdhury, R. Panigrahi, S. Perumal and K. Biswas, Ultrahigh Thermoelectric Figure of Merit and Enhanced Mechanical Stability of p-type $\text{AgSb}_{1-x}\text{Zn}_x\text{Te}_2$, *ACS Energy Lett.*, 2017, **2**, 349–356.
- 28 S. Roychowdhury, T. Ghosh, R. Arora, M. Samanta and L. Xie, Enhanced atomic ordering leads to high thermoelectric performance in AgSbTe_2 , *Science*, 2021, **371**, 722–727.
- 29 M. Hong, Z. G. Chen, L. Yang, Z. M. Liao, Y. C. Zou, Y. H. Chen, S. Matsumura and J. Zou, Achieving $zT > 2$ in p-Type $\text{AgSbTe}_{2-x}\text{Se}_x$ Alloys via Exploring the Extra Light Valence Band and Introducing Dense Stacking Faults, *Adv. Energy Mater.*, 2018, **8**, 1–7.
- 30 S. P. Jae Ki Lee, B. Ryu, S. Park, J. H. Son, J. Park, J. Jang and M.-W. Oh, Effect of microstructure on thermoelectric conversion efficiency in metastable δ -phase AgSbTe_2 , *Acta Mater.*, 2021, **222**, 117443.
- 31 J. Ki, B. Ryu, S. Park, J. Hee, J. Park, J. Jang, M. Oh and S. Park, Effect of microstructure on thermoelectric conversion efficiency in metastable δ -phase AgSbTe_2 , *Acta Mater.*, 2022, **222**, 117443.
- 32 S. Sahu, A. Manivannan, H. Shaik, G. M. Rao, S. Sahu, A. Manivannan, H. Shaik and G. M. Rao, Local structure of amorphous $\text{Ag}_5\text{In}_5\text{Sb}_{60}\text{Te}_{30}$ and In_3SbTe_2 phase change materials revealed by X-ray photoelectron and Raman spectroscopic studies Local structure of amorphous $\text{Ag}_5\text{In}_5\text{Sb}_{60}\text{Te}_{30}$ and In_3SbTe_2 phase change materials revealed by X-ray pho, *J. Appl. Phys.*, 2017, **122**, 1–6.
- 33 S. K. Pandey, S. K. Pandey, V. Awasthi, A. Kumar, U. P. Deshpande and S. Mukherjee, p-type conduction from Sb-doped ZnO thin films grown by dual ion beam sputtering in the absence of oxygen ambient, *J. Appl. Phys.*, 2013, **114**, 1–7.
- 34 Y. Liu, M. Li, S. Wan, K. H. Lim, Y. Zhang, M. Li, J. Li and M. Ib, Surface Chemistry and Band Engineering in AgSbSe_2 : Toward High Thermoelectric Performance, *ACS Nano*, 2023, **17**, 1–12.
- 35 S. P. Jae Ki Lee, B. Ryu, S. Park, J. H. Son, J. Park, J. Jang and M.-W. Oh, Effect of microstructure on thermoelectric conversion efficiency in metastable δ -phase AgSbTe_2 , *Acta Mater.*, 2021, **222**, 117443.
- 36 J. K. Lee, M. W. Oh, B. Ryu, J. E. Lee, B. S. Kim, B. K. Min, S. J. Joo, H. W. Lee and S. D. Park, Enhanced thermoelectric properties of AgSbTe_2 obtained by controlling heterophases with Ce doping, *Sci. Rep.*, 2017, **7**, 1–8.
- 37 G. Ehlers, T. Hong, A. Huq, W. Tian, V. M. Keppens and B. C. Sales, Glass-like phonon scattering from a spontaneous nanostructure in AgSbTe_2 , *Nat. Nanotechnol.*, 2013, **8**, 1–7.
- 38 T. Ghosh, S. Roychowdhury, M. Dutta and K. Biswas, High-Performance Thermoelectric Energy Conversion: A Tale of Atomic Ordering in AgSbTe_2 , *ACS Energy Lett.*, 2021, **6**, 2825–2837.
- 39 R. Pathak, L. Xie, S. Das, T. Ghosh, A. Bhui, K. Dolui, D. Sanyal, J. He and K. Biswas, Vacancy controlled nanoscale cation ordering leads to high thermoelectric performance, *Energy Environ. Sci.*, 2023, **16**, 3110–3118.
- 40 O. Ivanov and M. Yaprntsev, Variable-range hopping conductivity in Lu-doped Bi_2Te_3 , *Solid State Sci.*, 2018, **76**, 111–117.
- 41 L. Zhang and Z. Tang, Polaron relaxation and variable-range-hopping conductivity in the giant-dielectric-constant material $\text{CaCu}_3\text{Ti}_4\text{O}_{12}$, *Phys. Rev. B: Condens. Matter Mater. Phys.*, 2004, 174306.
- 42 L. Essaleh, S. M. Wasim, G. Marín, C. Rincón, S. Amhil and J. Galibert, Mott type variable range hopping conduction and magnetoresistance in p-type CuIn_3Te_5 semiconductor compound, *J. Appl. Phys.*, 2017, **122**, 15702.
- 43 Y. Huang, S. Chiu, Z. Zhu, Z. Li, J. Lin, Y. Huang, S. Chiu, Z. Zhu, Z. Li and J. Lin, Variable-range-hopping conduction processes in oxygen deficient polycrystalline ZnO films Variable-range-hopping conduction processes in oxygen deficient polycrystalline ZnO films, *J. Appl. Phys.*, 2010, **107**, 63715.
- 44 K. H. Kim, S. Lara-avila, H. He, H. Kang, S. J. Hong, M. Park, J. Eklöf, K. Moth, S. Matsushita, K. Akagi and S. Kubatkin, Probing variable range hopping lengths by magneto conductance in carbonized polymer nanofibers, *Sci. Rep.*, 2018, **8**, 1–7.
- 45 S. Hatayama, Y. Shuang, P. J. Fons, Y. Saito and V. Alexander, Cr-Triggered Local Structural Change in $\text{Cr}_2\text{Ge}_2\text{Te}_6$ Phase Change Material, *ACS Appl. Mater. Interfaces*, 2019, **11**, 43320–43329.
- 46 K. Xu, M. Yao, J. Chen, P. Zou, Y. Peng, F. Li and X. Yao, Effect of crystallization on the band structure and photoelectric property of SrTiO_3 sol e gel derived thin fi lm, *J. Alloys Compd.*, 2015, **653**, 7–13.
- 47 A. Phys, H. Lu, Y. Guo and H. Li, Modeling of surface gap state passivation and Fermi level de-pinning in solar cells Modeling of surface gap state passivation and Fermi level de-pinning in solar cells, *J. Appl. Phys.*, 2019, **114**, 222106.
- 48 V. Jovicic and J. P. Heremans, Measurements of the energy band gap and valence band structure of AgSbTe_2 , *Phys. Rev. B: Condens. Matter Mater. Phys.*, 2008, **77**, 245204.
- 49 H. Wu, S. Chen, T. Ikeda and G. J. Snyder, Reduced thermal conductivity in Pb-alloyed AgSbTe_2 thermoelectric materials, *Acta Mater.*, 2012, **60**, 6144–6151.
- 50 H. Wang, J. F. Li, M. Zou and T. Sui, Synthesis and transport property of AgSbTe_2 as a promising thermoelectric compound, *Appl. Phys. Lett.*, 2008, **93**, 202106.
- 51 L. Wang, X. Zhang and L. Zhao, Evolving Strategies Toward Seebeck Coefficient Enhancement, *Acc. Mater. Res.*, 2023, **4**, 448–456.
- 52 M. K. K. Suekuni, K. Tsuruta and T. Ariga, Variable-range-hopping conduction and low thermal conductivity in chalcogenide spinel $\text{Cu}_y\text{Fe}_4\text{Sn}_{12}\text{X}_{32}$ (X = S, Se), *J. Appl. Phys.*, 2017, **109**, 83709.
- 53 O. E. Parfenov and F. A. Shklyaruk, On the Temperature Dependence of the Thermoelectric Power in Disordered Semiconductors, *Semiconductors*, 2007, **41**, 1021–1026.
- 54 P. Zvyagin, On the Theory of Hopping Transport in Disordered Semiconductors, *Phys. Status Solidi*, 1973, **58**, 443–449.

- 55 K. Hoang, S. D. Mahanti, J. R. Salvador and M. G. Kanatzidis, Atomic Ordering and Gap Formation in Ag-Sb-Based Ternary Chalcogenides, *Phys. Rev. Lett.*, 2007, **99**, 1–4.
- 56 J. P. Heremans, Enhancement of Thermoelectric Efficiency in PbTe by Distortion of the Electronic Density of States, *Science*, 2008, **321**, 554–557.
- 57 J. Lee, S. Choi, W. Seo, Y. Lim, H. Lee and I. Kim, Thermoelectric properties of Spark Plasma Sintered $\text{In}_x\text{Yb}_y\text{La}_{0.3-x-y}\text{Co}_4\text{Sb}_{12}$ skutterudite system, *Renewable Energy*, 2012, **42**, 36–40.
- 58 J. P. Heremans, C. M. Thrush, D. T. Morelli, J. P. Heremans, C. M. Thrush and D. T. Morelli, Thermopower enhancement in PbTe with Pb precipitates Thermopower enhancement in PbTe with Pb precipitates, *J. Appl. Phys.*, 2005, **98**, 63703.
- 59 B. Du, H. Li, J. Xu, X. Tang and C. Uher, Enhanced thermoelectric performance and novel nanopores in AgSbTe_2 prepared by melt spinning, *J. Solid State Chem.*, 2011, **184**, 109–114.
- 60 A. Hmood, A. Kadhim and H. A. Hassam, Superlattices and Microstructures Yb-doped SnTe semimetal thin films deposited by thermal evaporation: Structural, electrical, and thermoelectric properties, *Superlattices Microstruct.*, 2014, **76**, 36–45.
- 61 J. H. Son, M. W. Oh, B. S. Kim, S. D. Park, B. K. Min, M. H. Kim and H. W. Lee, Effect of ball milling time on the thermoelectric properties of p-type $(\text{Bi,Sb})_2\text{Te}_3$, *J. Alloys Compd.*, 2013, **566**, 168–174.
- 62 A. Hmood, A. Kadhim, M. A. Mahdi and H. A. Hassan, Structural, characterization and electrical properties of $\text{AgPb}_m\text{SbTe}_m + 2$ compounds synthesized through a solid-state microwave technique, *Int. J. Hydrogen Energy*, 2016, **41**, 5048–5056.
- 63 H. J. Goldsmid and J. W. Sharp, Estimation of the Thermal Band Gap of a Semiconductor from Seebeck Measurements, *J. Electron. Mater.*, 1999, **28**, 1–4.
- 64 R. Xu, A. Husmann, T. F. Rosenbaum, M. L. Saboungi, J. E. Enderby and P. B. Littlewood, Large magnetoresistance in non-magnetic silver chalcogenides, *Nature*, 1997, **390**, 57.
- 65 M.-L. S. A. Husmann, J. B. Betts, G. S. Boebinger, A. Migliori and T. F. Rosenbaum, Megagauss sensors, *Nature*, 2002, **417**, 421–424.
- 66 J. Hu and T. F. Rosenbaum, Classical and quantum routes to linear magnetoresistance, *Nat. Mater.*, 2008, **7**, 697–700.
- 67 S. Tong, D. Pan, X. Wang and Z. Yu, Unsaturated linear magnetoresistance effect in high-quality free-standing InSb single-crystal nanosheets, *J. Phys. D: Appl. Phys.*, 2020, **53**, 1–9.
- 68 N. V. Kozlova, N. Mori, O. Makarovskiy, L. Eaves, Q. D. Zhuang and A. Krier, Linear magnetoresistance due to multiple-electron scattering by low-mobility islands in an inhomogeneous conductor, *Nat. Commun.*, 2012, **3**, 1–5.
- 69 A. Das, A. Chauhan, V. Trivedi, M. Tiadi, R. Kumar, M. Battabyal and D. K. Satapathy, Effect of iodine doping on the electrical, thermal and mechanical properties of SnSe for thermoelectric applications, *Phys. Chem. Chem. Phys.*, 2021, **23**, 4230–4239.
- 70 R. W. McKinney, P. Gorai and E. S. Toberer, Search for new thermoelectric materials with low Lorenz number, *J. Mater. Chem. A*, 2017, **5**, 17302–17311.
- 71 L. Ferrer-argemi, Z. Yu, J. Kim, N. V. Myung, J. Lim and J. Lee, Silver content dependent thermal conductivity and thermoelectric properties of electrodeposited antimony telluride thin films, *Sci. Rep.*, 2019, **9**, 1–8.
- 72 S. S. Ragimov, A. E. Babayeva and A. I. Aliyeva, On the thermal conductivity of AgSbTe_2 and $\text{Ag}_{0.82}\text{Sb}_{1.18}\text{Te}_{2.18}$, *Low Temp. Phys.*, 2018, **44**, 1–4.
- 73 N. Rezaei, S. J. Hashemifar and H. Akbarzadeh, Thermoelectric properties of AgSbTe_2 from first-principles calculations, *J. Appl. Phys.*, 2014, **116**, 1–5.
- 74 H. Wang, H. Hu, N. Man, C. Xiong and Y. Xiao, Band flattening and phonon-defect scattering in cubic SnSe- AgSbTe_2 alloy for thermoelectric enhancement, *Mater. Today Phys.*, 2020, **16**, 100298.
- 75 V. Vijay, S. Harish, J. Archana and M. Navaneethan, Cation disorder and bond anharmonicity synergistically boosts the thermoelectric performance of p-type AgSbSe_2 , *CrystEngComm*, 2021, **23**, 5522–5530.
- 76 Y. S.-H. Christopher, E. Carlton, R. De Armas, J. Ma, A. F. May and O. Delaire, Natural nanostructure and superlattice nanodomains in AgSbTe_2 , *J. Appl. Phys.*, 2014, **115**, 1–7.
- 77 B. Min, B. Kim, M. Oh, B. Ryu, J. Lee, S. Joo, S. Park, H. Lee and H. Lee, Effect of La-doping on AgSbTe_2 Thermoelectric Compounds, *J. Korean Phys. Soc.*, 2016, **68**, 164–169.
- 78 J. Ki, B. Ryu, S. Park, J. Hee, J. Park, J. Jang, M. Oh and S. Park, Effect of microstructure on thermoelectric conversion efficiency in metastable δ -phase AgSbTe_2 , *Acta Mater.*, 2022, **222**, 117443.
- 79 G. Tan, L. Zhao and M. G. Kanatzidis, Rationally Designing High-Performance Bulk Thermoelectric Materials, *Chem. Rev.*, 2016, **116**, 12123–12149.
- 80 L. Ye, K. Hoang, A. J. Freeman, S. D. Mahanti, J. He, T. M. Tritt and M. G. Kanatzidis, First-principles study of the electronic, optical, and lattice vibrational properties of AgSbTe_2 , *Phys. Rev. B: Condens. Matter Mater. Phys.*, 2008, **77**, 1–6.
- 81 E. Garc, J. Gainza, O. J. Dur, C. Dejoie, N. M. Nemes, L. Mart, A. Alonso and F. Serrano-Sánchez, Optimizing Thermoelectric Properties through Compositional Engineering in Ag-Deficient AgSbTe_2 Synthesized by Arc Melting, *ACS Appl. Electron. Mater.*, 2024, DOI: [10.1021/acsaelm.3c01653](https://doi.org/10.1021/acsaelm.3c01653).
- 82 B. Jonas, T. Brink, K. Tsuchiya, F. Meng, G. Wilde and K. Albe, Low temperature heat capacity of a severely deformed metallic glass, *Phys. Rev. Lett.*, 2014, **112**, 1–5.
- 83 J. J. Hamilton, E. L. Keatley, H. L. Ju, A. K. Raychaudhuri, V. N. Smolyaninova and R. L. Greene, Low-temperature specific heat of $\text{La}_{0.67}\text{Ba}_{0.33}\text{MnO}_3$ and $\text{La}_{0.8}\text{Ca}_{0.2}\text{MnO}_3$, *Phys. Rev. B: Condens. Matter Mater. Phys.*, 1996, **54**, 926–929.
- 84 E. S. R. Gopal, *Specific heat at low temperatures*, Plenum Press, 1st edn, 1966.
- 85 D. T. Morelli and V. Jovic, Intrinsically Minimal Thermal Conductivity in Cubic I–V–VI 2 Semiconductors, *Phys. Rev. Lett.*, 2008, 35901.

- 86 G. Tan, S. Hao, R. C. Hanus, X. Zhang, S. Anand, T. P. Bailey, A. J. E. Rettie, X. Su, C. Uher, V. P. Dravid, G. Je, C. Wolverton and M. G. Kanatzidis, High Thermoelectric Performance in SnTe–AgSbTe₂ Alloys from Lattice Softening, Giant Phonon–Vacancy Scattering, and Valence Band Convergence, *ACS Energy Lett.*, 2018, **3**, 705–712.
- 87 R. Hanus, M. T. Agne, A. J. E. Rettie, Z. Chen, G. Tan, D. Young, M. G. Kanatzidis, Y. Pei, P. W. Voorhees and G. J. Snyder, Lattice softening significantly reduces thermal conductivity and leads to high thermoelectric efficiency, *Adv. Mater. Lett.*, 2019, **31**, 1–21.
- 88 R. Hanus, M. T. Agne, A. J. E. Rettie, Z. Chen, G. Tan, D. Young, M. G. Kanatzidis, Y. Pei, P. W. Voorhees and G. J. Snyder, Lattice softening significantly reduces thermal conductivity and leads to high thermoelectric efficiency, *Adv. Mater. Lett.*, 2019, **31**, 1–21.
- 89 T. Su, X. Jia, H. Ma, F. Yu, Y. Tian, G. Zuo, Y. Zheng, Y. Jiang, D. Dong, L. Deng, B. Qin and S. Zheng, Enhanced thermoelectric performance of AgSbTe₂ synthesized by high pressure and high temperature, *J. Appl. Phys.*, 2009, **105**, 1–5.
- 90 B. L. Du, H. Li and X. F. Tang, Enhanced thermoelectric performance in Na-doped p-type nonstoichiometric AgSbTe₂ compound, *J. Alloys Compd.*, 2011, **509**, 2039–2043.
- 91 S. Roychowdhury, R. Panigrahi, S. Perumal and K. Biswas, Ultrahigh Thermoelectric Figure of Merit and Enhanced Mechanical Stability of p-type AgSb_{1-x}Zn_xTe₂, *ACS Energy Lett.*, 2017, **2**, 349–356.
- 92 J. Gainza, F. Serrano-Sánchez, O. J. Dura, N. M. Nemes, J. L. Martínez, M. T. Fernández-Díaz and J. A. Alonso, Reduced Thermal Conductivity in Nanostructured AgSbTe₂ Thermoelectric Material, Obtained by Arc-Melting, *Nanomaterials*, 2021, **12**(21), 3910.
- 93 J. Prado-Gonjal, E. García-Calvo, J. Gainza, O. J. Durá, C. Dejoie, N. M. Nemes, J. L. Martínez, J. A. Alonso and F. Serrano-Sánchez, Optimizing Thermoelectric Properties through Compositional Engineering in Ag-Deficient AgSbTe₂ Synthesized by Arc Melting, *ACS Appl. Electron. Mater.*, 2023, 1–9.
- 94 J. K. Lee, B. Ryu, S. Park, J. H. Son, J. Park, J. Jang, M. W. Oh and S. D. Park, Effect of microstructure on thermoelectric conversion efficiency in metastable δ -phase AgSbTe₂, *Acta Mater.*, 2022, **222**, 117443.
- 95 J. Heb, K. Biswas, R. Pathak, L. Xie, S. Das, T. Ghosh, A. Bhui, K. Dolui and D. Sanyal, Vacancy Controlled Nano-scale Cation Ordering Leads to High Thermoelectric Performance, *Energy Environ. Sci.*, 2023, **16**, 3110–3118.
- 96 R. Pathak, L. Xie, S. Das, T. Ghosh, A. Bhui, K. Dolui, D. Sanyal, J. He and K. Biswas, Vacancy controlled nano-scale cation ordering leads to high thermoelectric performance, *Energy Environ. Sci.*, 2023, **16**, 3110–3118.
- 97 R. Mohanraman, R. Sankar, F. C. Chou, C. H. Lee and Y. Y. Chen, Enhanced thermoelectric performance in Bi-doped p-type AgSbTe₂ compounds, *J. Appl. Phys.*, 2013, **114**, 1–6.
- 98 H. Liu, X. Zhang, W. Li and Y. Pei, Advances in thermoelectric (GeTe)_x(AgSbTe₂)_{100-x}, *Chin. Phys. B*, 2022, **31**, 1–9.
- 99 H. Kim, P. Dharmiah and S. Hong, Thermoelectric Properties of Texture-Controlled Fabricated by Gas-Atomization and Hot-Extrusion Processes, *J. Electron. Mater.*, 2018, **47**, 3119–3126.